THESIS

For obtaining the grade of

DOCTOR OF THE UNIVERSITY OF POITIERS

(ÉCOLE NATIONALE SUPÉRIEURE d'INGÉNIEURS de POITIERS)
(Diplôme National - Arrêté du 25 mai 2016)

École Doctorale n°651 :
MIMME – Mathématiques – Informatique – Matériaux – Mécanique - Énergétique

Specialty:
Energy, Thermal and Combustion

Presented by:

Cagatay HARATOKA

****
Conductive Thermotronics based on Phase Change Materials: Application to the case of VO_2
****

Director of the Thesis: Younès EZZAHRI

Co-director of the Thesis: Karl JOULAIN

Defended on October 14, 2025

In front of the commission of examination

JURY

Philippe BEN-ABDALLAH	Research Director at CNRS, Institut d'Optique	Reviewer
Konstantinos TERMENTZIDIS	Research Director at CNRS, INSA Lyon	Reviewer
Armande HERVÉ	Associate Professor at Gustave Eiffel University ESIEE PARIS	Examiner
Frédéric DUMAS-BOUCHIAT	Professor at University of Limoges	Examiner
Karl JOULAIN	Professor at University of Poitiers, Institute Pprime	Examiner
Younès EZZAHRI	Professor at University of Poitiers, Institute Pprime	Examiner

Acknowledgments

Firstly, I would like to express my sincere gratitude to my thesis director, Prof. Younès Ezzahri, and my thesis co-director, Prof. Karl Joulain. Throughout this study, I have always felt their continuous support, and their wisdom and guidance have been invaluable in helping me developing my academic research skills. I would also like to thank my thesis defense jury members Dr. Philippe Ben-Abdallah, Dr. Konstantinos Termentzidis, Assoc. Prof. Armande Hervé and Prof. Frédéric Dumas-Bouchiat for their insightful comments, encouragement, and suggestions as well as for taking the time to evaluate my work with great care.

I would also like to thank my mother Meral, my father Oktay, and my brother Altay for their support and encouragement throughout this journey. Their belief in me has been a great source of motivation to complete this thesis to the best of my ability.

My sincere appreciation goes to the Institut Pprime of the University of Poitiers, with which my connection dates back to my pre-doctoral years. I became a part of this institute when I was still a master's student, and for this reason, it holds a special place for me. The institute has always provided me with an excellent academic environment, rich research opportunities, and a supportive atmosphere. I therefore extend my sincere thanks to all colleagues, friends, administrative and technical staff. I would like to emphasize that I am particularly grateful to Jean-Christophe Vergez from the technical staff, who was always available and willing to resolve any technical issues as quickly as possible.

Contents

Abstract vii

Résumé ix

List of Figures xi

List of Tables xxiii

List of Symbols xxv

List of Acronyms/Abbreviations xxix

General Introduction 1

Introduction Générale 5

1 Theoretical Background and Literature Review 9

1.1 Introduction . . . 10

1.1.1 Fourier's law of heat conduction . . . 11

1.1.2 General heat conduction equation . . . 12

1.2 Thermal properties . . . 13

1.2.1 Thermal conductivity . . . 13

1.2.2 Specific heat capacity . . . 15

1.2.3 Interface thermal resistance . . . 16

1.3 Metal-insulator transition and vanadium dioxide . . . 17

1.3.1 Mott-Hubbard and Peierls theories . . . 18

1.3.2 Crystal and band structures of vanadium dioxide . . . 19

1.3.3 Phase behaviors of vanadium dioxide . . . 19

1.3.4 Changes in the properties of vanadium dioxides . . . 22

1.4 Enthalpy method . . . 24

1.5 Thermotronics and thermal components 25
1.5.1 Thermal diode 26
1.5.2 Thermal transistor 56
1.5.3 Thermal memristor 68
1.6 Potential applications 73
1.7 Motivation and objective of the study 81

Résumé du Chapitre 1 **83**

2 Conductive Thermal Memristor **91**
2.1 Introduction 91
2.2 Theoretical modeling 92
2.2.1 Implementation of a simple model 92
2.2.2 Verification of the numerical model in a simple case 94
2.2.3 The conductive thermal memristor and temperature modulation of the thermal baths 97
2.2.4 Modeling the hysteresis zone 98
2.2.5 Numerical modeling of the conductive thermal memristor 102
2.3 Results and discussion 105
2.4 Conclusion 123

Résumé du Chapitre 2 **125**

3 Conductive Thermal Diode **131**
3.1 Introduction 132
3.2 Theoretical modeling of the linear conductive thermal diode 132
3.3 Results and discussion of the linear conductive thermal diode 135
3.4 Theoretical modeling of the conductive thermal diode under Dirichlet boundary conditions 137
3.4.1 Nondimensionalization of the transient process 140
3.4.2 Nondimensionalization of the steady-state process 142
3.4.3 Thermal rectification analysis under steady-state conditions 147

3.5 Results and discussion of the conductive thermal diode under Dirichlet boundary conditions . . . 147
3.6 Theoretical modeling of the conductive thermal diode under dynamical boundary conditions . . . 158
3.6.1 Models and temperature modulation of the thermal baths . . . 158
3.7 Results and discussion of the conductive thermal diode under dynamical boundary conditions . . . 160
3.8 Theoretical modeling of the capacitive thermal diode . . . 163
3.8.1 Capacitive thermal diode with constant heat capacities . . . 164
3.8.2 Capacitive thermal diode with temperature dependent heat capacity . . . 165
3.9 Results and discussion of the capacitive thermal diode . . . 167
3.10 Conclusion . . . 176

Résumé du Chapitre 3 **179**

4 Conductive Thermal Transistor **185**
4.1 Introduction . . . 185
4.2 Conductive thermal transistor with a phase change material base . . . 187
4.3 Results and discussion of the conductive thermal transistor with a phase change material base . . . 192
4.4 Conductive thermal transistor made of different phase change materials . . . 206
4.5 Results and discussion of the conductive thermal transistor made of different phase change materials . . . 209
4.6 Conclusion . . . 219

Résumé du Chapitre 4 **223**

General Conclusion **227**

Conclusion Générale **229**

Bibliography **231**

Abstract

This thesis is devoted to study some of the main thermal components of thermotronics, which is an emerging research field that focuses on the development of the thermal analogues of basic electronic components. We deeply focus on thermal components such as the thermal diode, the thermal memristor and the thermal transistor. We investigate them in the conductive regime of heat transfer. Phase change materials (PCM) are one of the alternatives to be used in order to conceive these thermal components. Among PCM, vanadium dioxide (VO_2), showing metal-insulator transitions (MIT), is one of the promising ones, because its phase transition temperature which is around 340 K, is quite close to room temperature. In this thesis, we consider all of these thermal components while considering the full properties of VO_2. We conduct the analysis of the conductive thermal diode (CTD) and the conductive thermal memristor (CTM) under transient and dynamical conditions and also modeled the hysteresis region. Therefore, the study extends the analysis by examining the role of the capacitive effect, which is omitted in the literature. We use the enthalpy method to solve the heat transfer problem numerically for the CTD and CTM analysis. The general one-dimensional heat diffusion equation expressed in terms of enthalpy is solved numerically for the case of VO_2 by finite difference method. We found that the phase transition of VO_2 significantly affects the thermal rectification of the CTD and the Lissajous characteristic curve of the CTM. Furthermore, we consider the steady-state regime of operation of the conductive thermal transistor (CTT) which has an analogy with an electronic bipolar transistor. We conduct the study by examining two different CTT concepts. The first one is a CTT with a PCM base and the second one is a CTT made of different PCMs. We show that the transistor effect can be achieved using VO_2. We deeply analyze the CTT functions (modes) such as amplification and switch. The first concept offers various parameter configuration options to achieve for the two CTT functions. On the other hand, although the second concept allows for the two CTT functions, the parameter configuration options are quite limited.

Résumé

Cette thèse est consacrée à l'étude de certains des principaux composants thermiques de la thermotronique, un domaine de recherche émergent qui se concentre sur le développement d'analogues thermiques des composants électroniques de base. Nous nous intéressons plus précisément aux composants thermiques tels que la diode thermique, le memristor thermique et le transistor thermique. Nous les étudions dans le régime conductif du transfert de chaleur. Les matériaux à changement de phase (MCP) constituent l'une des alternatives à utiliser afin de concevoir ces composants. Parmi les MCP, le dioxyde de vanadium (VO_2), qui présente des transitions métal-isolant (TMI), est l'un des plus prometteurs, car sa température de transition de phase, d'environ 340 K, est assez proche de la température ambiante. Dans cette thèse, nous considérons tous ces composants thermiques tout en prenant en compte l'ensemble des propriétés de VO_2. Nous menons l'analyse de la diode thermique conductive (DTC) et du memristor thermique conductif (MTC) dans des conditions transitoires et dynamiques et nous modélisons également la région d'hystérésis. En conséquence, l'étude élargit l'analyse en examinant le rôle de l'effet capacitif, qui a été négligé jusqu'à présent dans la littérature. Nous utilisons la méthode enthalpique pour résoudre numériquement le problème du transfert de chaleur dans le cadre des analyses de la DTC et du MTC. L'équation générale unidimensionnelle de diffusion de la chaleur, exprimée en termes d'enthalpie, est résolue numériquement pour le cas du VO_2 par la méthode des différences finies. Nous avons découvert que la transition de phase de VO_2 affecte de manière significative la rectification thermique de les DTC et la courbe caractéristique de Lissajous du MTC. De plus, nous considérons le régime de fonctionnement à l'état stationnaire du transistor thermique conductif (TTC). Nous menons l'étude en examinant deux concepts différents du TTC. Le premier est un TTC avec une base en MCP et le second est un TTC composé de différents MCP. Nous montrons que l'effet transistor peut être obtenu en utilisant le VO_2. Nous analysons en profondeur les fonctions (modes) du TTC telles que l'amplification et la commutation. Le premier concept offre diverses options de configuration des paramètres pour réaliser les deux fonctions TTC. En revanche, bien que le second concept permette les deux fonctions du TTC, les options de configuration des paramètres sont assez limitées.

List of Figures

1.1 Heat conduction scheme of a passive plane geometry with constant boundary conditions (a) and heat conduction through the passive plane at a distance Δx (b). 10

1.2 Rectangular control volume element for general heat conduction equation. 12

1.3 Thermal conductivity of VO_2 as a function of temperature in the cooling and the heating processes through the phase transition. [1]. 15

1.4 Specific heat capacity of VO_2 as a function of temperature in the cooling and the heating processes [1]. 16

1.5 Illustrative scheme of the interface thermal resistance between two materials. . . 17

1.6 Transition temperatures of some MIT oxide materials [2]. 18

1.7 Monoclinic structure (a-top) at insulating state, and tetragonal-rutile structure (b-top), at metallic state of VO_2. Red and blue balls show vanadium and oxygen atoms, respectively. Electronic band structures for insulating (a-bottom) and metallic (b-bottom) phases of VO_2 [3]. 20

1.8 Phase diagram which relates the relative strain and temperature via the phonon frequency shift for VO_2 (a) and represents the phases with increasing strain at three different temperatures (b) [4]. 21

1.9 VO_2 crystal structure (a) and position of VO_2 atoms during the occurred phases at the insulating phase (b) [4]. 22

1.10 Variations of the electrical resistance (solid lines and dots from [5] and [6], respectively) (a) and the thermal conductivity (solid lines and dots from [5] and [7], respectively) (b) according to the temperature with phase transition [5]. 23

1.11 Enthalpy-temperature relationship of a substance with a single melting point (a) and a substance that performs a phase change over a temperature range (b) [8]. . 25

1.12 A simple sketch of a thermal diode. When the left side has a higher temperature than the right side, the device allows the heat transfer, but in contrast, the heat transfer is blocked [9]. 27

1.13 Schematic representation of the thermal rectifier from the review article of Li et al [9]. Heat current as a function of dimensionless temperature difference for different values of reference temperature (b) and temperature profile for different k_{int} (c). The value of N here is 100, which indicates the coupled particle chains [10]. . . . 29

1.14 Phonon spectra of the two particles, left (a) and right (b), at the interface for different temperatures [10]. 30

1.15 Schematic representation of $C_9H_{16}Pt$ doped nanotube (a), TEM images of the undoped (b) and $C_9H_{16}Pt$ doped CNT (c) [11]. 31

1.16 Schematic representation of mass-graded chain [12]. 32

1.17 Phonon spectra of two particles from two ends, when the heavy-mass (a) and light-mass (b) sides are at higher temperatures, respectively [12]. 32

1.18 Schematic representations of investigated asymmetric nanostructures for thermal rectification [9]: carbon nanotube junction (a) [13], carbon nanocone (b) [14], graphene ribbon structures (c) [15] and Möbius graphene strip (d) [16]. 33

1.19 Schematic representations of investigated asymmetric nanostructures for thermal rectification [17]: carbon nanotube junction (a) [13], graphene nanoribbons connected by single-layer and multi-layer graphenes (b) [18] and (c) [19], asymmetric silicon nanoribbons (d) [20], asymmetric graphane trapezoidal and T-shaped nanostructure (e) [21], asymmetric triangular shaped graphene nanoribbons (f) [22], cone-shaped bottlebrush polymers (g) [23], Y-shaped carbon nanotubes (h) [24] and (i) [25], and silicon nanocone (j) [26]. 35

1.20 Schematic representations of investigated hetero-structures for the thermal rectification: investigated interfaces by Roberts and Walker (a) [27], asymmetric grain boundary composed of armchair and zigzag graphenes (b) [28], hetero-structure composed of graphene and silicene monolayer where the silicine sheet is placed between two graphene sheets (c) [29], hetero-structure composed of graphene-like material (Gx) and graphene (Gr) (d) [30], heteronanotube composed of carbon and boron nitride with two different structures; zigzag and armchair structures (e) [31]. 38

1.21 Schematic representation of the investigated thermal rectifier concept (a), the thermal conductivity variations of $LaCoO_3$ and $La_{0.7}Sr_{0.3}CoO_3$ with respect to temperature (b), schematic representation of the experimental set-up (c), and the thermal rectifications according to the calculated and measured values (d) [32]. . 42

1.22 Schematic representation of the set-up and investigated pyramidal shaped thermal rectifier with its sectional area (a), the thermal conductivity variations of $LaCoO_3$ and $La_{0.7}Sr_{0.3}CoO_3$ with respect to temperature (b), and heat currents (c) and the thermal rectifications (d) according to the calculated and measured values [33]. 43

1.23 The thermal conductivity variations of $La_{1.98}Nd_{0.02}CuO_4$ and MnV_2O_4 with respect to temperature (a), and the thermal rectifications according to the calculated and measured values (b) [34]. 44

1.24 Schematic representations of a single PCM (a) [35], a thermal diode composed of two PCMs (b) [36] and a spherical (cylindrical) thermal diode (c) [37] in forward and backward directions. 47

1.25 The dimensionless time (t^*) behaviors of the thermal rectification factor for three different thermal diffusivity ratios, 1100 (black), 1.1 (red) and 0.0011 (blue) when the uniform thermal conductivity ratios (the ratio of the second material to the first material) are 0.001 (a), 1 (b) and 1000 (c). ε_1 represents the nonlinear factor for the thermal conductivity parameter for the material 1, which is taken as 0.1 [38]. 50

1.26 Schematic representation of the thermal diode with a triangular-shaped (a) and crescent-shaped (b) holes [39]. 52

1.27 The thermal transistor model of Li et al. (a), heat current vs the control temperature for the thermal switch (b) and for the thermal modulation modes (c) [9]. 58

1.28 The thermal repeater model of Wang and Li (a) and their T_{input} and T_{output} relations (b) [40]. 60

1.29 The thermal logic gates model of Wang and Li (a), T_{input} and T_{output} relations for thermal AND gate (b) and for thermal OR gate (c) [40]. 61

1.30 Classical field-effect transistor (a) and near-field radiative thermal transistor model of Ben-Abdallah and Biehs (b) [41]. 61

1.31 The behaviors of the heat flux density profiles ϕ_S, ϕ_D and ϕ_G as functions of the gate temperature T_G [41]. 62

1.32 Schematic representation of the thermal transistor (a), the behaviors of the heat fluxes density profiles ϕ_1, ϕ_2 and ϕ_3 (b) and the amplification factor (c) as functions of the gate temperature T [42]. 64

1.33 The behaviors of the heat flux density profiles ϕ_1, ϕ_2 and ϕ_3 for the amplification (a) and the switch (b) modes as functions of the gate temperature T [43]. 65

1.34 Zoomed-in version on the heat flux density ϕ_3, which shows the critical temperatures and their corresponding input heat flux densities. The region shown by the blue line is the NDTR region [43]. 66

1.35 Schematic representation of a classical FET (a), the far-field RTT model (b) and its experimental set-up (c) [44]. 67

1.36 The behaviors of the measured (symbols) and calculated (dashed lines) heat flux density profiles ϕ_S, ϕ_D and ϕ_G for the switch mode (a) and the amplification factors (b) as functions of the gate temperature T_G [44]. 67

1.37 Fundamental circuit elements and their symmetry relationships [45]. 69

1.38 The voltage-current relationship of Pt-TiO_2-Pt device [45, 46]. 70

1.39 Temperature profile across the system according to the heating and cooling processes when T_L and T_R are 370 K and 330 K, respectively, and the sketch of the thermal memristor (inside of the figure) (a), the thermal resistance (b) and heat flux through the system according to the temperature difference ΔT variation when T_R is 330 K [47]. 71

1.40 The Lissajous characteristic curve with different temperature amplitudes T_a when the thermal conductivity ratio r is fixed (a) and with different thermal conductivity ratios when the temperature amplitude is fixed (b). T_L and T_R symbolize the temperatures on the left and right sides of their investigated thermal memristor, respectively [48]. 72

1.41 The sketch of the radiative thermal memristor (a), the Lissajous characteristic curves (b) and the thermal memristances (c) with different hysteresis. T_0, ΔT, ε_1 and ε_2 symbolize the steady-state temperature, the temperature difference modulated in time t between PCM and non-PCM blocks, the emissivities of the PCM and non-PCM, respectively [49]. 73

1.42 Schematic representation of the thermal energy storage system during the daytime (a) and at night (b). The temperature variations of the input temperature (purple solid line), the thermal storage units 1 (T_1) and 2 (T_2), and ground temperature (black solid line) (c). The power electricity output with and without the thermal diode bridge (d) [50]. 75

1.43 Schematic representations of the caloric refrigeration systems with thermal diodes with (a)-(b) and without a working fluid (c)-(d) [50]. 77

1.44 Schematic representation of the near-field radiative thermal diode. Initial form of the thermal diodes when the top part is at low (a) and high (b) temperatures. Reverse (c) and forward (d) biases that cause increased and decreased gap between the blocks, respectively [51]. 79

1.45 Schematic representation of the constructed AND gate (a), the first memristor temperature T_1 and the output temperature T_3 (b), and the AND gate table with the first input T_1, the second input (the time derivative of T_1) and their output ($\tilde{T_1}$ and $\tilde{T_3}$ in the table are the horizontal dashed lines that show the temperatures where the phase transition occurs) (c) [47]. 80

2.1 Sketch of the analyzed simple case. 93

2.2 Sketch of the numerical model. 94

2.3 Comparison of analytical and numerical nondimensionalized solution. 97

2.4 Schematic representation of the studied CTM. 98

2.5 Computed behaviors of the thermal conductivity (a) and enthalpy (b) of VO_2 as functions of temperature [52]. 99

2.6 The first-order reversal curves during the cooling (a) and heating (b) analysis in the study of Ramirez et al. [53]. 100

2.7 The flattened loops for electric-resistance (a) and optical reflectivity (b) in the study of Gurvitch et al. when the excursion length is short [54]. 101

2.8 Comparison of the results with our calculation and Krapez's work [55] for T_r = 343 K (a), for T_r = 339 K when the system starts on the heating line (b), when the system starts on the cooling line (c) and for T_r = 339 K when there is a lag of $3\pi/2$ on the sinusoidal boundary condition (d). 104

2.9 Correlation between the threshold frequency and the CTM length to obtain a pinched symmetrical Lissajous characteristic curve. 106

2.10 Computed time behaviors of the heat flux density corresponding to the left and right sides for different values of f. 107

2.11 Normalized heat flux density-temperature difference curve according to the left (a) and right sides (b) for different values of f. The arrows indicate the direction of motion of the Lissajous characteristic curve. 108

2.12 Computed time behaviors of the heat flux density corresponding to the left and right sides for different values of T_r. 109

2.13 Normalized heat flux density-temperature difference curve according to the left (a) and right sides (b) for different values of T_r. The arrows indicate the direction of motion of the Lissajous characteristic curve. 109

2.14 Corresponding thermal conductivity and enthalpy values according to the temperature distribution at 0.25 (a and b), 0.5 (c and d), 0.75 (e and f) and 1 (g and h) of the time cycle for T_r = 330.9 K, respectively. 111

2.15 Corresponding thermal conductivity and enthalpy values according to the temperature distribution at 0.25 (a and b), 0.5 (c and d), 0.75 (e and f) and 1 (g and h) of the time cycle for T_r = 334.9 K, respectively. 112

2.16 Corresponding thermal conductivity and enthalpy values according to the temperature distribution at 0.25 (a and b), 0.5 (c and d), 0.75 (e and f) and 1 (g and h) of the time cycle for T_r = 338.9 K, respectively. 113

2.17 Corresponding thermal conductivity and enthalpy values according to the temperature distribution at 0.25 (a and b), 0.5 (c and d), 0.75 (e and f) and 1 (g and h) of the time cycle for T_r = 342.9 K, respectively. 114

2.18 Corresponding thermal conductivity and enthalpy values according to the temperature distribution at 0.25 (a and b), 0.5 (c and d), 0.75 (e and f) and 1 (g and h) of the time cycle for $T_r = 346.9$ K, respectively. 115

2.19 Computed time behaviors of the heat flux density corresponding to the left and right sides for different values of T_a when T_r is set to be equal to the average of T_{oc} and T_{oh}. 117

2.20 Normalized heat flux density-temperature difference curve according to the left (a) and right sides (b) for different values of T_a when T_r is set to be equal to the average of T_{oc} and T_{oh}. The arrows indicate the direction of motion of the Lissajous characteristic curve. 118

2.21 Computed time behaviors of the normalized heat flux density-temperature difference curve corresponding to the left side for different values of T_a when T_r equals T_{oc} (a) and T_{oh} (b). The arrows indicate the direction of motion of the Lissajous characteristic curve. 118

2.22 Corresponding thermal conductivity and enthalpy values according to the temperature distribution at 0.25 (a and b), 0.5 (c and d), 0.75 (e and f) and 1 (g and h) of the time cycle for $T_a = 4$ K when T_r is set to be equal to the average of T_{oc} and T_{oh}, respectively. 120

2.23 Corresponding thermal conductivity and enthalpy values according to the temperature distribution at 0.25 (a and b), 0.5 (c and d), 0.75 (e and f) and 1 (g and h) of the time cycle for $T_a = 8$ K when T_r is set to be equal to the average of T_{oc} and T_{oh}, respectively. 121

2.24 Corresponding thermal conductivity and enthalpy values according to the temperature distribution at 0.25 (a and b), 0.5 (c and d), 0.75 (e and f) and 1 (g and h) of the time cycle for $T_a = 20$ K, 32 K and 44 K when T_r is set to be equal to the average of T_{oc} and T_{oh}, respectively. 122

3.1 Schematic representation of the linear CTD in the forward (a) and backward (b) configurations. 133

3.2 Computed dimensionless time behaviors of the nondimensional heat flux densities corresponding to the forward and backward configurations of the linear CTD and their corresponding computed dimensionless time behaviors of the thermal rectification factors for the fixed Dirichlet boundary condition for the parameters a (a)-(b), b (c)-(d) and r^* (e)-(f), respectively. 138

3.3 Computed dimensionless time behaviors of the nondimensional heat flux densities corresponding to the forward and backward configurations of the linear CTD and their corresponding computed dimensionless time behaviors of the thermal rectification factors for the sinusoidal Dirichlet boundary condition for the parameters a (a)-(b), b (c)-(d) and r^* (e)-(f), respectively. 139

3.4 Schematic representation of the studied CTD in the forward and backward configurations [1]. 140

3.5 Computed time behaviors of the nondimensional heat flux density at the cold boundary and thermal rectification factor in the heating [(a) and (b)] and cooling [(c) and (d)] processes, respectively, for different values of BCs [1]. 150

3.6 Computed time behaviors of the nondimensional heat flux density at the cold boundary and thermal rectification factor in the heating [(a) and (b)] and cooling [(c) and (d)] processes, respectively, for different values of β. 152

3.7 Computed time behaviors of the nondimensional heat flux density at the cold boundary and thermal rectification factor in the heating [(a) and (b)] and cooling [(c) and (d)] processes, respectively, for different values of L_n [1]. 153

3.8 Computed time behaviors of the nondimensional heat flux density at the cold boundary and thermal rectification factor in the heating [(a) and (b)] and cooling [(c) and (d)] processes, respectively, for different values of k_r [1]. 154

3.9 Computed time behaviors of the nondimensional heat flux density at the cold boundary and thermal rectification factor in the heating [(a) and (b)] and cooling [(c) and (d)] processes, respectively, for different values of ΔT_o [1]. 155

3.10 Computed time behaviors of the nondimensional heat flux density at the cold boundary and thermal rectification factor in the heating [(a) and (b)] and cooling [(c) and (d)] processes, respectively, for different values of r [1]. 156

3.11 Schematic representation of the studied CTD during the forward (a) and backward (b) configurations [52]. 159
3.12 Computed time behaviors of the heat flux density at the cold boundary corresponding to the forward and backward configurations of the CTD for different values of T_a when f is set to 10^{-4} Hz (a), 10^{-3} Hz (b), 10^{-2} Hz (c) and 10^{-1} Hz (d) [52]. 162
3.13 Computed time behaviors of R for different values of T_a when f is set to 10^{-4} (a), 10^{-3} (b), 10^{-2} (c) and 10^{-1} (d) [52]. 163
3.14 Schematic representation of the capacitive thermal diode [52]. 164
3.15 Computed time behaviors of $\phi_+^{*,I}$ and $\phi_-^{*,I}$ corresponding to the configuration of the capacitive thermal diode with constant heat capacities for the two layers for various investigated parameters: ξ (a), T_a (b), w^* (c) and $\overline{\Delta T}$ (d) [52]. 168
3.16 Computed time behaviors of R corresponding to the configuration of the capacitive thermal diode with constant heat capacities for the two layers for various investigated parameters: ξ (a), T_a (b), w^* (c) and $\overline{\Delta T}$ (d) [52]. 169
3.17 Computed time behaviors of $\phi_+^{*,II}$ and $\phi_-^{*,II}$ when the left layer has a temperature-dependent heat capacity for various investigated parameters: r_r (a), ξ (b), T_a (c), w^* (d) and $\overline{\Delta T}$ (e). The insets show the computed time behavior of $\phi_+^{*,II}$ separately [52]. 172
3.18 Computed time behaviors of R when the left layer has a temperature-dependent heat capacity for various investigated parameters: r_r (a), ξ (b), T_a (c), w^* (d) and $\overline{\Delta T}$ (e) [52]. 173

4.1 Schematic representation of the CTT with a PCM base [56]. 186
4.2 Schematic representation of the CTT with different PCMs. 186
4.3 Schematic representation of a CTT made of the same PCMs. 191
4.4 The computed behaviors of the nondimensional heat flux density profiles ϕ_C^*, ϕ_B^* and ϕ_E^* (a), and the amplification factors Γ_C and Γ_E (b) as functions of the base temperature T for different values of g [56]. 194
4.5 The computed behaviors of the maximum amplification factors Γ_C^{max} and Γ_E^{max}, and the optimal base temperature T_{max} as functions of g [56]. 194

4.6 The computed behaviors of the nondimensional heat flux density profiles ϕ_C^*, ϕ_B^* and ϕ_E^* (a), and the amplification factor Γ_E (b) as functions of the base temperature T for case 1 (i). The region shown by the dotted lines is the region we see the NDTR regime and the amplification. A zoom of this region is reported in the inset of (a) [56]. 195

4.7 The computed behaviors of the nondimensional heat flux density profiles ϕ_C^*, ϕ_B^* and ϕ_E^* (a), and the amplification factors Γ_C and Γ_E (b) as functions of the base temperature T for different values of T_E [56]. 196

4.8 The computed behaviors of the maximum amplification factors Γ_C^{max} and Γ_E^{max}, and the optimal base temperature T_{max} (a), the infinity profile caused by the two local extrema that induce the bistability regime (b), T_{max}, the critical and the post-critical base temperatures (c), the nondimensional heat flux densities for the critical and the post-critical base temperatures from collector-to-base (d) and from base-to-emitter (e), the switching input amplitude and the switching ratios (f) as functions of T_E [56]. 197

4.9 The zoomed version of case 2 (iv) on ϕ_B^*, which shows the critical temperatures and their corresponding input nondimensional heat flux densities. The region shown by the dotted lines between $T_{cri.,up}$ and $T_{cri.,down}$ is the region where the NDTR regime occurs [56]. 198

4.10 The computed behaviors of the nondimensional heat flux density profiles ϕ_C^*, ϕ_B^* and ϕ_E^* (a), and the amplification factors Γ_C and Γ_E (b) as functions of the base temperature T for different values of T_C. 200

4.11 The computed behaviors of the maximum amplification factors Γ_C^{max} and Γ_E^{max}, and the optimal base temperature T_{max} (a), the infinity profile caused by the two local extrema that induce the bistability regime (b), T_{max}, the critical and the post-critical base temperatures (c), the nondimensional heat flux densities for the critical and the post-critical base temperatures from collector-to-base (d) and from base-to-emitter (e), the switching input amplitude and the switching ratios (f) as functions of T_C [56]. 201

4.12 The computed behaviors of the nondimensional heat flux density profiles ϕ_C^*, ϕ_B^* and ϕ_E^* (a), and the amplification factors Γ_C and Γ_E (b) as functions of the base temperature T for different values of T_o [56]. 203

4.13 The computed behaviors of the maximum amplification factors Γ_C^{max} and Γ_E^{max}, and the optimal base temperature T_{max} (a), the infinity profile caused by the two local extrema that induce the bistability regime (b), T_{max}, the critical and the post-critical base temperatures (c), the nondimensional heat flux densities for the critical and the post-critical base temperatures from collector-to-base (d) and from base-to-emitter (e), the switching input amplitude and the switching ratios (f) as functions of T_o [56]. 204

4.14 The computed behaviors of the nondimensional heat flux density profiles ϕ_C^*, ϕ_B^* and ϕ_E^* (a), and the amplification factors Γ_C and Γ_E (b) as functions of the base temperature T for different values of β [56]. 205

4.15 The computed behaviors of the maximum amplification factors Γ_C^{max} and Γ_E^{max}, and the optimal base temperature T_{max} as functions of β [56]. 206

4.16 The computed behaviors of the nondimensional heat flux density profiles ϕ_C^*, ϕ_B^* and ϕ_E^* for case 1 (a), case 2 (c) and case 3 (e), respectively, and their corresponding amplification factors Γ_C and Γ_E (b), (d) and (f) in the same order as functions of the base temperature T for different values of g_L. 211

4.17 The infinity profile caused by the two local extrema that induce the bistability regime when $g_R = 5$, and $g_D = 0.5$ (a), $g_D = 1$ (c) and $g_D = 2$ (e), respectively, and the computed behaviors of the maximum amplification factors Γ_C^{max} and Γ_E^{max}, and the optimal base temperature T_{max} (b), (d) and (f) in the same order as functions of g_L. 213

4.18 The computed behaviors of T_{max}, the critical and the post-critical base temperatures (a), the nondimensional heat flux densities for the critical and the post-critical base temperatures from collector-to-base (b) and from base-to-emitter (c), the switching input amplitude and the switching ratios (d) when $g_R = 5$ and $g_D = 2$ as functions of g_L. 214

4.19 The computed behaviors of the nondimensional heat flux density profiles ϕ_C^*, ϕ_B^* and ϕ_E^* as functions of the base temperature T for different values of T_o^L (a), T_o^R (b), β_L (c) and β_R (d). 217

4.20 The amplification factors Γ_C and Γ_E as functions of the base temperature T for case 4 and case 5. 218

4.21 The computed behaviors of the nondimensional heat flux density profiles ϕ_C^*, ϕ_B^* and ϕ_E^* (a), and the amplification factors Γ_C and Γ_E (b) as functions of the base temperature T for different values of T_o^L (T_o^R) when the temperatures of the left and right PCMs are taken to be the average temperatures of the collector T_C and base T temperatures, and the base T and emitter T_E temperatures, respectively. 218

List of Tables

2.1 Investigated parameters and cases for the CTM. 106

3.1 Investigated parameters and cases for the linear CTD. 136
3.2 Investigated parameters and cases [1]. 148
3.3 Calculated values for the maximum thermal rectification factor, thermal rectification factor at steady-state conditions and time-integrated thermal rectification factor for all investigated cases [1]. 157
3.4 Investigated parameters and cases for the conductive and capacitive thermal diodes [52]. 161

4.1 Investigated parameters and cases for the CTT with a PCM base [56]. 193
4.2 Investigated parameters and cases for the CTT made of different PCMs. 210

List of Symbols

Latin Letters

a	Ratio of the thermal conductivity of material 1 to material 2
b	Ratio of the multiplication of the specific heat and density of material 1 to material 2
B	Nondimensional phase transition slope of VO_2
c	Specific heat [kJ kg^{-1} K^{-1}]
c^D	Specific heat predicted by Debye model [kJ kg^{-1} K^{-1}]
$cri.$	Critical
c_s	Specific heat of SiO_2 [kJ kg^{-1} K^{-1}]
f	Frequency of the applied boundary condition [Hz]
g	Ratio of the thermal conductances in the metallic phase to the dielectric phase
g_D	Ratio of the two PCM thermal conductances in the dielectric phase
g_L	Ratio of the thermal conductances of the metallic phase to dielectric phase of the left PCM
g_R	Ratio of the thermal conductances of the metallic phase to dielectric phase of the right PCM
G_D	Thermal conductance in the dielectric phase [W m^{-2} K^{-1}]
G_M	Thermal conductance in the metallic phase [W m^{-2} K^{-1}]
G_Δ	Absolute difference between the thermal conductance values in the dielectric and metallic phases [W m^{-2} K^{-1}]
H	Specific enthalpy [kJ kg^{-1}]
i	Space index
k	Thermal conductivity [W m^{-1} K^{-1}]
k_d	Thermal conductivity of VO_2 in the dielectric phase [W m^{-1} K^{-1}]
k_e	Effective thermal conductivity [W m^{-1} K^{-1}]
k_m	Thermal conductivity of VO_2 in the metallic phase [W m^{-1} K^{-1}]
k_r	Ratio of the thermal conductivity in the metallic phase to the dielectric phase

k_s	Thermal conductivity of SiO_2 [W m^{-1} K^{-1}]
l	Length [m]
$\overline{L}$	Nondimensional latent heat
L_n	Latent heat [kJ kg^{-1}]
max	Maximum
n	Time index
$post-cri.$	Post critical
r	Interface thermal resistance [K m^2 W^{-1}]
r^*	Nondimensional thermal resistance at the interface
r_d	Interface thermal resistance in the dielectric phase [K m^2 W^{-1}]
r_m	Interface thermal resistance in the metallic phase [K m^2 W^{-1}]
r_r	Ratio of the interface thermal resistance in the metallic phase to the dielectric phase
R	Thermal rectification factor
R_{max}	Maximum thermal rectification factor
R_{ss}	Thermal rectification factor at steady-state conditions
$\widetilde{R}$	Time-integrated thermal rectification factor
t	Time [s]
t^*	Dimensionless time
t_m	Time when the first peak in the thermal rectification profile is reached [s]
t_{ss}	Time when the steady-state conditions are reached [s]
T	Temperature [K]
T_a	Temperature amplitude of the applied boundary condition [K]
T_{amb}	Ambient temperature [K]
T_c	Cold temperature [K]
T_C	Collector temperature [K]
T_E	Emitter temperature [K]
T_{eq}	Equilibrium temperature [K]
T_h	Hot temperature [K]

T_m	Mean temperature of the hot and cold temperatures [K]
T_{max}	Temperature at which the amplification factor reaches its maximum [K]
T_o	Phase transition temperature of VO_2 [K]
T_{oc}	Phase transition temperature of VO_2 during the cooling process [K]
T_{oh}	Phase transition temperature of VO_2 during the heating process [K]
T_r	Reference temperature [K]
v	Volume fraction of the metallic domains during the heating process or reciprocally, the insulating domains during the cooling process
x	Spatial coordinate
x^*	Dimensionless spatial coordinate
I	Studies related to the capacitive thermal diode with constant heat capacities
II	Studies related to the capacitive thermal diode with temperature dependent heat capacity
$+$	Forward configuration
$-$	Backward configuration

Greek Letters

α	Thermal diffusivity [$m^2\ s^{-1}$]
$\overline{\alpha}$	Average thermal diffusivity between the one of the dielectric structure of VO_2 and SiO_2 [$m^2\ s^{-1}$]
α_d	Thermal diffusivity value of VO_2 in the dielectric phase [$m^2\ s^{-1}$]
α_m	Thermal diffusivity value of VO_2 in the metallic phase [$m^2\ s^{-1}$]
α_s	Thermal diffusivity value of SiO_2 [$m^2\ s^{-1}$]
β	Phase transition slope of VO_2 [K^{-1}]
γ	Isothermal compressibility [Pa^{-1}]
Γ	Amplification factor of the conductive thermal transistor
Γ_C	Amplification factor with respect to the collector
Γ_E	Amplification factor with respect to the emitter
δ	Coefficient of thermal expansion [K^{-1}]

ΔT_o	Difference between the transition temperatures of the heating and cooling processes [K]
η	Switching ratio of the conductive thermal transistor
θ	Nondimensional temperature
θ_a	Nondimensional temperature amplitude of the applied boundary condition
θ_m	Nondimensional mean temperature of hot and cold temperatures
θ_{oc}	Nondimensional phase transition temperature of VO_2 during the cooling process
θ_{oh}	Nondimensional phase transition temperature of VO_2 during the heating process
ρ	Density [kg m^{-3}]
ρ_s	Density of SiO_2 [kg m^{-3}]
ρ_v	Density of VO_2 [kg m^{-3}]
τ	Laplace transform of the nondimensional temperature
ϕ	Nondimensional heat flux density
$\phi^*_{B,dif.}$	Switching input amplitude
φ	Laplace transform of the nondimensional heat flux density

List of Acronyms/Abbreviations

BC	Boundary condition
BJT	Bipolar junction transistor
BNNT	Boron nitride nanotube
CNT	Carbon nanotube
CTD	Conductive thermal diode
CTM	Conductive thermal memristor
CTT	Conductive thermal transistor
FEM	Finite element method
FET	Field-effect transistor
FK	Frenkel-Kontorova
FPU	Fermi-Pasta-Ulam
GNR	Graphene nanoribbons
GR	Graphene ribbon
MIT	Metal-to-insulator transition
NDTR	Negative differential thermal resistance
NEMD	Non-equilibrium molecular dynamics
PCM	Phase change material
PDMS	Polydimethylsiloxane
PE	Polyethylene
PNIPAM	Poly(*N*-isopropylacrylamide)
RTT	Radiative thermal transistor
SiO_2	Silicon dioxide
TEG	Thermoelectric generator
TEM	Transmission electron microscopic
TQM	Thermal quadrupoles method
VO_2	Vanadium dioxide

General Introduction

The importance of thermal management is increasing everyday as we face more problems than before such as global warming, energy crysis and system safety. These challenges increase the importance of understanding the behaviors of thermal components that enable manipulating the heat flux and controlling temperature. Moreover, although there are two main energy transport processes in solids, namely electric and heat conduction, studies have focused more on the electric side of these energy transport processes. While this side is technologically quite advanced and takes place in our daily lives such as electronic transistor, studies on its thermal counterpart has not received enough attention. However, since studies show that phonons can be manipulated and even can carry information, this has opened up the possibility of further benefiting of phonons and increased the focus on the counterpart technology of electronics. Therefore, it can be said that thermotronics as an emerging research field that focuses on the development of the thermal analogues of basic electronic components has a great potential. This thesis is devoted to study some of its main thermal components in the conductive regime such as the thermal diode, thermal memristor and thermal transistor and examine their behaviors to understand them better.

Phase change materials (PCM) are one of the alternatives to be used to conceive these thermal components. There are different contexts for PCM such as solid-liquid transition as well as crystal structure transition. They transform their structures according to a critical phase transition temperature, which leads to perform different thermal, electrical and optical properties. Among PCM, vanadium dioxide (VO_2), showing metal-insulator transitions (MIT), is one of the most prominent ones, because its phase transition temperature is quite close to room temperature. As one of our originality in this thesis, we consider the full properties of VO_2 while including its hysteresis region, which has been ignored in the literature.

We divided this thesis into four chapters: the first one is state of the art and the remaining three chapters are our contributions to the literature:

- We start our thesis with state of the art chapter (Chapter 1). First, we provide a general overview of heat transfer and detail the phenomenon of heat conduction, taking into account that our investigations in this thesis are conducted in the conductive regime of heat transfer. We explain thermal properties, such as thermal conductivity and specific heat, from a broad perspective. We also explain these from the perspective of the characteristic of VO_2 as considering it is our investigated material in this thesis. We then continue with the characteristic properties of VO_2 and discuss the underlying mechanism of its MIT. We also inform the reader about its phase behaviors and its structures depending on its state that cause to change its thermal, electrical and optical properties as a consequence of phase transition. Then, we mention the enthalpy method which is a popular approach to solve a heat transfer problem numerically where a PCM is involved. After that, we continue with an extensive literature review section on the thermal components in thermotronics that we examine in this thesis: the thermal diode, the thermal memristor and the thermal transistor, respectively. After we concretized these components in the reader's mind in the literature review section, we then present some potential applications of these components.

- We start our investigation on the thermal components with the conductive thermal memristor in Chapter 2. There are very few studies on the thermal memristor and although these studies analyze a thermal memristor based on VO_2, they conduct their studies under quasi-steady-state conditions. Therefore, they omit the capacitive effect. This is one of our novelty in our study in this thesis. We conduct the analysis under dynamical boundary conditions and include the capacitive effect while considering the full properties of VO_2 as previously stated. In this chapter, we first describe our modeling for our investigations in this thesis. In addition, we show how to model the hysteresis zone of VO_2 under transient and dynamical conditions and provide details on solving the general one-dimensional heat diffusion equation in terms of enthalpy by finite difference method. Moreover, we conduct a case study to verify our modeling and present these results in this chapter before starting our analysis. Next, we continue with our main analysis on the conductive thermal memristor, for which we analyze the thermal memristor effect and the Lissajous characteristic curve by changing various parameters individually.

- We conduct a large-scale study for a conductive thermal diode that is made of VO_2 and SiO_2 with both fixed and sinusoidal boundary conditions in Chapter 3. We begin this chapter with a small introductory case study before our main analysis. We analyze a thermal diode that is made of two different solid materials with constant thermal properties under fixed and dynamical boundary conditions. Then, we start the main analysis. In the literature, studies on thermal diodes are generally conducted under steady-state conditions, and although interest in studies under transient conditions is increasing, there are still very few studies. Therefore, in this thesis, our goal was to explore the case of transient conditions. First, we examine the thermal rectification of the conductive thermal diode in detail by individually changing different intrinsic and extrinsic parameters under Dirichlet boundary conditions. Here, we avoid including phase transition processes inside the hysteresis region of VO_2 by adjusting the boundary conditions accordingly, which always lead to complete phase transition processes on the heating and cooling curves. We also evaluate the thermal rectification with three different metrics for this analysis: the maximum thermal rectification factor, the thermal rectification factor at the steady-state conditions and the time-integrated thermal rectification factor to qualify the capacitive effects. Next, we continue our analysis with the same conductive thermal diode under dynamical boundary conditions with various parameters, but in this case we also include the hysteresis region of VO_2. Finally, we conclude this chapter with a separate case study where we focus on a simple configuration of a conductive thermal diode, which we call the capacitive thermal diode, to reveal the capacitive effect on the thermal rectification in depth.

- In Chapter 4, which is our last chapter, we examine the conductive thermal transistor in two different concepts. Although there are many studies on thermal transistors in the literature, the majority of them consider the thermal transistor in the radiative regime of heat transfer. There are very few studies that examine the conductive thermal transistor. Therefore, we study a thermal transistor in the conductive regime of heat transfer in this thesis and consider its operation under the steady-state regime. We deeply investigate the functions of a transistor such as amplification and switch. We first start with the theory of our first concept and present its results. In the first concept, we study a conductive thermal transistor with the base made of an insulating-metal PCM, which is VO_2. Next, we continue

our investigation for the second concept, in which the conductive thermal transistor is made of different insulating-metal PCMs and examine it with different hypothetical parameter values.

We finish with a general conclusion and perspectives or future investigations related to the work accomplished during this thesis.

Introduction Générale

L'importance de la gestion thermique s'accroît de jour en jour, car nous sommes confrontés à des problèmes plus nombreux que jamais, tels que le réchauffement climatique, la crise de l'énergie et la sécurité des systèmes. Ces défis augmentent l'importance de la compréhension des composants thermiques qui permettent de manipuler le flux de chaleur et de contrôler la température. En outre, bien qu'il existe deux principaux processus de transport d'énergie dans les solides, à savoir la conduction électrique et la conduction thermique, les études se sont davantage concentrées sur le côté électrique de ces processus de transport d'énergie. Alors que ce côté est technologiquement très avancé et intervient dans notre vie quotidienne, comme le transistor électronique, les études sur sa contrepartie thermique n'ont pas reçu suffisamment d'attention. Cependant, depuis que des études ont montré que les phonons peuvent être manipulés et même transporter des informations, cela a ouvert la possibilité de tirer davantage profit des phonons et a renforcé l'attention portée à une technologie thermique équivalente de l'électronique. Par conséquent, on peut dire que la thermotronique, en tant que domaine de recherche émergent qui se concentre sur le développement d'analogues thermiques des composants électroniques de base, a un grand potentiel. Cette thèse est consacrée à l'étude de certains de ses principaux composants thermiques, tels que la diode thermique, le memristor thermique et le transistor thermique, et à l'examen de leurs comportements afin de mieux les comprendre.

Les matériaux à changement de phase (MCP) constituent l'une des alternatives pouvant être utilisées pour concevoir ces composants thermiques. Il existe différents contextes pour les MCP, tels que la transition solide-liquide et la transition de la structure cristalline. Ils transforment leurs structures en fonction d'une température critique de transition de phase, ce qui leur confère des propriétés thermiques, électriques et optiques différentes. Parmi les MCP, le dioxyde de vanadium (VO_2), montrant des transitions métal-isolant (TMI), est l'un des plus remarquables car sa température de transition de phase est assez proche de la température ambiante. L'une des originalités de cette thèse est de prendre en compte l'ensemble des propriétés du VO_2, y compris sa région d'hystérésis, qui a été ignorée jusqu'à présent dans la littérature.

Nous avons divisé cette thèse en quatre chapitres : le premier consiste en une revue de l'état de l'art du domaine de la thermotronique, et les trois autres sont nos contributions à la littérature :

- Nous commençons notre thèse par un chapitre de l'étude l'art (Chapitre 1). Tout d'abord, nous donnons un aperçu général du transfert de chaleur et détaillons le phénomène de la conduction thermique, en tenant compte du fait que nos recherches dans cette thèse sont menées dans le régime conductif du transfert de chaleur. Nous expliquons les propriétés thermiques, telles que la conductivité thermique et la chaleur spécifique, d'un point de vue général. Nous expliquons également ces notions du point de vue des caractéristiques du VO_2, étant donné qu'il s'agit du matériau étudié dans cette thèse. Nous passons ensuite aux propriétés caractéristiques du VO_2 et discutons du mécanisme sous-jacent de sa TMI. Nous informons également le lecteur des comportements de phase et des structures du VO_2 en fonction de son état, qui entraînent une modification de ses propriétés thermiques, électriques et optiques lors d'une transition de phase. Nous mentionnons ensuite la méthode d'enthalpie, qui est une approche populaire pour résoudre numériquement un problème de transfert de chaleur lorsqu'un MCP est impliqué. Ensuite, nous poursuivons avec une section de revue de littérature extensive sur les composants thermiques en thermotronique que nous examinons dans cette thèse : la diode thermique, le memristor thermique et le transistor thermique, respectivement. Après avoir concrétisé ces composants dans l'esprit du lecteur à l'aide de la section de revue de la littérature, nous présentons ensuite quelques applications potentielles de ces composants.

- Nous commençons nos recherches sur les composants thermiques avec le memristor thermique conductif dans le Chapitre 2. Il existe très peu d'études sur le memristor thermique, et bien que ces études analysent un memristor thermique à base de VO_2, elles sont menées dans des conditions quasi-stationnaires. Par conséquent, elles omettent l'effet capacitif. C'est l'une des nouveautés de notre étude dans cette thèse. Nous menons l'analyse dans des conditions limites dynamiques et incluons l'effet capacitif, tout en considérant les propriétés complètes du VO_2 comme mentionné précédemment. Dans ce chapitre, nous

décrivons d'abord notre modélisation pour nos recherches dans cette thèse. En outre, nous montrons comment modéliser la zone d'hystérésis du VO_2 dans des conditions transitoires et dynamiques fournissons des détails sur la résolution de l'équation générale unidimensionnelle de diffusion de la chaleur en termes d'enthalpie par la méthode des différences finies. Nous menons également une étude de cas pour vérifier notre modélisation et présentons ces résultats dans ce chapitre avant de commencer notre analyse dans cette thèse. Ensuite, nous poursuivons avec notre analyse principale sur le memristor thermique conductif, dans laquelle nous analysons l'effet du memristor thermique et la courbe caractéristique de Lissajous en changeant les différents paramètres individuellement.

- Dans le Chapitre 3, nous menons une étude à grande échelle d'une diode thermique conductive composée de VO_2 et de SiO_2, avec des conditions aux limites fixes et sinusoïdales. Nous commençons ce chapitre par une petite étude de cas introductive avant notre analyse principale. Nous analysons une diode thermique composée de deux matériaux solides différents ayant des propriétés thermiques constantes dans des conditions aux limites dynamiques et fixes. Nous commençons ensuite notre analyse principale avec la diode thermique conductive composée de VO_2 et de SiO_2. Dans la littérature, les études sur les diodes thermiques sont généralement menées dans des conditions stationnaires, et bien que l'intérêt pour les études dans des conditions transitoires augmente, il y a encore très peu d'études. Par conséquent, notre but fut l'exploration du cas des condition transitoires. Tout d'abord, nous examinons en détail la rectification thermique de la diode thermique conductive en modifiant individuellement différents paramètres intrinsèques et extrinsèques dans des conditions limites de Dirichlet. Nous évitons d'inclure des processus de transition de phase dans la région d'hystérésis du VO_2 en ajustant les conditions limites en conséquence, ce qui conduit toujours à des processus de transition de phase complets sur les courbes de chauffage et de refroidissement. Nous évaluons également la rectification thermique avec trois mesures différentes pour cette analyse : le facteur de rectification thermique maximal, le facteur de rectification thermique en régime permanent et le facteur de rectification thermique intégré dans le temps, afin de quantifier les effets capacitifs. Ensuite, nous poursuivons notre analyse avec la même diode thermique conductive dans des conditions limites dynamiques avec différents paramètres, mais dans ce cas, nous incluons également la région d'hystérésis de

VO_2. Enfin, nous concluons ce chapitre par une étude de cas distincte dans laquelle nous nous concentrons sur une configuration simple d'une diode thermique conductive, que nous appelons diode thermique capacitive, afin de révéler en profondeur l'effet capacitif sur la rectification thermique.

- Dans le Chapitre 4, qui est notre dernier chapitre, nous examinons le transistor thermique conductif selon deux concepts différents. Bien qu'il existe de nombreuses études sur les transistors thermiques dans la littérature, la majorité d'entre elles considèrent le transistor thermique dans le régime radiatif du transfert de chaleur. Il y a très peu d'études qui examinent le transistor thermique conductif. Par conséquent, nous étudions un transistor thermique dans le régime conductif de transfert de chaleur dans cette thèse et son fonctionnement en régime permanent. Nous étudions en profondeur les fonctions d'un transistor telles que l'amplification et la commutation. Nous commençons par la théorie de notre premier concept et présentons ses résultats. Dans le premier concept, nous étudions un transistor thermique conductif à base de MCP à transition de phase métal-isolant, qui est le VO_2. Nous poursuivons ensuite nos recherches pour le deuxième concept, dans lequel nous étudions un transistor thermique conductif composé de différents MCP à transition de phase métal-isolant et nous l'examinons avec différentes valeurs hypothétiques de ses paramètres.

Nous terminons par une conclusion générale et des perspectives ou investigations futures liées aux travaux accomplis au cours de cette thèse.

Chapter 1

Theoretical Background and Literature Review

Contents

1.1 Introduction . . . 10

1.1.1 Fourier's law of heat conduction . . . 11

1.1.2 General heat conduction equation . . . 12

1.2 Thermal properties . . . 13

1.2.1 Thermal conductivity . . . 13

1.2.2 Specific heat capacity . . . 15

1.2.3 Interface thermal resistance . . . 16

1.3 Metal-insulator transition and vanadium dioxide . . . 17

1.3.1 Mott-Hubbard and Peierls theories . . . 18

1.3.2 Crystal and band structures of vanadium dioxide . . . 19

1.3.3 Phase behaviors of vanadium dioxide . . . 19

1.3.4 Changes in the properties of vanadium dioxides . . . 22

1.4 Enthalpy method . . . 24

1.5 Thermotronics and thermal components . . . 25

1.5.1 Thermal diode . . . 26

1.5.2 Thermal transistor . . . 56

1.5.3 Thermal memristor . . . 68

1.6 Potential applications . . . 73

1.7 Motivation and objective of the study . . . 81

1.1 Introduction

Heat transfer is a physical phenomenon which occurs from a medium (high-temperature medium) to another medium (low-temperature medium) as a result of a temperature difference. This phenomenon exists as long as the two media considered have a different temperature. There are three different modes of heat transfer: conduction, convection and radiation [57]. Conduction is the transfer of energy which is typically occurring in a material. It can happen in solids, liquids and gases. In solids, it is primarily carried by electrons in metals and by phonons in semiconductors and insulators [58]. In liquids and gases, it happens due to the scattering and collisions of the molecules. Convection is the transfer of energy between a solid surface and a moving liquid or gas at different temperatures. In fact, it is a phenomenon that can be interpreted as a conduction heat transfer process occurring in a boundary layer between the solid and the fluid. Radiation heat transfer is a mode of transfer by electromagnetic waves or photons and can also take place in a vacuum. So, unlike the other 2 heat transfer modes, it does not require any medium for it to take place [57].

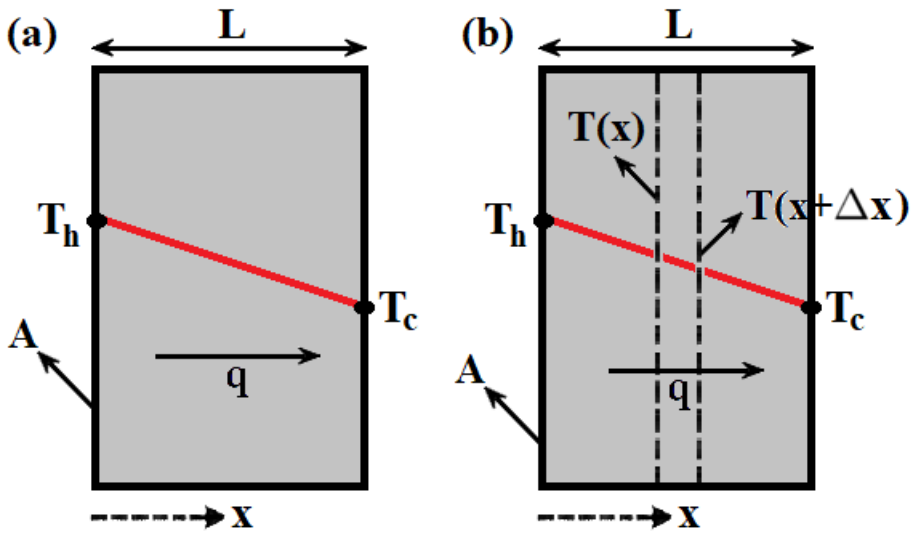

Figure 1.1: Heat conduction scheme of a passive plane geometry with constant boundary conditions (a) and heat conduction through the passive plane at a distance Δx (b).

1.1.1 Fourier's law of heat conduction

The Fourier's law is a well-known law of heat conduction that is named after a study of J. Fourier in 1822. The law can be basically explained by examining the passive plane geometry that is illustrated in Fig.1.1(a). Since the left side of the plane geometry has a higher temperature than the right side, it has to be a heat flow through it from high to low temperatures according to the second law of thermodynamics. The heat flow rate is constant under steady-state conditions according to the first law of thermodynamics [59]. Therefore, heat flow under steady-state conditions can be formulated as [59]:

$$q = kA\frac{T_h - T_c}{L} \tag{1.1}$$

k is the thermal conductivity, A is the area and L is the thickness of the plane. T_h and T_c are the hot and cold temperatures, respectively. Eq.1.1 shows that heat flow is proportional to k, A and temperature difference while inversely proportional to L. If we consider a portion Δx inside of the plane as illustrated in Fig.1.1(b), q through the plane can be formulated as:

$$q = -kA \lim_{\Delta x \to 0} \frac{T(x + \Delta x) - T(x)}{\Delta x} \tag{1.2}$$

after considering the limiting case, $\lim_{\Delta x \to 0}$, Eq.1.2 can transform to Eq.1.3 and this is known as Fourier's law of heat conduction [57]:

$$q = -kA\frac{dT}{dx} \tag{1.3}$$

where dT/dx is the temperature gradient. In addition, heat flux density, which is the quantity transferred across a unit area, can be formulated as:

$$q'' = -k\frac{dT}{dx} \tag{1.4}$$

The temperature gradient is negative if the flow is in positive x direction. Therefore, the negative sign in Eq.1.2, Eq.1.3 and Eq.1.4 make the quantity positive if the flow is in positive direction.

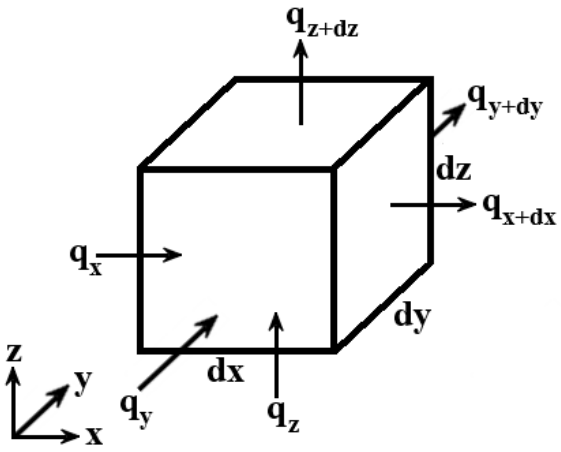

Figure 1.2: Rectangular control volume element for general heat conduction equation.

1.1.2 General heat conduction equation

The energy balance of a control volume element as illustrated in Fig.1.2 can be written according to the first law of thermodynamics as [8]:

$$\dot{Q} + \dot{E}_{gen} = \frac{dE_{element}}{dt} \tag{1.5}$$

where $\dot{Q}$, $\dot{E}_{gen}$ and $dE_{element}/dt$ represent the net rate of heat transfer to the system, the net heat generated by the system and the net rate of energy change of the system, respectively. If we consider these separately and start with the net rate of heat transfer to the system, it is:

$$\dot{Q} = (q_x - q_{x+dx}) + (q_y - q_{y+dy}) + (q_z - q_{z+dz}) \tag{1.6}$$

and it should be remembered that q_x, q_y and q_z are already defined by Fourier's law of heat conduction in Eq.1.3. So, q_x can be written as [8]:

$$q_x = -kA_x \frac{\partial T}{\partial x} \tag{1.7}$$

where $A_x = dydz$. In the same manner, q_y and q_z can be written like q_x, but they are not shown here for brevity. q_{x+dx}, q_{y+dy} and q_{z+dz} can be expressed by using a Taylor series expansion and q_{x+dx} (q_{y+dy} and q_{z+dz} can be obtained in the same manner) is as follows [8]:

$$q_{x+dx} = q_x + \frac{\partial q_x}{\partial x} dx \tag{1.8}$$

where the second term of the right side of the equation is actually:

$$\frac{\partial q_x}{\partial x}dx = \frac{\partial}{\partial x}\left(-kA_x\frac{\partial T}{\partial x}\right)dx \tag{1.9}$$

therefore, we obtain the net rate of heat transfer to the system, Eq.1.6, as follows:

$$\dot{Q} = \left[\frac{\partial}{\partial x}\left(k\frac{\partial T}{\partial x}\right)+\frac{\partial}{\partial y}\left(k\frac{\partial T}{\partial y}\right)+\frac{\partial}{\partial z}\left(k\frac{\partial T}{\partial z}\right)\right]dxdydz \tag{1.10}$$

If we consider the second term, $\dot{E}_{gen}$, of Eq.1.5, it is the internal rate of the energy generation and can be expressed as [8]:

$$\dot{E}_{gen} = \dot{e}_{gen}dxdydz \tag{1.11}$$

The net rate of energy change, $dE_{element}/dt$, can be expressed as [8]:

$$\frac{dE_{element}}{dt} = \rho c\frac{\partial T}{\partial t}dxdydz \tag{1.12}$$

where ρ and c are the density and specific heat of the material, respectively. After we substitute Eq.1.10, Eq.1.11 and Eq.1.12 into Eq.1.5 and eliminate $dxdydz$ from all equations, we will obtain the general heat conduction equation for cartesian coordinates:

$$\rho c\frac{\partial T}{\partial t} = \frac{\partial}{\partial x}\left(k\frac{\partial T}{\partial x}\right)+\frac{\partial}{\partial y}\left(k\frac{\partial T}{\partial y}\right)+\frac{\partial}{\partial z}\left(k\frac{\partial T}{\partial z}\right)+\dot{e}_{gen} \tag{1.13}$$

In our investigations in this thesis, there is no heat generation and we assume that heat conduction is one-dimensional and negligible in other directions. Therefore, Eq.1.13 can be reformulated for one-dimensional general heat conduction equation without heat generation as:

$$\rho c(T)\frac{\partial T}{\partial t} = \frac{\partial}{\partial x}\left[k(T)\frac{\partial T}{\partial x}\right] \tag{1.14}$$

1.2 Thermal properties

1.2.1 Thermal conductivity

Thermal conductivity is a quantity that measures the ability of a material to allow heat to flow in it. Materials show different thermal conductivities and they are depending on the temperature [57]. For instance, while nonmetallic crystals such as diamond or metals such as copper have high thermal conductivities, gases such as hydrogen or insulators such as fibers have low

thermal conductivities [57]. The thermal conductivity formula under steady-state condition can be actually obtained by rewriting Eq.1.1 as:

$$k = \frac{q/A}{(T_h - T_c)/L} \tag{1.15}$$

Eq.1.15 shows that the thermal conductivity is actually the heat transfer rate in a unit area that goes through a unit thickness per unit temperature difference.

Generally, the variation of the thermal conductivity with temperature might be neglected if the investigated range of the temperature is small enough or it does not have a quite temperature-dependence. However, we cannot make this assumption for phase change materials (PCM). It is worth mentioning that PCMs have different contexts in different communities. They include solid-liquid transition as well as crystal structure transformation (crystalline-amorphous transition and dielectric-metallic transition). Consequently, they manifest different thermal, electrical and optical properties according to their critical transition temperatures [60]. In our study, we focus on vanadium dioxide (VO_2) which is a PCM that manifests a metal-insulator transition. The thermal conductivity, $k(T)$, of it varies strongly with temperature. The thermal conductivity of VO_2 can be described using the following equation as formulated in the study of Ordonez-Miranda et al. [35]:

$$k(T) = k_d + \frac{k_m - k_d}{1 + e^{-\beta(T - T_o)}} \tag{1.16}$$

where k_d and k_m represent the thermal conductivity of VO_2 in the dielectric and metallic phases, respectively. T_o is the phase critical transition temperature and β is the phase transition slope. The values of these parameters for VO_2 are as follows: 3.6 W m^{-1} K^{-1} for k_d, 6 W m^{-1} K^{-1} for k_m and 1.6 K^{-1} for β. The values of k_d and k_m were measured experimentally by Oh et al. [7], while the value of β corresponds to the best fit of the experimental data using Eq.1.16 [35]. In addition, T_o takes the values $T_{oh} = 342.9$ K and $T_{oc} = 334.9$ K during the heating and cooling processes, respectively, which results in an 8 K hysteresis effect for VO_2 between these processes [35]. Therefore, T_{oh} and T_{oc} represent the transition temperatures of the heating and cooling processes, respectively. The temperature behaviors of the thermal conductivity of VO_2 are reported in Fig.1.3.

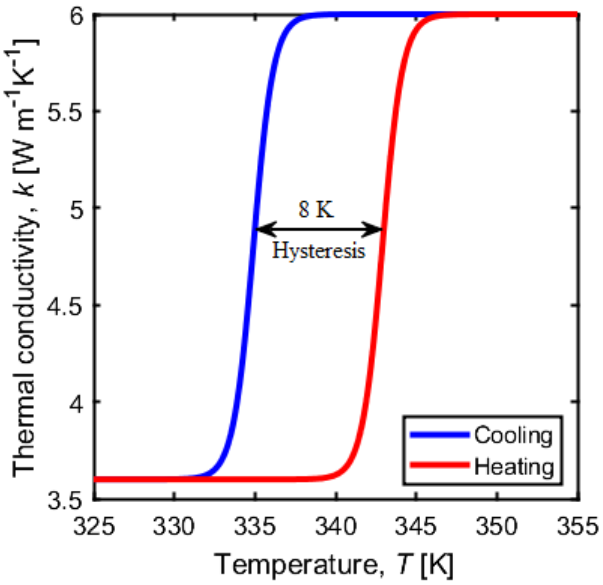

Figure 1.3: Thermal conductivity of VO_2 as a function of temperature in the cooling and the heating processes through the phase transition. [1].

1.2.2 Specific heat capacity

Specific heat capacity is the ability of a material to store the thermal energy and it is basically the energy needed to increase the temperature of a unit mass of a material by 1 K [57]. For VO_2, the specific heat capacity at constant pressure changes sharply during the phase transition and as reported in [5], the expression of the specific heat capacity of VO_2 is given by:

$$c_p(T) = c^D(T) + T\frac{\delta^2}{\rho_v \gamma} + L_n \frac{\partial f}{\partial T} \tag{1.17}$$

where c^D, ρ_v, δ, γ and L_n represent the specific heat capacity predicted by Debye model, density of VO_2, coefficient of thermal expansion, isothermal compressibility and latent heat, respectively. Since the variation of c^D within the range of the considered boundary conditions (BC) in this thesis is negligible, we assume it to be constant and we take the average of the values of c^D at the BC temperatures as 0.71 kJ kg^{-1} K^{-1}. Moreover, ρ_v of VO_2 changes according to its crystalline structure. However, for simplicity sake throughout the study, we assume ρ_v to be also constant and we take the average of the values of the dielectric monoclinic and metallic tetragonal-rutile crystalline structures as 4612 kg m^{-3}. L_n equals 51.45 kJ kg^{-1} for the heating

process of VO_2 [61] and we assume the same value for the cooling process. As explained in the study of Ordonez-Miranda et al. [5], the second term in the right side of Eq.1.17 can be neglected, because the values of this term are much smaller than the values of c^D within the phase transition temperatures interval. Thus, its contribution is neglected throughout the study. On the contrary, the third term is strongly dominant at the transition temperature. At this temperature, it represents the amount of heat needed to change the material phase. The temperature behaviors of the specific heat capacity of VO_2 are reported in Fig.1.4.

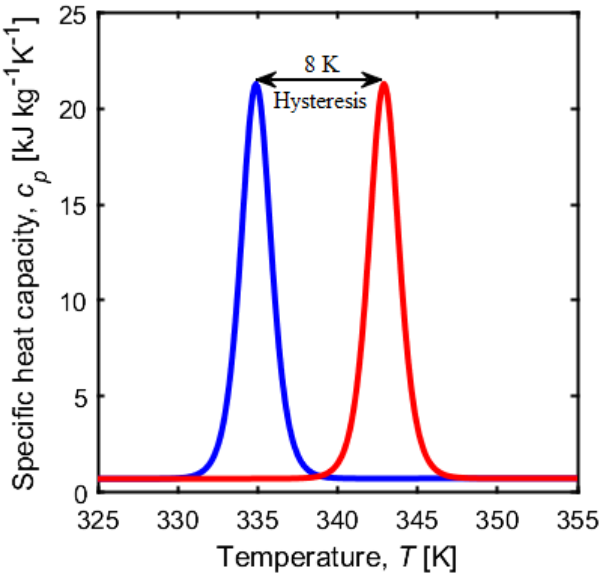

Figure 1.4: Specific heat capacity of VO_2 as a function of temperature in the cooling and the heating processes [1].

1.2.3 Interface thermal resistance

The interface thermal resistance, which is also known as the Kapitza resistance, was firstly discovered by Kapitza in 1941. In the study of Kapitza, this phenomenon was experimentally observed at the interface of a helium II film and a solid (here copper) [62]. A temperature drop is observed at the interface of two layers due to interface thermal resistance as seen in Fig.1.5. It can be formulated as follows:

$$r = \frac{\Delta T}{q} \tag{1.18}$$

where ΔT is the temperature drop that occurs at the interface of the materials and r is the interface thermal resistance while applying a constant heat flux through the system.

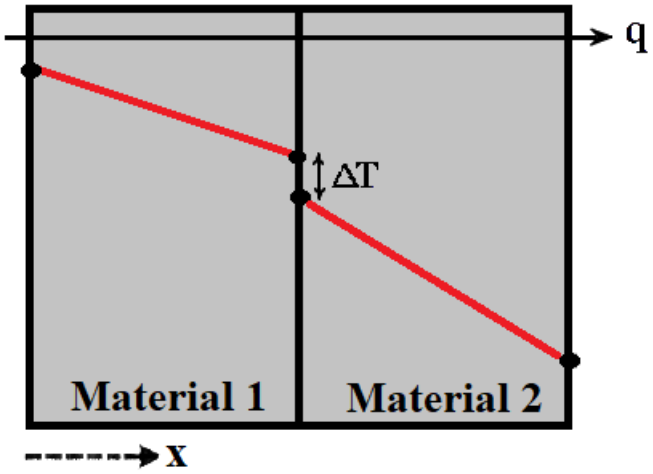

Figure 1.5: Illustrative scheme of the interface thermal resistance between two materials.

1.3 Metal-insulator transition and vanadium dioxide

Metal to insulator transitions (MIT) have been studied for a long time and especially MIT in oxide materials took a great interest after the study of Morin, who discovered the MIT in VO_2 by measuring the electrical conductivity as a function of temperature [63]. The properties of these materials such as electrical, thermal or optical properties can be changed by a thermal, electrical, optical, magnetic or strain excitation [2]. Properties of several materials exhibiting a phase transition with temperature can be seen in Fig.1.6. We note that there are various oxide materials from low phase transition temperatures to high transition temperatures. Among these oxides, vanadium oxides, especially VO_2 attracted much attention [64], because it has a phase transition temperature, 340 K, close to the room temperature with a quick phase change as seen in Fig.1.6. Another interesting feature is the variation of its electrical resistivity by five orders of magnitude around the transition temperature on a timescale of the order of the picosecond [2]. Although there are various theoretical and experimental studies to understand the transition mechanisms of VO_2, there is not a full understanding or consensus for this process currently [64]. There are basically two theories for the MIT phase transition, which are Mott-Hubbard

and Peierls theories [2].

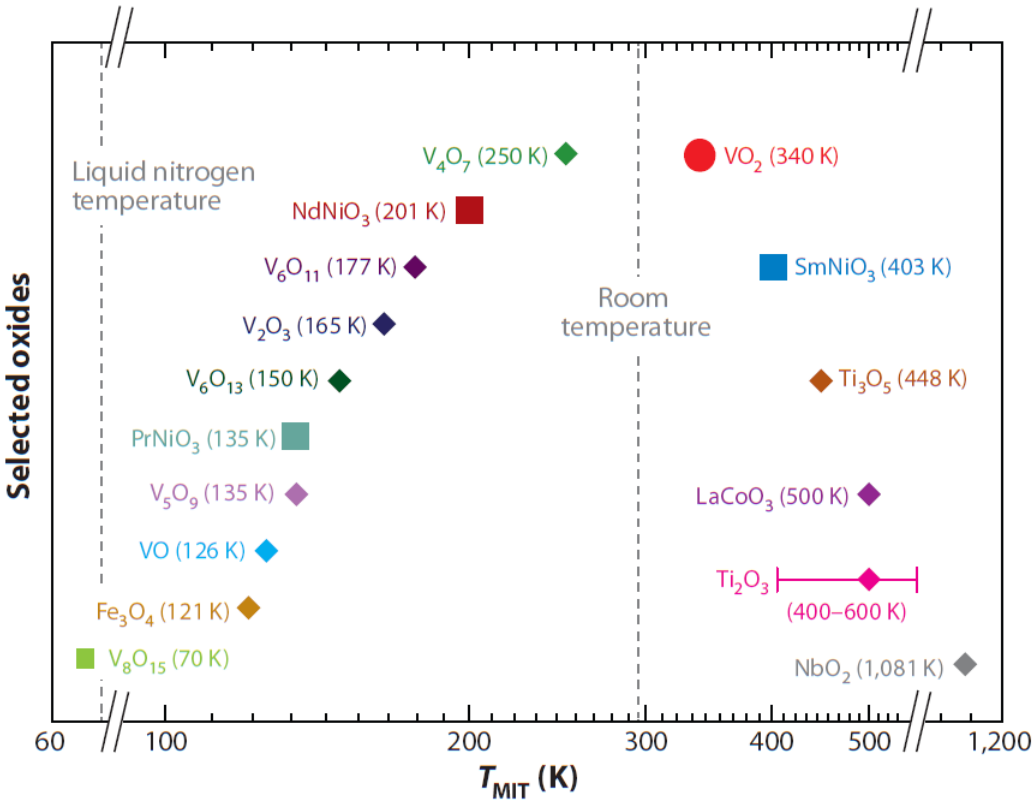

Figure 1.6: Transition temperatures of some MIT oxide materials [2].

1.3.1 Mott-Hubbard and Peierls theories

Mott proposed a model to explain that MIT transition occurs due to electron-electron interaction and energy band structure changes with the transition [65]. According to Mott theory, when the electron density is higher than the critical electron density, the transition from insulating state to metallic state occurs. It is believed that MIT phase transition does not happen just due to electron-electron interaction, but happens also due to electron-phonon (electron-lattice) interaction, which was proposed by Peierls [66]. Actually, it is believed that both, the structural and the electronic transition, occur at the same time and this makes understanding the logic behind the transition of VO_2 difficult [64].

1.3.2 Crystal and band structures of vanadium dioxide

VO_2 has a monoclinic structure in the insulating phase and a tetragonal-rutile structure in the metallic phase. These structures are illustrated on the top side of Fig.1.7(a) and (b), respectively. In the metallic phase, V atoms create a tetragonal structure [67]. V^{4+} ions place on the vertex and the center of the structure that are surrounded by 6 O^{2-} ions and they result in an octohedral VO_6 unit [64]. The cell dimensions a, b and c are 0.455 nm, 0.455 nm and 0.286 nm, respectively [67]. However, when there is a transition to insulating phase, V-V bond is formed. Also, the shape of O atoms barely changes during the transition, but V atoms create a monoclinic structure with a less symmetry than in the tetragonal structure and two effective unit cells, which are represented by solid lines in Fig.1.7 at the metallic phase, transformed to one and doubled [3]. The cell dimensions a, b, c and $\overline{\beta}$ are changed to 0.575 nm, 0.453 nm, 0.538 nm and 122.6°, respectively [67]. $\overline{\beta}$ is the angle between the a and c axes.

The electronic band structure of VO_2 is shown in the bottom side of Fig.1.7(a) and (b) for the insulating and metallic phases, respectively. During the insulating phase, the 3d band splits into two energy bands as lower energy d_{II} band and higher energy d^*_{II} band, in addition to π^* band above the Fermi energy. This results in a forbidden bandgap, which is around 0.7 eV. It causes VO_2 to show insulating properties. However, these two bands are above the Fermi energy in the metallic phase as seen in Fig.1.7(b) and this makes VO_2 to exhibit metallic properties [64, 68].

1.3.3 Phase behaviors of vanadium dioxide

As already indicated, VO_2 exhibits a monoclinic structure in the insulating phase and a tetragonal-rutile structure in the metallic phase. However, VO_2 can also exhibit an insulating behavior in the monoclinic M1, monoclinic M2 and triclinic T phases. Atkin et al. [4] conducted a study to identify them by Raman microspectroscopy by measuring the relative strain and temperature. The phase diagram that relates the relative strain and temperature via the phonon frequency shift can be seen in Fig.1.8(a). It is clearly seen that three monoclinic phases can be observed during the insulating phase. When the relative strain is weak, M1 phase is mostly observed, but when it is slightly higher, M2 phase appears. Also, when the relative strain increases at

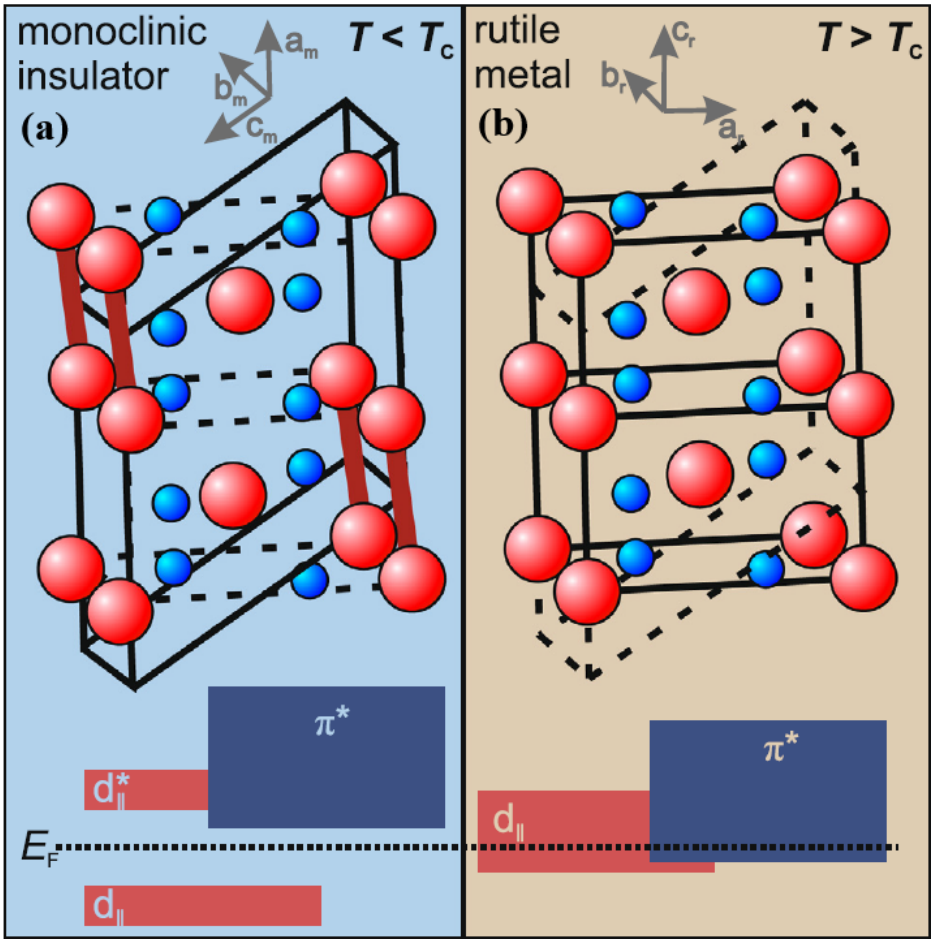

Figure 1.7: Monoclinic structure (a-top) at insulating state, and tetragonal-rutile structure (b-top), at metallic state of VO_2. Red and blue balls show vanadium and oxygen atoms, respectively. Electronic band structures for insulating (a-bottom) and metallic (b-bottom) phases of VO_2 [3].

low temperatures, it is possible to see the T phase. Structural transition of these phases can be observed in Fig.1.8(a) and (b). One notes that transition from M1 to T, then to M2 phases can be observed at low temperatures. One also sees that direct transition from M1 to M2 is much likely at high temperatures. This study shows that various combinations of transition of VO_2 at the insulating phase are possible [4]. Moreover, the crystal structure of VO_2 at the insulating phase can be seen in Fig.1.9(a) and the position of atoms during the occurred phases are seen in Fig.1.9(b) [4]. V atoms are paired and tilted in the M1 phase. In addition, there are two different sublattices for M2 phases, A and B. V atoms are paired in the M2 phase A,

but unpaired in the M2 phase B. On the other hand, they are tilted in the M2 phase B, but not in the M2 phase A. Moreover, T phase can be observed in the intermediate of these phases [4].

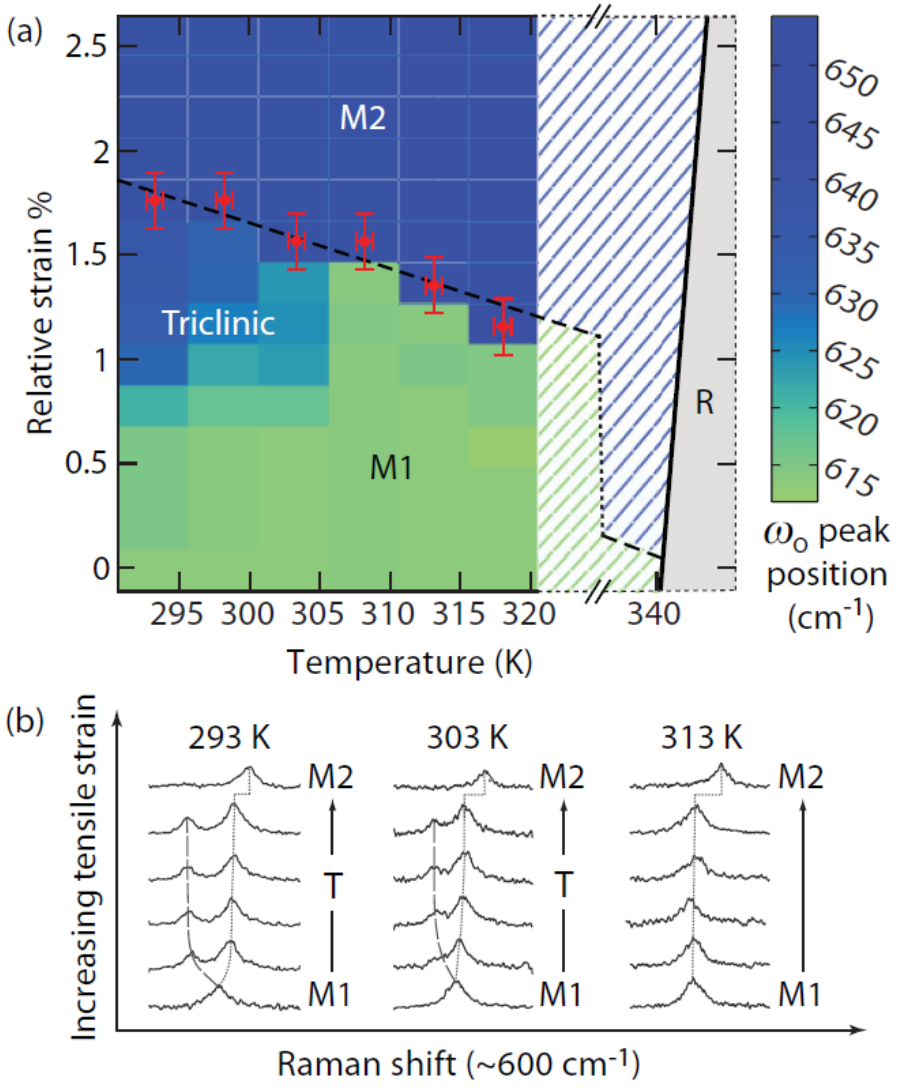

Figure 1.8: Phase diagram which relates the relative strain and temperature via the phonon frequency shift for VO_2 (a) and represents the phases with increasing strain at three different temperatures (b) [4].

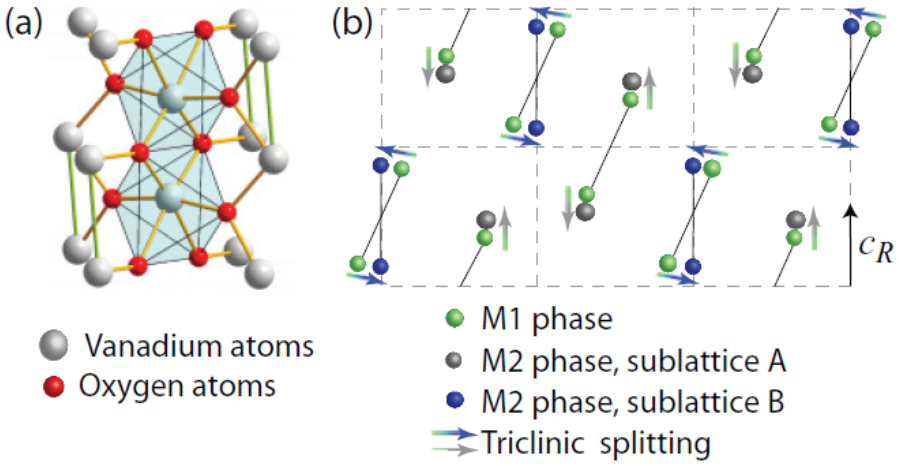

Figure 1.9: VO_2 crystal structure (a) and position of VO_2 atoms during the occurred phases at the insulating phase (b) [4].

1.3.4 Changes in the properties of vanadium dioxides

The mechanisms that were discussed in the previous section are at the origin of the strong variations of electrical resistance, thermal conductivity and optical properties with the temperature. Changes of electrical resistance and thermal conductivity according to the temperature of VO_2 can be seen in Fig.1.10(a) and (b), respectively. One can notice a 4 orders of magnitude decrease in the electrical resistance after phase transition as seen from the experimental results (dots in the figure) of Qazilbash et al. study [6]. The solid lines have been theoretically modeled by Ordonez-Miranda et al. [5] for the heating and cooling processes. Qazilbash et al. also observed a hysteresis exhibiting an 8 K shift between the heating and the cooling processes [2].

Oh et al. [7] observed in their experimental study that the thermal conductivity increases through the phase transition from 3.6 W m^{-1} K^{-1} to 6 W m^{-1} K^{-1}. The dots in Fig.1.10(b) show the experimental results of Oh et al. [7] compered with the theoretical study of Ordonez-Miranda et al. [5]. In our study, we also use the theoretical modeling of Ordonez-Miranda et al. for the thermal conductivity, which is previously formulated in Eq.1.16 [35].

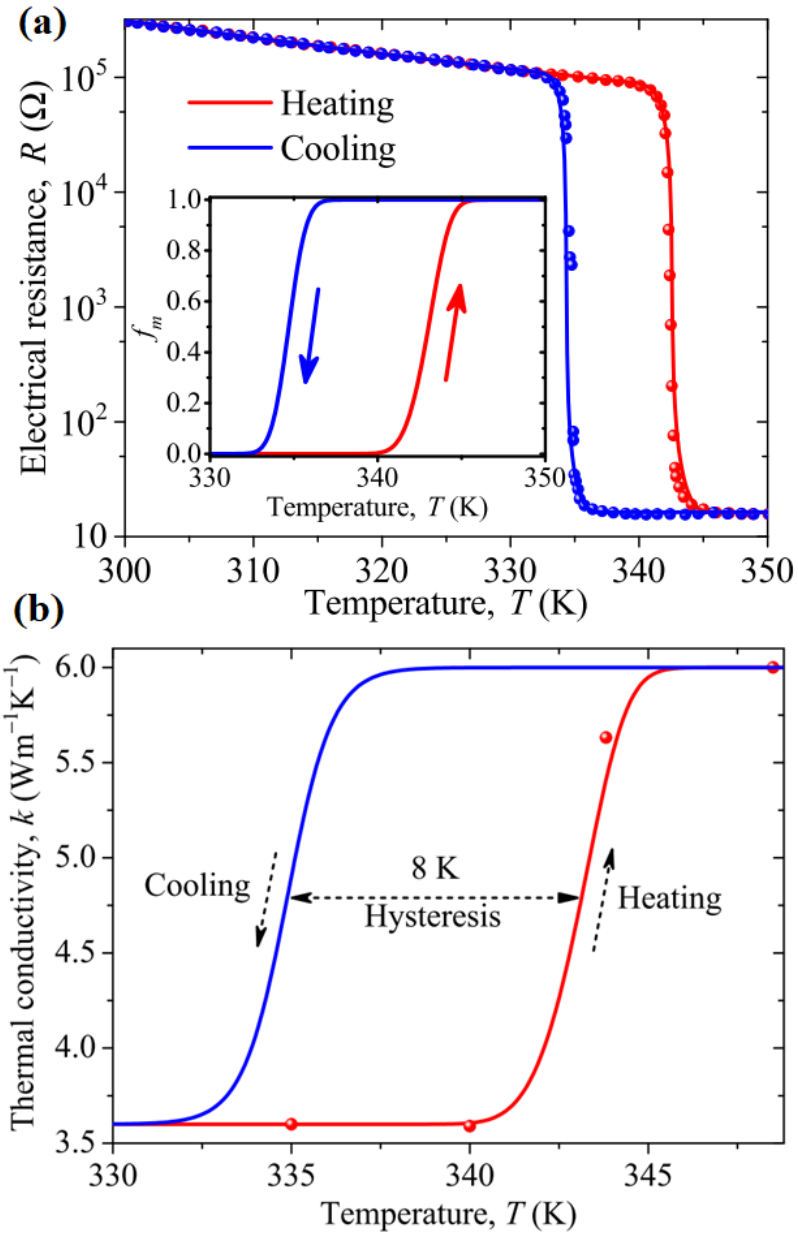

Figure 1.10: Variations of the electrical resistance (solid lines and dots from [5] and [6], respectively) (a) and the thermal conductivity (solid lines and dots from [5] and [7], respectively) (b) according to the temperature with phase transition [5].

1.4 Enthalpy method

Phase change materials (PCM) have different contexts in different communities such as solid-liquid transition as well as crystal structure transformation (crystalline-amorphous transition and dielectric-metallic transition) and enthalpy method is a popular approach to solve a heat transfer problem numerically where a PCM is involved [69]. This method was firstly proposed by Eyres [70]. Enthalpy method does not require the phases to be considered separately, and it basically reformulates the problem and makes a single energy equation to be applicable to the entire physical domain [8]. Therefore, the problem can be solved by reformulating the energy equation with enthalpy method without having to consider the phases of the system or their interfaces separately [8]. The reformulated heat diffusion equation within a PCM can be written as [71]:

$$\rho \frac{\partial H(T)}{\partial t} = \nabla.(k \nabla T) \tag{1.19}$$

This method can be applied to PCMs that exhibit a phase transition at a specific temperature or over a temperature range as shown in Fig.1.11(a) and (b), respectively [8]. T_m^*, H_L and H_S represent the melting temperature, enthalpy values at liquid and solid forms, respectively.

The relationship between enthalpy and temperature is nonlinear for the second kind of PCM which is shown in Fig.1.11(b) [8]. The nonlinear version will be detailed in the relevant chapter (Chapter 2) for our investigated PCM, which is VO_2 including modeling the hysteresis zone. Therefore, if the enthalpy equation is explained on the first kind of PCM which is shown in Fig.1.11(a) as an introductory explanation, the enthalpy function $H(T)$ can be written [8, 69]

$$H(T) = c_p(T - T_m^*) + L_n v(T) \tag{1.20}$$

where the reference temperature is T_m^*. $v(T)$ indicates the volume faction in the liquid form. The enthalpy function only contains the sensible heat until the melting temperature which corresponds to the solid region, where $v(T) = 0$. However, since there is a vertical increase after the melting temperature as seen in Fig.1.11(a), the whole system transforms into liquid form. This means that $v(T) = 1$. As a result, we see the contribution of latent heat in the equation.

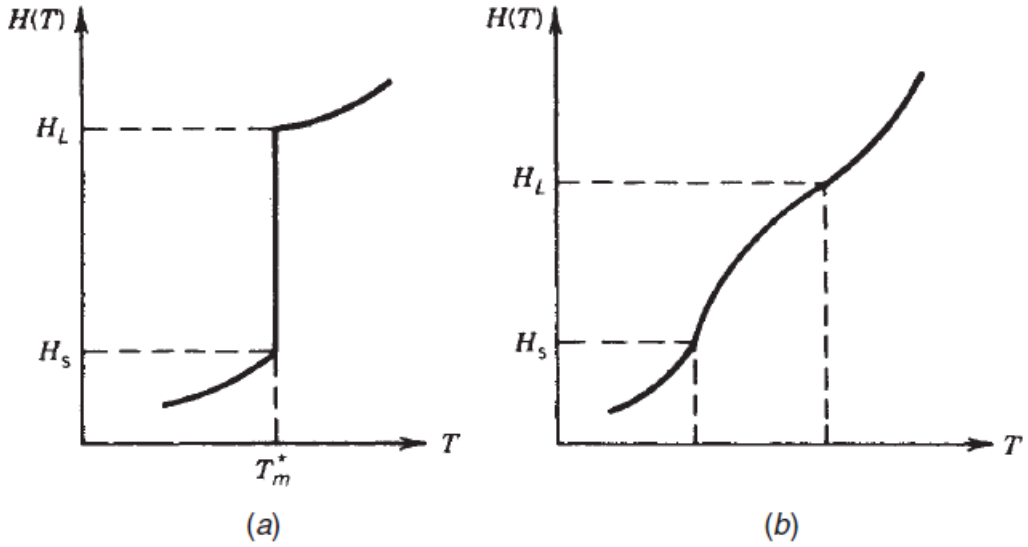

Figure 1.11: Enthalpy-temperature relationship of a substance with a single melting point (a) and a substance that performs a phase change over a temperature range (b) [8].

Therefore, inversely, the corresponding temperature of a specific enthalpy value can be found in the region up to the melting temperature and in the region after the melting temperature by using the equations: $T = T_m^* + H/c_p$ and $T = T_m^* + (H - L_n)/c_p$, respectively [8].

Finite difference method is one of the favored methods to solve the reformulated equation with enthalpy method (Eq.1.19) [8]. Basically, Eq.1.19 can be discretized in time and space with implicit or explicit schemes. Then, the corresponding temperature of the determined enthalpy at next time steps can be found inversely.

1.5 Thermotronics and thermal components

There are two main energy transport processes in solids: electric and heat conduction [9]. These two transport processes could be equally important for the information processing and could constitute a useful tool for technological advancement. However, this is not accomplished unfortunately. Although there has been a great deal of work on the electronic (electric) side of these energy transport processes since the invention of the electronic transistor by Bardeen and

Brattain in 1948 [72], which has indeed become one of the main electronic toolkit today, the heat flow counterpart has not received much attention, because there was a widespread belief that phonons were not useful for carrying and processing information as a result of their nature [9]. Phonons are quasiparticles and do not have a bare mass or charge [9]. However, studies have shown that phonons can be manipulated and even, contrary to old belief, can carry information. This has indeed opened the world up to the possibility of using phononics, the counterpart technology of electronics, and making some concepts possible such as thermal computing [9]. In this part of this chapter, we will discuss some fundamental steps that help in the development of this research area such as thermal rectification and phononic devices that we examine in this thesis such as the thermal diode, the thermal transistor and the thermal memristor. It should be noted here that although the literature review will be on conduction-related studies, we will also mention some noteworthy studies on the other heat transfer modes such as radiation, which help to develop the thermal components.

1.5.1 Thermal diode

Thermal rectification is a process that occurs as soon as the device thermal properties depend on the temperature so that the heat flux depends on the direction of the temperature gradient between the device terminals [73]. It is possible to conceive and construct thermal diodes based on the three different modes of heat transfer: conduction, convection and radiation [50, 73, 74]. A simple sketch of a thermal rectifier or a thermal diode for the perspective of conductive heat transfer can be seen in Fig.1.12 [9]. As seen from the sketch, it is expected from the device that while heat transfer is allowed in one direction, it is blocked in the other direction when the temperatures are exchanged [9]. The topic was firstly studied in 1936 by Starr [75] who examined the rectification of Copper/Cuprous Oxide interfaces experimentally. He noticed the existence of the thermal rectification while examining the electrical rectification and found that the thermal and electrical conductances are both higher in the same direction [75]. Since then, rectification has been a strong topic of interest. Especially, lots of studies have been made on this topic in 1960s as a result of the increased interest on composite materials. However, the peak point of the interest was reached in 2000s after the emergence of the nanoscale studies. Understanding the thermal rectification can allow us to develop better thermal devices such

as thermal diodes. In this manner, among thermal rectification devices, researches on thermal diodes have dramatically increased in the past decade [50, 74, 76]. There are various studies for rectification devices in macroscopic scale that occur thanks to a temperature difference or external triggers such as strain. Roberts and Walker [73], Li et al. [9] and Wehmeyer et al. [74] summarized some of the important studies on these topics in their review articles, but interest in nanometer-scale thermal rectification by phonon transport has increased significantly since 2002, thanks to the work of Terraneo et al. [77, 78].

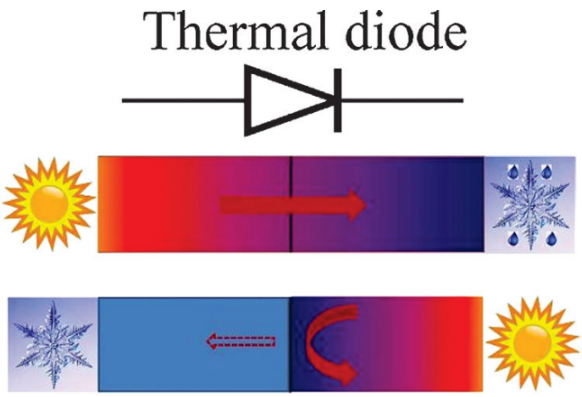

Figure 1.12: A simple sketch of a thermal diode. When the left side has a higher temperature than the right side, the device allows the heat transfer, but in contrast, the heat transfer is blocked [9].

1.5.1.1 Conductive thermal diode studies

Studies investigating thermal rectification based on nonlinear lattices

Terraneo et al. [77] analyzed the thermal rectification by modeling a thermal rectifier by three element structures composed of different nonlinear lattices and connected to two thermal reservoirs. They showed that the control of heat conduction by nonlinearity can provide a thermal rectifier [77]. Basically, the physical systems have a natural frequency and energy can be transported by stimulating it with vibrations [78]. In fact, Terraneo et al. examined a nonlinear region sandwiched between two weak anharmonic segments and found that the frequency allowing the phonon transport depends on the temperature applied at the ends of the device and not only at the temperature difference exhibiting thermal rectification [77].

Later in 2004, Li et al. [10] modified the study of Terraneo et al. [77] by investigating a thermal rectifier model with coupling two nonlinear one dimensional lattices by a constant harmonic spring k_{int} by using the Frenkel-Kontorova (FK) model instead of three-element structures as shown in Fig.1.13(a). Heat current as a function of dimensionless temperature difference for different values of reference temperature can be seen in Fig.1.13(b). It is clearly seen that when the dimensionless temperature difference is positive, i.e. the left side of the model is hotter than the right side, there is a heat current and it even increases as the dimensionless temperature difference increases. Oppositely, when it is negative, i.e. the right side is hotter than the left side, the system shows thermal insulator behavior [10]. In addition, Fig.1.13(c) shows the temperature jump at the interface for different k_{int} due to the Kapitza resistance. The temperature jump is higher in the case of negative dimensionless temperature difference and results in a decrease of the heat current to a very close value of zero [10]. Moreover, they analyzed the energy spectrum of the interface particles as seen in Fig.1.14, which helps to explain the main mechanism of the thermal rectification behavior [10]. If the frequencies of the particle at the left and right of the interface overlap, the heat current can be easily transferred throughout the system. The results of the spectra of the particles at the left and right of the interface can be seen in Fig.1.14(a) and (b), respectively [10]. As seen from the figures, if the left side has a higher temperature than the right side, the spectra of the two particles overlap over a wider range of frequencies, which allows the heat current to be transferred. In the opposite case, there is a mismatch, which hinders it [10].

Li et al. [79] conducted another study on thermal rectification due to the interface effect in 2005. In their system, two dissimilar anharmonic lattices are modeled by the FK and Fermi-Pasta-Ulam (FPU) models, which are located on the left and right sides of the interface, respectively [79]. By the same basic mechanism, when the temperature of the left side is higher than the temperature of the right side, the phonon bands of both lattices overlap as the consequence of the frequency movement of the FPU lattice, because both are at the lower frequencies with this condition. Thus, they behave like a good conductor. However, when the right temperature has a higher temperature, the frequency of the FK lattice is at high frequencies and the phonon bands do not overlap. In fact, this causes an insulator behavior [79]. Consequently, they obtained

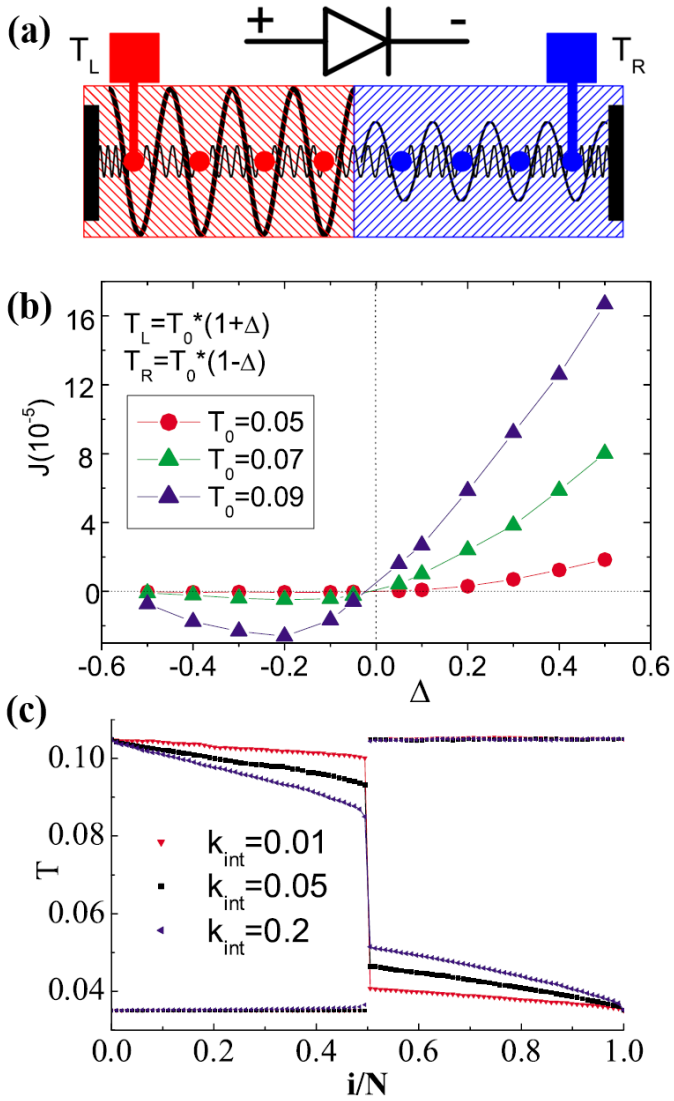

Figure 1.13: Schematic representation of the thermal rectifier from the review article of Li et al [9]. Heat current as a function of dimensionless temperature difference for different values of reference temperature (b) and temperature profile for different k_{int} (c). The value of N here is 100, which indicates the coupled particle chains [10].

a strong rectification behavior and also found the asymmetric interface thermal resistance as a result of the two dissimilar anharmonic lattices [79].

Later in 2006, the first pioneering experimental work on microscopic solid-state thermal rec-

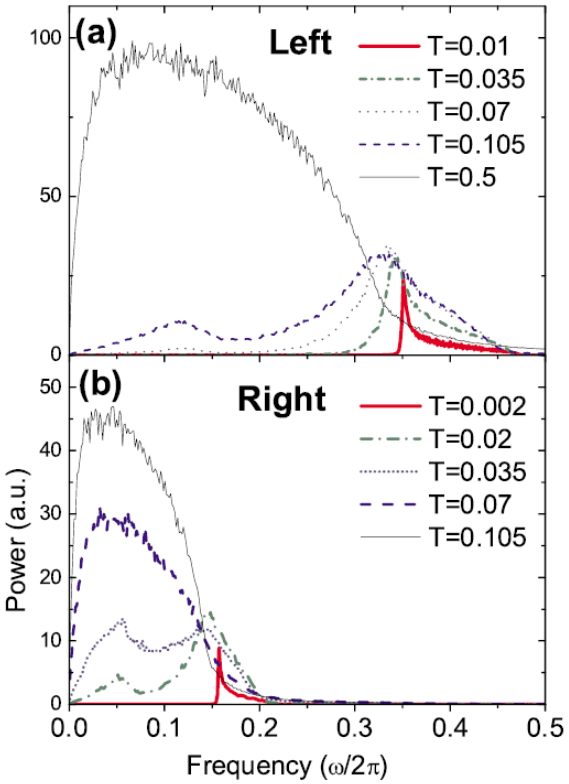

Figure 1.14: Phonon spectra of the two particles, left (a) and right (b), at the interface for different temperatures [10].

tification was done by Chang et al. [11], which is inspired by the mentioned theoretical studies until here [78]. They examined the rectification on mass-loaded nanotubes: carbon nanotubes (CNTs) and boron nitride nanotubes (BNNTs) [11]. They investigated the rectification effect on these nanotubes, because they are almost 1D and their thermal conductivity is dominated by phonons [11, 80, 81]. They deposited trimethyl-cyclopentadienyl platinum ($C_9H_{16}Pt$) on the nanotubes for non-uniformity as shown in Fig.1.15(a) [11]. In addition, transmission electron microscopic (TEM) images of the undoped and $C_9H_{16}Pt$ doped CNT can be seen in Fig.1.15(b) and (c), respectively [11]. There is a heater on one side of the nanotube in their set-up, while there is a sensor on the other side [11]. They also provide a vacuum condition for the body part in their set-up [11]. They observed that the thermal conductivity is the same from both sides for undoped CNTs and BNNTs, but when the tubes are asymmetric, i.e. mass loaded, they obtained thermal rectification factors up to 2% and 7% for CNTs and BNNTs, respectively [11].

Moreover, they found that the heat flow is always higher from the mass loaded side towards decreasing mass density [11].

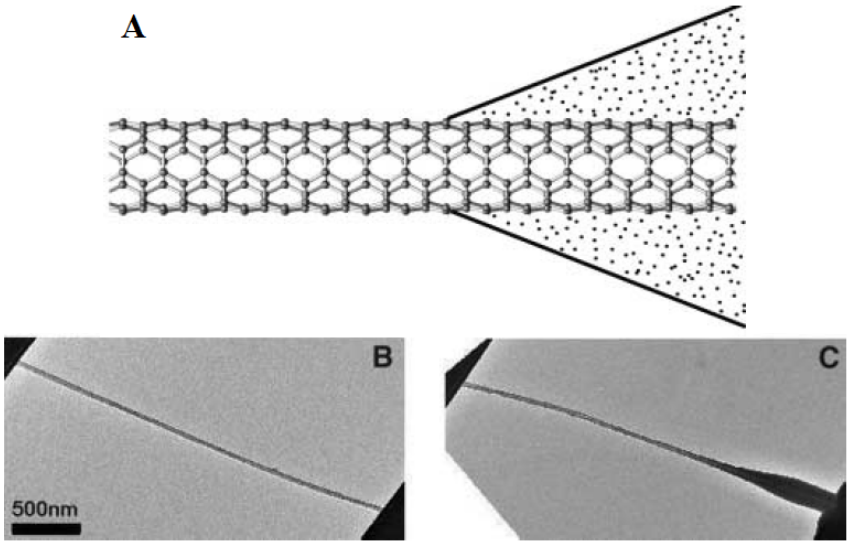

Figure 1.15: Schematic representation of $C_9H_{16}Pt$ doped nanotube (a), TEM images of the undoped (b) and $C_9H_{16}Pt$ doped CNT (c) [11].

After the experimental study of Chang et al. [11], Yang et al. [12] continued to study the thermal rectification due to mass loading and theoretically investigated a 1D mass-graded chain as shown in Fig.1.16, where N indicates the particle amount, to understand the underlying mechanism that causes the thermal rectification. They obtained a consistent result with the experimental study of Chang et al. [11], the heat flux is higher when the temperature is higher at the left end, which is the heavily massed side [12]. They explained this by the overlap of the phonon spectra as seen in Fig.1.17 [12]. When the particle on the heavily massed side is hot, it can be observed from Fig.1.17(a) that there is an overlap. Otherwise, the light-mass particle oscillates at high frequencies as seen in Fig.1.17(b), resulting in an insulating behavior [12]. Furthermore, they observed that the thermal rectification is higher when the mass gradient is larger [12].

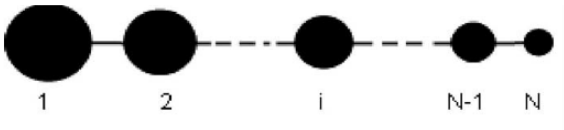

Figure 1.16: Schematic representation of mass-graded chain [12].

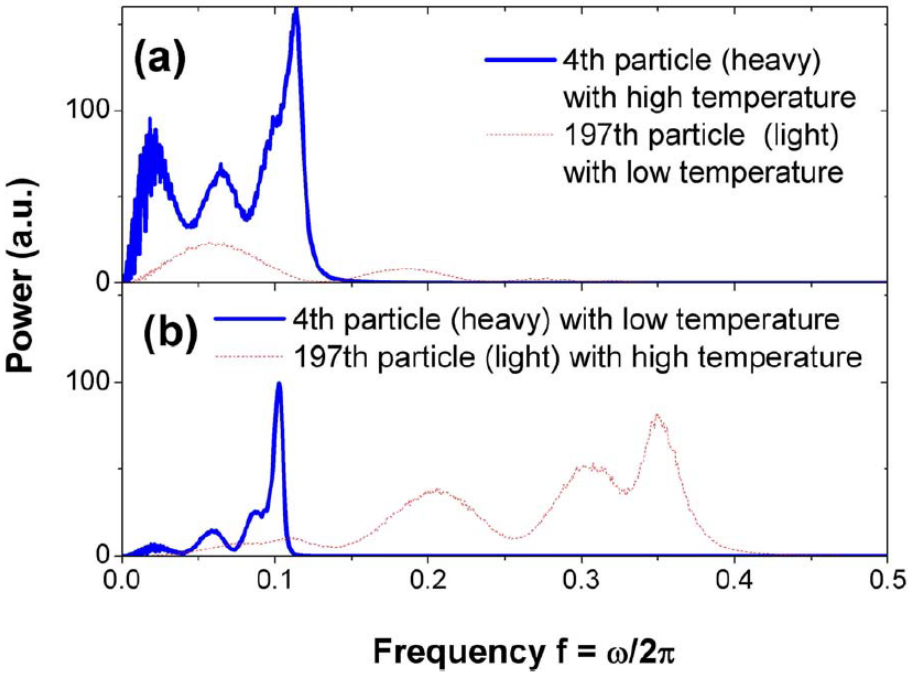

Figure 1.17: Phonon spectra of two particles from two ends, when the heavy-mass (a) and light-mass (b) sides are at higher temperatures, respectively [12].

Studies investigating thermal rectification based on asymmetric geometry

Moreover, there are more studies that have investigated the thermal rectification based on asymmetric nanostructures, some of which have schematic representations shown in Fig.1.18 [9]. Wu and Li [13] analyzed CNT intramolecular junctions as shown in Fig.1.18(a). In their system, nanotubes of equal size with different diameters are connected [13]. As seen before, they observed that the heat flux is higher from the higher radius direction to the lower radius direction [13]. They explained this by the overlapping of power spectra at the interface, as seen during previous studies considering nonlinear lattices [13]. Later, Yang et al. [14] analyzed the thermal rectification on a carbon nanocone and it is naturally a highly asymmetric geometry as can be

seen in Fig.1.18(b). In addition, they also studied the carbon nanocone system with asymmetric mass distribution [14]. Naturally, the heat flux is higher from higher to lower radius, but when they also deposited the CNTs asymmetrically, which means the top atoms have minimum mass while the bottom atoms have maximum mass, they observed 2% higher thermal rectification than the nanocone with uniform mass [14].

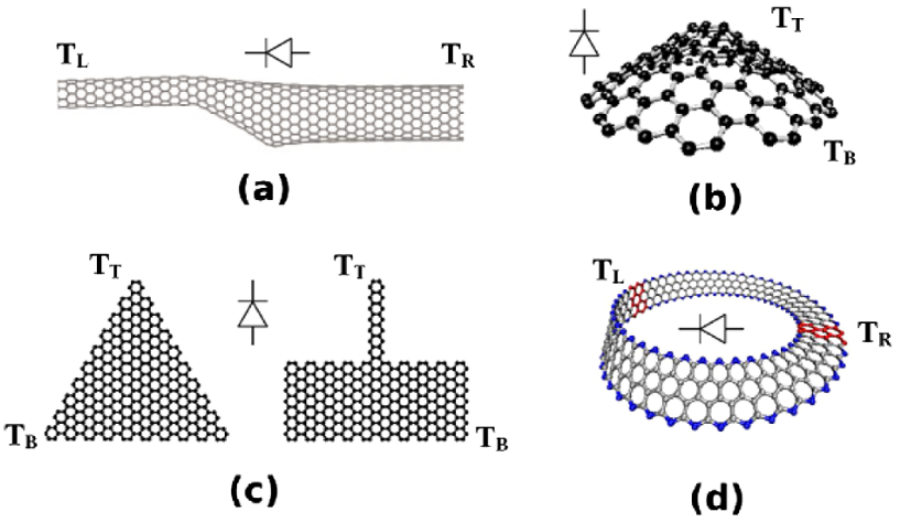

Figure 1.18: Schematic representations of investigated asymmetric nanostructures for thermal rectification [9]: carbon nanotube junction (a) [13], carbon nanocone (b) [14], graphene ribbon structures (c) [15] and Möbius graphene strip (d) [16].

In 2009, Yang et al. [15] analyzed two different graphene ribbon (GR) structures: trapezoidal and two rectangular shaped, as can be seen in Fig.1.18(c), considering the superior thermal conductivity of graphene and its possible use as a phononic device. As previously seen, the heat flux moves much more easily in the direction from high to low width. Thus, they observed that a positive thermal bias leads to a conductive behavior [15]. They also observed that the trapezoidal GR is more advantageous than the rectangular GR with the same thermal bias for thermal rectification, which causes higher thermal rectification and a thermal rectifier based on a GR gives generally a better performance than CNT [15]. This study showed that two dimensional membrane materials have a great potential for the thermal rectification and further increased

researchers' interest in two-dimensional asymmetry [17]. Moreover, a similar study was made by Hu et al. [82] in the same year and they obtained similar results [82]. The last schematic system as shown in Fig.1.18(d), which is based on Möbius graphene strip, was studied by Jiang et al. [16] and they found that although the position of the heat bath plays an important role for the thermal rectification, the size of the system is not very effective [16].

Interest in thermal rectifier studies has continued to grow over the last decade since 2010 and a significant number of studies on thermal rectification based on asymmetric geometry have been conducted. [17, 50]. Schematic representations of some of the important ones can be seen in Fig.1.19 [17]. In 2011, Zhong et al. [18] considered possible further researches on thermal rectification mechanisms by two- and three-dimensional systems and investigated asymmetric graphene nanoribbons (GNR) that are connected by single-layer and multi-layer graphenes as shown in Fig.1.19(b). They realized that the asymmetry caused by the thickness difference of each side affects the thermal rectification differently according to the thickness ratios of both sides and the temperature difference at the edges of the system [18]. Interestingly, when the thickness ratio is low, the increase of the temperature difference at the edges causes the thermal rectification to increase. Oppositely, when the thickness ratio is high, its increase causes the thermal rectification to decrease [18]. Later in 2018, Rojo et al. [19] conducted a study combining experimental and simulation, and investigated the connected mono- and bi-layer graphenes as shown in Fig.1.19(c). However, they experimentally observed that there is no thermal rectification in this system unlike the theoretical study of Zhong et al. [18, 19].

Ju and Liang [20] investigated the thermal rectification due to asymmetric geometry as seen in Fig.1.19(d). They analyzed silicon nanoribbons by changing their temperatures, aspect ratios and lengths by non-equilibrium molecular dynamics (NEMD) method, considering the wide usage of silicon in microelectronics [20]. They observed that the heat flow is higher from the thin side to the thick side [20]. Although the thermal conductivity in both directions increases with the increase of the length, the change in the length does not significantly affect the thermal rectification [20]. However, the aspect ratio is advantageous for thermal rectification and it increases as the aspect ratio increases [20].

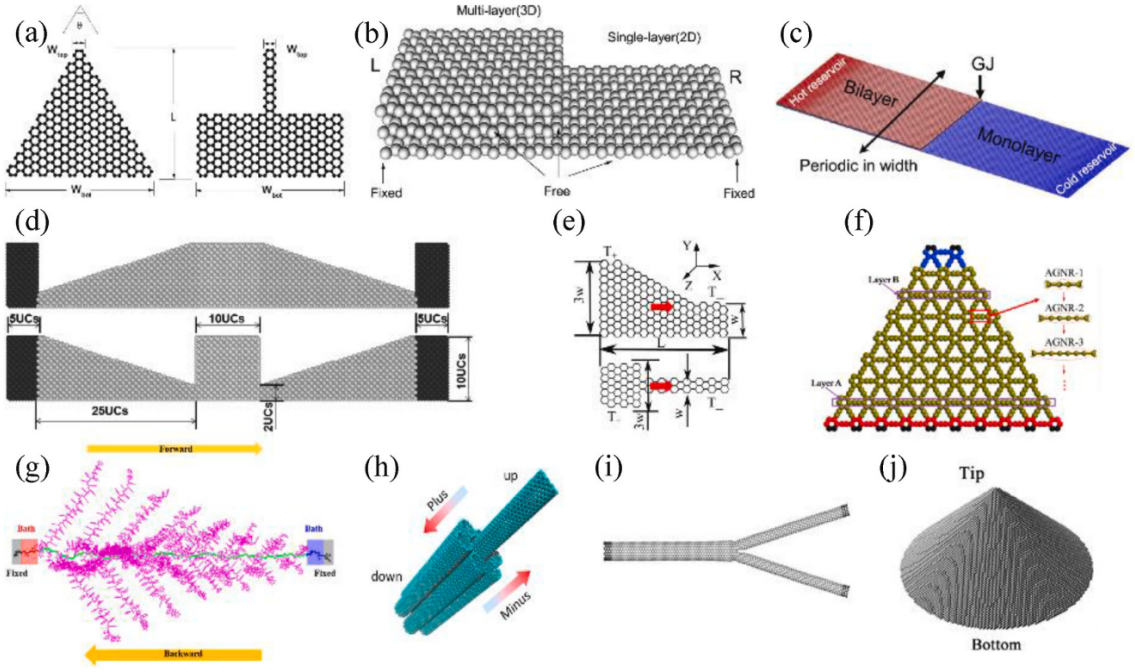

Figure 1.19: Schematic representations of investigated asymmetric nanostructures for thermal rectification [17]: carbon nanotube junction (a) [13], graphene nanoribbons connected by single-layer and multi-layer graphenes (b) [18] and (c) [19], asymmetric silicon nanoribbons (d) [20], asymmetric graphane trapezoidal and T-shaped nanostructure (e) [21], asymmetric triangular shaped graphene nanoribbons (f) [22], cone-shaped bottlebrush polymers (g) [23], Y-shaped carbon nanotubes (h) [24] and (i) [25], and silicon nanocone (j) [26].

Wang et al. [21] examined the thermal rectification resulting from the asymmetric nanostructure (Trapezoidal and T-shaped) composed of GNR caused by phonon confinement in the lateral dimension by NEMD method as seen in Fig.1.19(e). They observed that there is a noticeable thermal rectification in nanoscale, but it decreases with the increase of the geometry's length [21]. They even noticed that there is no thermal rectification at the bulk size [21].

Later in 2016, Lei et al. [22] analyzed asymmetric GNR for thermal rectification by NEMD method as seen in Fig.1.19(f). They observed that when they increase the length, the heat flux first increases and then decreases in both directions, and the heat flux is always higher from

the bottom to the top [22]. However, the thermal rectification always decreases as the length increases, and even disappears after a point [22]. They explained this by examining the phonon spectra. The phonon spectra of atoms in the A and B layers generally overlap when the heat flux is in the top direction, resulting in a higher heat flux. On the contrary, there is usually a mismatch, resulting in a lower heat flux [22]. They also noticed that the tensile strain positively affects the thermal rectification [22]. Finally, they examined the number of acetylenic linkages and found that although the heat flux in both directions decreases with their increases, there is no significant change in the thermal rectification [22].

Ma and Tian [23] studied an asymmetric nanoscale organic material which is cone-shaped bottlebrush polymers as seen in Fig.1.19(g). The main and side chains are composed of polynorbornene and polystyrene, respectively [23]. Interestingly, they found that the heat flow in the backward direction from the narrow end to the wide end is higher unlike the previously mentioned studies [23]. They realized that the length is important for this geometry and its impact is different, because after increasing the length beyond a limit causes the thermal conductivity to increase in the backward direction, while the thermal conductivity remains almost constant in the forward direction [23]. Therefore, this causes the thermal rectification to increase with length, but they assumed that the change in the backward direction would also reach saturation after a certain length, although they could not confirm this because of the computational limitations [23].

In addition, Y-shaped CNTs were analyzed for the thermal rectification by Li et al. [24] and Aiyiti et al. [25] in 2012 and 2018, respectively. The investigated asymmetric geometries can be seen in Fig.1.19(h) and (i) from the studies of Aiyiti et al. [25] and Li et al. [24], respectively. They observed the thermal rectification as a result of the different phonon spectrum distributions in both directions by NEMD method [24, 25]. Moreover, Aiyiti et al. experimentally confirmed the existence of thermal rectification in Y-shaped geometry [25]. The thermal conductivity is higher in the forward direction from top to bottom. Although the thermal conductivity in both directions increases with the increase of the ambient temperature while the temperature difference at both ends is constant, the thermal conductivity in the forward direction increases faster than the backward direction, which leads to an increase in thermal rectification [25]. In addition,

they found that thermal rectification decreases as the length of the geometry increases, which is similar to the previously summarized studies [25].

Zhang et al. [26] considered the silicon nanocone in three dimension for thermal rectification as seen in Fig.1.19(j) and observed an interesting issue that is different than the traditional results regarding asymmetry. When they analyzed the thermal rectification as a result of the asymmetric behavior of the nanocones with different vertex angles by NEMD method, they noticed that the thermal rectification behavior varies with the vertex angle of the nanocone [26]. Thermal rectification increases with the increase of asymmetry as previously observed until the vertex angle is 90°, but it starts to decrease when the angle is more than 90°. The reason is that the heat flux is greater from the bottom to the top end and until the vertex angle is 90°. The heat flux from the bottom to the top increases faster than the heat flux from the top to the bottom, which causes an increase of the thermal rectification, but after this angle, the heat fluxes in both directions increase rapidly and the thermal rectification starts to decrease [26].

Studies investigating thermal rectification based on hetero-structures

Researchers have not only focused on the thermal rectification behavior resulting from an asymmetric geometry, but many studies have also been conducted since 2010 to understand the thermal rectification behavior caused by the hetero-structures. As previously mentioned, Li et al. [10] showed their potential with their study in 2004. Especially, considering the high thermal conductivity of graphene-based heterostructures, researchers have extensively studied them. [50]. In 2011, Roberts and Walker [27] made a detailed study using molecular dynamics method for the thermal rectification which is caused by the attachment of two dissimilar medias, half of it is argon and the other half is krypton. They performed their simulation by assuming different interfaces as can be seen in Fig.1.20(a) [27]. They showed theoretically that the thermal rectification is possible by hetero-structures, but a perfect interface is advantageous to obtain a better thermal rectifier, because the thermal rectification performance decreases when the interface degrades [27].

In 2012, Cao et al. [28] analyzed an asymmetric grain boundary composed of armchair

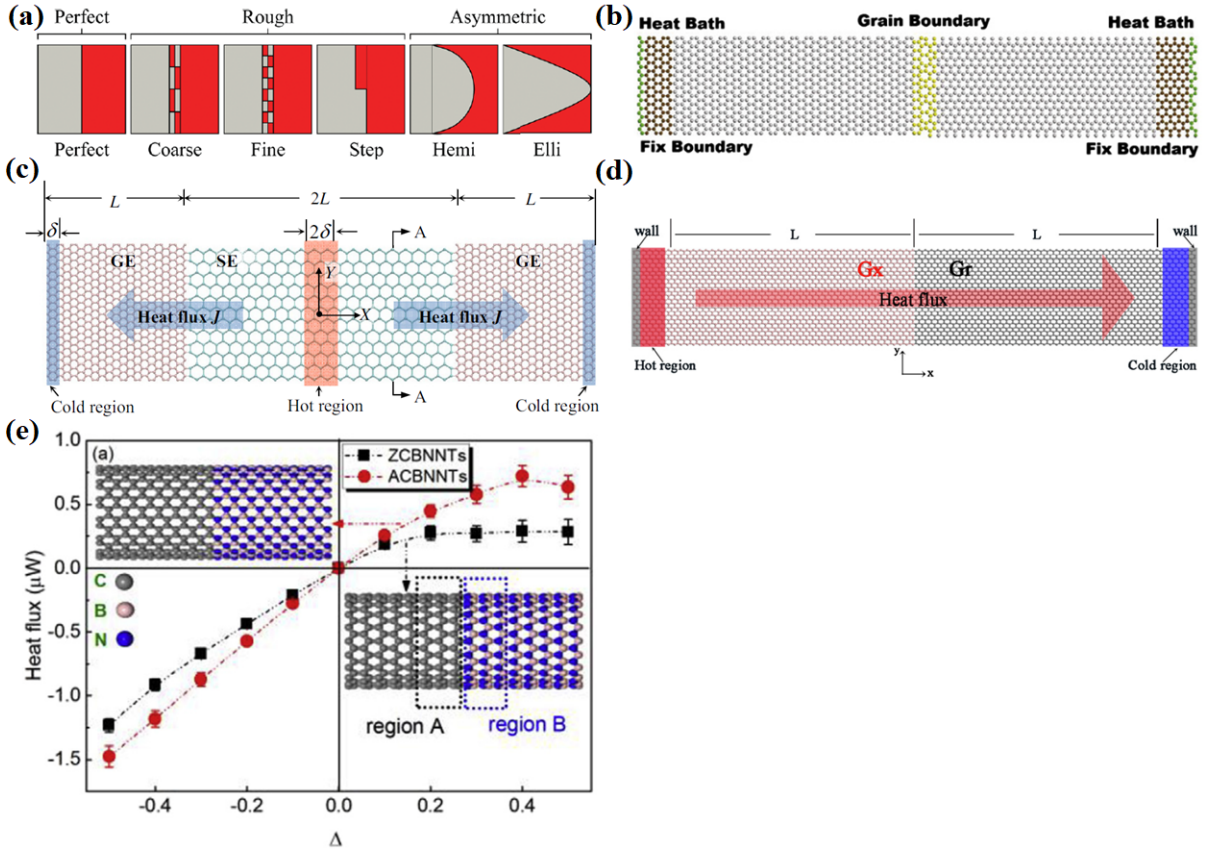

Figure 1.20: Schematic representations of investigated hetero-structures for the thermal rectification: investigated interfaces by Roberts and Walker (a) [27], asymmetric grain boundary composed of armchair and zigzag graphenes (b) [28], hetero-structure composed of graphene and silicene monolayer where the silicine sheet is placed between two graphene sheets (c) [29], hetero-structure composed of graphene-like material (Gx) and graphene (Gr) (d) [30], heteronanotube composed of carbon and boron nitride with two different structures; zigzag and armchair structures (e) [31].

graphene and zigzag graphene, as seen in Fig.1.20(b), by NEMD method and observed a thermal rectifier behavior. They found that both the Kapitza conductance and thermal conductivity are asymmetric as a result of this configuration [28]. They observed that the heat flux density is larger from the direction of the armchair graphene to zigzag graphene [28]. In addition, they observed that the thermal rectification decreases when the temperature difference at both ends is fixed and the average simulation temperature increases. On the other hand, it decreases

when the temperature difference increases and the average simulation temperature is fixed [28]. They explained the thermal rectification behavior by the mismatch of the phonon power spectra between the two parts of the geometry [28]. They observed that when the armchair has a higher temperature, the phonon power spectra of both parts mostly overlap, but it decreases in the opposite case [28]. Furthermore, the mismatch also increases as the temperature difference increases, which leads to an increased thermal rectification [28]. Similarly, higher thermal rectification at lower temperatures is explained by the greater shift of the phonon power spectra at lower temperatures compared to higher temperatures, which causes less overlap [28].

Liu et al. [29] made a detailed study to examine the behaviors of the interface thermal conductance and the thermal rectification of a hetero-structure composed of graphene and silicene monolayer. They used molecular dynamics simulation in their study [29]. They placed a silicene sheet between two graphene sheets as seen in Fig.1.20(c) and studied various parameters such as temperature, length of the system and external strain [29]. They found that the interface thermal conductance from the direction of silicene to graphene is higher than that from graphene to silicine and this induces a thermal rectification [29]. In addition, when the length of the system or the temperature of the system at a fixed length increases, the interface thermal conductance increases [29]. However, the interface thermal conductances in the forward and backward directions start to converge when the length continues to increase and this causes the thermal rectification to decrease. It even reaches a negligible thermal rectification value after a certain length [29]. They explained this by the mismatch between the phonon spectra of graphene and silicene, because the phonon frequency range of graphene is larger than the one of silicene. Therefore, most of the phonons from silicene can propagate in graphene, while the reverse is less likely, because the frequency overlap takes place at low frequencies [29]. They noticed that when the length increases, there are more available phonons at low frequencies and when the temperature of the system increases, more phonons at high frequencies are excited, which explains the increase of the thermal conductances with the increase of these parameters [29]. Lastly, they observed that increasing the tensile strain affects the thermal rectification performance positively, but it decreases the interface thermal conductances in both directions [29].

Another graphene based hetero-structure study, which is shown in Fig.1.20(d), was made by Li et al. [30]. They investigated the interface thermal resistance of a hetero-structure composed of graphene and graphene-like material [30]. They examined the change of the atomic mass and interatomic potential of the graphene-like material for the interface thermal resistance and noticed that the change of the atomic mass and interatomic potential significantly affect the overlap of the phonon spectra between interface of the graphene and graphene-like material, which causes a thermal rectification [30].

Chen et al. [31] studied a heteronanotube composed of carbon and boron nitride for the thermal rectification and analyzed two different structures, which are zigzag and armchair structures as seen in Fig.1.20(e), with different parameters such as length, tube diameter, and operating temperature. They observed that the temperature bias caused by the difference between the hot and cold temperatures affects the heat flux for the two structures differently [31]. When the heat flow direction is from carbon nanotubes to boron nitride nanotubes and the temperature bias decreases, the heat flux decreases linearly for both structures. In the opposite direction, the increase of the temperature bias causes almost linear increase in the heat flux for the armchair structure. However, the heat flux initially increases for the zigzag structure, but then it is not affected after a value as seen from the right side of Fig.1.20(e) [31]. This asymmetry observed in the heat flux in forward and backward directions induces a thermal rectification behavior in both structures, but more with the zigzag one [31]. In addition, although increasing the tube length and the temperature negatively affects thermal rectification, they noticed a different behavior for the tube diameter parameter [31]. Increasing the tube diameter to some extent induces thermal rectification to increase, but it causes a decrease after reaching the maximum thermal rectification [31].

Studies investigating thermal rectification caused by temperature-dependent thermal conductivity

PCM and the materials that exhibit temperature-dependent thermal conductivity are another alternative to generate thermal rectification. PCMs manifest different thermal, electrical and optical properties according to their critical transition temperatures [60]. Therefore, thermal diodes based on PCM constitute a beneficial solution for thermal management due to their alter-

ing characteristics. In the literature, there are various studies for a thermal diode based on the temperature-dependent thermal conductivity. In 2006, Peynard [83] theoretically showed that a thermal rectifier is possible with a material whose thermal conductivity depends on space and temperature. In fact, he showed the thermal rectifier behavior by juxtaposing two materials with two opposite thermal conductivity behaviors [83]. The thermal conductivity of the one increases over a certain temperature range while the other one decreases, or two materials where only one of them has a temperature-dependent thermal conductivity [83]. In 2009, Dames [84] also showed that the thermal rectification occurs when the thermal conductivities of the two parts of the thermal rectifier have different temperature dependencies.

Later in 2009, Kobayashi et al. [32] conducted a detailed study for a bulk thermal rectifier composed of two cobalt oxides based on Peyrard's theory [83] and experimentally obtained a thermal rectifier. The schematic representation of the thermal rectifier which they investigated can be seen in Fig.1.21(a) [32]. Parts A and B are made of $LaCoO_3$ and $La_{0.7}Sr_{0.3}CoO_3$, respectively, and their thermal conductivities as functions of temperature can be seen in Fig.1.21(b) [32]. In the first configuration in Fig.1.21(a), when the right side has a higher temperature than the left side, both materials perform high thermal conductivities so that the thermal rectifier behaves like a good conductor. Oppositely, in the second configuration, when the applied temperature are reversed, the thermal conductivities of both materials are low and show more insulating behavior [32]. Their experimental set-up can be seen in Fig.1.21(c), they blocked the thermal radiation and measured the temperatures at 4 different locations [32]. The thermal rectification, which is defined as the ratio of forward and backward heat current densities in their study, with respect to different temperature differences can be seen in Fig.1.21(d) according to the calculated and measured values at point 1 [32]. They obtained 1.43 as the maximum for the thermal rectification with about 60 K temperature difference at the boundaries [32].

In 2011, Sawaki et al. [33] continued their study in 2009 [32] and made a similar study for a pyramidal shaped thermal rectifier instead of a rectangular shape. Again, they made the rectifier with $LaCoO_3$ and $La_{0.7}Sr_{0.3}CoO_3$ as shown in Fig.1.22(a) [33]. In addition, the thermal conductivity changes of the two materials with temperature can be seen in Fig.1.22(b) [33]. As done

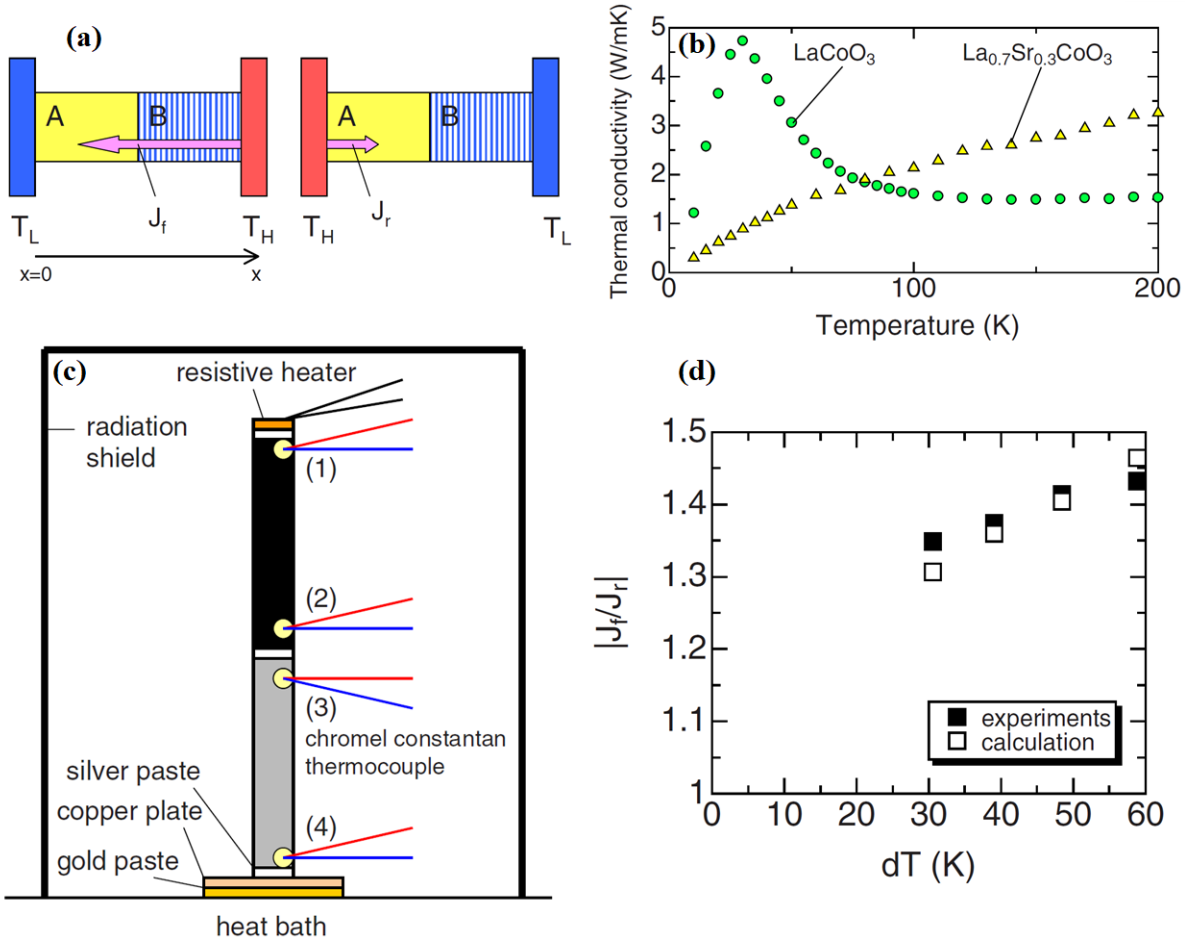

Figure 1.21: Schematic representation of the investigated thermal rectifier concept (a), the thermal conductivity variations of $LaCoO_3$ and $La_{0.7}Sr_{0.3}CoO_3$ with respect to temperature (b), schematic representation of the experimental set-up (c), and the thermal rectifications according to the calculated and measured values (d) [32].

before, they measured the temperatures at 4 different locations [33]. As seen from Fig.1.22(c), when $La_{0.7}Sr_{0.3}CoO_3$ is on top, the heat current is higher than the opposite configuration where $LaCoO_3$ is on top [33]. Moreover, although the thermal rectification increases with the increase of the temperature difference at the boundaries as observed in their previous study for the rectengular shape, they obtained a smaller thermal rectification with the pyramidal shape, which is 1.35 with 60 K temperature difference, as seen in Fig.1.22(d) [33].

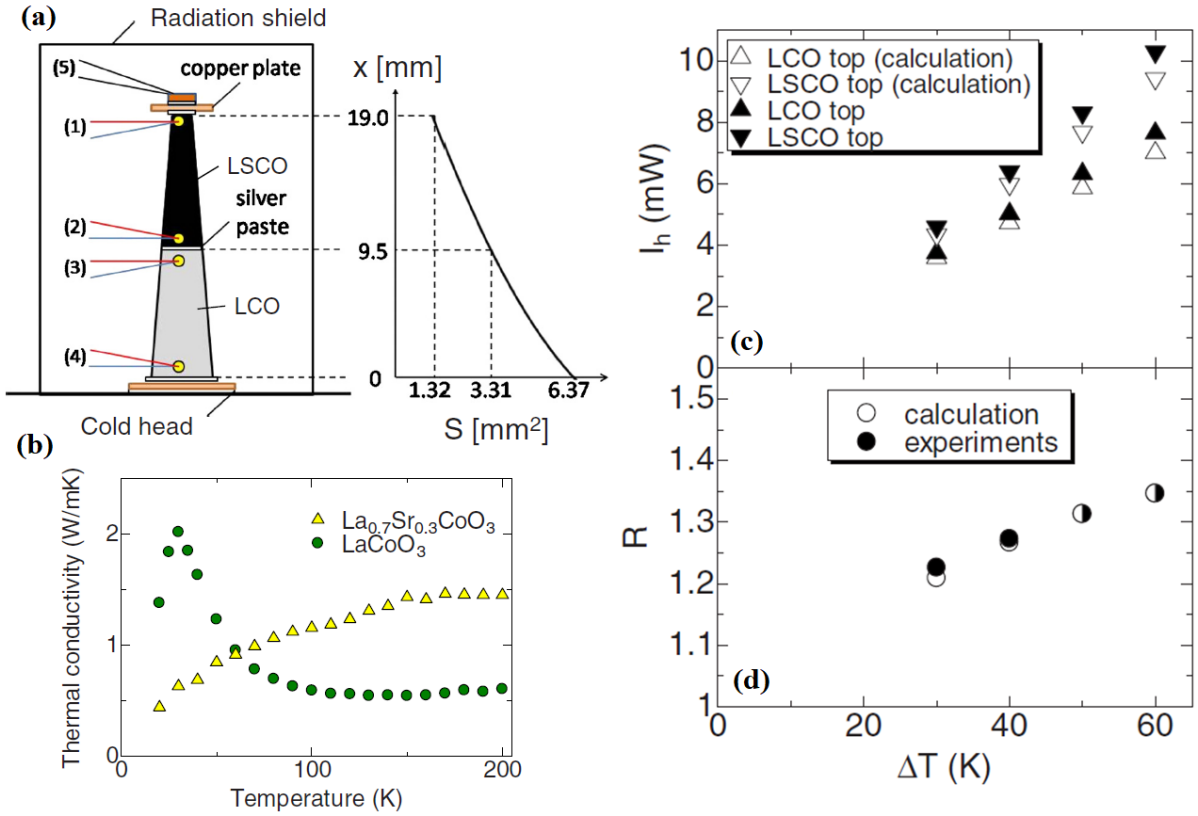

Figure 1.22: Schematic representation of the set-up and investigated pyramidal shaped thermal rectifier with its sectional area (a), the thermal conductivity variations of $LaCoO_3$ and $La_{0.7}Sr_{0.3}CoO_3$ with respect to temperature (b), and heat currents (c) and the thermal rectifications (d) according to the calculated and measured values [33].

Kobayashi et al. [34] made another study considering the need of a high temperature difference to achieve a thermal rectification behavior as observed in their previous studies. They made the thermal rectifier with MnV_2O_4 and $La_{1.98}Nd_{0.02}CuO_4$. The thermal conductivity variations with temperature of the two materials can be seen in Fig.1.23(a) [34]. There is a significant change in the thermal conductivity of MnV_2O_4 at 57 K, while the thermal conductivity of $La_{1.98}Nd_{0.02}CuO_4$ can be considered almost constant for temperature larger than 50 K [34]. Therefore, they made a 3 mm and 7 mm rectangular bar with MnV_2O_4 and $La_{1.98}Nd_{0.02}CuO_4$, respectively, and juxtaposed them [34]. Then, as in their previous works, they experimentally measured the thermal rectification by increasing the cold temperature from 53 K to 57 K while

maintaining a 2 K difference with the hot temperature [34]. As a result, they observed a high thermal rectification of 1.14, which is close to the transition temperature of MnV_2O_4 at 55.4 K, with a small temperature difference thanks to the sudden thermal conductivity change as seen in Fig.1.23(b) [34].

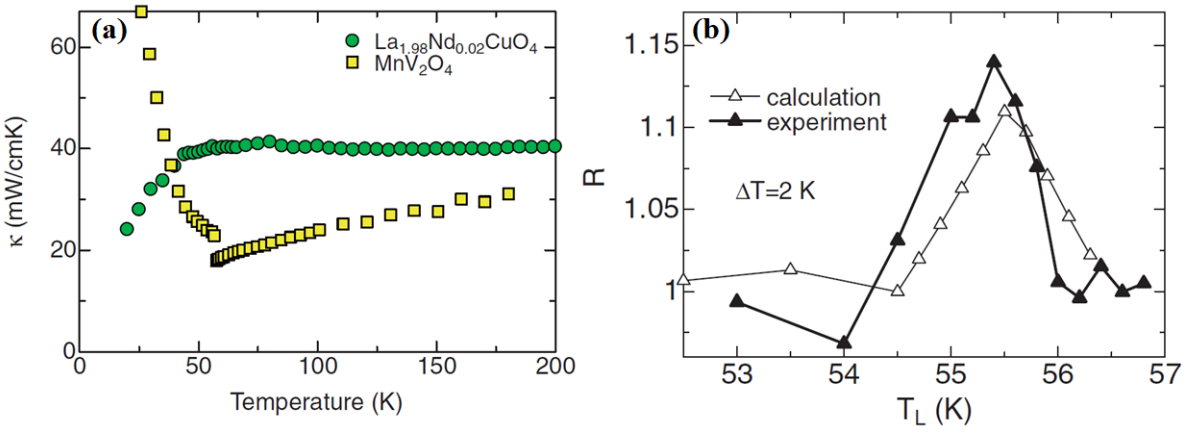

Figure 1.23: The thermal conductivity variations of $La_{1.98}Nd_{0.02}CuO_4$ and MnV_2O_4 with respect to temperature (a), and the thermal rectifications according to the calculated and measured values (b) [34].

Later in 2014, Pallecchi et al. [85] conducted another experimental study on a PCM based thermal diode. Their thermal diode is composed of poly(*N*-isopropylacrylamide) (PNIPAM) and polydimethylsiloxane (PDMS) [85]. While PNIPAM shows a phase transition at 32 °C and changes its phase from hydrophilic to hydrophobic, which causes it to exhibit a more conductive behavior, the thermal conductivity of PDMS remains almost constant [85]. Therefore, they obtained higher heat flux in the forward direction from PNIPAM to PDMS than in the backward direction [85]. In 2015, Zhang and Luo [86] theoretically investigated a thermal diode that is achieved by phase-dependent thermal conductivity of polyethylene (PE) nanofibers. They made their thermal diode by connecting crystalline PE fiber and cross-linked PE [86]. The thermal conductivity of PE fiber changes according to a phase transition temperature around 397 K, where its thermal conductivity decreases from 25 $Wm^{-1}K^{-1}$ to 5 $Wm^{-1}K^{-1}$ in a short temperature range, while the thermal conductivity of cross-linked part PE remains unchanged [86]. By

utilizing this configuration, they achieved a thermal rectification up to 1.20 in a small temperature difference at the boundaries such as 20 K [86].

Moreover, Chen et al. [87] made a new thermal rectifier with a solid-liquid phase transition concept, and they experimentally and numerically investigated it for the thermal rectification. Two different PCMs, which are eicosane and PEG4000, are placed into a reduced graphene oxide, and they do not mix with each other in the liquid state. [87]. The phase transition temperature of eicosane is lower than PEG4000 [87]. Eicosane and PEG4000 transform from solid to liquid around 36 °C and 60 °C, respectively, and the thermal conductivity of both decrease after the phase transition [87]. They observed that when the hot side is the PEG4000 side and the hot temperature is lower than the transition temperature of PEG4000, both PCMs remain in the solid state [87]. However, if the eicosane side is hotter, it is in the liquid state with low thermal conductivity, while PEG4000 is still in solid state [87]. Therefore, it shows a thermal rectifier behavior and they achieved a thermal rectification ratio of 1.23 [87].

There is an increasing interest in thermal diodes based on temperature-dependent materials, but there was a lack of analytical approach. Therefore, in 2015, Cottrill and Strano [88] performed a detailed mathematical analysis for a thermal diode consisting of two materials, one with a temperature-dependent thermal conductivity and the other one with a constant thermal conductivity with temperature. They proposed some analytical formulas at steady-state that can be used under some limitations [88]. They compared their analytical model with the works of Garcia et al. [89] and Pallecchi et al. [85], and obtained consistent results [88]. However, this study was limited to only one PCM. Hence, Cottrill et al. extended their analytical approach to a thermal diode composed of two different PCMs in 2018 [90]. They again compared their analytical model with an experimental result and obtained consistent result [90].

In 2018, Yang et al. [91] also made a study with an analytical approach for a bulk thermal diode consisting of two materials with a temperature-dependent thermal conductivity. They did not consider the interface thermal resistance and modeled the thermal conductivities of the materials as linear and quadratic dependent with temperature [91]. The thermal conduc-

tivity of the first material increases with temperature, while the thermal conductivity of the second material decreases in their study [91]. They found that the maximum thermal rectification is higher with the quadratic temperature-dependent thermal conductivity than the linear temperature-dependent thermal conductivity [91]. They compared their analytical model with some experimental results from studies in the literature. Their model gives very consistent results with bulk thermal diodes in the studies such as [33, 92, 93], but not with a study on graphene heterostructures where the interface thermal resistance is included [94] and they indeed obtained a thermal rectification ratio 28% less than the experimental result [91].

Studies investigating thermal rectification caused by phase change materials

As a practical advantage of PCM, the drawback of the requirement of high temperature difference between the boundaries can be overcome thanks to their thermal conductivity alteration to some extent. Among PCMs, VO_2 has attracted great attention due to its critical transition temperature as being close to room temperature. It is also an ideal candidate to manipulate conductive heat flux and in which thermal rectification can occur. It can generate even with smaller temperature difference between the terminals of the thermal diode. Thus, there have been detailed investigations to use VO_2 in thermal diodes as a single PCM or in combination with another PCM. In 2018, Ordonez-Miranda et al. [35] examined a thermal diode with a single PCM (VO_2 or nitinol) as shown in Fig.1.24(a). They predicted 19.7% of thermal rectification and concluded that a higher thermal conductivity contrast, smaller thermal hysteresis and faster phase transition can generate higher thermal rectification [35]. In addition, they exploited an expression for the thermal conductivity variation with temperature, which is usable for both VO_2 and nitinol [35]. They determined the values of the parameters in the expression, such as the thermal conductivities in both states or the phase transition slope, by fitting the equation with a real experimental result for the heating process of both materials separately [35]. In fact, we also use this expression (Eq.1.16) and its determined values for VO_2 in this thesis.

Again in 2018, Kang et al. [95] analyzed the thermal rectification of a thermal diode composed of polyethylene and VO_2. They analytically developed their model by assuming the temperature-dependent thermal conductivities of both PCMs are as step functions and obtained a thermal

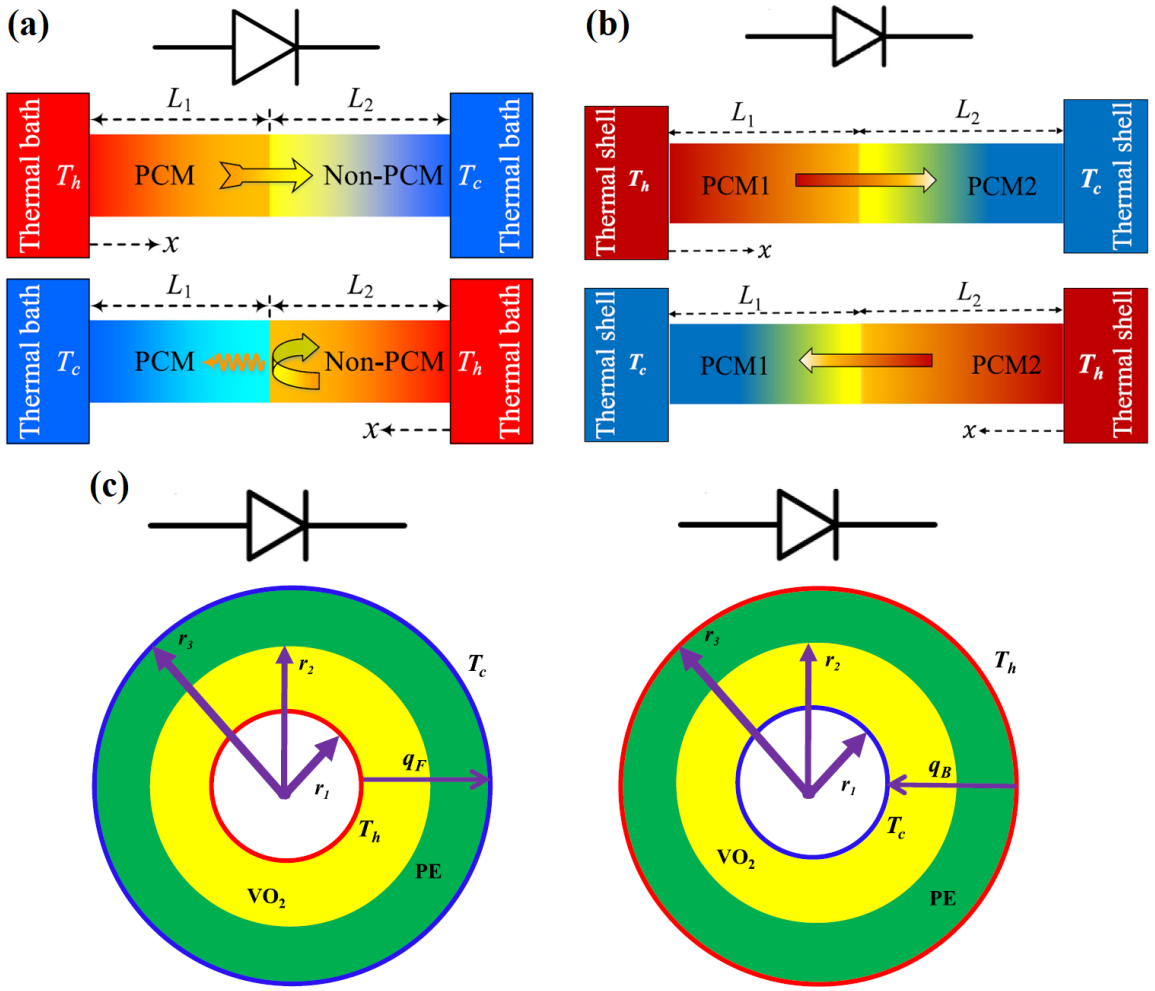

Figure 1.24: Schematic representations of a single PCM (a) [35], a thermal diode composed of two PCMs (b) [36] and a spherical (cylindrical) thermal diode (c) [37] in forward and backward directions.

rectification of approximately 140% according to the thermal rectification factor formula they used in their study [95]. However, their thermal conductivity model was not as realistic as the model of Ordonez-Miranda et al. due to the step function assumption [36]. Therefore, later Kasali et al. [36] theoretically investigated the thermal diode that was made by two PCMs as the combination of VO_2 and Polyethylene as shown in Fig.1.24(b), and modeled the thermal conductivity like in the study of Ordonez-Miranda et al. [35]. In their study, they predicted a thermal rectification of 60%. Later, they analyzed the influence of the thermal diode geometry

and examined the thermal rectification with spherical and cylindrical thermal diodes as shown in Fig.1.24(c) [37]. They obtained a thermal rectification of 63.5% and 63.2% for spherical and cylindrical thermal diodes, respectively, that were made by VO_2 and Polyethylene. These values of thermal rectification, which are very close, are higher than the one obtained in the plane geometry [37].

Studies investigating thermal rectification under transient conditions

Studies in the literature, including those summarized here, have mostly focused on exploring conductive thermal rectification under steady-state conditions. Nevertheless, not much effort has been devoted to the study of conductive thermal rectification under transient conditions. However, the latter needs to be well understood to be able to utilize thermal components in transient conditions when they experienced rapid temperature variations. Herrera et al. [38] published the first study related to thermal diodes under transient conditions. They calculated the thermal rectification of thermal diodes composed of two materials whose thermal conductivity and specific heat vary linearly with temperature by applying finite difference method. In addition, as used in the summarized steady-state studies, the thermal rectification formula, which is usually the ratio of forward heat flux density to backward heat flux density, are not applicable under transient conditions, because the heat flux is not constant throughout the thermal diode. Therefore, they introduced a time-dependent thermal rectification factor [38].

As seen in Fig.1.25 [38], the dimensionless time behaviors of the thermal rectification factor follow a similar trend in any studied case. It first increases and reaches a maximum value, then decreases and saturates at the steady-state value. This means that a higher thermal rectification factor under transient conditions is obtained compared to steady-state conditions. Furthermore, they observed that multiple peaks are possible as seen in the case shown in blue line in Fig.1.25(c). The results of Herrera et al. [38] show that understanding the capacitive effect for the thermal rectification under transient conditions is very important, which is naturally ignored during the steady-state analysis. In Fig.1.25, the black, red and blue colored lines show the time behaviors of the thermal rectification factors with respect to the ratio of thermal diffusivity of the first material to second material and their values are 1100, 1.1 and 0.0011, respectively. These three

colored lines are reported according to three different values of the uniform thermal conductivity ratios (the ratio of the second material to the first material). The reported results can be seen in Fig.1.25(a), (b) and (c) when the uniform thermal conductivity ratios are 0.001, 1 and 1000, respectively [38]. If the figures are briefly examined in a general perspective to emphasize the importance of studying thermal rectification under transient condition, it can be seen that thermal diffusivity has a non-negligible effect on transient thermal rectification. The time required to saturate the system to steady-state increases when the thermal diffusivity of material 1 is higher than that of material 2 regardless of the thermal conductivity ratios. However, as expected, the thermal diffusivity does not affect the steady-state thermal rectification value, which is affected by the uniform thermal conductivity ratios. Also, it should clearly be noted that the thermal diffusivity even affects the time interval of transient thermal rectification when the uniform thermal conductivity ratio is 1 as seen in Fig.1.25(b). Consequently, this study [38], which is the first conductive thermal rectification study under transient conditions, has inevitably helped researchers to draw attention to this perspective of the thermal diodes.

Klinar et al. [96] carried out a numerical study to investigate the influence of a thermal diode in a magneto-caloric refrigeration device under transient conditions. They analyzed various temperature dependent thermal conductivity profiles for thermal diodes and numerically solved the heat conduction by using implicit finite difference method [96]. Similar to the work of Herrera et al. [38], they found that the thermal rectification reaches higher values under transient conditions than steady-state conditions [96].

In 2022, Shimokusu et al. [97] developed a model with analytical perturbation solution by combining finite element method (FEM) to determine optimized rectification under transient conditions for applications such as waste heat scavenging and passive thermal control. They validated the perturbation solutions with FEM [97]. Their thermal diode is composed of two temperature-dependent materials, where the thermal conductivities and the specific heats vary linearly with temperature [97]. While they apply a sinusoidal boundary condition at one side of the thermal diode, the other side has a constant temperature [97]. In their study, they defined a rectification asymmetry metric, which is the difference between forward and backward heat

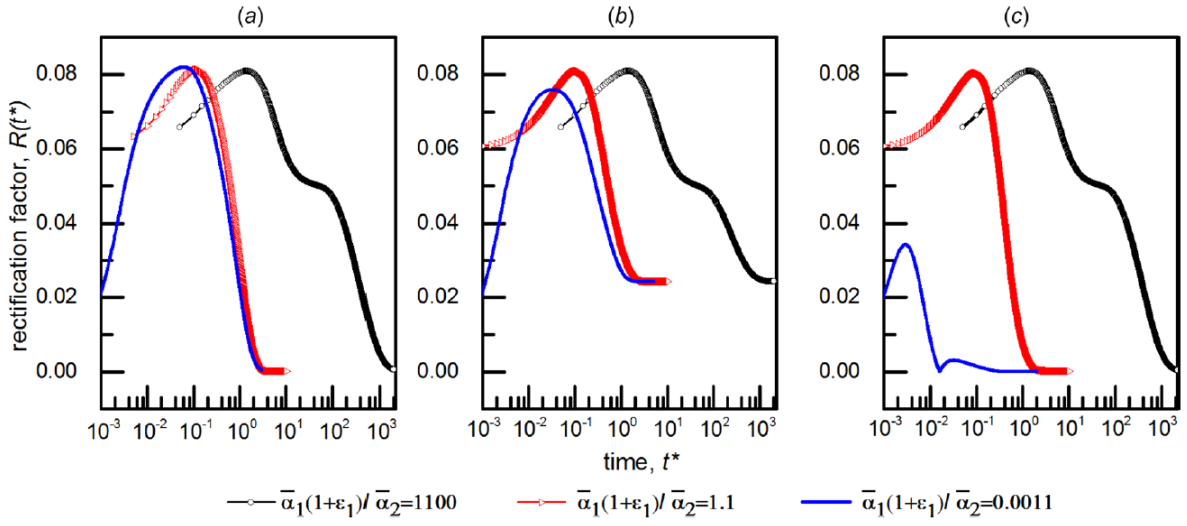

Figure 1.25: The dimensionless time (t^*) behaviors of the thermal rectification factor for three different thermal diffusivity ratios, 1100 (black), 1.1 (red) and 0.0011 (blue) when the uniform thermal conductivity ratios (the ratio of the second material to the first material) are 0.001 (a), 1 (b) and 1000 (c). ε_1 represents the nonlinear factor for the thermal conductivity parameter for the material 1, which is taken as 0.1 [38].

fluxes, and investigated various parameters such as time-dependent linear thermal conductivity, geometric parameters and frequency of the applied sinusoidal temperature for the maximum rectification asymmetric metric by conducting a parametric study [97]. In fact, they realized that the rectification asymmetric metric can be twice as large as the quasi steady-state value at high frequency values of the applied sinusoidal temperature [97].

In 2023, we also published an article related to a thermal diode made of a PCM and a non-PCM, which are VO_2 and SiO_2, respectively [1]. In summary, we analyzed the thermal rectification behavior by applying the Dirichlet boundary conditions under transient conditions [1]. The thermal rectification behavior was investigated with the real characteristic values of VO_2 as well as with different intrinsic and extrinsic parameters. We found that the thermal rectification reaches very high values under transient conditions than the steady-state thermal rectification [1]. Moreover, we recently published another study and extend the former analysis by examining the capacitive effect, including the cases where there is not a full transition cycle by applying

modulated boundary conditions [52]. We observed that the phase transition and capacitive effect have significant affects on the thermal rectification. Furthermore, as the frequency of the applied boundary conditions increases, the thermal rectification factor oscillates more and its maximum value increases [52]. Therefore, although the studies are generally conducted under steady-state conditions as seen from the literature summary, it is also crucial to study the thermal diodes under transient conditions [1, 52]. These two articles are actually an outcome of this thesis and we will detail these works in the relevant Chapter 3.

In 2024, Zurdo et al. [39] investigated a square thermal diode with triangular and crescent-shaped holes as seen in Fig.1.26(a) and (b), respectively. They examined the heat flow behavior in two different cases, which they called left-case and right-case in their study [39]. A sinusoidal boundary condition is applied to the left side of the thermal diode for the left-case, while the right side of the system has a constant temperature [39]. Oppositely, the applied boundary conditions are reversed for the right-case [39]. In their model, they solved the heat conduction equation by finite difference method by assuming the thermal properties are constant and examined the thermal rectification with different geometry, cross-section, size and the frequency of the input boundary condition [39]. They found that the thermal diode with the triangular-shaped hole causes a better global thermal rectification than the crescent-shaped hole and obtained a global thermal rectification value up to 10% [39].

1.5.1.2 Radiative thermal diode studies

We have deeply summarized the studies on conductive thermal diodes, taking into account our examination of thermal diodes in this thesis based on the conductive regime of heat transfer. However, there are also various studies on radiative thermal diodes in the literature and we will briefly summarize some of the prominent ones here. In 2010, Otey et al. [98] investigated a near-field radiative thermal rectifier made of two different silicon carbide (SiC) slabs with a vacuum gap. Their thermal rectifier is based on different dielectric function-temperature dependencies of materials and they achieved a thermal rectification of 0.41 at a temperature difference of 300 K by applying fixed boundary conditions [98]. Similarly, in 2011, Basu and Francoeur [99] also investigated a near-field thermal rectifier with different dopant levels and vacuum gaps by apply-

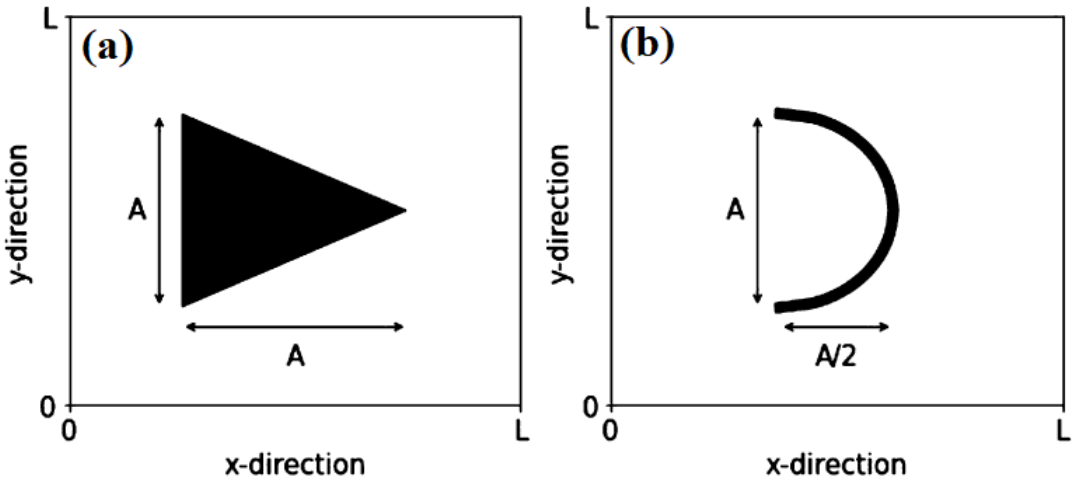

Figure 1.26: Schematic representation of the thermal diode with a triangular-shaped (a) and crescent-shaped (b) holes [39].

ing fixed boundary conditions, but they used silicon (Si) as the material of the thermal rectifier instead of SiC. They [99] achieved a thermal rectification of 0.5 at a temperature difference of 100 K, which is indeed higher than the thermal rectification in the study of Otey et al. [98]. Later in 2013, Wang and Zhang [100] made another study for near-field radiative thermal rectifiers. They investigated near-field radiative thermal rectifiers with different vacuum gaps made of intrinsic Si and different materials such as doped Si, SiO_2 and Au. They found that increasing the vacuum gaps negatively affects the thermal rectification of the thermal rectifier made of intrinsic Si and doped Si as well as the thermal rectifier made of intrinsic Si and SiO_2, but does not affect the thermal rectification of the thermal rectifier made of intrinsic Si and Au up to 500 nm [100].

In 2011 and 2012, various studies have been done on the heat flux modulation for both near-field and far-field radiative heat transfer with PCM, VO_2 [101, 102, 103, 104]. Then, Ben-Abdallah and Biehs [105] made a far-field radiative thermal diode based on IMT materials in 2013. In fact, their radiative thermal diode is made of VO_2 and SiO_2 [105]. As mentioned before, the properties of VO_2, including its optical properties, change depending on a phase transition temperature [105]. Ben-Abdallah and Biehs actually achieved to obtain a higher thermal rectification than the previous summarized radiative thermal rectifier studies with a small temperature

difference thanks to this optical property change of VO_2 [105]. They also observed that the thermal rectification ratio increases with the increase of the temperature difference between the two bodies [105]. In the same year 2013, Yang et al. [106] investigated a radiative thermal rectifier made of VO_2 and SiO_2, but in the near-field regime. They observed that the thermal rectification increases when the vacuum gap distance decreases, and even achieved a higher thermal rectification at the same vacuum gap distance when they used 10 nm thin SiO_2 film instead of a bulk SiO_2 [106].

Nefzaoui et al. [107, 108] conducted two separate studies on far-field radiative thermal rectifiers in 2014: one is based on superconducting materials [107] and the other one is based on selective emitters [108]. In the study based on superconducting materials, they investigated two different radiative thermal rectifier configurations [107]. The first one is made of $Tl_2Ba_2CaCu_2O_8$ and a black body, and the second one is made of $Tl_2Ba_2CaCu_2O_8$ and $YBa_2Cu_3O_7$ [107]. Although they achieved high thermal rectification ratios in both configurations, they achieved a better performance with the first configuration [107]. In their second study, they studied a thermal rectifier made of two multilayer selective emitters [108]. They made the multilayer selective emitters with two structures: one with Au and Si structures, and another with HDSi and Si structures [108]. They observed that the thermal rectification ratio increases by increasing the temperature difference [108].

In 2014, experimental demonstration of a far-field radiative thermal rectifier made of VO_2 was done by Ito et al. [109]. Their radiative thermal rectifier is made of a fused quartz and VO_2 deposited on silicon substrates with a vacuum gap [109]. They investigated the thermal rectification experimentally [109]. In their study, while VO_2 exhibits insulating behavior in the forward direction, it exhibits metallic behavior in the backward direction [109]. Therefore, they obtained thermal rectification. They also doped VO_2 with tungsten (W) to modify the phase transition temperature of it, thereby changing the operating range of the radiative thermal rectifier [109]. They obtained a high thermal rectification ratio and compared their experimental results with the theoretical results in their study and obtained consistent results [109]. Moreover, another study was made by Fiorino et al. [110], but they studied the radiative thermal diode

in the near-field regime instad of the far-field. They achieved thermal rectification up to about 60% with a radiative thermal diode composed of Si and VO_2 with a vacuum gap of 140 nm and a temperature difference of 70 K [110]. In 2020, Forero-Sandoval et al. [111] also conducted an experimental study on a radiative thermal diode in the far-field regime. They studied three different configurations, namely VO_2 films deposited on r- and c- sapphire as well as silicon substrates [111]. They achieved a high thermal rectification of 61% with a very low temperature difference, which is 40 °C, with r-sapphire [111]. They also compared their experimental results with an analytical result and obtained consistent results [111].

There are also some studies that investigated the thermal rectification performance of thermal diodes made of grating surfaces [112, 113]. Ghanekar et al. [112] studied a near-field radiative thermal diode made of 1-D VO_2 grating surfaces in 2016. They investigated two different structures: the first one is rectangular shaped grating and the second one is triangular shaped grating [112]. The radiative thermal diode consists of two parts with a distance between them. The first part of the thermal diode is made of VO_2 grating surfaces placed on a gold layer deposited on a substrate and the second part is made of boron nitride (BN) and similarly placed on a gold layer deposited on a substrate [112]. In addition, Ghanekar et al. [113] conducted another study on grating surfaces in 2018. They compared a near-field radiative thermal diode made of a bulk VO_2 and BN with their previously described 1-D rectangular shaped one [113]. Both studies showed that grating shaped structures have a significant effect to increase the thermal rectification [112, 113].

1.5.1.3 Thermal rectification formula

As presented in the literature summary, the most basic formula for the thermal rectification factor R is the ratio of the heat fluxes in the forward and backward directions. However, there are other formulas to define the thermal rectification in the literature and the most used ones

with the most basic formula are as follows [50]:

$$R = \frac{k_+}{k_-} \tag{1.21}$$

$$R = \frac{k_+ - k_-}{k_-} \tag{1.22}$$

$$R = \frac{|k_+ - k_-|}{max(k_+, k_-)} \tag{1.23}$$

$$R = \frac{k_+ - k_-}{k_+ + k_-} \tag{1.24}$$

where k_+ and k_- are the thermal conductivities in the forward and backward directions, respectively. Eq.1.21 is the most basic formula to quantify R. It is basically the ratio of the thermal conductivities in the forward and backward directions, respectively. In this form, if the value of R is 1, this means there is no rectification [50]. Eq.1.22 is the ratio of the difference between forward and backward thermal conductivities to the backward thermal conductivity. Eq.1.23 is the ratio of the absolute difference between forward and backward thermal conductivities to the maximum thermal conductivity. Eq.1.24 is the ratio of the difference between forward and backward thermal conductivities to the sum of them. If the value of R is 0, it means there is no rectification for Eq.1.23 and Eq.1.24.

In the absence of an internal heat source, the heat flux remains constant throughout the system under steady-state conditions. Therefore, the thermal rectification can be calculated by using one of the formulas that was mentioned above. However, this is not valid for transient conditions as emphasized by Herrera et al. [38], because heat flux can vary throughout the system under these conditions. Thus, in this thesis, we always analyzed the thermal rectification on the basis of the heat flux density at the cold end by considering the fact that heat spontaneously moves from the hot side to the cold side according to the second law of thermodynamics. Consequently, we define the thermal rectification in this thesis as

$$R(t) = \frac{||q_+| - |q_-||}{max(|q_+|, |q_-|)} \tag{1.25}$$

Eq.1.25 is the temporal analogous of Eq.1.23. The thermal rectification is evaluated using three different metrics as proposed by Herrera et al. [38]: (a) The first metric is R_{max} which represents the maximum thermal rectification factor, (b) the second metric is R_{ss} which is the

thermal rectification factor at steady-state conditions, and (c) the third metric is the time-integrated thermal rectification factor, $\widetilde{R}$, which allows a better quantification of the capacitive effects,

$$\widetilde{R} = \int_{t_m}^{t_{ss}} R(t)dt \tag{1.26}$$

where t_{ss} and t_m represent the times for which R_{ss} and the first peak in the thermal rectification profile are reached, respectively. It is also worth mentioning that the first peak in the thermal rectification profile as a function of time coincides very often with R_{max}. As a general rule, we considered t_{ss} to be the time at which the full numerical solution of the thermal rectification in the transient regime analysis equals 99% of the semi-analytical solution obtained under steady-state conditions.

1.5.2 Thermal transistor

The revolutionary invention of the electronic transistor was made by Bardeen and Brattain [72] in 1948. It has massively helped the technological advancement that we reached today as being one of the main tools for information treatment and computing technology. It basically controls the current as having three functions which are amplifying, switching and modulating. Although the electronic transistor is widely studied and became an indispensable part of our electronic toolkit, the thermal transistor which is the thermal analogue of the electronic transistor is not sufficiently investigated. Nowadays scientists and engineers should consider the subject of thermal flow management more deeply as we encounter challenges such as global warming and energy resources limitations. In addition, thermal computing is seen as a possible alternative for electronic computing that can undergo huge limitation during extreme conditions such as in very high or very low temperature regimes [51]. Therefore, using phonons instead of electrons has a great potential for processing information and it can benefit developing thermal computing [9, 40, 114].

The electronic transistor is basically classified into two categories: bipolar junction transistor (BJT) [72] and field-effect transistor (FET) [115]. BJT is driven by current and it is formed by three elements that are the collector, base and emitter whereas FET is driven by voltage and it

is similarly formed by three elements that are the drain, source and gate.

The first theoretical realization of the thermal analogue of an electronic transistor was made by Li et al. [116]. In this first study, Li et al. [116] modeled these three elements by FK lattices: D, S and G symbolize the drain, source and gate of a classical FET as shown in Fig.1.27(a). Basically, the flux of the electrons can be controlled from the drain to the source according to the applied voltage on the gate in a classical FET. In the same manner, Li et al. showed that the amplification and switch functions (modes) of the thermal transistor are possible using phonon transport by fixing the temperatures of the drain and the source elements while adjusting the temperature of the gate element accordingly [116]. By appropriately adjusting the parameters such as T_S and T_D and changing the value of T_G, Li et al. demonstrated the switching function (mode) of the transistor as shown in Fig.1.27(b). The thermal transistor shows "off", "semi-on" and "on" states by increasing T_G and can be made to behave as an insulator or a conductor [116]. Another function (mode) of the transistor, the modulator, is shown in Figure1.27(c). Similarly, the transistor can act like a modulator by adjusting the parameters properly, meaning that while the heat current through the gate J_G remains almost the same, the heat currents through the source J_S and the drain J_D increase as T_G increases [116].

Li et al. also showed the negative differential thermal resistance (NDTR) phenomenon, which is indeed a criterium to have a transistor effect [116]. Its electronic counterpart, which is negative differential electric resistance, was realized a long time ago [117]. The amplification factor Γ of the thermal transistor can be defined as follows [116]:

$$\Gamma = \left|\frac{\partial J_D}{\partial J_G}\right| = \left|\frac{R_S}{R_S + R_D}\right| \tag{1.27}$$

where the differential thermal resistances R_S and R_D are expressed as $R_S = (\partial J_S/\partial T_O)^{-1}$ and $R_D = -(\partial J_D/\partial T_O)^{-1}$. Generally, heat current increases with increasing thermal gradient, causing R_S and R_D to be positive, but this would cause the amplification factor to be less than 1 and there would be no transistor effect. Therefore, R_S or R_D has to be negative in order to have an amplification, for which Γ would be greater than 1. In their study, Li et al. showed that the conditions necessary for this equation to be satisfied are possible [116].

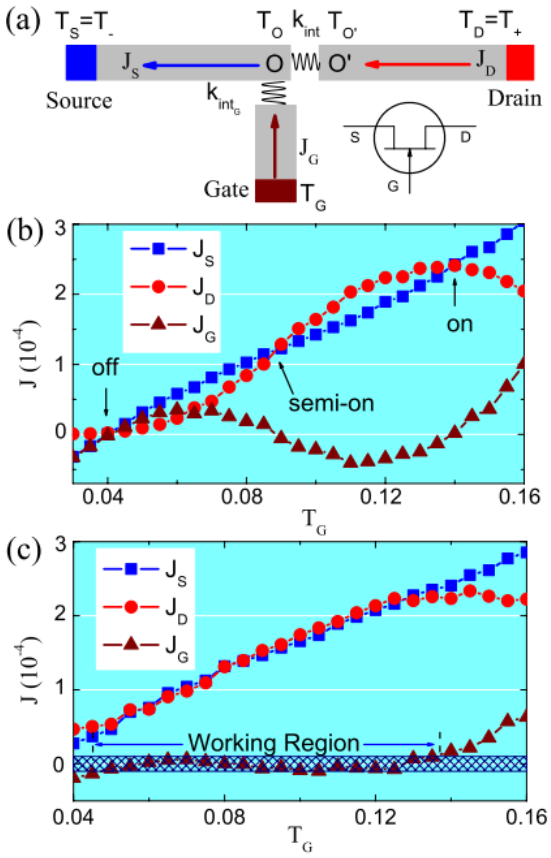

Figure 1.27: The thermal transistor model of Li et al. (a), heat current vs the control temperature for the thermal switch (b) and for the thermal modulation modes (c) [9].

Later, Wang and Li [40] conducted a theoretical study to demonstrate that phonons as heat carriers can be utilized for phononic computing in a similar fashion to electronic computing. The voltages in an electrical logic gate and the temperatures in a thermal logic gate must remain constant at some spots through a power supply [40]. However, a linear device can only provide a similar change relative to the initial change. For example, a change in the voltage across a linear device will similarly change the voltage at another spot [40]. Therefore, Wang and Li developed concepts of different thermal logic gates which need nonlinear devices to operate and they indeed used the thermal transistor as such a nonlinear device [40].

Wang and Li used the thermal transistor, as shown in Fig.1.27(a), to construct logic gates

in their study. They set two temperatures, T_{on} and T_{off}, corresponding to the values 1 and 0 in a digital circuit [40]. In a logic gate, if the input is less than a critical value, the output must be off state T_{off} and vice versa. Wang and Li [40] showed that this is possible with a thermal transistor as shown in Fig.1.28(a). In fact, they achieved a result closer to an ideal repeater by connecting several thermal transistors in series, meaning that the output of one device is the input of the following one, as shown in Fig.1.28(b). Then, they also demonstrated AND and OR gates with a device that has two inputs and one output as shown in Fig.1.29(a). When one input is in off state, the output is also always in off state for AND gate, but when one input is in on state, the output is always in on state for OR gate. Indeed, they showed that this is possible by configuring the inputs accordingly, which Fig.1.29(b) and Fig.1.29(c) show for AND gate and OR gate, respectively [40]. Therefore, although these logic gates are simple models, they clearly showed that thermal logic gates are possible thanks to thermal transistors, which also opens a way for thermal computing.

In 2024, a recent study for a thermal transistor in the conductive regime of heat transfer was made by Wu et al. [118]. They modeled the heat transfer process of the thermal transistor based on the modified Lorentz gas model and studied the amplification and switch functions, and their operating ranges with various parameters such as length, width and thermal conductance of the system [118]. They found that a higher amplification can be obtained by increasing the thermal conductance, but this inversely affects the switch function [118].

Recently, we published a study on a thermal transistor, in which we theoretically analyze the behavior of an oxide PCM based conductive thermal transistor which has an analogy with a bipolar transistor [56]. In fact, this article is an outcome of this thesis and we will detail this work in the relevant Chapter 4. In summary, the base of the transistor is made by VO_2 that induces the NDTR or transistor effect. The thermal transistor functions that are obtained by utilizing VO_2 such as amplification and switching are deeply investigated by individually changing various parameters [56]. We found that while the amplification mostly depends on the ratio of the thermal conductances between the insulating and metallic states and the stiffness of the phase transition, the bistability regime that allows the thermal switching is observed ac-

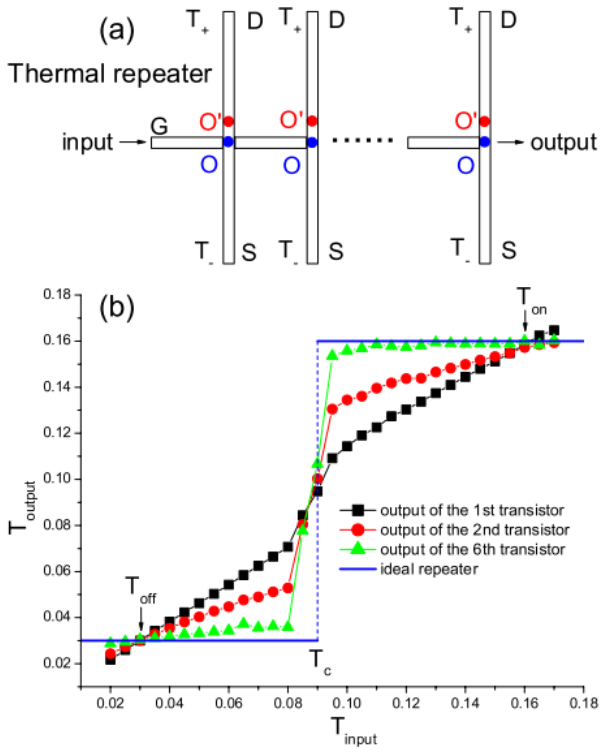

Figure 1.28: The thermal repeater model of Wang and Li (a) and their T_{input} and T_{output} relations (b) [40].

cording to the temperatures of the collector, the emitter and the phase transition of the PCM [56].

The speed of phonons is smaller than the speed of photons by 4 or 5 orders of magnitude and this constitutes one of the main reasons that limit the phonons performance when considering the 3rd modulation mode of the transistor operation [41]. In order to overcome this drawback, Ben-Abdallah and Biehs [41] proposed the near-field radiative thermal transistor (RTT) where heat is transferred by photons instead of phonons, as shown in Fig.1.30(b). In a similar analogy, the RTT was made by three elements, which are the source, drain and gate like a FET, shown in Fig.1.30(a). In their study, an IMT material as the gate with a thin thickness is placed between two media by taking into account the distance that preserves the near-field effect. They used VO_2 for this purpose.

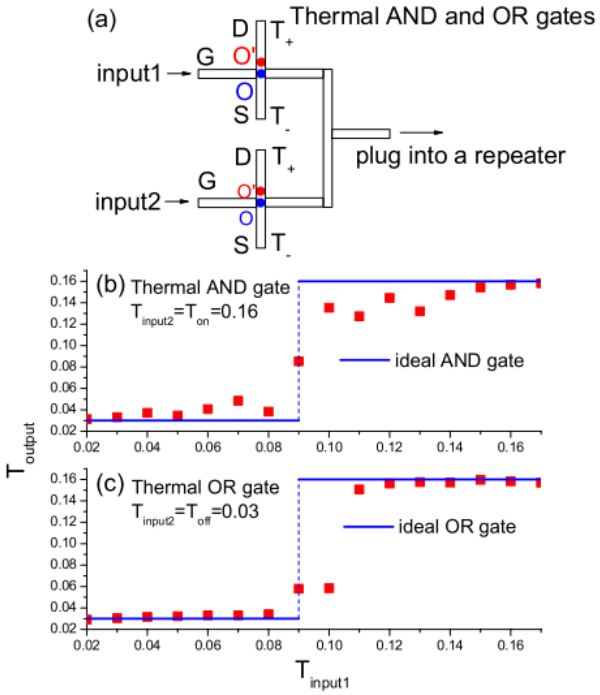

Figure 1.29: The thermal logic gates model of Wang and Li (a), T_{input} and T_{output} relations for thermal AND gate (b) and for thermal OR gate (c) [40].

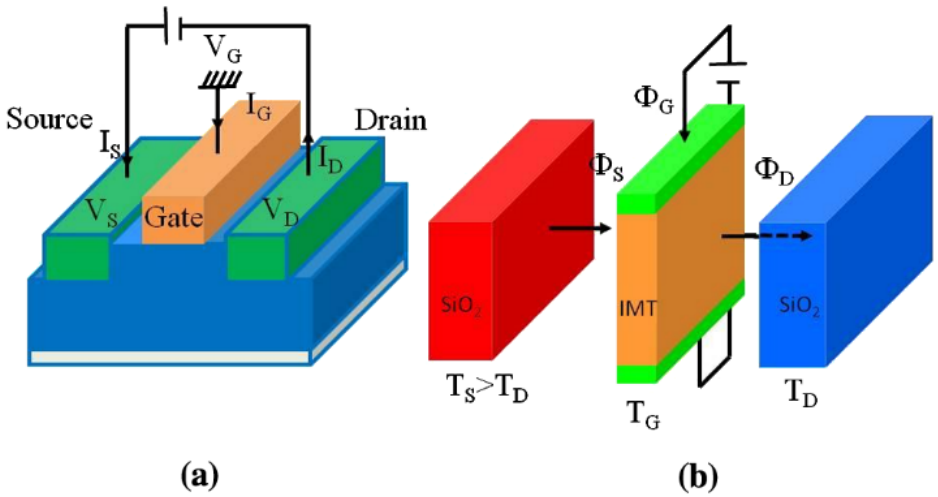

Figure 1.30: Classical field-effect transistor (a) and near-field radiative thermal transistor model of Ben-Abdallah and Biehs (b) [41].

Ben-Abdallah and Biehs [41] examined the model after configuring the inputs such as the thickness of the gate and the distance between the gate and the two other elements by considering the near-field effect. In their study, the source and drain temperatures are set to 360 K and 300 K, respectively [41]. Therefore, the equilibrium temperature, which is the temperature at which the net flux received by the gate ϕ_G is 0, is obtained as 332 K. Thus, they observed that the heat flux exchanged between the source and the drain can be controlled which allows either switching, amplification or modulation, with a small increase of the gate temperature around the critical transition temperature of VO_2 when the temperatures of the source and the drain are fixed [41]. For instance, when T_G increases 10 degrees from the equilibrium temperature, ϕ_S and ϕ_D decrease significantly after the phase transition as seen in Fig.1.31 [41]. Therefore, two operating modes are possible, on and off, before and after the phase transition, respectively [41].

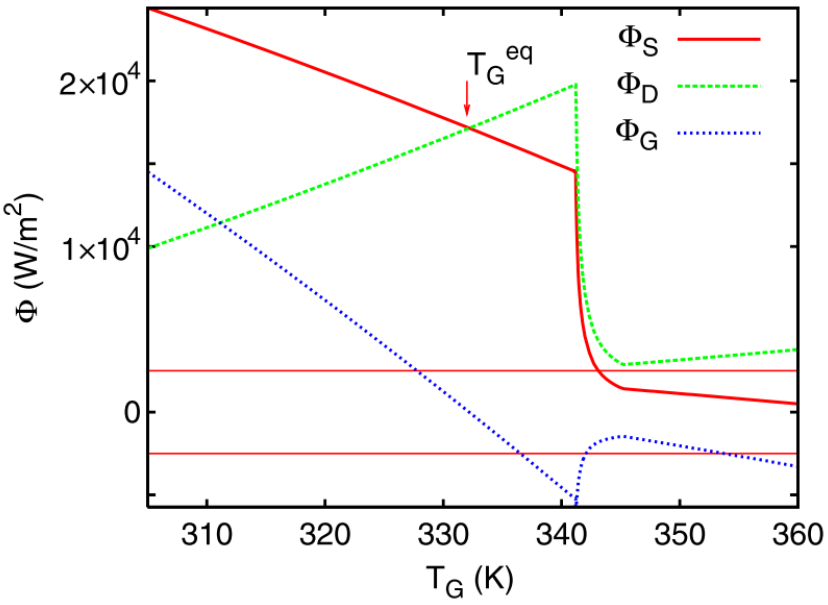

Figure 1.31: The behaviors of the heat flux density profiles ϕ_S, ϕ_D and ϕ_G as functions of the gate temperature T_G [41].

Later, Joulain et al. [42] considered the configuration of Ben-Abdallah and Biehs for the far-field as shown in Fig.1.32(a), because this realization is useful as being an easier alternative for an experimental verification. They showed that the RTT in the far-field is possible with a

PCM that manifests dielectric and metallic behaviors. For this purpose, the far-field RTT is made of two blackbodies and VO_2. They set the temperatures of the blackbodies as 372.5 K and 300 K, which allows an equilibrium temperature of 342 K and makes the thermal transistor close to the phase transition temperature of VO_2 as in the work of Ben-Abdallah and Biehs [42]. The sudden decrease of heat flux densities ϕ_1 and ϕ_2, which correspond to ϕ_S and ϕ_D of the configuration of Ben-Abdallah and Biehs respectively, around the phase transition when there is a slight increase in heat flux density ϕ_3, which corresponds to ϕ_G, results in an amplification during the phase transition region as seen in Fig.1.32(b) and (c) [42].

Then, Prod'homme et al. [43] analyzed the far-field RTT more deeply by using the same configuration, especially concentrating on the switch function (mode) of the thermal transistor. Only one of the two mechanisms of the thermal transistor, which are the amplification and the switch, can be seen at a time. Prod'homme et al. [43] clearly showed these functions (modes) by configuring the inputs accordingly as seen in Fig.1.33(a) and (b), which exhibit the amplification and the switch mechanisms, respectively. The collector temperature of the transistor is 375 K in Fig.1.33(a), which causes amplification during the phase transition of VO_2 as observed before, but when the collector temperature is 365 K, the profile of ϕ_3 changes and actually shows a temperature region of the base that is not attainable. The temperature of the base will always make jumps between the limits of this region. This region corresponds to the NDTR region [43]. Therefore, the transistor exhibits the switch function (mode) as seen in Fig.1.33(b) [43].

In order to understand the switch mechanism of the thermal transistor more deeply, we can examine Fig.1.34, which is the zoomed version of Fig.1.33(b) on the heat flux density ϕ_3 [43]. There are two critical temperatures, which are $T_{c,up}$ and $T_{c,down}$, as represented in Fig.1.34. At these temperatures, $d\phi_3$ approaches a value extremely close to 0, resulting in the amplification factor reaching infinite values [43]. Therefore, it can be said that there are two local extrema, which cause bistability [43]. One of them $T_{c,up}$ is for the heating case and the other one is for the cooling case $T_{c,down}$. Moreover, the region represented by the blue line is the NDTR region where $d\phi_3$ is negative. It should be remembered that the input in the thermal transistor is actually ϕ_3, not the base temperature T. Therefore, when there is a heating, the same heat flux

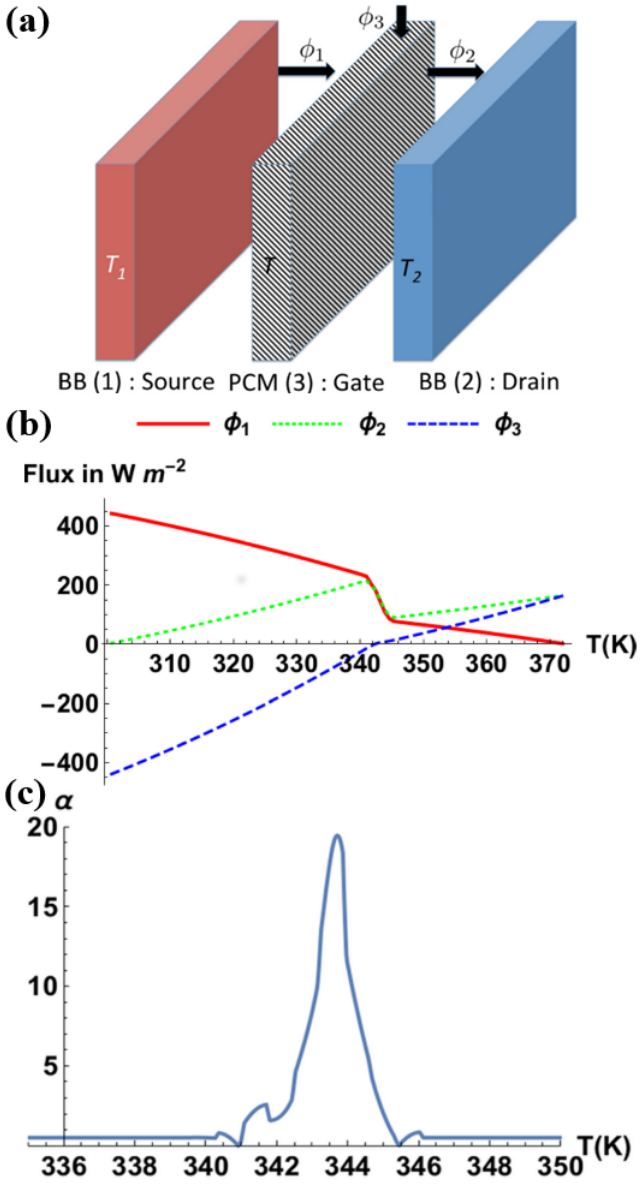

Figure 1.32: Schematic representation of the thermal transistor (a), the behaviors of the heat fluxes density profiles ϕ_1, ϕ_2 and ϕ_3 (b) and the amplification factor (c) as functions of the gate temperature T [42].

density $\phi_{3c,up}$ corresponding to $T_{c,up}$ will be obtained again at a post-critical temperature $T_{pc,up}$. Similarly, when there is a cooling, the same heat flux density $\phi_{3c,down}$ corresponding to $T_{c,down}$ will be obtained at $T_{pc,down}$ [43].

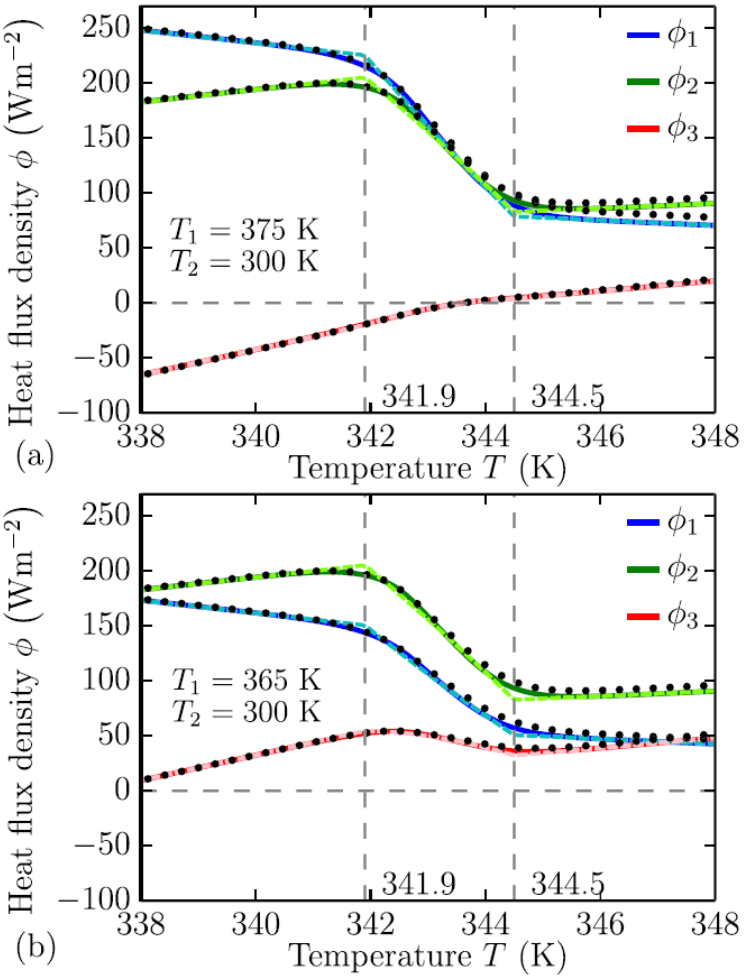

Figure 1.33: The behaviors of the heat flux density profiles ϕ_1, ϕ_2 and ϕ_3 for the amplification (a) and the switch (b) modes as functions of the gate temperature T [43].

The first experimental realization of the far-field RTT was made recently by Li et al. in 2023 [44]. They created a set-up with a similar analogy to a classical FET, which is shown in Fig.1.35(a) [44]. Their far-field RTT model and its experimental setup can be seen in Fig.1.35(b) and (c), respectively [44]. In their set-up, VO_2 thin-film-coated silica substrates for the gate are placed between two blackbody paint coated thermostats for the source and the drain [44]. They showed the core operating functions (modes) of the transistor such as switch and modulation by changing the temperature of the gate while both the source and the drain are fixed to different

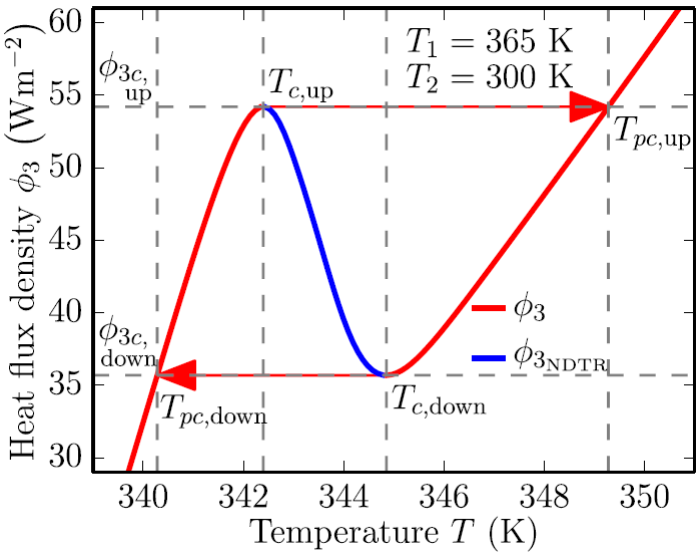

Figure 1.34: Zoomed-in version on the heat flux density ϕ_3, which shows the critical temperatures and their corresponding input heat flux densities. The region shown by the blue line is the NDTR region [43].

temperatures. In fact, they set T_S to a fixed temperature with a thermostat, while T_D is set to the ambient temperature [44]. Then, they used embedded sensors and thermistors to measure the heat fluxes and the temperatures on the medias of the system, respectively [44]. They clearly demonstrated the switch mode of the thermal transistor experimentally by configuring the inputs as $T_S = 357.7$ K and $T_D = 298.1$ K, which results in the equilibrium temperature of 331.9 K. Their measured and calculated heat fluxes are represented by symbols and dashed lines in the figure, respectively, as seen in Fig.1.36(a) [44]. They experimentally showed that when T_G increases, the transistor exhibits NDTR in the region of the phase transition of VO_2, as clearly seen in the inset in Fig.1.36(a) [44]. In fact, they even measured an amplification factor that is higher than 20 as seen in Fig.1.36(b), it should be noted that these measured peak values of the amplification are actually at the gate temperatures that cause extrema values [44].

In the same year 2023, Castelli et al. [119] made another experimental study where they fabricated a centimeter scaled magnetic thermal transistor that can be controlled using a temperature dependent magnetization of a ferromagnetic material on the gate. They observed the

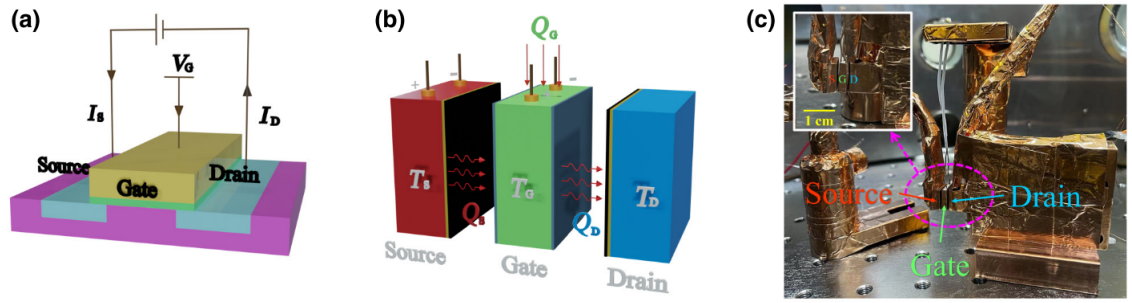

Figure 1.35: Schematic representation of a classical FET (a), the far-field RTT model (b) and its experimental set-up (c) [44].

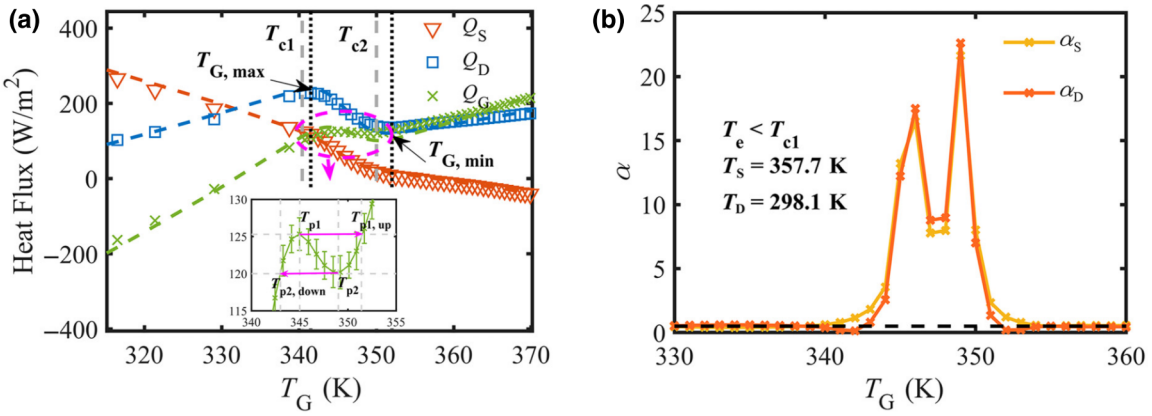

Figure 1.36: The behaviors of the measured (symbols) and calculated (dashed lines) heat flux density profiles ϕ_S, ϕ_D and ϕ_G for the switch mode (a) and the amplification factors (b) as functions of the gate temperature T_G [44].

switching function (mode) of the transistor and even measured an amplification factor that is higher than 30 [119]. Moreover, another important point of the study is that they obtained thermal AND and OR gates, which are the key devices for thermal computing, as highlighted earlier [119]. While the two thermal transistors are connected in series for the AND gate, they are connected in parallel for the OR gate [119]. For AND gate, if both input temperatures T_1 and T_2 are higher than the transition temperature, then both transistors are ON, otherwise the transistor is OFF, corresponding to Boolean 1 and 0, respectively [119]. However, if either the input temperature T_1 or T_2 is higher than the transition temperature, then the output is high, which corresponds to Boolean 1, for the OR gate [119]. Although this work is not based on the

VO_2 phase transition, it is an important experimental realization that proved AND and OR logic gates operations of the thermal transistor in detail.

Recently in 2024, Alonzo-Zapata et al. [120] experimentally measured the emissivity of VO_2 thin films after depositing them on three different substrates, which are c-sapphire, r-sapphire and Si/SiO_2. They obtained different behaviors such as different emissivity variation and hysteresis width. Then, they theoretically studied these measured values on a radiative thermal diode and a radiative thermal transistor. The thermal diode with r-sapphire substrate caused very high thermal rectification particularly [120]. In addition, the radiative thermal transistors with c-sapphire and r-sapphire both show very close maximum amplification values, but at different base temperatures [120].

1.5.3 Thermal memristor

The electrical memristor (short form of the memory resistor) was firstly envisioned by Chua based on symmetry arguments in 1971 and it was seen as the fourth fundamental passive circuit element together with the resistor, the capacitor and the inductor [121]. As seen from Fig.1.37, the resistor relates the voltage (v) versus the electric current (i), the capacitor relates the voltage versus the charge (q) and the inductor relates the magnetic flux (φ) versus the electric current [45]. Therefore, the missing element, the memristor, should relate the magnetic flux versus the charge from this symmetry. Besides these core 4 equations, there are also 2 equations that are indicated in the rectangles in Fig.1.37 [45]. They show that q is the time integral of i and φ is the time integral of v. $M = d\varphi/dq$, which is called memristance, makes a relation between q and φ [45]. If M were constant, it would just be a resistance and would lose its specialty, but M is indeed a function of q. Therefore, this makes the equation nonlinear [45].

The Lissajous characteristic curve is a characteristic property of the memristor, which signifies the existence of the memristor effect. In fact, it cannot be created by the combination of other circuit elements [45]. The pinched Lissajous characteristic curve means that the current and the voltage must intersect at the origin, in other words, when the voltage is 0, the current is also 0 [122]. The Lissajous characteristic curve, as seen in Fig.1.38 from an experimental result of

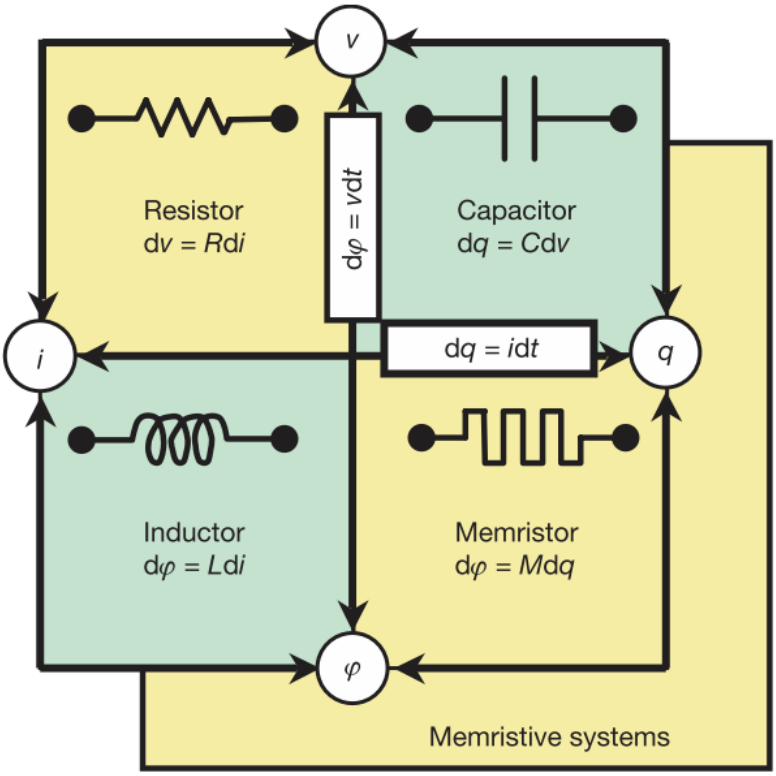

Figure 1.37: Fundamental circuit elements and their symmetry relationships [45].

Pt-TiO_2-Pt device [46], is a figure that shows the relationship between the current flow through the memristor and the applied voltage across it, and their values are 0 at the origin [45].

Nevertheless, it has taken almost 40 years to adopt and concretize the memristor concept. Strukov et al. made an experiment by using TiO_2, shown inside Fig.1.38, and the first realization was performed by them in 2008 [45]. Basically, a semiconductor film has two distinct regions with high and low concentrations of dopants, resulting in high and low resistances, respectively. The charged dopants move when they are excited by an electric field accordingly. Thus, this causes the changes of the boundary between doped and undoped concentrations in the system and varies the resistance [45]. This is the fundamental difference of the memristance of a memristor from the resistance of a resistor, because the resistance of a resistor is fixed, but a memristor can retain its last internal state even the external stimuli is stopped, and when reapplied, it can resume from its last internal state. In fact, this is the reason that gives the memristor a memory

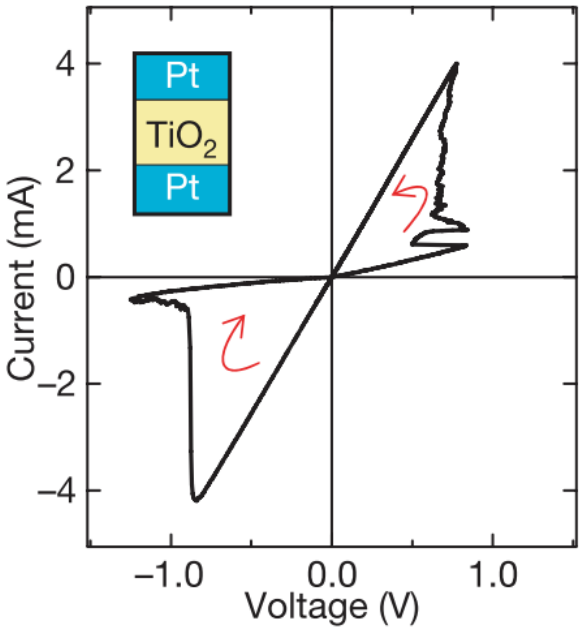

Figure 1.38: The voltage-current relationship of Pt-TiO_2-Pt device [45, 46].

feature [123, 124]. As the memristor device is minimized to the nanoscale, the voltage-current characteristic behavior can become pronounced with a small applied voltage, because even a small applied voltage has a larger effect on the dopant, which can lead to a huge change in the resistance [45].

There are just very few studies on the thermal counterpart of the memristor. In 2017, to pursue the establishment of full thermal analogues to all electronic elementary components, Ben-Abdallah theoretically proposed the existence of the conductive thermal memristor by exploiting the thermal hysteresis of the thermal conductivity of VO_2 [47]. He examined the thermal memristor that is made by VO_2, shown as a small figure inside of Fig.1.39(a), under quasi-steady-state conditions by applying modulated BCs (T_R<T_L). According to the variation of the temperature difference at the boundaries, ΔT, the boundary between the two phases of VO_2 moves at the device, and this causes a change in the thermal resistance similar to what is observed due to the drift of dopants in the electrical memristor. The heat flux and the temperature are the equivalent thermal quantities of the electronic quantities which are current and voltage, respectively [47]. Thus, the thermal memristance can be defined as $M_t = \Delta T/\varphi$ [49].

The temperature profile when $T_L = 370$ K and $T_R = 330$ K can be seen in Fig.1.39(a), and the behavior of the thermal resistances and the heat fluxes as functions of the change of temperature difference when T_R is 330 K can be seen for both heating and cooling processes in Fig.1.39(b) and (c), respectively [47]. As can be seen from Fig.1.39(a) and (b), there is a nonlinear temperature profile across the conductive thermal memristor as a result of the fact that the interface thermal resistance between two phases is temperature-dependent. In fact, the effects of these on the heat fluxes are shown in Fig.1.39(c), where we also see a nonlinear behavior. Ben-Abdallah theoretically showed that the conductive thermal memristor is possible by using metal-insulator phase change materials and conceived neuromorphic networks by using it, which is detailed in the potential applications section [47].

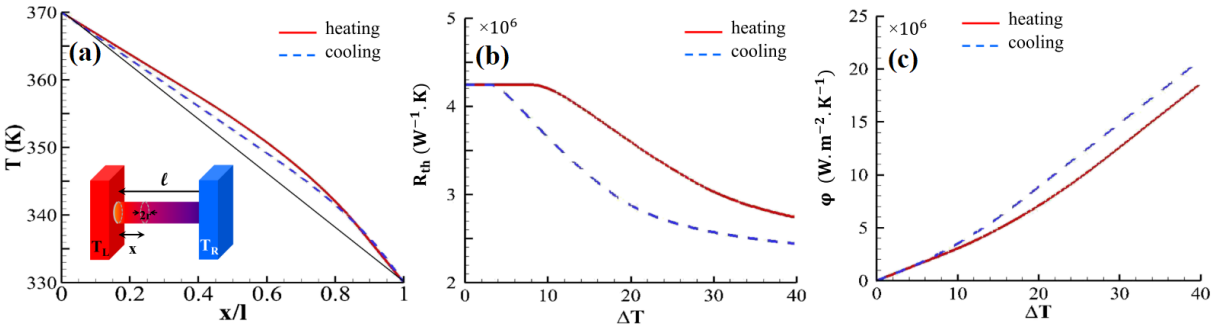

Figure 1.39: Temperature profile across the system according to the heating and cooling processes when T_L and T_R are 370 K and 330 K, respectively, and the sketch of the thermal memristor (inside of the figure) (a), the thermal resistance (b) and heat flux through the system according to the temperature difference ΔT variation when T_R is 330 K [47].

Although Ben-Abdallah showed the existence of the conductive thermal memristor, the Lissajous characteristic curve is not investigated in his study. Yang et al. [48] conducted a theoretical study and examined a micrometer-sized conductive thermal memristor made of a solid-solid phase change material. They made an examination according to the characteristics of tungsten (W) doped VO_2 under quasi-steady-state conditions by changing various parameters such as thermal conductivity ratio of the phases, temperature amplitude of the boundary conditions,

and they revealed it is possible to obtain the Lissajous characteristic curve. They arranged the sinusoidal boundary conditions so that when one boundary condition is at high temperature, the other is at low temperature [48]. The behaviors of the Lissajous characteristic curves can be seen with different temperature amplitudes when the thermal conductivity ratio is fixed and with different thermal conductivity ratios when the temperature amplitude is fixed in Fig.1.40(a) and (b), respectively [48]. As can be seen from the figures, when the temperature amplitude is too low to produce a phase transition cycle or when the thermal conductivity ratio is quite low, it shapes a straight line instead of a Lissajous characteristic curve [48]. However, when they continue to increase, the Lissajous characteristic curve will reach saturation and no change will be observed after a point [48]. Thus, there is a need of the phase transition to obtain the Lissajous characteristic curve, but their values are also important for the shape of this curve.

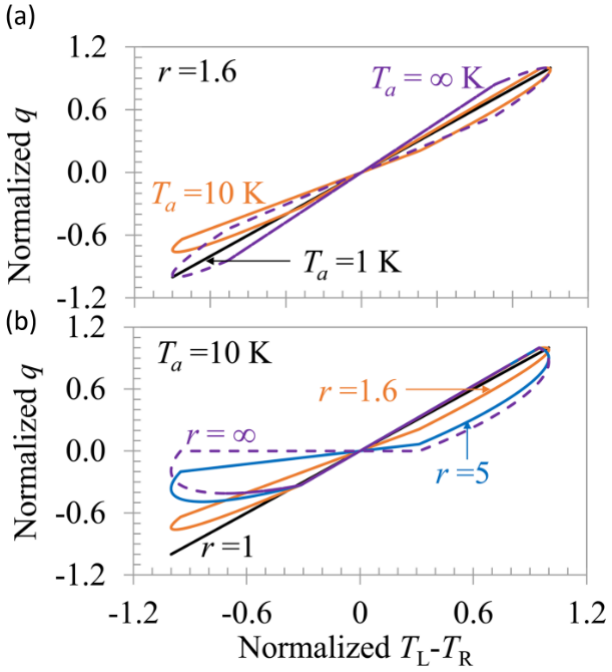

Figure 1.40: The Lissajous characteristic curve with different temperature amplitudes T_a when the thermal conductivity ratio r is fixed (a) and with different thermal conductivity ratios when the temperature amplitude is fixed (b). T_L and T_R symbolize the temperatures on the left and right sides of their investigated thermal memristor, respectively [48].

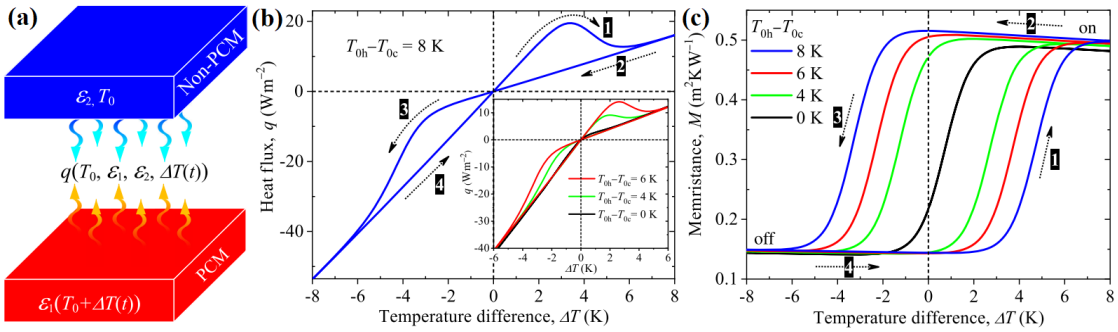

Figure 1.41: The sketch of the radiative thermal memristor (a), the Lissajous characteristic curves (b) and the thermal memristances (c) with different hysteresis. T_0, ΔT, ε_1 and ε_2 symbolize the steady-state temperature, the temperature difference modulated in time t between PCM and non-PCM blocks, the emissivities of the PCM and non-PCM, respectively [49].

The first radiative thermal memristor was theoretically presented by Ordonez-Miranda et al. [49] in 2019. They conceived a radiative thermal memristor composed of VO_2 and a non-PCM as shown in Fig.1.41(a) [49]. In their system, the non-PCM is a blackbody, but the emissivity of the PCM varies with respect to temperature with a characteristic hysteresis. The temperature of the side composed of VO_2 varies sinusoidally, while the non-PCM has a constant temperature [49]. Therefore, the exchanged heat flux varies with temperature difference with time. They obtained the Lissajous characteristic curve under these conditions as seen in Fig.1.41(b) [49]. Moreover, the behavior of thermal memristance produced according to the Lissajous curves with respect to the temperature difference is reported in Fig.1.41(c) [49]. As seen from both figures, the parts 1 and 3 are where VO_2 undergoes phase transition and causes nonlinear behaviors [49]. When the hysteresis width, where VO_2 exhibits an 8 K shift between the heating and cooling processes as mentioned before, decreases, the area between the curves 1 and 3 or 2 and 4 decreases as well and even they disappears if there is no hysteresis [49].

1.6 Potential applications

One of the experimentally validated areas for utilizing thermal diodes is solar energy harvesting. Although solar energy has a great potential as an energy source, electricity generation is highly dependent on daytime. Westwood [125] and Zhao [126] conducted a master's degree project at

the University of California, Berkeley in 2015 by considering this issue to improve the efficiency of solar energy generation. While Westwood [125] conducted an experimental study, Zhao [126] focused on the numerical approach. They combined thermal diodes and thermal energy storage with a thermoelectric generator (TEG) as seen in Fig.1.42(a) and (b), which represent the system during the daytime and at night, respectively [50]. As seen in the scheme, the system consists of a thermal diode bridge with two thermal diodes, two thermal storage units and a TEG. As the input temperature, which represent the solar variation, is higher than the temperature of the thermal storage unit 1 thanks to the solar energy during the daytime, the system allows the heat flow in the clockwise direction, which causes the temperature of the thermal storage unit 1 to increase, but the thermal storage unit 2 is blocked. However, there is no input temperature at night. In fact, although the thermal storage 1 has a higher temperature than the ambient temperature, the thermal diode prevents some heat loss from the system. Therefore, the temperature difference between both sides of the TEG can be compensated and electricity production continues. The temperature variations of the sinusoidal input temperature, ground temperature, the temperatures of the thermal storage units 1 and 2 are reported in Fig.1.42(c) [50]. As seen from the figure, they achieved to keep the temperature difference between the storage units similar thanks to the thermal diode bridge, and the comparison of the power electricity output with and without the thermal diode bridge are reported in Fig.1.42(d) [50]. We see a clear inequality between the 2 configurations.

Buildings are another application area of the thermal diodes. They have potential to reduce energy consumption. For instance, Pugsley et al. [127] conducted an experimental study in 2019 and examined a planar liquid-vapour thermal diode that can benefit the building envelope for climate control. Their thermal diode provides different heat transfer rates in the forward and backward directions thanks to latent heat transfer, which only occurs in the forward direction. In 2023, Zhao et al. [128] also conducted an experimental study. They investigated jumping-droplet thermal diodes for building envelope performance and examined this thermal diode for the roofs of the buildings, which they achieved energy savings up to 22.11% according to their simulations [128]. In the same year, Wu et al. [129] conducted simulations in various climates in China to examine a composite wall that involves a thermal diode for office buildings and achieved

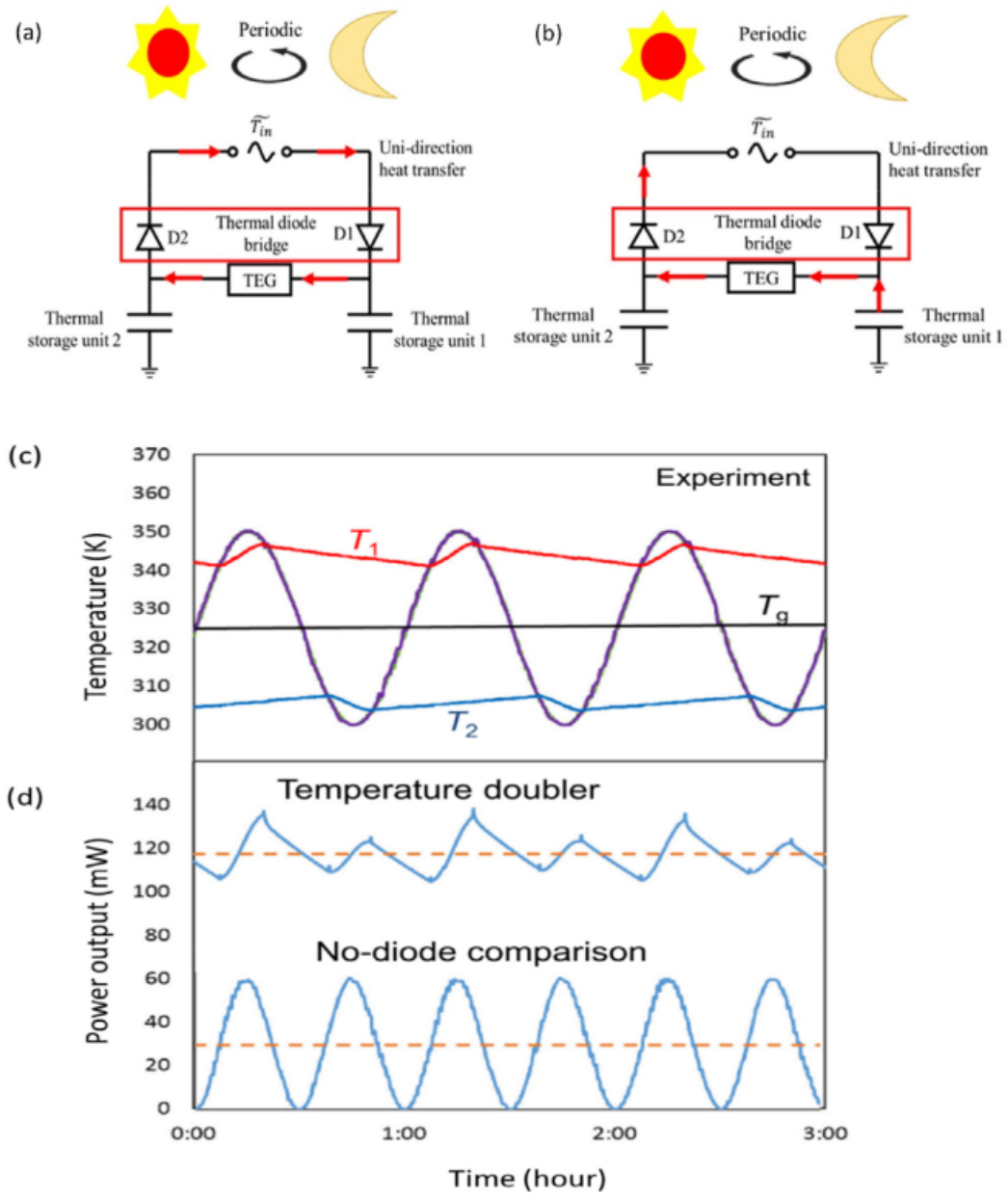

Figure 1.42: Schematic representation of the thermal energy storage system during the daytime (a) and at night (b). The temperature variations of the input temperature (purple solid line), the thermal storage units 1 (T_1) and 2 (T_2), and ground temperature (black solid line) (c). The power electricity output with and without the thermal diode bridge (d) [50].

energy savings up to 69.3%. Recently, another experimental study is made on thermal diodes for building applications by Castelli et al. [130]. They investigated an insulation for buildings

based on magnetic thermal diode, which can provide passive energy saving. They examined this system in different climate zones of the US and achieved a reduction in HVAC thermal loading. The reduction reached as high as 47% [130].

Another potential area of the thermal diodes application is caloric refrigeration systems, which is a strong alternative to vapor-compression refrigeration systems [50]. In caloric refrigeration systems, there is a caloric material which changes its temperature under external stimuli such as a magnetic field, applied voltage or electric field. The two schematic representations from the review article of Wong et al. [50] that is based on the articles [131] and [132], which represent the caloric refrigeration systems with and without a working fluid in Fig.1.43(a)-(b), and Fig.1.43(c)-(d), respectively, can help to explain the advantage of using thermal diodes. Two thermal diodes placed on both sides of the caloric material can be seen in Fig.1.43(a) and (b) when the caloric material is at hot and cold temperatures, respectively [50]. The temperatures of the portions T_1, T_2, T_3 and T_4 are in order from hot to cold, which means that while T_1 has the highest temperature, T_4 has the lowest. The thermal diode strongly allows the forward heat flow in this system due to its working nature and this helps the heat to flow from the hot caloric material to the working fluid as seen in Fig.1.43(a), but when the caloric material is cold, it helps heat absorption from the working fluid for the caloric material as seen in Fig.1.43(b) [50]. Another caloric refrigeration system, which does not include any working fluid, can be seen in Fig.1.43(c) and (d) when the caloric material is cold and hot, respectively [50]. Two thermal diodes, each with the forward heat flow direction upwards, are placed between the heat sink and the caloric material and between the caloric material and the heat source. As expected from the natural working principles of thermal diodes, they allow the heat flow from the heat source to the caloric material as seen from Fig.1.43(c), while it blocks the heat flow on the other side. Oppositely in Fig.1.43(d), when the caloric material has a high temperature, it allows the heat flow from the caloric material to the heat sink [50].

The thermal logic gates are another application area of the thermal components that we investigate. Thermal diodes and thermal transistors are the main cornerstones of them. Although thermal computing can still be considered to be in its initial state, it has a great potential to

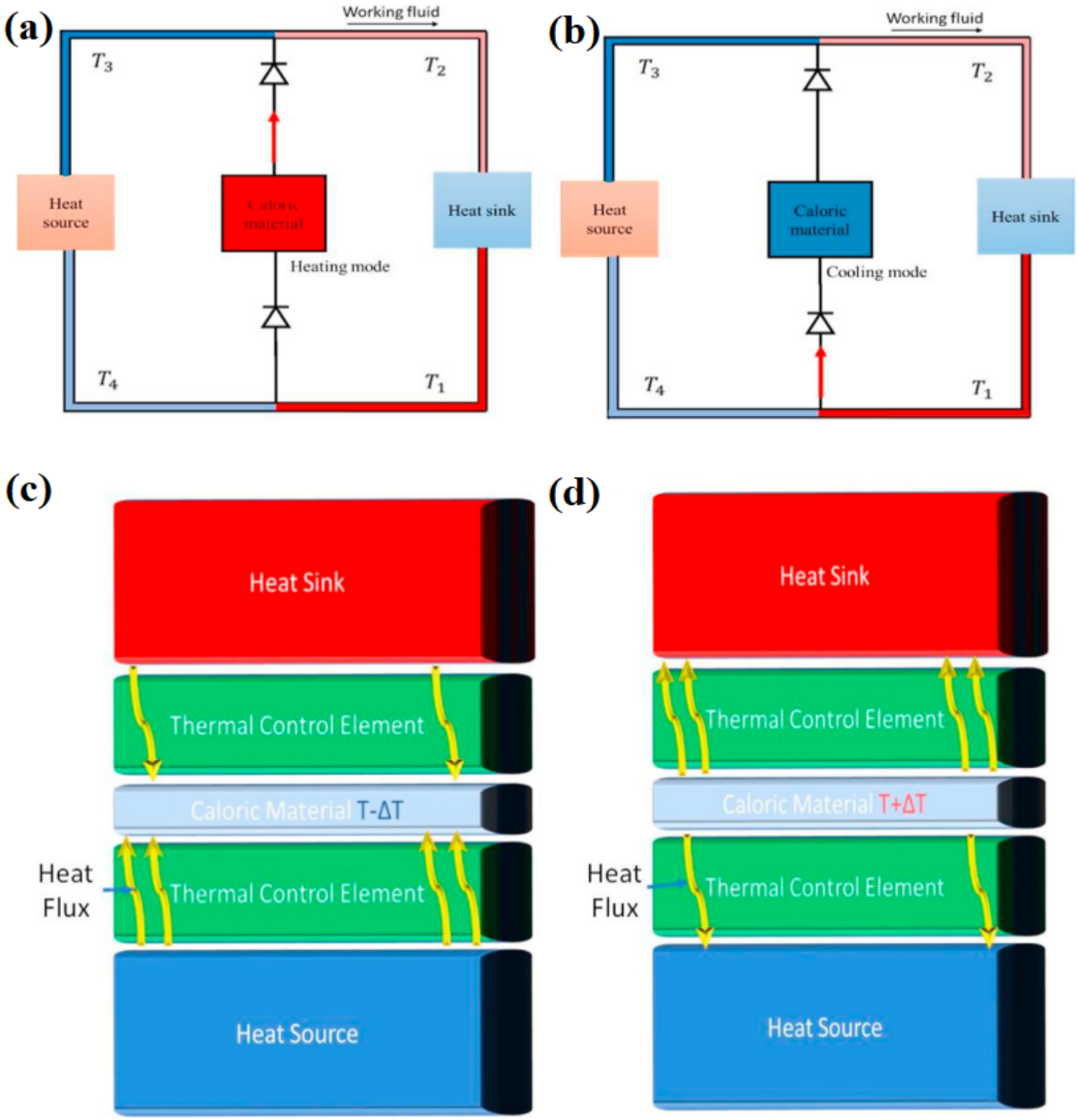

Figure 1.43: Schematic representations of the caloric refrigeration systems with thermal diodes with (a)-(b) and without a working fluid (c)-(d) [50].

be an alternative for electronic computing as mentioned before. As previously outlined in the thermal transistor section, Wang and Li [40] conducted a pioneering study on thermal transistors and used them to construct logic gates, and successfully showed that thermal logic gates

are theoretically possible with thermal transistors. Furthermore, using a radiative thermal transistor, Ben-Abdallah and Biehs [133] theoretically obtained NOT, OR and AND thermal logic gates composed of SiO_2 and VO_2 in the near-field regime. The study of Castelli et al. [119] in 2023, which were outlined in the transistor section in detail, can be given as an example of the experimental verification of the thermal logic gates with thermal transistors, even though they are not based on phase transition materials.

Moreover, the study of Hamed et al. [51] can be given as a remarkable example for the potential application of the thermal diodes for the thermal logic gates, because Hamed and Ndao [134] pursued their system in their theoretical study and conducted an experimental analysis after fabrication of it in 2020. Hamed et al. [51] theoretically modeled NOT, OR and AND thermal logic gates, and showed a thermal calculator by a near-field radiative thermal diode that is coupled by MEMS thermal actuation and the illustration of their thermal diode system can be seen in Fig.1.44 [51]. In Fig.1.44(a) and (b), the thermal diode is in its initial form when the top parts is at low and high temperatures, respectively [51]. Later, when the top block is at low temperatures during the reverse bias as seen in Fig.1.44(c), the top block moves away and increases the distance between the blocks, which causes a decrease of the heat flow [51]. On the other hand, when the top block is at high temperatures during the forward bias as seen in Fig.1.44(d), the distance between the blocks decreases, which causes an increase of the heat flow due to the near-field regime [51]. The detail of their thermal diode system and its fabrication can be found in [134]. They succeeded to obtain AND and OR thermal logic gates with this thermal diode system by placing them between a heat source and a heat sink with a conduction thermal resistance, which is connected to a heat source or a heat sink depending on the AND or OR logic gates, respectively [134].

A potential area where expectations are high for the thermal diodes is thermal management of electronic components, especially considering that they are becoming smaller and more widespread in the micro-scale [50]. As a general rule, 10 °C increase in temperature can double the probability of a failure of an electronic system, and even considering the possible hot spot formation in an electronic component, thermal management for cooling purposes becomes more

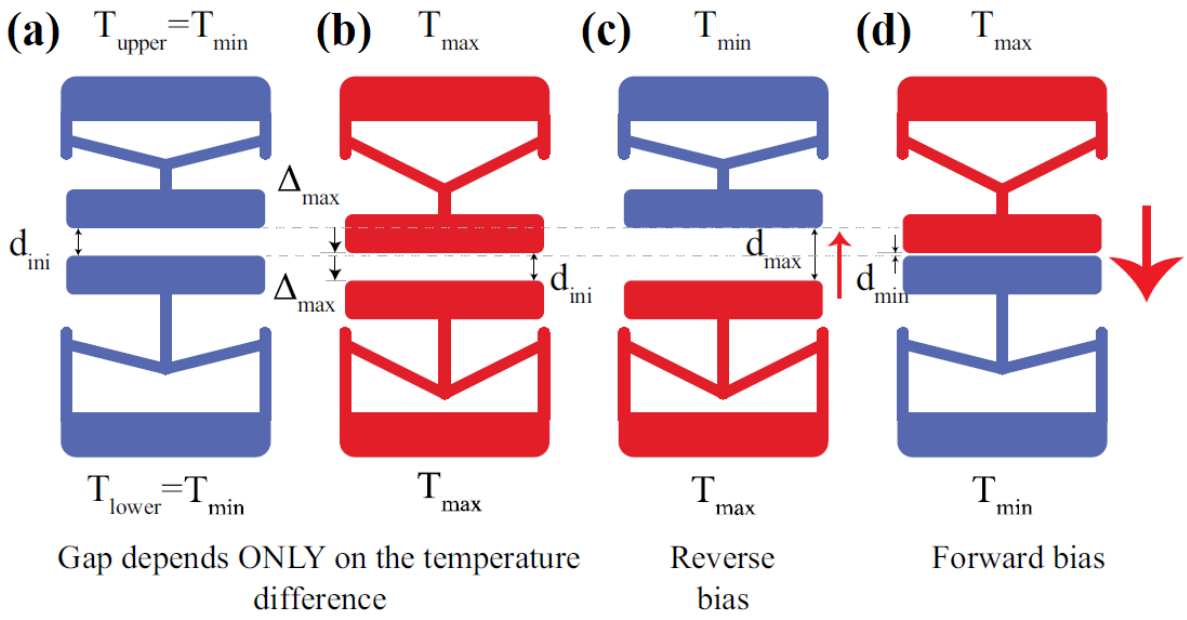

Figure 1.44: Schematic representation of the near-field radiative thermal diode. Initial form of the thermal diodes when the top part is at low (a) and high (b) temperatures. Reverse (c) and forward (d) biases that cause increased and decreased gap between the blocks, respectively [51].

important [50, 135]. There are numerous studies examining the asymmetric behavior of thermal diodes for the heat transfer as widely outlined in the thermal diode review section. This feature can actually be one of the expected solutions for overheating of the micro-sized electronic components. For example, the heat flow to the hot spot that can cause a system failure can be blocked thanks to thermal diodes and this actually prevents excessive temperature rise of the electronic component [50]. Moreover, thermal diodes are expected to offer some possible solutions for thermal management of space systems such as spacecrafts or satellites that both encounter unusual environmental conditions such as extreme temperatures or sudden temperature changes. For example, radiative thermal diodes are seen as a promising solution to deal with thermal management issues in this harsh environment, as they can operate in a vacuum environment [50].

The application areas of the electrical memristor have been widely investigated since its concretization by Strukov et al. in 2008, and it shows a very promising potential for various

areas such as information storage, neuromorphic computing, informatics, spintronics and memory [123, 124, 136, 137, 138]. For instance, Pershin et al. used an electrical memristor to model the learning behavior of amoeba, which can memorize and react to the periodical changes of outside environment even though these are at a primitive level [136]. In addition, a recent review study that has numerous studies related to the electrical memristor for simulating human senses can be found in [123]. However, although the thermal counterpart of the electrical memristor which is the thermal memristor has a similar potential, the work done in this area is very little. Ben-Abdallah conceived neuromorphic networks by using the thermal memristors [47]. He connected two thermal memristors as seen in Fig.1.45(a). While the first one acts as an input signal and its temperature changes with time, the second one has a fixed temperature [47]. The first input is directly the temperature of the first memristor, while the second input is its time derivative [47]. The two thermal memristors are both connected to an output and the output temperature varies

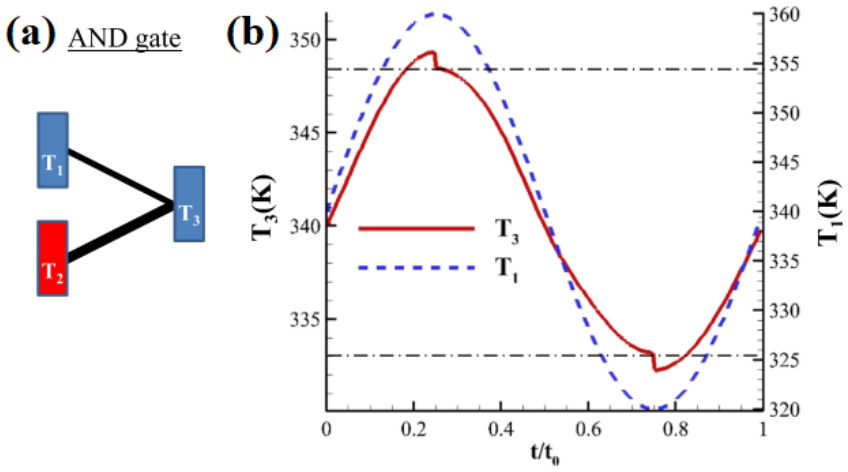

(c)

T_1	dT_1/dt	T_3
$\lvert T_1 - T_2\rvert > \tilde{T}_1 \rightarrow 1$	$dT_1/dt > 0 \rightarrow 1$	$\lvert T_3 - \bar{T}\rvert > \tilde{T}_3 \rightarrow 1$
$\lvert T_1 - T_2\rvert > \tilde{T}_1 \rightarrow 1$	$dT_1/dt < 0 \rightarrow 0$	$\lvert T_3 - \bar{T}\rvert < \tilde{T}_3 \rightarrow 0$
$\lvert T_1 - T_2\rvert < \tilde{T}_1 \rightarrow 0$	$dT_1/dt > 0 \rightarrow 1$	$\lvert T_3 - \bar{T}\rvert < \tilde{T}_3 \rightarrow 0$
$\lvert T_1 - T_2\rvert < \tilde{T}_1 \rightarrow 0$	$dT_1/dt < 0 \rightarrow 0$	$\lvert T_3 - \bar{T}\rvert < \tilde{T}_3 \rightarrow 0$

Figure 1.45: Schematic representation of the constructed AND gate (a), the first memristor temperature T_1 and the output temperature T_3 (b), and the AND gate table with the first input T_1, the second input (the time derivative of T_1) and their output ($\tilde{T}_1$ and $\tilde{T}_3$ in the table are the horizontal dashed lines that show the temperatures where the phase transition occurs) (c) [47].

with respect to their temperatures as seen in Fig.1.45(b) [47]. When there is a phase transition, there is a sharp change in the output temperature as shown by the dashed horizontal line, which actually helps to set Boolean 1 and 0 for the AND gate [47]. The AND gate relationship of the two inputs and output generated by two thermal memristors can be seen in the table in Fig.1.45(c) [47].

1.7 Motivation and objective of the study

Manipulating heat transfer and controlling the temperature of a system constitute the two key aspects in thermal management. They have become crucial nowadays due to emerging problems such as global warming, energy crisis and system safety [76]. Thermal management is a helpful tool to tackle some problems that arise due to a sudden rise or an undesired change of the temperature of a device which undoubtedly affect the system performance and longevity. We can name a few examples such as hot spots in electronic circuits [135], safety issues in photovoltaic panels [139], overheating and reduction of lifetime of batteries [140] or mismatch problems between energy demand and energy supply of thermal storage systems [141]. As can be seen in our detailed literature review, the thermal diode, the thermal memristor and the thermal transistor can be given as three illustrative examples which can benefit the manipulation of the heat flux and control the temperature to overcome these issues to some extent [47, 73]. Moreover, thermal computing is seen as a possible alternative for electronic computing that can undergo huge limitations during extreme conditions such as in the very high or very low temperature regimes [51]. Therefore, the thermal transistors, i.e. using phonons or photons instead of electrons have a great potential for processing information and it can benefit developing thermal computing [9, 40, 114].

In this thesis, we examine these 3 thermal devices; the thermal diode, the thermal memristor and the thermal transistor in detail. As seen in the literature review, there are many studies that examine the thermal rectification of thermal diodes in steady-state conditions and the interest for transient analysis is increasing. However, we have not encountered any prior work that studied thermal diodes while considering properties of VO_2 in full aspects under transient conditions. Even less work has been done on the thermal memristors and those that have been

done considered their analysis under quasi-steady-state conditions. Thus, the capacitive effect was omitted. For the thermal transistors, although there are many studies that examine the thermal transistor concept in the literature, the majority of it is related to the radiative regime of heat transfer; either the near-field or the far-field as well as the quantum framework. Indeed, to the best of our knowledge, except the pioneer work of Li et al. [116] and the recent work of Wu et al. [118], no other macroscopic concept of a thermal transistor in the conductive regime of heat transfer has been presented. Therefore, the objective as well as the novelty of the works in this thesis is to investigate these three thermal components while considering the full properties of VO_2. First, we will present our work on the thermal memristor in Chapter 2, then move on to the thermal diode in Chapter 3, and finally finish with the thermal transistor in Chapter 4.

Résumé du Chapitre 1

Nous commençons le Chapitre 1 en donnant un aperçu général du transfert de chaleur et en détaillant le phénomène de conduction de la chaleur dans un solide, tout en tenant compte du fait que nos recherches dans cette thèse sont menées dans le régime conductif. Nous expliquons les propriétés thermiques, telles que la conductivité thermique et la chaleur spécifique, d'un point de vue général, puis nous abordons également ces notions à la lumière des caractéristiques du dioxyde de vanadium (VO_2), étant donné qu'il s'agit du matériau étudié dans cette thèse. Le VO_2 présente une transition de premier ordre métal-isolant (TMI) autour d'une température critique de $T_o = 341$ K [63]. Sa structure cristalline se transforme d'une structure monoclinique diélectrique à une structure tétragonale-rutile métallique après avoir passé la température critique, et il manifeste différentes propriétés thermiques, électriques et optiques [7, 142]. Bien que plusieurs études théoriques et expérimentales aient été menées pour comprendre les mécanismes de transition du VO_2, il n'existe pas actuellement de compréhension complète ou de consensus sur ce processus [64]. Deux théories principales tentent d'expliquer ce processus : les théories de Mott-Hubbard et de Peierls [2]. Mott a proposé un modèle expliquant que la transition TMI se produit en raison de l'interaction électron-électron et que la structure des bandes d'énergie change lors de la transition [65]. Cependant, Peierls a proposé qu'elle se produit également en raison de l'interaction électron-phonon (électron-réseau) [66]. En effet, on pense que les deux transitions, structurelle et électronique, se produisent en même temps, ce qui rend difficile la compréhension de la logique qui sous-tend la transition du VO_2 [64].

Le dioxyde de vanadium et ses propriétés thermiques

La conductivité thermique du VO_2 peut être décrite à l'aide de l'Éq.1.16, formulée dans l'étude d'Ordonez-Miranda et al. [35]. Oh et al. [7] ont mesuré expérimentalement les valeurs de la conductivité thermique du VO_2 dans les phases diélectrique et métallique et ont trouvé qu'elles étaient respectivement de 3.6 W m^{-1} K^{-1} pour k_d et de 6 W m^{-1} K^{-1} pour k_m. De plus, la valeur de β, qui est la pente de transition de phase du VO_2, est de 1.6 K^{-1}. Cette valeur correspond au meilleur ajustement des données expérimentales à l'aide de l'Éq.1.16 [35]. De

plus, T_o prend les valeurs T_{oh} = 342.9 K et T_{oc} = 334.9 K pendant les processus de chauffage et de refroidissement, respectivement, ce qui entraîne un effet d'hystérésis de 8 K pour le VO_2 entre ces processus [35]. Par conséquent, T_{oh} et T_{oc} représentent les températures de transition de phase des processus de chauffage et de refroidissement, respectivement. Les comportements de la conductivité thermique du VO_2 en fonction de la température sont présentés dans la Fig.1.3.

La chaleur spécifique à pression constante du VO_2 varie fortement au cours de la transition de phase et comme indiqué dans [5], elle peut être décrite à l'aide de l'Éq.1.17. La densité du VO_2 varie en fonction de sa structure cristalline, mais par souci de simplicité, nous la prenons égale à 4670 kg m^{-3} dans l'étude [143]. La chaleur latente L_n est égale à 51.45 kJ kg^{-1} pour le processus de chauffage du VO_2 [61] et nous supposons la même valeur pour le processus de refroidissement. Comme expliqué dans l'étude d'Ordonez-Miranda et al. [5], le deuxième terme du côté droit de l'Éq.1.17 peut être négligé. Les comportements en température de la capacité thermique spécifique de VO_2 sont présentés dans la Fig.1.4.

Méthode de l'enthalpie

La méthode de l'enthalpie constitue une approche répandue pour la résolution numérique des problèmes de transfert de chaleur impliquant un MCP [69]. Cette approche a été proposée pour la première fois par Eyres dans le cadre de la résolution des problèmes dont les propriétés thermiques varient avec la température [70]. Dans notre étude, l'Éq.1.19, qui représente l'équation générale unidimensionnelle de diffusion de la chaleur exprimée en termes d'enthalpie, est résolue pour le cas du VO_2. En effet, il est possible de discrétiser l'Éq.1.19 dans le temps et dans l'espace à l'aide de schémas implicites ou explicites. Ainsi, la température correspondante de l'enthalpie peut être déterminée aux étapes temporelles suivantes et inversement.

Thermotronique et ces composants thermiques

Il existe deux principaux processus de transport d'énergie dans les solides : la conduction électrique et la conduction thermique [9]. Ces deux processus de transport pourraient être tout aussi importants pour le traitement de l'information et constituer un outil utile pour le pro-

grès technologique. Malheureusement, ce n'est pas encore le cas. Bien que l'aspect électronique (électrique) de ces processus de transport d'énergie ait fait l'objet de nombreux travaux depuis l'invention du transistor électronique par Bardeen et Brattain en 1948 [72], la contrepartie de la conduction thermique n'a pas reçu suffisamment d'attention, car on pensait généralement que les phonons n'étaient pas utiles pour le transport et le traitement de l'information en raison de leur nature [9]. Cependant, des études ont montré que les phonons peuvent être manipulés et même, contrairement à ce que l'on croyait, qu'ils peuvent transporter de l'information. Cela a en effet ouvert le monde à la possibilité d'utiliser la phononique, la technologie homologue de l'électronique, et de rendre possible certains concepts tels que l'informatique thermique [9]. Cela a également montré que la thermotronique, en tant que domaine de recherche émergent se concentrant sur le développement d'analogues thermiques des composants électroniques de base, présente un potentiel considérable. Dans le cadre de cette thèse, une analyse approfondie de la littérature pertinente a été conduite. Cette analyse s'est concentrée sur trois composants thermiques, à savoir la diode thermique, le transistor thermique et le memristor thermique, qui font l'objet de notre étude.

Diode thermique

La rectification thermique est un processus qui se produit dès que les propriétés thermiques d'un dispositif dépendent de la température, de sorte que le flux de chaleur dépend de la direction du gradient de température entre les bornes du dispositif [73]. Starr a étudié le sujet pour la première fois en 1936 [75]. En ce qui concerne le transfert de chaleur par conduction, un simple croquis d'un redresseur thermique ou d'une diode thermique est présenté à la Fig.1.12 [9]. Comme le montre le schéma, le dispositif devrait permettre le transfert de chaleur dans une direction, mais le bloquer dans l'autre lorsque les températures s'échangent [9].

Dans la littérature, les études disponibles se sont principalement concentrées sur l'étude de la rectification thermique conductive dans des conditions stationnaires. Néanmoins, les études sur la rectification thermique conductive dans des conditions transitoires sont rares. Herrera et al. [38] ont publié la première étude relative aux diodes thermiques dans ce type de conditions. Ils ont calculé la rectification thermique de diodes thermiques dont la conductivité thermique

varie linéairement avec la température en appliquant la méthode des différences finies. Ils ont également introduit un facteur de rectification thermique dépendant du temps et ont observé un facteur de rectification plus élevé dans des conditions transitoires [38]. Ensuite, Klinar et al. [96] ont réalisé une étude numérique pour étudier l'influence d'une diode thermique dans un dispositif de réfrigération magnétocalorique. Ils ont analysé différents profils de conductivité thermique en fonction de la température et ont découvert que la rectification thermique atteint des valeurs plus élevées dans des conditions transitoires que dans des conditions stationnaires. En 2022, Shimokusu et al. [97] ont développé un modèle avec une solution de perturbation analytique en combinant la méthode des éléments finis afin de déterminer la rectification thermique optimisée dans des conditions transitoires. Leur diode thermique est composée de deux matériaux dont les conductivités thermiques et les chaleurs spécifiques varient linéairement avec la température [97]. Ils ont constaté que la métrique asymétrique de redressement peut être deux fois plus grande que la valeur de quasi-stationnaire pour des valeurs élevées de la fréquence de la température sinusoïdale imposée. En 2023, nous avons également publié un article relatif à une diode thermique conductive composée d'un MCP et d'un non-MCP, qui sont respectivement le VO_2 et le SiO_2 [1]. Cet article est en effet un résultat de cette thèse et nous détaillerons ce travail dans le Chapitre 3 correspondant [1]. Nous avons constaté que la rectification thermique atteignait des valeurs très élevées dans les conditions transitoires par rapport à la rectification thermique en régime permanent [1]. En 2024, Zurdo et al. [39] ont étudié une diode thermique carrée avec des trous triangulaires et en forme de croissant à l'intérieur. Ils ont constaté que la diode thermique avec un trou en forme de triangle permet une meilleure rectification thermique globale que le trou en forme de croissant, et ont obtenu une valeur de rectification thermique globale atteignant 10% [39].

Transistor thermique

L'invention révolutionnaire du transistor électronique a été réalisée par Bardeen et Brattain [72] en 1948. Il permet fondamentalement de contrôler le courant en remplissant trois fonctions : l'amplification, la commutation et la modulation. Bien que le transistor électronique ait fait l'objet de nombreuses études et est devenu un élément indispensable de notre boîte à outils électronique, le transistor thermique, qui est son analogue thermique, n'a pas fait l'objet d'études

suffisantes. Cependant, l'utilisation de phonons au lieu d'électrons présente un grand potentiel pour le traitement de l'information et peut contribuer au développement de l'informatique thermique [9, 40, 114].

Le transistor électronique est fondamentalement classé en deux catégories : le transistor à jonction bipolaire (TJB) [72] et le transistor à effet de champ (TEC) [115]. Le TJB est piloté par le courant et se compose de trois éléments : le collecteur, la base et l'émetteur. Le TEC est quant à lui piloté par la tension et se compose de trois éléments : le drain, la source et la grille. Il existe de nombreuses études sur le concept de transistor thermique dans la littérature, mais la majorité d'entre elles concernent le régime radiatif du transfert de chaleur, qu'il s'agisse du champ proche ou lointain, ainsi que le cadre quantique. À notre connaissance, à l'exception des travaux pionniers de Li et al. [116] et des travaux récents de Wu et al. [118], aucun autre concept macroscopique de transistor thermique dans le régime conductif du transfert de chaleur n'a été présenté. La première réalisation théorique de l'analogue thermique d'un transistor électronique a été effectuée par Li et al. [116]. Ces derniers ont modélisé les éléments drain, source et grille d'un transistor à effet de champ classique par des lattices de Frenkel-Kontorova. Fondamentalement, le flux d'électrons peut être contrôlé du drain vers la source en fonction de la tension appliquée à la grille dans un transistor à effet de champ classique. De la même manière, Li et al. [116] ont montré que les fonctions d'amplification et de commutation (modes) du transistor thermique sont possibles en utilisant le transport de phonons en fixant les températures des éléments drain, et source tout en ajustant la température de l'élément de la grille en conséquence. Ils ont également montré que le phénomène de résistance thermique différentielle négative (RTDN) était un critère essentiel pour obtenir un effet transistor [116]. En 2024, une étude récente a été réalisée sur le transfert de chaleur dans le régime conductif d'un transistor thermique par Wu et al. [118]. Ces derniers ont modélisé le processus de transfert de chaleur du transistor thermique sur la base du modèle de gaz de Lorentz modifié, et ont étudié les fonctions d'amplification et de commutation, ainsi que leurs plages de fonctionnement, en fonction de divers paramètres tels que la longueur, la largeur et la conductance thermique du système [118]. Ils ont constaté qu'une amplification plus importante pouvait être obtenue en augmentant la conductance thermique, mais que cela affectait inversement la fonction de commutation [118].

Memristor thermique

Le memristor électrique, un dispositif à deux bornes reliant la charge électrique au flux magnétique dans les circuits électroniques, a été conceptualisé et conçu pour la première fois par Chua sur la base d'arguments de symétrie en 1971 [121]. Il a été considéré comme le quatrième élément électronique fondamental avec la résistance, le condensateur et l'inductance [121]. Cependant, il a fallu près de quarante ans pour que le concept soit adopté et concrétisé. La première réalisation du memristor électrique a été effectuée par Strukov et al. en 2008 [45].

Afin de poursuivre l'établissement d'analogues thermiques complets pour tous les composants électroniques élémentaires, Ben-Abdallah [47] a proposé théoriquement l'existence du memristor thermique conductif, en exploitant l'hystérésis thermique de la conductivité thermique du VO_2 en 2017. Dans le cadre de ses recherches, il a été constaté que l'effet memristor thermique est rendu possible par la nature de la relation flux de chaleur-différence de température. Cette observation s'appuie sur l'utilisation de la transition de phase métal-isolant du VO_2 [47]. Cependant, il est à noter que la courbe caractéristique de Lissajous, qui est l'une des caractéristiques définissant le memristor, n'a pas été étudiée dans l'étude de Ben-Abdallah. Par analogie avec la relation entre le courant passant et la tension appliquée pour le memristor électrique, la courbe caractéristique de Lissajous dans le memristor thermique manifeste la relation entre le flux de chaleur à travers le memristor et la différence de température modulée appliquée entre ses deux bornes. À l'origine, ces deux courbes sont situées à l'intersection, et leur corrélation produit la courbe caractéristique de Lissajous pincée [45, 121]. Dans le cadre de leurs recherches, Yang et al. [48] ont étudié, pour la première fois, la courbe caractéristique de Lissajous du memristor thermique conductif à base de VO_2. En 2019, un memristor thermique radiatif à champ lointain à base de VO_2 avec des terminaux sans contact a été introduit, manifestant les mêmes caractéristiques que le memristor conductif [49].

Conclusion

De nombreuses études ont examiné la rectification thermique conductives des diodes thermiques dans des conditions stationnaires, et l'intérêt pour l'analyse transitoire s'est accru. Cependant,

à notre connaissance, il n'existe pas de travaux antérieurs qui aient étudié les diodes thermiques conductives en tenant compte des propriétés du VO_2 sous tous leurs aspects dans des conditions transitoires. En outre, les recherches menées sur les memristors thermiques sont encore limitées, et celles qui ont été conduites ont essentiellement considéré leur analyse dans des conditions quasi-stationnaires. En conséquence, l'effet capacitif a été négligé. Concernant les transistors thermiques, bien que de nombreuses études aient examiné le concept de transistor thermique dans la littérature, la majorité de ces études sont liées au régime radiatif du transfert de chaleur. À notre connaissance, à l'exception du travail de pionnier Li et al. [116] et du travail récent de Wu et al. [118], aucun autre concept macroscopique de transistor thermique dans le régime conductif de transfert de chaleur n'a été présenté. En conséquence, l'objectif de cette étude, ainsi que son aspect novateur, réside dans l'analyse des trois composantes thermiques en régime conductif en prenant en considération l'ensemble des propriétés du VO_2.

Chapter 2

Conductive Thermal Memristor

Contents

2.1 Introduction 91

2.2 Theoretical modeling 92

2.2.1 Implementation of a simple model 92

2.2.2 Verification of the numerical model in a simple case 94

2.2.3 The conductive thermal memristor and temperature modulation of the thermal baths 97

2.2.4 Modeling the hysteresis zone 98

2.2.5 Numerical modeling of the conductive thermal memristor 102

2.3 Results and discussion 105

2.4 Conclusion 123

2.1 Introduction

There are very few studies on the thermal memristor as summarized in the literature review section in Chapter 1. In fact, there are just two studies about the conductive thermal memristor (CTM), the ones of Ben-Abdallah [47] and Yang et al. [48]. Both studies explored the case of a VO_2 based device and considered this PCM under quasi-steady-state conditions by changing various parameters such as the thermal conductivity ratio of the material and the temperature amplitude of the modulated boundary conditions. The capacitive effect was omitted in these analyses. Therefore, in this chapter, we will study a VO_2 based CTM while considering the full properties of VO_2 by applying the modulated boundary conditions and hence extend the former

analysis by examining the capacitive effect and its impact by changing various parameters such as frequency, reference temperature and temperature amplitude of the applied modulated boundary conditions. First, we will start by explaining how we model the hysteresis zone of VO_2 and how we apply the enthalpy model. Then, we will present our work that compares the results of our calculations with Krapez's work [55] to verify our modeling.

2.2 Theoretical modeling

2.2.1 Implementation of a simple model

We firstly started our study by investigating a simple case as illustrated in Fig.2.1 to develop our complex model step by step. Therefore, one-dimensional general heat diffusion equation is solved by finite difference method, because it is a useful alternative to solve a problem under transient conditions when the thermal conductivity and the specific heat capacity vary with respect to temperature. As previously explained in Chapter 1, the one-dimensional general heat diffusion equation with no internal heat source is [144]:

$$\rho c_p(T)\frac{\partial T}{\partial t} = \frac{\partial}{\partial x}\left[k(T)\frac{\partial T}{\partial x}\right] \tag{2.1}$$

where the specific heat capacity, $c_p(T)$, and the thermal conductivity, $k(T)$, vary with respect to the temperature. The model is discretized in time and space to analyze the temperature distribution and heat flux density in the transient regime. Heat flux densities at both ends of the model and temperatures at each nodes are determined for each time step iteratively. Then, the temperatures are used to determine the thermal conductivity, $k(T)$, and the specific heat capacity, $c_p(T)$ for every time step.

The finite difference representation of Eq.2.1 can be written as [144]:

$$\begin{aligned}\Delta x(\rho c_p)_i\frac{T_i^{n+1}-T_i^n}{\Delta t} = \theta&\left[k_{i-1/2}\frac{T_{i-1}^{n+1}-T_i^{n+1}}{\Delta x}+k_{i+1/2}\frac{T_{i+1}^{n+1}-T_i^{n+1}}{\Delta x}\right]\\ &+(1-\theta)\left[k_{i-1/2}\frac{T_{i-1}^{n}-T_i^{n}}{\Delta x}+k_{i+1/2}\frac{T_{i+1}^{n}-T_i^{n}}{\Delta x}\right]\end{aligned} \tag{2.2}$$

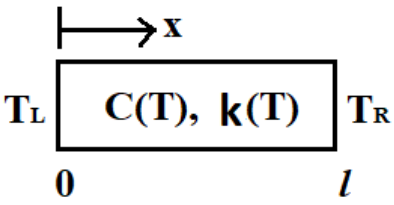

Figure 2.1: Sketch of the analyzed simple case.

where $\theta = 0$ for explicit and $\theta = 1$ for implicit schemes [144]. In addition, i and n are the space and time indices, respectively. Here we used the implicit scheme in numerical modeling, which has an advantage over the others due to its stability. The implicit formulation of the finite difference representation can be written as in Eq.2.3:

$$-A_i T_{i-1}^{n+1} + (1 + 2B_i) T_i^{n+1} - C_i T_{i+1}^{n+1} = T_i^n \tag{2.3}$$

where A_i, B_i and C_i are as follows:

$$A_i = \frac{k_{i-1/2}^n}{(\rho c_p)_i} \frac{\Delta t}{(\Delta x)^2} \tag{2.4}$$

$$B_i = \frac{1}{2} \frac{k_{i-1/2}^n + k_{i+1/2}^n}{(\rho c_p)_i} \frac{\Delta t}{(\Delta x)^2} \tag{2.5}$$

$$C_i = \frac{k_{i+1/2}^n}{(\rho c_p)_i} \frac{\Delta t}{(\Delta x)^2} \tag{2.6}$$

and the thermal conductivity between two nodes can be approximated by taking the arithmetic or harmonic means of neighboring nodes for each step. The arithmetic and harmonic formulations can be seen in Eqs.2.7 and 2.8, respectively [144]:

$$k_{i+1/2} = \frac{k_i + k_{i+1}}{2} \tag{2.7}$$

$$k_{i+1/2} = \frac{2 k_i k_{i+1}}{k_i + k_{i+1}} \tag{2.8}$$

We used the harmonic mean as suggested by Ozisik et al. [144], because the arithmetic mean

does not overcome the sharp changes in the thermal conductivity as the harmonic mean does.

The numerical implementation of the model by the finite difference method is illustrated in Fig.2.1 and explained in this section. The system needs to be discretized in time and space. In this section, it is divided into 10 parts and there are 9 nodes with two prescribed boundary conditions as an example to explain the method as shown in Fig.2.2. i and T show the nodes and the corresponding temperature at that node, respectively.

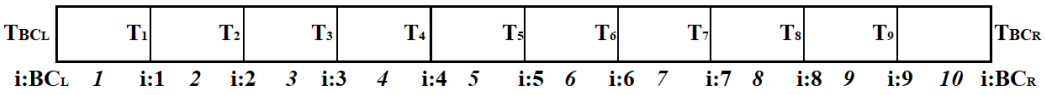

Figure 2.2: Sketch of the numerical model.

The solution of Eq.2.3 is shown for node 5 to clarify the implementation. The numerical implementation for node 5 can be seen in the Eqs.(2.9-2.12). The system is solved for the other nodes for each time step by using the same procedure as shown for node 5.

$$-A_5 T_4^1 + (1 + 2B_5) T_5^1 - C_5 T_6^1 = T_5^0 \tag{2.9}$$

where

$$A_5 = \frac{k_{4.5}}{(\rho c_p)_5} \frac{\Delta t}{(\Delta x)^2} \tag{2.10}$$

$$B_5 = \frac{1}{2} \frac{k_{4.5} + k_{5.5}}{(\rho c_p)_5} \frac{\Delta t}{(\Delta x)^2} \tag{2.11}$$

$$C_5 = \frac{k_{5.5}}{(\rho c_p)_5} \frac{\Delta t}{(\Delta x)^2} \tag{2.12}$$

2.2.2 Verification of the numerical model in a simple case

The simple case illustrated in Fig.2.1 is firstly examined to verify our numerical model's accuracy before making the model more complex and considering the hysteresis zone. The heat diffusion equation in Eq.2.1 is nonlinear due to the temperature dependence of the thermal conductivity

and the specific heat capacity. Therefore, a nondimensionalization and a simplification procedure are made in this equation to obtain a linear solution in order to compare it with the numerical solution. The thermal conductivity and specific heat capacity are assumed to be proportional to the third power of the temperature as follows: $k(T) = k_o T^3$ and $c(T) = c_o T^3$, respectively. Therefore, the heat equation can be written as in Eq.2.13:

$$T^3 \frac{\partial T}{\partial t^*} - \frac{\partial}{\partial y}\left(T^3 \frac{\partial T}{\partial y}\right) = 0 \tag{2.13}$$

where $t^* = \frac{\alpha_o t}{l^2}$, $y = \frac{x}{l}$ and $\alpha_o = \frac{k_o}{\rho c_o}$. Eq.2.14 can be obtained after the temperature is also nondimensionalized by $\theta = \frac{T}{T_L}$:

$$\theta^3 \frac{\partial \theta}{\partial t^*} - \frac{\partial}{\partial y}\left(\theta^3 \frac{\partial \theta}{\partial y}\right) = 0 \quad ; \quad d\chi = \theta^3 d\theta \Rightarrow \chi = \int_0^\theta \theta^3 d\theta = \frac{\theta^4}{4} \Rightarrow \theta = (4\chi)^{1/4} \tag{2.14}$$

Then, the final form can be written as:

$$\frac{\partial \chi}{\partial t^*} - \frac{\partial^2 \chi}{\partial y^2} = 0 \tag{2.15}$$

After applying Laplace transform to Eq.2.15, $\tau(s, y) = L[\chi(t^*, y)](s)$, $\chi(0, y) = 0$ it will become:

$$s\tau - \frac{d^2\tau}{dy^2} = 0 \tag{2.16}$$

then the following Eq.2.17 can be obtained:

$$\tau(s, y) = A\cosh(\sqrt{s}y) + B\sinh(\sqrt{s}y) \tag{2.17}$$

the space boundary expressions of $\tau(s, 0)$ and $\tau(s, 1)$ are given by:

$$\tau(s, 0) = A \tag{2.18}$$

$$\tau(s, 1) = A\cosh(\sqrt{s}) + B\sinh(\sqrt{s}) \tag{2.19}$$

then after a simple arrangement, B can be determined as:

$$B = \frac{1}{\sinh(\sqrt{s})}\tau(s, 1) - \frac{\cosh(\sqrt{s})}{\sinh(\sqrt{s})}\tau(s, 0) \tag{2.20}$$

In addition, the nondimensional heat flux density is $\varphi(s,y) = \frac{\xi(s,y)}{\xi_0} = -\partial\tau/\partial y$ where $\xi_0 = \frac{k_0 T_L^4}{l}$ and the following Eq.2.21 can be obtained:

$$-\frac{\partial\tau}{\partial y} = -\left[A\sqrt{s}\sinh(\sqrt{s}y) + B\sqrt{s}\cosh(\sqrt{s}y)\right] \tag{2.21}$$

$\varphi(s,0)$ and $\varphi(s,1)$ are obtained as:

$$\varphi(s,0) = -B\sqrt{s} \tag{2.22}$$

$$\varphi(s,1) = -\sqrt{s}\left[A\sinh(\sqrt{s}) + B\cosh(\sqrt{s})\right] \tag{2.23}$$

If we take Eq.2.18, Eq.2.19, Eq.2.22 and Eq.2.23, we can express a matrix relation relating τ and φ at y=0 to τ and φ at y=1. It is indeed:

$$\begin{bmatrix}\tau(s,0)\\ \varphi(s,0)\end{bmatrix} = \begin{bmatrix}\cosh(\sqrt{s}) & \sinh(\sqrt{s})/\sqrt{s}\\ \sqrt{s}\sinh(\sqrt{s}) & \cosh(\sqrt{s})\end{bmatrix}\begin{bmatrix}\tau(s,1)\\ \varphi(s,1)\end{bmatrix} \tag{2.24}$$

Finally, the nondimensional heat flux densities at the left and right edges of the problem as seen in Fig.2.1 can be obtained by Eq.2.25 and Eq.2.26, respectively:

$$\varphi(s,0) = \frac{\sqrt{s}\cosh(\sqrt{s})}{\sinh(\sqrt{s})}\tau(s,0) - \frac{\sqrt{s}}{\sinh(\sqrt{s})}\tau(s,1) \tag{2.25}$$

$$\varphi(s,1) = \frac{\sqrt{s}}{\sinh(\sqrt{s})}\tau(s,0) - \frac{\sqrt{s}\cosh(\sqrt{s})}{\sinh(\sqrt{s})}\tau(s,1) \tag{2.26}$$

where $\tau(s,0)$ and $\tau(s,1)$ are the boundary conditions of the left and right edges after applying the Laplace transform, respectively. After finding these expressions, the solution in the real time domain is found by using an inverse Laplace transform algorithm. Then, these results are compared with the numerical solution by solving the nonlinear diffusion equation.

The heat conduction equation is solved both numerically and analytically as explained before according to the following conditions: The left and right boundary conditions, and the initial condition of the system are $T(t^*,0) = T_L H(t^*)$, $T(t^*,1) = T_R H(t^*)$ and $T(0,l) = 0$, respectively. $H(t^*)$ is the Heaviside step function. Boundary conditions at the left and right edges

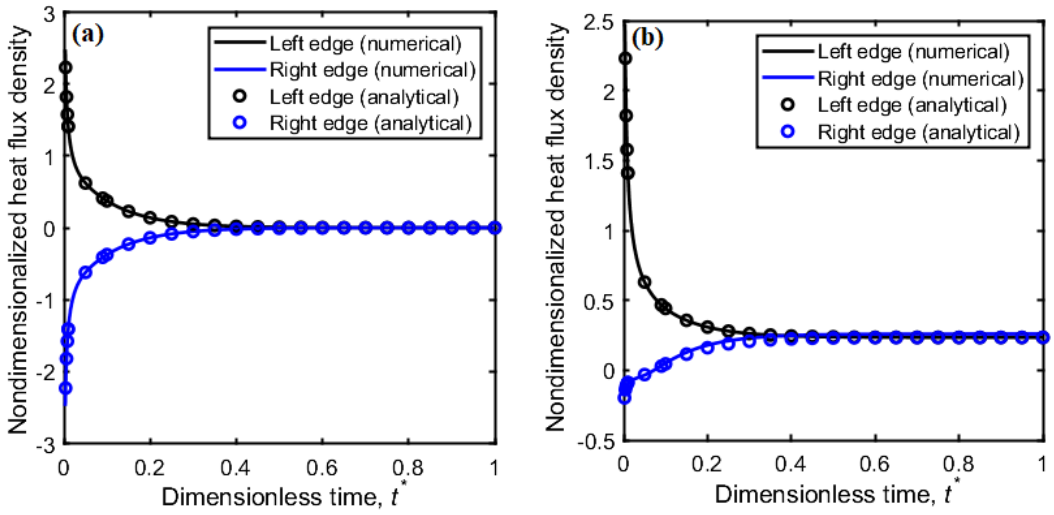

Figure 2.3: Comparison of analytical and numerical nondimensionalized solution.

after Laplace transform will be $\tau(s,0) = 1/4s$ and $\tau(s,1) = \varepsilon/s$ where ε is $\frac{1}{4}\left(\frac{T_R}{T_L}\right)^4$, respectively.

The nondimensional heat flux density with respect to the dimensionless time according to analytical and numerical solutions can be seen in Fig.2.3. T_R is 100 K for both cases illustrated in Figs.2.3(a) and (b). However, T_L is 100 K and 200 K for case (a) and case (b), respectively. It is clearly seen that the analytical and numerical results have an excellent agreement. This shows that our numerical approach handles the heat conduction equation with the mentioned assumptions of the thermal conductivity and the specific heat capacity properly.

2.2.3 The conductive thermal memristor and temperature modulation of the thermal baths

We consider a CTM in a plane geometry. The CTM is made of a piece of VO_2 as seen in Fig.2.4. The length of the CTM is 1 mm. We assume the system to be placed between two thermal baths in a vacuum chamber so that we can neglect any heat exchange due to convection. We also assume heat exchange due to radiation to be negligible and consider conduction to be the only heat transfer mode between the two thermal baths.

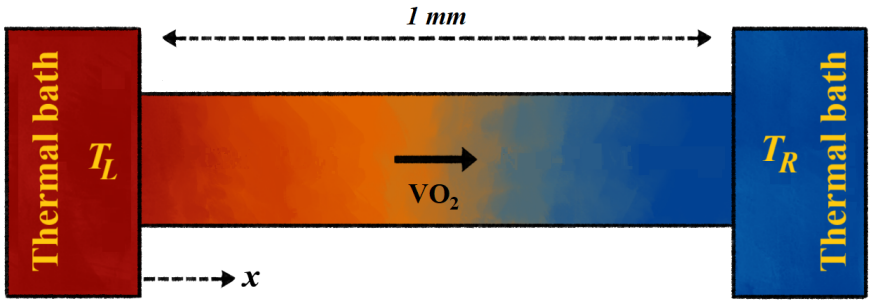

Figure 2.4: Schematic representation of the studied CTM.

In our model, we apply two sinusoidal temperatures at the two boundaries of the CTM, which are expressed in Eqs. (2.27) and (2.28) for the left and right sides, respectively:

$$T_L = T_r + T_a \sin(2\pi f t) \tag{2.27}$$

$$T_R = T_r + T_a \cos(2\pi f t) \tag{2.28}$$

where T_r is a reference temperature, f is frequency, t is time and T_a is the amplitude of the temperature modulated component. Throughout the study, we use the average of the phase transition temperatures of the heating and cooling processes of VO_2 for T_r as shown in Eq.2.29 unless otherwise indicated:

$$T_r = (T_{oh} + T_{oc})/2 \tag{2.29}$$

where $T_{oh} = 342.9$ K and $T_{oc} = 334.9$ K represent the values of the phase critical transition temperature of VO_2 for the heating and cooling processes, respectively [35]. There is an 8 K hysteresis width between heating and cooling phase transition temperatures as stated before. Fig.2.5(a) and (b) show, respectively, the computed behaviors of the thermal conductivity and enthalpy of VO_2 as functions of temperature around the phase transition zone for both the heating and cooling processes.

2.2.4 Modeling the hysteresis zone

When there is only heating or cooling in a case with Dirichlet boundary conditions, this can be modeled relatively more easily than in cases with dynamical boundary conditions, because we

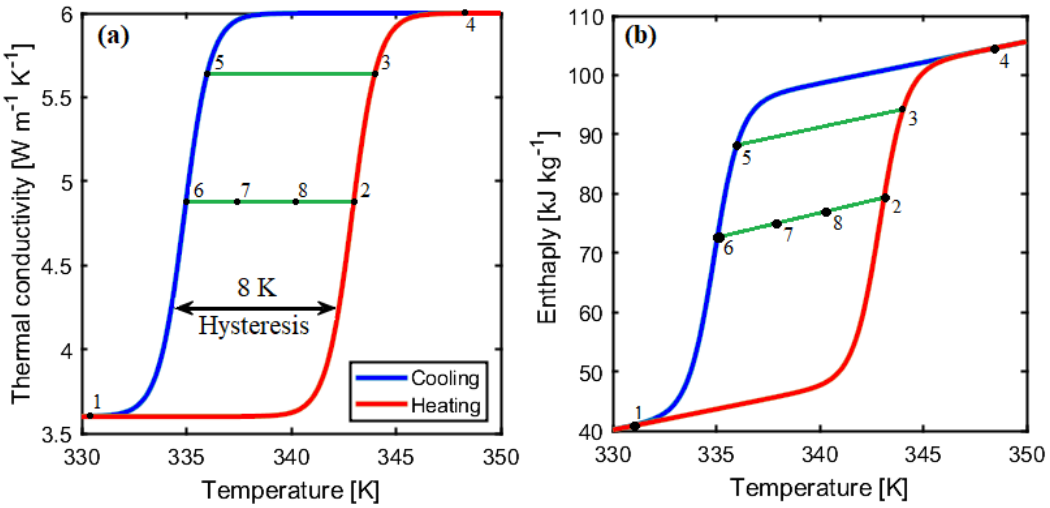

Figure 2.5: Computed behaviors of the thermal conductivity (a) and enthalpy (b) of VO_2 as functions of temperature [52].

can model the thermal conductivity and heat capacity without considering the hysteresis zone in a case with Dirichlet boundary conditions by carefully adjusting the applied boundary temperatures; for which we indeed modeled some cases of the conductive thermal diode (CTD) as will be shown in the following Chapter 3. Therefore, we can directly use Eq.1.16 for the thermal conductivity and Eq.1.17 for the specific heat capacity in this type of analysis. However, this is not possible when performing an analysis with dynamical boundary conditions. We need to consider the hysteresis zone. Therefore, we use the enthalpy method to model the hysteresis zone for the dynamical boundary condition analysis.

When we consider a full cycle on the hysteresis loop of the thermal conductivity and enthalpy including both the heating and cooling processes, the modeling of these conditions is easily applicable. In this case, we follow the path represented by the points sequence [1-2-3-4-5-6-1] as illustrated in Fig.2.5(a) or (b). However, there is a difficulty to model the hysteresis effect when the heating or cooling stops on the points of the curves such as 2, 3, 5 or 6 before reaching the end points, which are 1 and 4. This situation was examined by Ramirez et al. [53]. They made a study to analyze the hysteresis effect of VO_2 for the temperature behavior of the electric-

resistance. In their study, the temperature decreased or increased from fully metallic temperature or insulating temperature according to the heating or cooling analysis. Then, it returned to the starting temperature. This process was performed with small steps of the temperature change repeatedly. For example, they cooled down until a specific temperature from 380 K, then they heated up until the starting temperature for the heating analysis and this process generated some curves that are called first-order reversal curves as shown in Fig.2.6(b). Additionally, the first-order reversal curves for the cooling analysis that are obtained by a similar process can be seen in Fig.2.6(a) [53].

Gurvitch et al. [54] made a study on the hysteresis loop of VO_2 for both the electric-resistance and optical reflectivity. They decreased or increased the temperature according to the cooling or heating processes with a small temperature change, which they called excursion length. Then, they went back to the starting temperature. They observed that small loops occurred inside of the main hysteresis loop. When the excursion length gets smaller, these loops even flattened out and generated nonhysteretic branches [54]. For example, when the excursion length is 4 K, the flattened loops in the work of Gurvitch et al. can be observed for the electric-resistance and

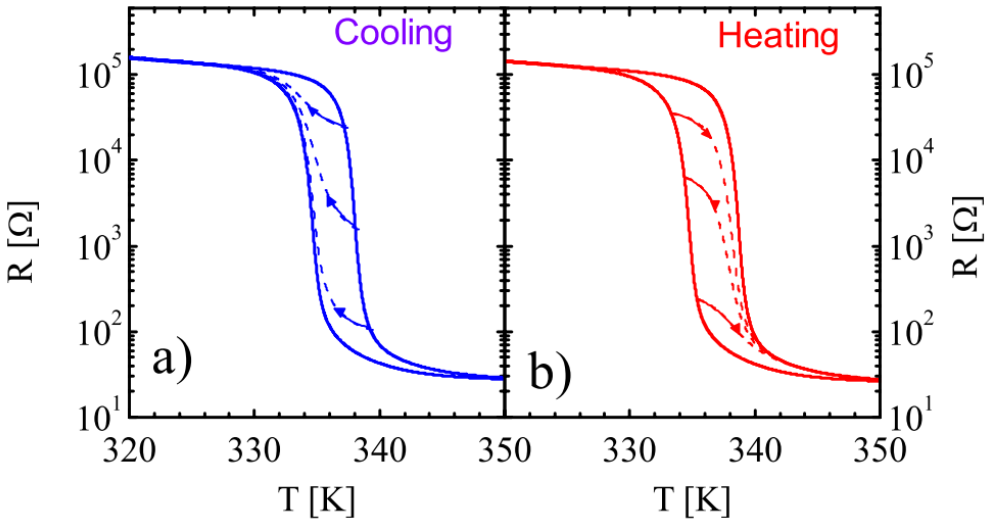

Figure 2.6: The first-order reversal curves during the cooling (a) and heating (b) analysis in the study of Ramirez et al. [53].

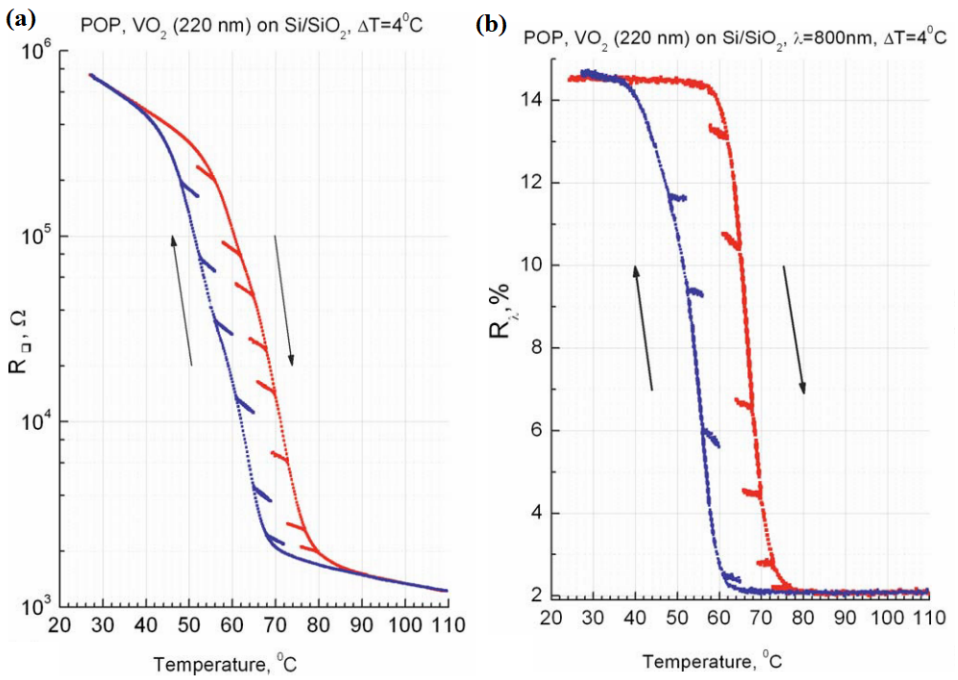

Figure 2.7: The flattened loops for electric-resistance (a) and optical reflectivity (b) in the study of Gurvitch et al. when the excursion length is short [54].

optical reflectivity in Fig.2.7(a) and (b), respectively [54].

Recently, Krapez [55] made a detailed numerical study to investigate the shuttling effect of heat conduction in VO_2 while including the hysteresis effect. In his study, Krapez exploited the nonhysteretic branches that were seen during the analysis of the electric-resistance and optical reflectivity in the study of Gurvitch et al. [54]. He assumed these branches should also be observed in the temperature behavior of the thermal conductivity and adopted this assumption for his study [55]. Additionally, he assumed the minor loops that are shown as the result of small excursions can also be seen in large excursions for modeling the hysteresis effect [55]. The method of Krapez [55] is the cornerstone of our study. We adapted his modeling in this work. Thus, when the heating or cooling stops in the middle of the transition such as points 2, 3, 5 or 6 in Fig.2.5(a) or (b) and we begin cooling or heating, the transition follows the green curves. For example, when there is a heating and the system begins to cool down in the middle of the phase transition at point 2, it follows the green curve until the cooling curve (point 6). However,

if the cooling stops while on the green curve before reaching the cooling curve such as points 7 or 8 and the system begins to heat up again, the phase transition follows the green curve until the heating curve (point 2).

2.2.5 Numerical modeling of the conductive thermal memristor

The following equation which represents the general one-dimensional heat diffusion equation without internal heat source expressed in terms of enthalpy is solved numerically by explicit finite difference method:

$$\rho\frac{\partial H}{\partial t} = \frac{\partial}{\partial x}\left[k(T)\frac{\partial T}{\partial x}\right] \tag{2.30}$$

where ρ is the density of VO_2, which is supposed constant and equal to 4670 kg m^{-3} [143]. Also, the thermal conductivity $k(T)$ of VO_2 is previously described by Eq.1.16 in Chapter 1.

The expression of the specific heat capacity of VO_2 is previously described by Eq.1.17 in Chapter 1. The variation of the specific heat predicted by Debye's model c^D within the range of the considered boundary conditions (BC) is very small. Therefore, we assumed it to be a constant value that is 0.71 kJ kg^{-1} K^{-1} [61]. Then, the enthalpy of VO_2 can be expressed as:

$$H(T) = c^D(T - T_{ref}) + L_n v(T) \tag{2.31}$$

where L_n is the latent heat equal to 51.45 kJ kg^{-1} for the heating process of VO_2 [61] and we assume the same value for the cooling process as we mentioned in Chapter 1. Besides, T_{ref} is a reference temperature and its value is taken as 273 K. The temperature behaviors of the thermal conductivity and enthalpy of VO_2 are reported in Fig.2.5(a) and (b), respectively.

After Eq.2.30 is discretized in space (index i) and time (index n), its explicit formulation of the finite difference representation can be written as

$$\Delta x\rho\frac{H_i^{n+1} - H_i^n}{\Delta t} = k_{i-1/2}^n\frac{T_{i-1}^n - T_i^n}{\Delta x} + k_{i+1/2}^n\frac{T_{i+1}^n - T_i^n}{\Delta x} \tag{2.32}$$

The enthalpy in the next time step can be found after rearranging Eq.2.32 as follows

$$H_i^{n+1} = A_i T_{i-1}^n - B_i T_i^n + C_i T_{i+1}^n + H_i^n \tag{2.33}$$

where A_i, B_i and C_i are:

$$A_i = \frac{k_{i-1/2}}{\rho}\frac{\Delta t}{(\Delta x)^2} \tag{2.34}$$

$$B_i = \frac{k_{i-1/2}+k_{i+1/2}}{\rho}\frac{\Delta t}{(\Delta x)^2} \tag{2.35}$$

$$C_i = \frac{k_{i+1/2}}{\rho}\frac{\Delta t}{(\Delta x)^2} \tag{2.36}$$

After obtaining the enthaply at each nodes for the next time step, we find the temperatures that correspond to those enthalpy values inversely. After that, the thermal conductivities at each nodes will be determined. We determine the temperature values from the current enthalpy values using a full numerical procedure that gives the same result as the semi-analytical procedure of Krapez by identifying the current process (cooling/heating) of the system. The details of the modeling are clearly explained in Krapez's paper [55].

It should be noted that some transient effects appear at the first periods when the dynamical boundary conditions are applied to the system. Therefore, in our analysis, we always consider a period after these transient effects have disappeared, i.e. when the dynamical regime is fully established. In addition, the time step is arranged according to the following criterion throughout the study by taking into account the stability consideration of the explicit approach [144]:

$$\Delta t = \frac{(\Delta x)^2}{2\alpha} \tag{2.37}$$

α is the thermal diffusivity. The values of the thermal diffusivity according to the dielectric and metallic phases of VO_2 are $\alpha_d = 1.09 \times 10^{-6}$ m^2 s^{-1} and $\alpha_m = 1.81 \times 10^{-6}$ m^2 s^{-1}, respectively. For the safety of the stability criterion, we used the value of α_m which is the highest between the two values.

Krapez analyzed a similar system that was illustrated in Fig.2.4. He examined a 1 mm layer that is made of VO_2 and applied a sinusoidal boundary condition at the left boundary as expressed in Eq.2.38 while the right boundary has a fixed temperature as expressed in Eq.2.39 [55]. We also followed the same procedure with the same parameters as described in Krapez's paper to make a verification of our model before starting the analysis in our study. We obtained

almost identical results according to various parameters that were used in his work as shown in Fig.2.8.

$$T_L = T_r + T_a \sin(2\pi f t) \tag{2.38}$$

$$T_R = T_r \tag{2.39}$$

where $T_a = 8$ K and $f = 0.3$ Hz. He examined the shuttling effect of heat conduction with various reference temperatures T_r. In addition, he validated the numerical modeling of his work

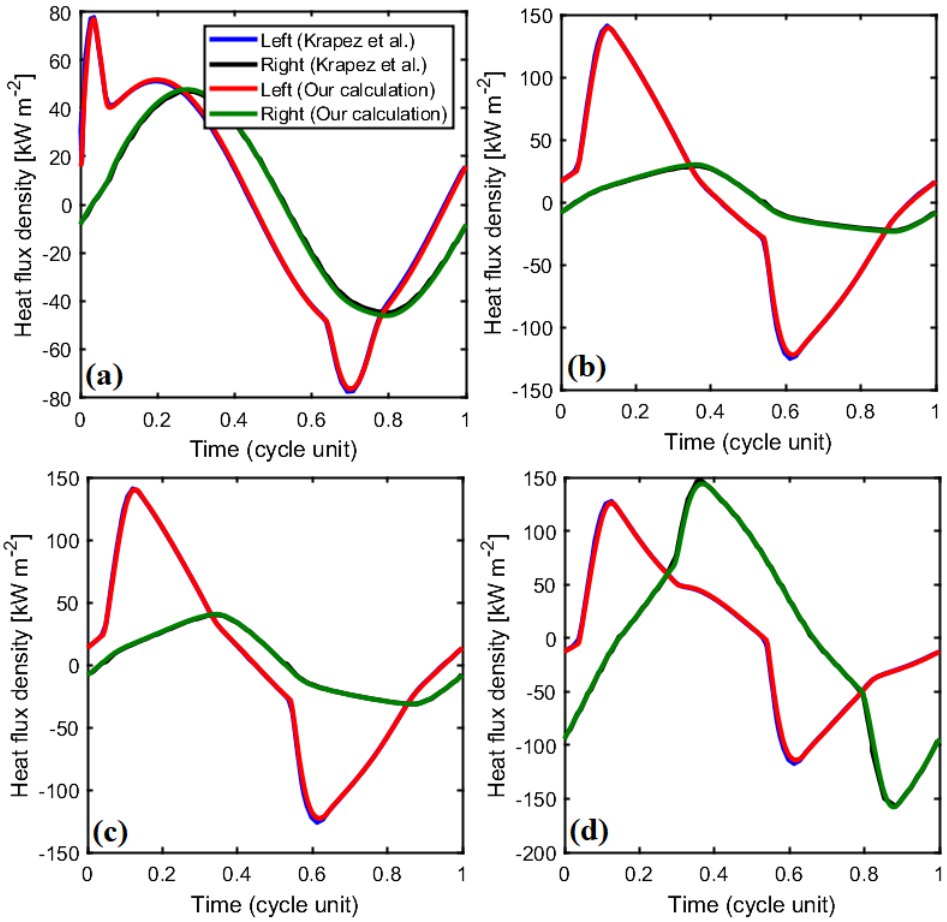

Figure 2.8: Comparison of the results with our calculation and Krapez's work [55] for $T_r = 343$ K (a), for $T_r = 339$ K when the system starts on the heating line (b), when the system starts on the cooling line (c) and for $T_r = 339$ K when there is a lag of $3\pi/2$ on the sinusoidal boundary condition (d).

by comparing it with the analytical solution for a linear material case. He compared the analytical results with numerically obtained results and the results were reasonable [55]. After we had our code ready for our CTM and CTD studies, we compared it with the same values and parameters in Krapez's study before moving on to our own analysis. For example, when $T_r = 343$ K, the heat flux densities at the left and right boundaries according to the Krapez results and our results are shown in Fig.2.8(a). The results for $T_r = 339$ K are shown when the system starts on the heating line in Fig.2.8(b) and on the cooling line in Fig.2.8(c), respectively. Besides, when there is a lag of $3\pi/2$ in the sinusoidal boundary condition, the results for $T_r = 339$ K can be seen in Fig.2.8(d). The comparison of the results shows that the code we created for our analysis following the same modeling procedure by Krapez gives identical results.

2.3 Results and discussion

We investigate the impacts of three different parameters which are f, T_r and T_a for the CTM analysis as seen in Table 2.1. Note that, only one parameter is changed at a time. First, we analyzed several frequencies to find the starting frequency that causes a deformation on the heat flux density and Lissajous characteristic curves according to the dimensions of 1 mm, 1 cm, 1 dm and 1 m. In other words, we searched for the threshold frequencies above which we start losing the pinched symmetrical Lissajous type heat flux-temperature difference curve. T_a is taken as 10 K. This value is large enough to show both VO_2 phases and provide full cycles on the heating and cooling curves. In addition, T_r is taken as the average of T_{oh} and T_{oc} as mentioned before. We found that the threshold frequency is inversely proportional to the square of the length of the CTM as reported in Fig.2.9. When the dimension of the CTM increases, the threshold frequency needs to get lower to generate a pinched symmetrical Lissajous characteristic curve. It is interesting to note here that this behavior corresponds exactly to Fourier classical length scaling law.

The effect of various frequencies on the heat flux density and the Lissajous characteristic curves are shown in Fig.2.10 and Fig.2.11, respectively. The values of T_a and T_r are taken the same as mentioned before and the investigated frequencies can be seen as case 1 in Table 2.1.

Table 2.1: Investigated parameters and cases for the CTM.

Case 1 - f					
	(i)	(ii)	(iii)	(iv)	(v)
f [Hz]	0.002	0.01	0.02	0.04	0.08
Case 2 - T_r					
	(i)	(ii)	(iii)	(iv)	(v)
T_r [K]	330.9	334.9	338.9	342.9	346.9
Case 3 - T_a					
	(i)	(ii)	(iii)	(iv)	(v)
T_a [K]	4	8	20	32	44

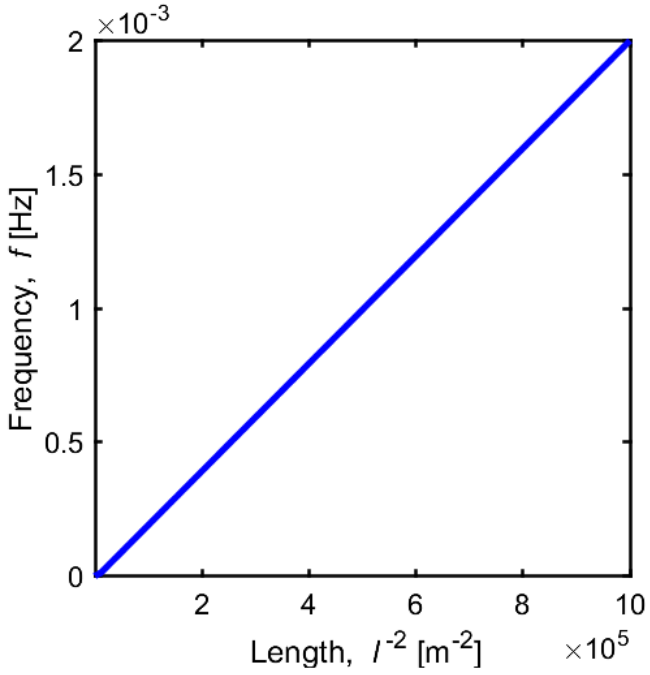

Figure 2.9: Correlation between the threshold frequency and the CTM length to obtain a pinched symmetrical Lissajous characteristic curve.

We report the computed time behaviors of the heat flux densities at the left and right edges of the CTM in Fig.2.10 and those of the Lissajous characteristic curves according to the left and right edges in Fig.2.11(a) and (b), respectively. The arrows in Fig.2.11(a) and (b) indicate the direction of motion of the Lissajous characteristic curve. It should be noted that the heat

flux density and the temperature difference of the Lissajous characteristic curves are normalized to their maximum values in the study. When the frequency is low enough to obtain a proper pinched symmetrical Lissajous characteristic curve, the heat flux densities at the left edge and the right edge are almost the same as expected. We observe that when we increase the frequency, the heat flux densities at the left and right edges diverge from each others and we start to see a distortion on the Lissajous characteristic curve. As shown in Fig.2.11(a) and (b), the Lissajous characteristic curves are fully distorted in case 1 (iii). In fact, there is even no intersection in case 1 (iv) and (v) at the left edge. Therefore, it can be deduced that the frequency of the applied boundary sinusoidal temperature plays a key role in the appearance of the memristor effect as one can see in Fig.2.10 and Fig.2.11. There is a threshold frequency above which, the Lissajous characteristic curve of the CTM starts to get distorted and its symmetry breaks down. This frequency depends on the size of the CTM following the classical length scaling law of Fourier.

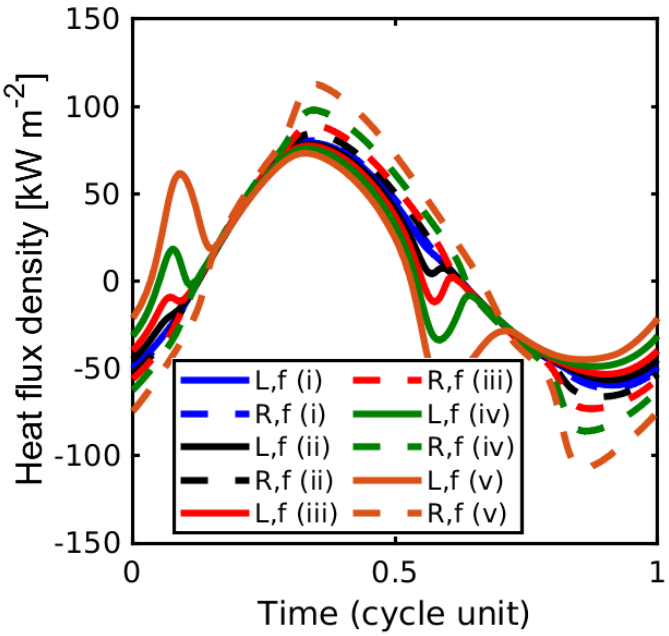

Figure 2.10: Computed time behaviors of the heat flux density corresponding to the left and right sides for different values of f.

Five different values of T_r which are shown as case 2 in Table 2.1 are investigated to analyze

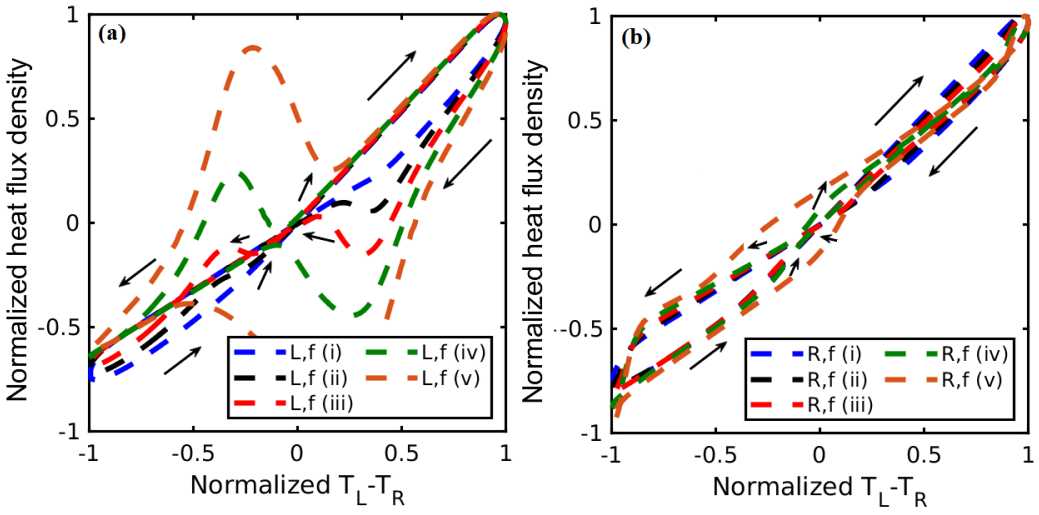

Figure 2.11: Normalized heat flux density-temperature difference curve according to the left (a) and right sides (b) for different values of f. The arrows indicate the direction of motion of the Lissajous characteristic curve.

its impact on the thermal memristor effect. We set three different values of T_r that are inside the hysteresis zone while two values are outside of it. The values of T_a and frequency are set as 10 K and 0.002 Hz, respectively. When T_r increases, the oscillation amplitude of the heat flux density becomes higher as shown in Fig.2.12. For $T_r = 338.9$ K, which is the temperature at the middle of the hysteresis zone, the nonlinear effect becomes quite evident and the memristor effect is clearly seen as reported in Fig.2.13(a) and (b) according to the left and right edges, respectively, because the material behaves in both phases and can experience a full cycle on the heating and cooling curves with this condition. However, when we approach the values of T_{oc} and T_{oh}, we start to lose the memristor effect because of the incomplete phase change process. There is not a full transition on the heating and cooling curves with these conditions. The heating stops before completing the heating branch in case 2 (ii) and the cooling stops before completing the cooling branch in case 2 (iv). Indeed, we fully lose the memristor effect and obtain a straight line in case 2 (i) and (v) as a result of a negligible phase change process.

Having a full or partial transition and their impacts on the thermal conductivity and enthalpy behaviors can be seen in more detail for the case 2 (i), (ii), (iii), (iv) and (v) in Fig.2.14, Fig.2.15,

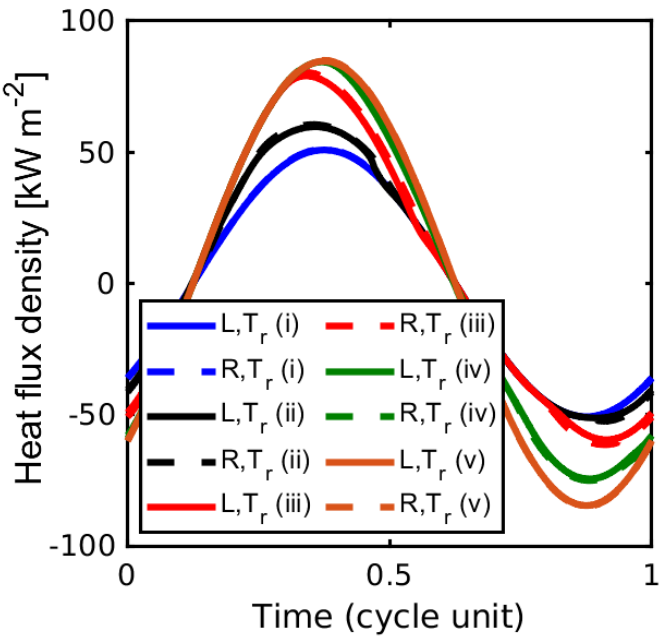

Figure 2.12: Computed time behaviors of the heat flux density corresponding to the left and right sides for different values of T_r.

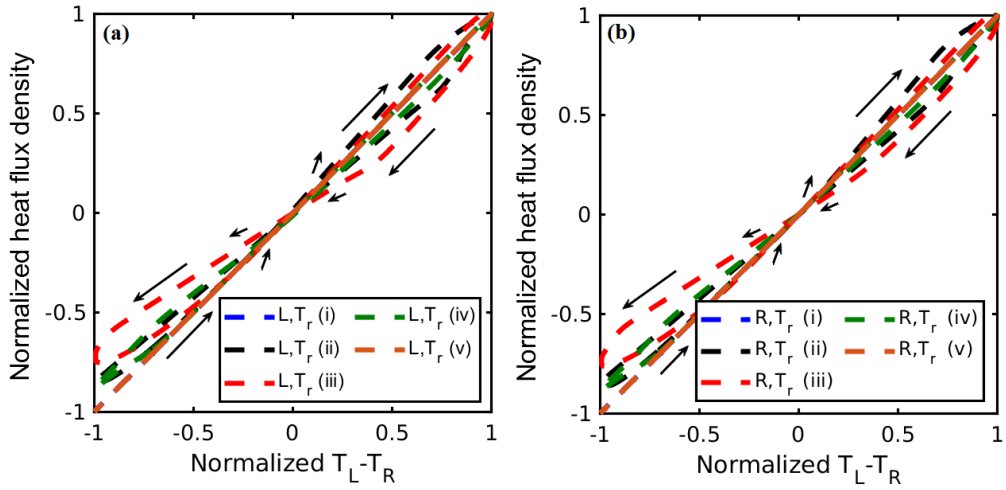

Figure 2.13: Normalized heat flux density-temperature difference curve according to the left (a) and right sides (b) for different values of T_r. The arrows indicate the direction of motion of the Lissajous characteristic curve.

Fig.2.16, Fig.2.17 and Fig.2.18, respectively. When T_r is outside of the hysteresis zone, which is case (i) and (v), there is almost no transition as seen in Fig.2.14 and Fig.2.18, respectively. When $T_r = 330.9$ K, the dots (20 dots in the figures), which represent the temperatures on the CTM, are moving close to the fully dielectric phase and they mostly move on the heating line except they just move a little bit inside of the hysteresis zone while cooling. This means that the CTM is generally in the dielectric phase. The positions of the dots according to the temperatures for the thermal conductivity and the enthalpy can be seen in Fig.2.14(a) and (b) at 0.25 of the time cycle, in Fig.2.14(c) and (d) at 0.5 of the time cycle, in Fig.2.14(e) and (f) at 0.75 of the time cycle and in Fig.2.14(g) and (h) at 1 of the time cycle, respectively. On the contrary, when we consider $T_r = 346.9$ K, we observe a similar behavior, but the dots are moving close to the fully metallic phase and they mostly move on the cooling line except they just move a little bit inside of the hysteresis zone while heating. Therefore, this means that the CTM generally shows the behaviors of the metallic phase in this case. In addition, the positions of the dots according to the temperatures for the thermal conductivity and the enthalpy can be seen in Fig.2.18(a) and (b) at 0.25 of the time cycle, in Fig.2.18(c) and (d) at 0.5 of the time cycle, in Fig.2.18(e) and (f) at 0.75 of the time cycle and in Fig.2.18(g) and (h) at 1 of the time cycle, respectively. As mentioned before, these behaviors cause a loss of the memristor effect and form a straight line on the Lissajous characteristic curve.

When we look at the case 2 (ii) and (iv) more deeply, although there is not a full transition, we see more transition effect on the CTM in these cases as seen in Fig.2.15 and Fig.2.17. When $T_r = 334.9$ K, which is case 2 (ii), the CTM can show fully dielectric behavior and a transition process on the hysteresis zone, but it cannot reach the temperatures that show fully metallic behavior. The positions of the dots according to the temperatures for the thermal conductivity and the enthalpy can be seen in Fig.2.15(a) and (b) at 0.25 of the time cycle, in Fig.2.15(c) and (d) at 0.5 of the time cycle, in Fig.2.15(e) and (f) at 0.75 of the time cycle and in Fig.2.15(g) and (h) at 1 of the time cycle, respectively. Firstly, the CTM heats up and the dots move on the heating line. At 0.25 of the time cycle, it starts to cool down and the dots move on the hysteresis zone to reach the cooling line. After that, it reaches the fully dielectric phase and starts to heat again as seen in Fig.2.15(c) and (d). Finally, it heats up and the dots follow the

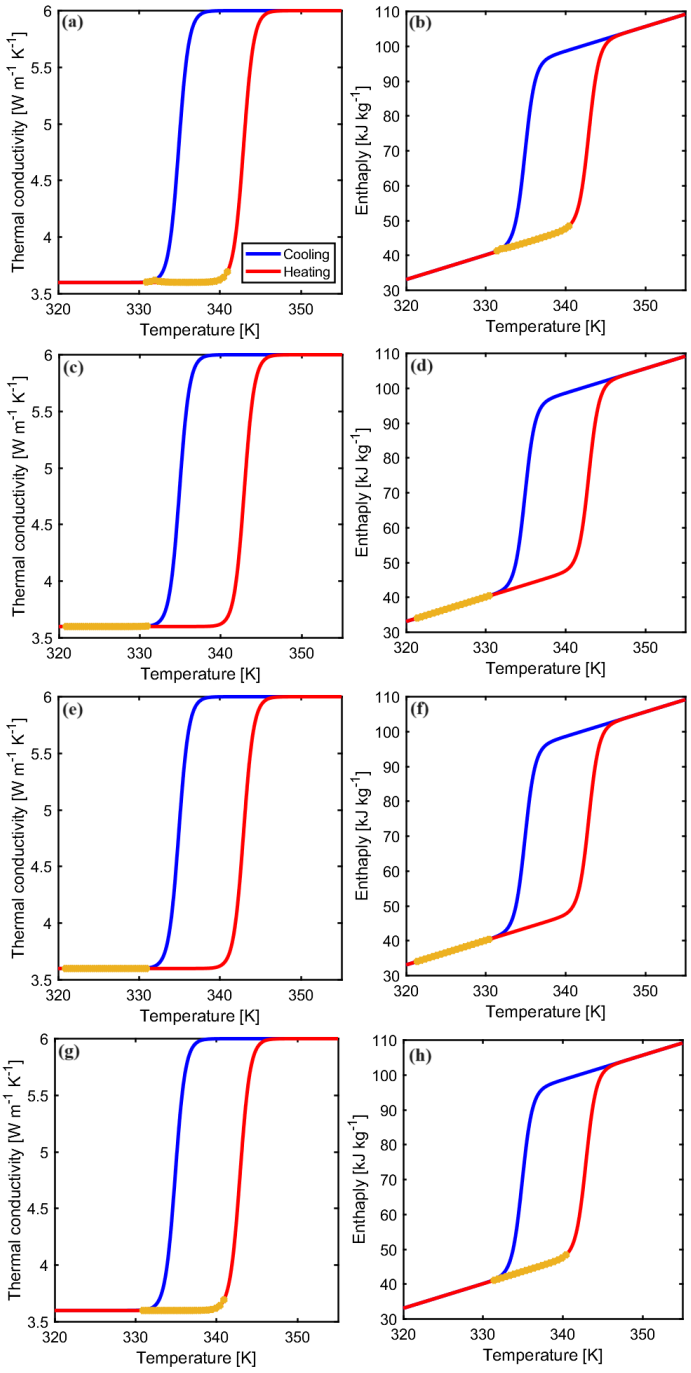

Figure 2.14: Corresponding thermal conductivity and enthalpy values according to the temperature distribution at 0.25 (a and b), 0.5 (c and d), 0.75 (e and f) and 1 (g and h) of the time cycle for $T_r = 330.9$ K, respectively.

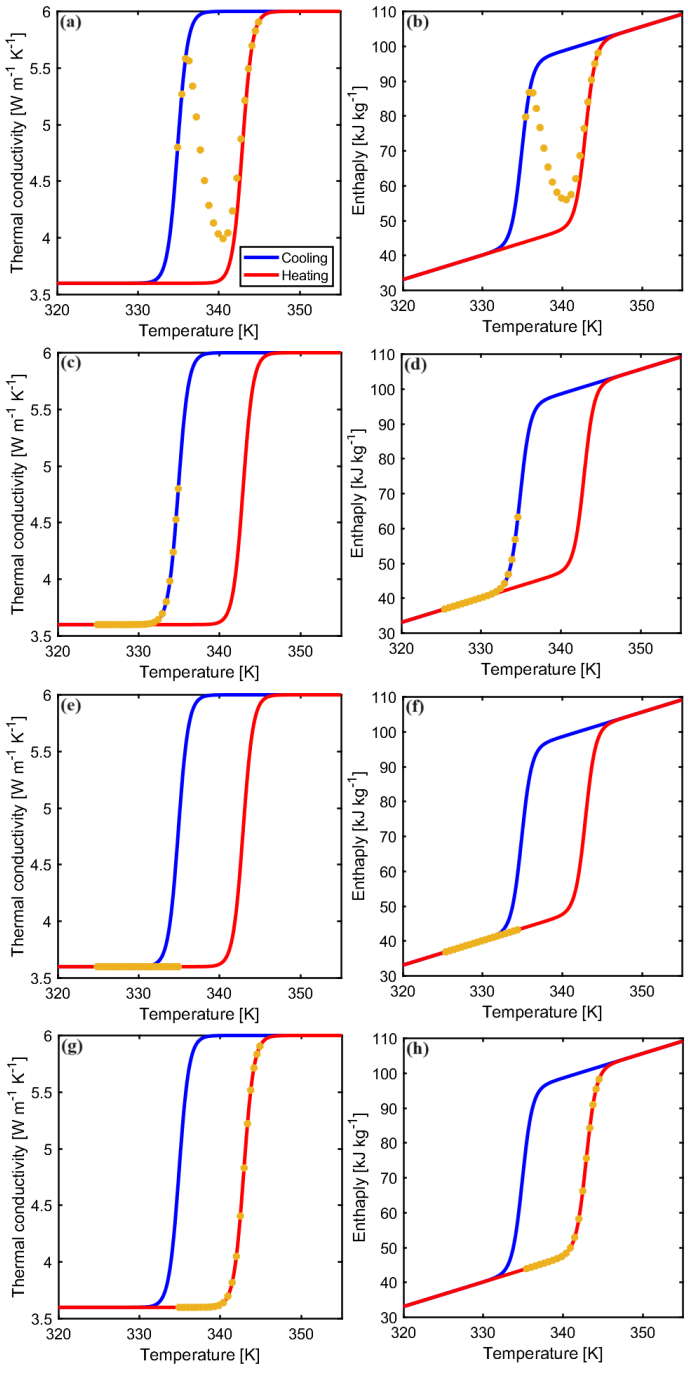

Figure 2.15: Corresponding thermal conductivity and enthalpy values according to the temperature distribution at 0.25 (a and b), 0.5 (c and d), 0.75 (e and f) and 1 (g and h) of the time cycle for $T_r = 334.9$ K, respectively.

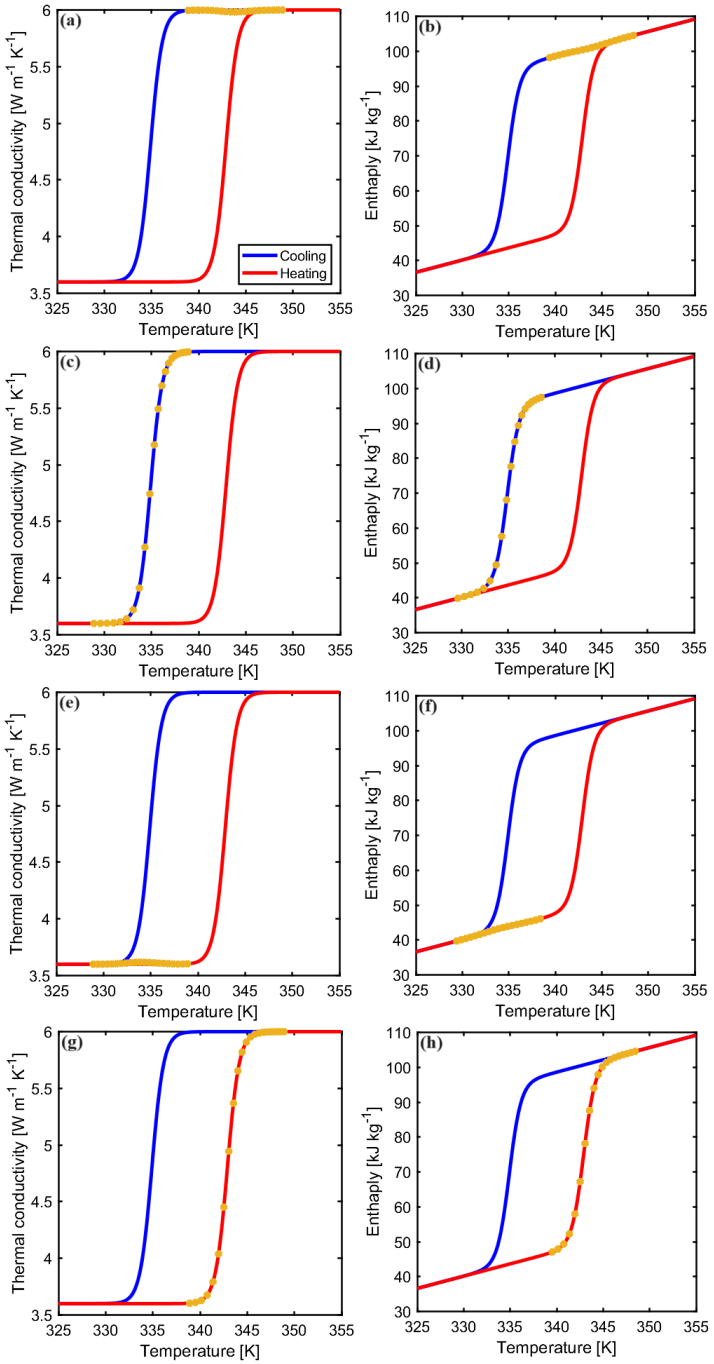

Figure 2.16: Corresponding thermal conductivity and enthalpy values according to the temperature distribution at 0.25 (a and b), 0.5 (c and d), 0.75 (e and f) and 1 (g and h) of the time cycle for $T_r = 338.9$ K, respectively.

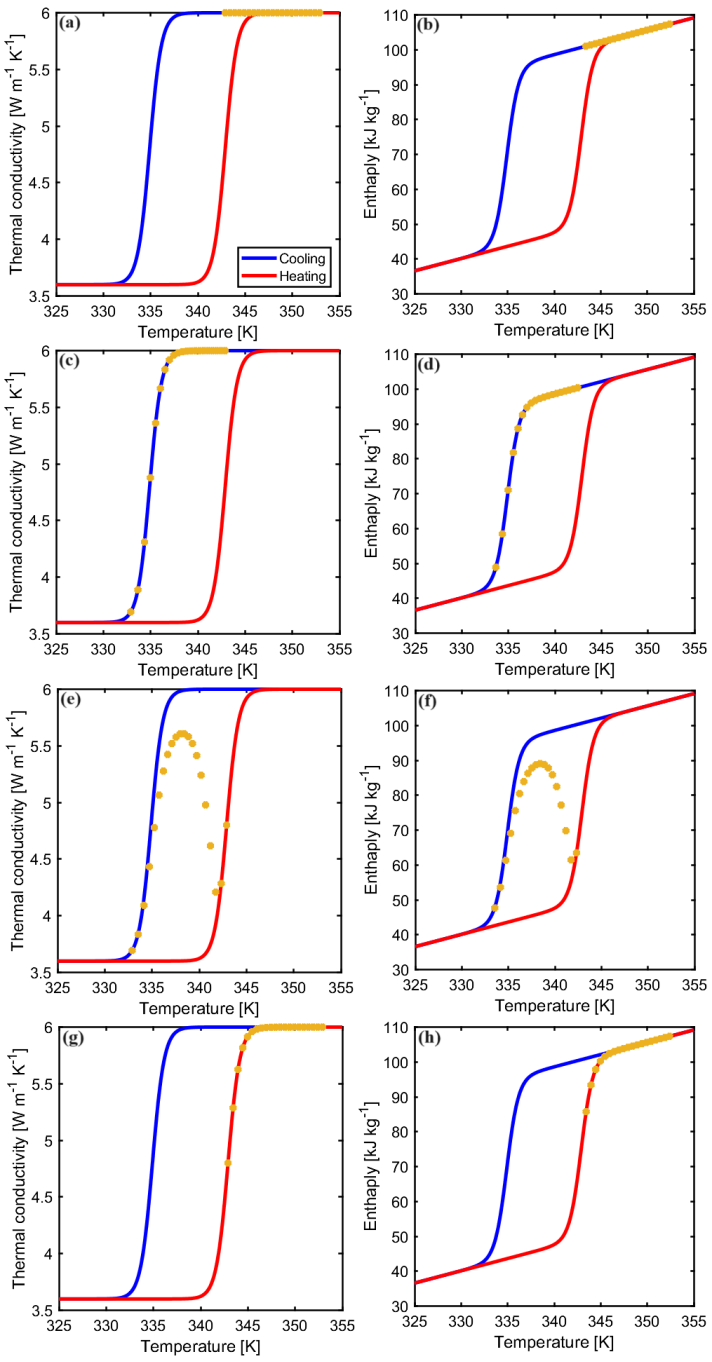

Figure 2.17: Corresponding thermal conductivity and enthalpy values according to the temperature distribution at 0.25 (a and b), 0.5 (c and d), 0.75 (e and f) and 1 (g and h) of the time cycle for $T_r = 342.9$ K, respectively.

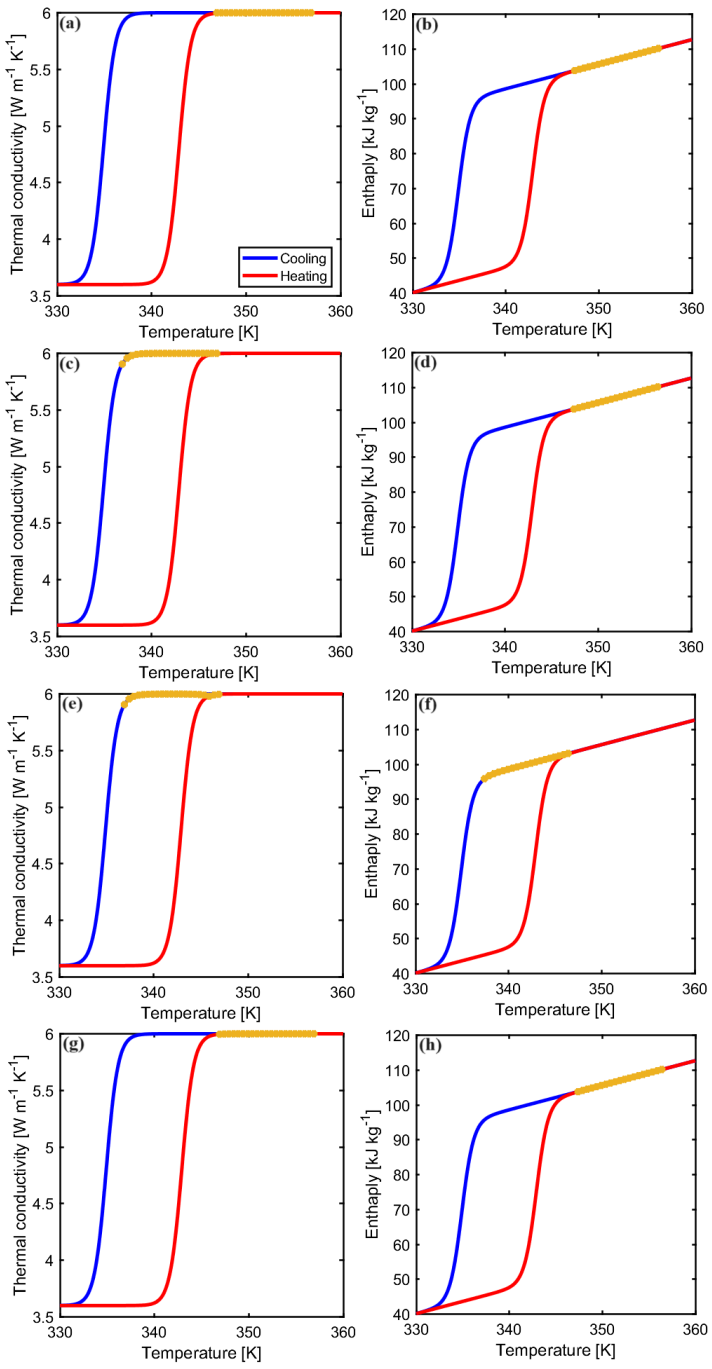

Figure 2.18: Corresponding thermal conductivity and enthalpy values according to the temperature distribution at 0.25 (a and b), 0.5 (c and d), 0.75 (e and f) and 1 (g and h) of the time cycle for $T_r = 346.9$ K, respectively.

heating line. Moreover, when $T_r = 342.9$ K, which is case 2 (iv), the CTM show fully metallic behavior, but cannot show a dielectric behavior. The positions of the dots according to the temperatures for the thermal conductivity and the enthalpy can be seen in Fig.2.17(a) and (b) at 0.25 of the time cycle, in Fig.2.17(c) and (d) at 0.5 of the time cycle, in Fig.2.17(e) and (f) at 0.75 of the time cycle and in Fig.2.17(g) and (h) at 1 of the time cycle, respectively. If we look at them more deeply, the CTM cools down from fully metallic phase as seen in Fig.2.17(a) and (b). Then, it starts to heat up as seen in Fig.2.17(c) and (d) and the dots move on the hysteresis zone (Fig.2.17(e) and (f)) until they reach the heating line. After that, the dots follow the heating line as shown in Fig.2.17(g) and (h). As mentioned before, we started to observe the memristor effect with these conditions as a result of seeing nonlinear behaviors due to the phase transition process.

Lastly, when we examine the case 2 (iii), which is $T_r = 338.9$ K, the CTM can have a full transition on the heating and cooling curves with this condition as mentioned before. The positions of the dots according to the temperatures for the thermal conductivity and enthalpy can be seen in Fig.2.16(a) and (b) at 0.25 of the time cycle, in Fig.2.16(c) and (d) at 0.5 of the time cycle, in Fig.2.16(e) and (f) at 0.75 of the time cycle and in Fig.2.16(g) and (h) at 1 of the time cycle, respectively. The CTM reaches the fully metallic phase and starts to cool down until the dielectric phase. After that, it heats up again until the metallic phase. We clearly see the memristor effect with these conditions as previously mentioned.

The temperature amplitude, T_a, is another parameter that affects the thermal memristor effect. We investigated five different values of T_a which are shown as case 3 in Table 2.1. The value of the frequency is taken as before and the value of T_r is set to be equal to the average of T_{oc} and T_{oh}. When T_a increases, the oscillation amplitude of the heat flux density becomes higher and more pronounced as shown in Fig.2.19. Besides, the Lissajous characteristic curve gets much wider and the nonlinear effect becomes more evident as shown in Fig.2.20(a) and (b) according to the left and right edges, respectively. In fact, we start with a straight line in case 3 (i) and the memristor effect is completely absent as previously experienced during the analysis of T_r. When the value of T_a is large enough starting the case 3 (iii), the material begins to manifest a complete phase change and the memristor effect becomes clearer. However, if the value of T_a continues

to increase, its impact saturates and does not cause any change on the Lissajous characteristic curve as experienced in case 3 (iv) and (v). On the other hand, the oscillation amplitude of the heat flux densities continues to increase when T_a increases even after the saturation is reached as seen in Fig.2.19. Furthermore, we report the results according to the values of $T_r = T_{oc}$ and $T_r = T_{oh}$ in Figs.2.21(a) and (b), respectively, while the remaining conditions remain the same. We observe similar behaviors and the Lissajous characteristic curve gets a little bit distorted at lower T_a for both $T_r = T_{oc}$ and $T_r = T_{oh}$. We almost see a straight line in case 3 (ii), because the phase change process in the material is even less complete in these conditions than what we observe in the case where $T_r = (T_{oc} + T_{oh})/2$.

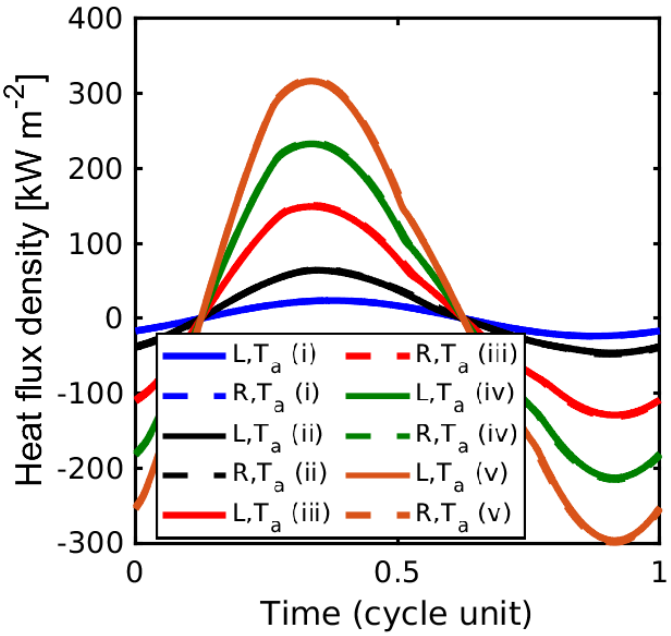

Figure 2.19: Computed time behaviors of the heat flux density corresponding to the left and right sides for different values of T_a when T_r is set to be equal to the average of T_{oc} and T_{oh}.

The effect of the temperature amplitude, T_a, on the thermal conductivity and enthalpy can be seen in more detail for the case 3 (i), (ii) and (iii)-(iv)-(v) in Fig.2.22, Fig.2.23 and Fig.2.24, respectively. When $T_a = 4$ K, the dots move on the hysteresis zone except some of them touch the heating and cooling lines at some points. However, they never follow the heating or cooling

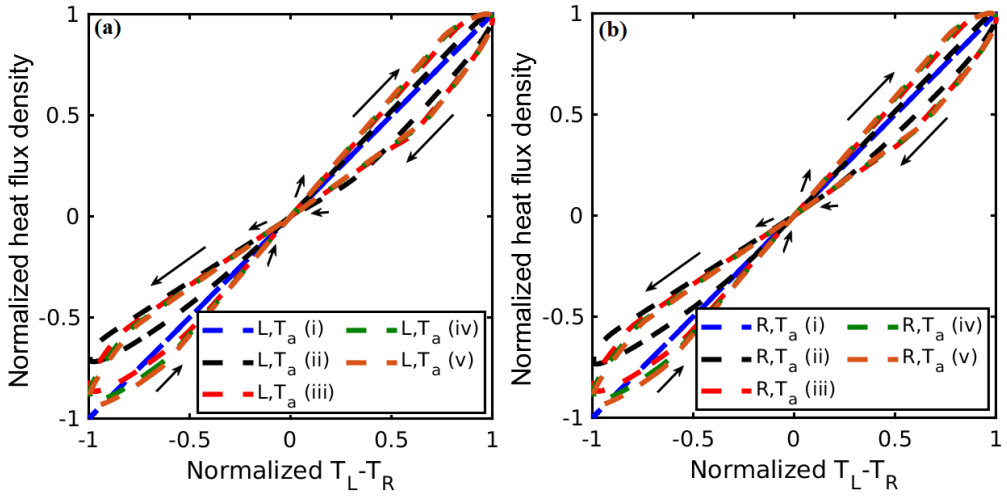

Figure 2.20: Normalized heat flux density-temperature difference curve according to the left (a) and right sides (b) for different values of T_a when T_r is set to be equal to the average of T_{oc} and T_{oh}. The arrows indicate the direction of motion of the Lissajous characteristic curve.

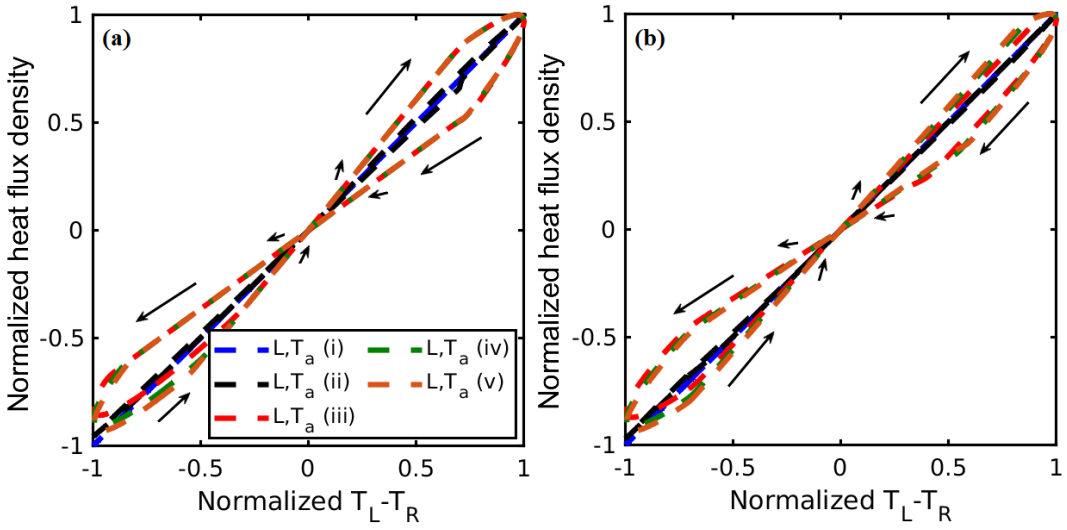

Figure 2.21: Computed time behaviors of the normalized heat flux density-temperature difference curve corresponding to the left side for different values of T_a when T_r equals T_{oc} (a) and T_{oh} (b). The arrows indicate the direction of motion of the Lissajous characteristic curve.

lines. Therefore, this means that the dots individually show the same values of the thermal conductivity even if their temperatures change with time. The positions of the dots according to

the temperatures for the thermal conductivity and enthalpy can be seen in Fig.2.22(a) and (b) at 0.25 of the time cycle, in Fig.2.22(c) and (d) at 0.5 of the time cycle, in Fig.2.22(e) and (f) at 0.75 of the time cycle and in Fig.2.22(g) and (h) at 1 of the time cycle, respectively. For instance, it starts like a bell-shaped curve while some dots on the heating line. After that, the CTM cools down and they move until the cooling line with the similar shape even if it expands and contracts with time during the movement. Then, they move back to the heating line as the CTM heats up. Therefore, we do not see the memristor effect as a result of these behaviors of the thermal conductivity and enthalpy and we observe a straight line instead of the Lissajous characteristic curve.

When we increase the value of the temperature amplitude, $T_a = 8$ K, we start to see almost a full phase transition except a little portion of the CTM. The positions of the dots according to the temperatures for the thermal conductivity and enthalpy can be seen in Fig.2.23(a) and (b) at 0.25 of the time cycle, in Fig.2.23(c) and (d) at 0.5 of the time cycle, in Fig.2.23(e) and (f) at 0.75 of the time cycle and in Fig.2.23(g) and (h) at 1 of the time cycle, respectively. It should be noticed in the beginning during the cooling process that some dots are in the metallic phase even if we see a movement inside of the hysteresis zone. After that, the CTM fully cools down and the dots fully move on the cooling line until reaching the dielectric phase, we start to see again the same behavior that we observed during the beginning of the cooling, but this time during the heating process of the CTM. Finally, the CTM again heats up and the dots move on the heating line until reaching the metallic phase. Therefore, we start to obtain the Lissajous characteristic curve with a more pronounced nonlinear effect with these conditions.

When we continue to increase the value of T_a, it will saturate and its impact on the memristor effect does not change as previously mentioned, because the CTM starts to show a complete phase change. This situation is clearly seen in Fig.2.24. The whole dots on the CTM show fully metallic phases at 0.25 of the time cycle in all cases: case 3 (iii), (iv) and (v). Then, the CTM cools down and the dots follow the cooling line until fully transforming to the dielectric phase. After that, the CTM heats up and the dots follow the heating line until reaching the fully metallic phase. Therefore, although the value of T_a affects the oscillation amplitude of the heat flux density, it does not cause any change on the Lissajous characteristic curve after the saturation.

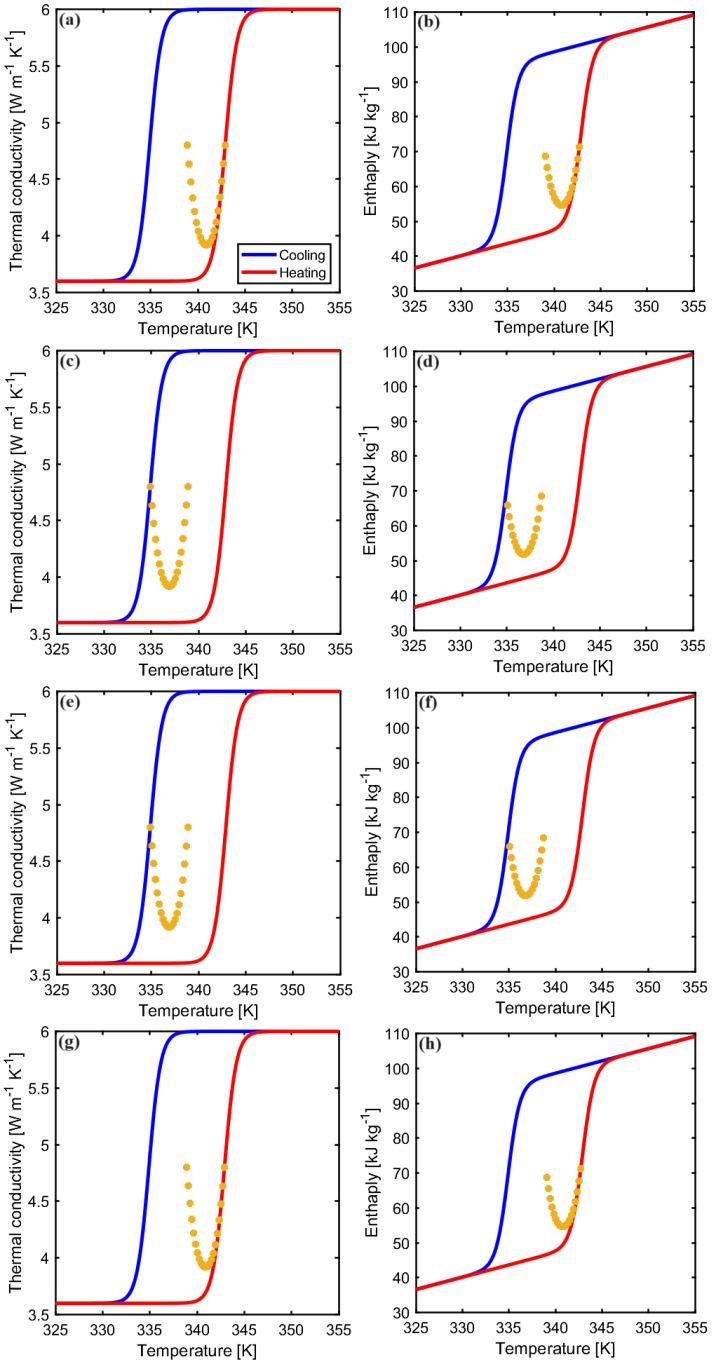

Figure 2.22: Corresponding thermal conductivity and enthalpy values according to the temperature distribution at 0.25 (a and b), 0.5 (c and d), 0.75 (e and f) and 1 (g and h) of the time cycle for $T_a = 4$ K when T_r is set to be equal to the average of T_{oc} and T_{oh}, respectively.

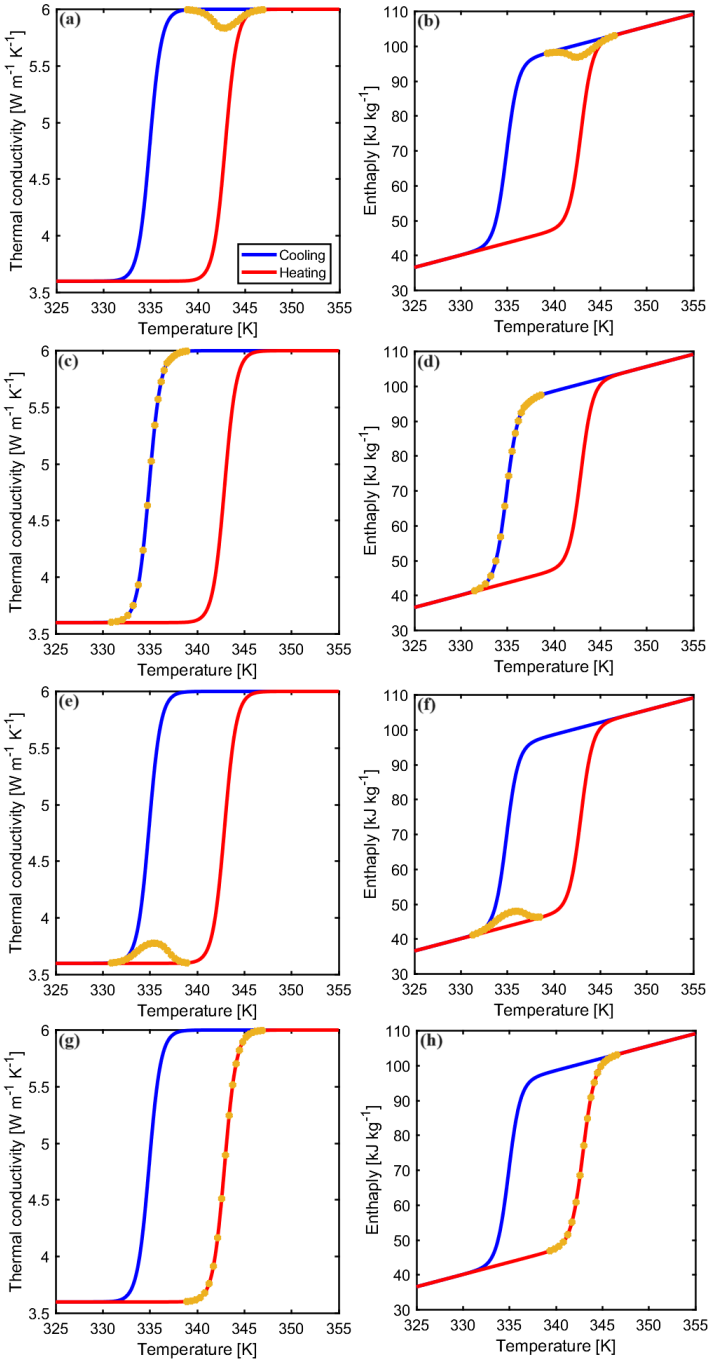

Figure 2.23: Corresponding thermal conductivity and enthalpy values according to the temperature distribution at 0.25 (a and b), 0.5 (c and d), 0.75 (e and f) and 1 (g and h) of the time cycle for $T_a = 8$ K when T_r is set to be equal to the average of T_{oc} and T_{oh}, respectively.

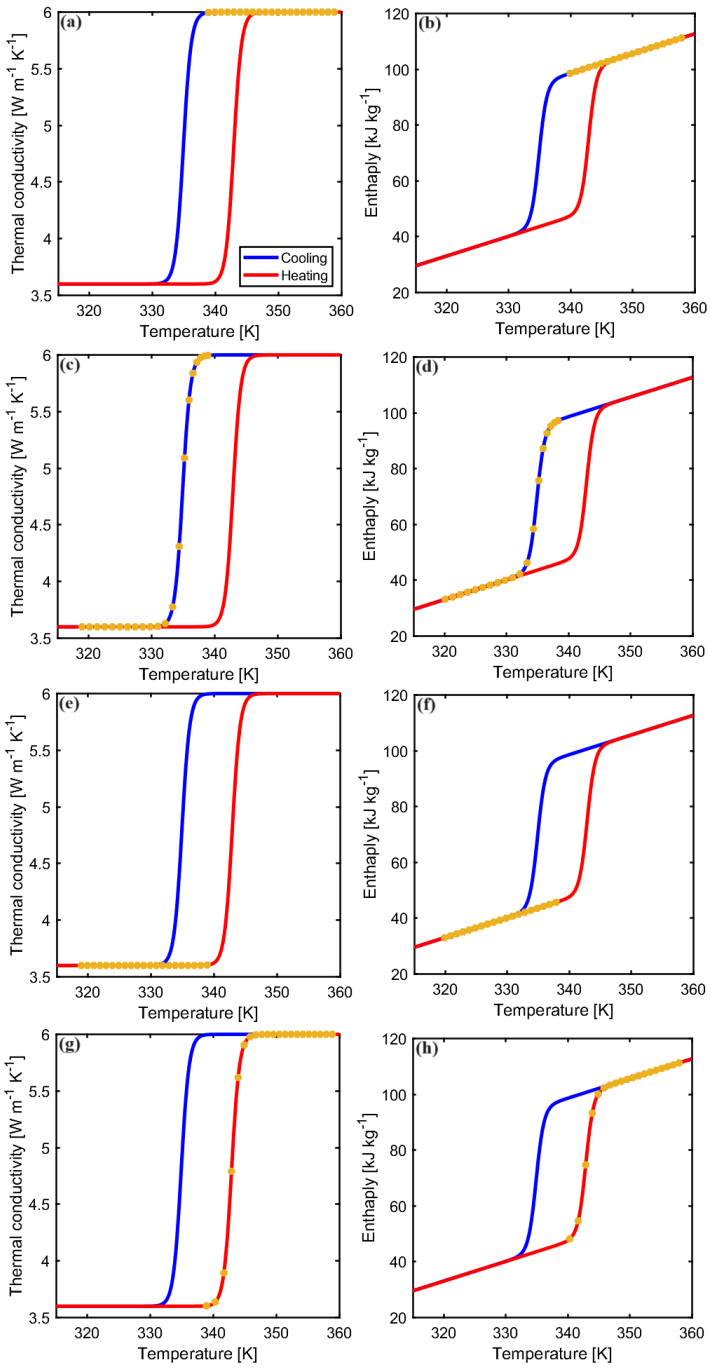

Figure 2.24: Corresponding thermal conductivity and enthalpy values according to the temperature distribution at 0.25 (a and b), 0.5 (c and d), 0.75 (e and f) and 1 (g and h) of the time cycle for T_a = 20 K, 32 K and 44 K when T_r is set to be equal to the average of T_{oc} and T_{oh}, respectively.

2.4 Conclusion

In this chapter, we have studied a CTM that is made of a piece of VO_2 under dynamical conditions while considering the full properties of VO_2, including the hysteresis zone. Throughout the study, various parameters, such as the frequency f, the reference temperature T_r and the temperature amplitude T_a of the applied modulated boundary conditions, are examined by changing them separately to understand their effects on the Lissajous characteristic curve for the CTM. We observed that the nonlinear variations of the thermal conductivity and specific heat of VO_2, combined with the hysteresis zone, significantly affect the Lissajous characteristic curve. When the reference temperature and the temperature amplitude of the applied boundary conditions are set accordingly to provide a complete phase change, we start to see a clear Lissajous characteristic curve. Otherwise, the Lissajous characteristic curve gets distorted and indeed becomes a straight line if there is no phase change. In addition, the temperature amplitude of the applied boundary conditions affects the Lissajous characteristic curve up to a certain value, after which its effect becomes insignificant. This temperature amplitude value corresponds to the smallest one leading to a complete phase transition cycles. Another key point that affects the CTM and the Lissajous characteristic curve is the frequency of the applied boundary sinusoidal temperature. The Lissajous characteristic curve gets distorted as it increases. There is a threshold frequency above which the thermal memristor effect vanishes. Consequently, this study has demonstrated the importance of examining the CTM by considering the hysteresis region of VO_2 in a full transient and dynamical heat conduction regime. The capacitive effect has undoubtedly a crucial role in the occurrence and vanishing of the thermal memristor effect. As mentioned before, there are very few studies on the thermal memristor in the literature. Considering the outcomes of this study, more studies should be conducted under transient and dynamical conditions by including the hysteresis zone to better understand the behaviors of the thermal memristor and to reveal its further potential.

Résumé du Chapitre 2

Le chapitre 2 est consacré à nos travaux sur les memristors thermiques. Dans la littérature, il n'existe que deux études sur le memristor thermique conductif (MTC), celles de Ben-Abdallah [47] et de Yang et al. [48]. Bien que ces deux études aient exploré le cas d'un memristor basé sur le VO_2, elles ont mené leurs études dans des conditions quasi-stationnaires, en changeant divers paramètres tels que le rapport de conductivité thermique du matériau et l'amplitude de la température des conditions limites modulées. Par conséquent, ils ont omis l'effet capacitif. Dans notre analyse, nous étudions un MTC à base de VO_2 tout en considérant l'ensemble des propriétés de ce matériau en appliquant les conditions limites modulées, et nous élargissons donc l'analyse précédente en examinant l'effet capacitif et son impact en changeant divers paramètres. Tout d'abord, nous commençons ce chapitre en expliquant comment nous modélisons la zone d'hystérésis du VO_2 et comment nous appliquons le modèle enthalpique. Ensuite, nous présentons notre travail qui compare les résultats de nos calculs avec ceux de Krapez afin de vérifier notre modélisation. Dans la deuxième partie du chapitre, nous faisons la présentation des résultats et leur discussion.

Modélisation théorique

Mise en œuvre d'un modèle simple

Notre étude a débuté par l'examen d'un cas simple, illustré en Fig.2.1, afin de développer notre modèle complexe étape par étape. À cette fin, l'équation générale unidimensionnelle de diffusion de la chaleur sans source de chaleur interne (Éq.2.1) est résolue par la méthode des différences finies. Sa représentation en différences finies peut s'écrire sous la forme de l'Éq.2.2 [144]. Pour vérifier la précision de notre modèle numérique, nous avons simplifié et non-dimensionnalisé l'Éq.2.1 afin d'obtenir une solution linéaire et la comparer à la solution numérique. Ensuite, nous avons comparé les solutions analytiques et numériques dimensionnées pour ce cas simple avant de rendre notre modélisation plus complexe. Nous avons obtenu un excellent accord entre les deux approches, comme le montre la Fig.2.3.

Le memristor thermique conductif et la modulation de la température des bains thermiques

Dans notre analyse, nous considérons un MTC dans une géométrie plane. Il est constitué d'un morceau de VO_2 de 1 mm, comme le montre la Fig.2.4, et nous considérons que la conduction est le seul mode de transfert de chaleur entre les deux bains thermiques. Nous appliquons deux températures sinusoïdales aux deux frontières du MTC, qui sont exprimées dans les Éqs. (2.27) et (2.28) pour les côtés gauche et droit, respectivement.

Modélisation de la zone d'hystérésis

Lorsqu'il n'y a que du chauffage ou du refroidissement dans un cas avec des conditions limites de Dirichlet, cela peut être modélisé relativement plus facilement que dans les cas avec des conditions limites dynamiques, parce que dans un cas avec des conditions limites de Dirichlet, nous pouvons modéliser la conductivité thermique et la capacité thermique sans tenir compte de la zone d'hystérésis en ajustant soigneusement les températures limites appliquées. Par conséquent, dans ce type d'analyse, nous pouvons utiliser directement l'Éq.1.16 pour la conductivité thermique et l'Éq.1.17 pour la capacité thermique spécifique. Cependant, cela n'est pas possible lors d'une analyse avec des conditions aux limites dynamiques. Nous devons prendre en compte la zone d'hystérésis. Nous utilisons la méthode enthalpique pour modéliser la zone d'hystérésis pour l'analyse des conditions limites dynamiques. Les Fig.2.5(a) et (b) montrent, respectivement, les comportements calculés de la conductivité thermique et de l'enthalpie du VO_2 en fonction de la température autour de la zone de transition de phase pour les processus de chauffage et de refroidissement.

Ramirez et al. [53] et Gurvitch et al. [54] ont réalisé des études pour comprendre le comportement de l'hystérésis pour les cas qui s'arrêtent au milieu des courbes de chauffage ou de refroidissement, tels que les points 2, 3, 5 ou 6 dans les Fig.2.5(a) et (b). Plus tard, en 2023, Krapez [55] a réalisé une étude numérique détaillée sur l'effet de pompage de la conduction thermique dans le VO_2, tout en prenant en compte l'effet d'hystérésis. Dans son étude, Krapez a exploité les branches non hystérétiques observées lors de l'analyse de la résistance électrique et de la réflectivité optique dans l'étude de Gurvitch et al. [54]. Il a supposé que ces branches

devraient également être observées dans le comportement de la conductivité thermique, et a adopté cette hypothèse pour son étude [55]. Afin de modéliser l'effet d'hystérésis, il a également supposé que les boucles mineures observées lors de petites excursions pouvaient également être observées lors de grandes excursions [55]. La méthode de Krapez [55] constitue le fondement de notre étude. Nous avons adapté sa modélisation dans le cadre de ce travail. Ainsi, lorsque le chauffage ou le refroidissement s'arrête au milieu de la transition, comme aux points 2, 3, 5 ou 6 de la Fig.2.5(a) ou (b), et que l'on commence à refroidir ou à chauffer, la transition suit les courbes vertes. Par exemple, lorsqu'il y a un chauffage et que le système commence à refroidir au milieu de la transition de phase au point 2, il suit la courbe verte jusqu'à la courbe de refroidissement (point 6). Toutefois, si le refroidissement s'arrête sur la courbe verte avant d'atteindre la courbe de refroidissement, comme aux points 7 ou 8, et que le système recommence à chauffer, la transition de phase suit la courbe verte jusqu'à la courbe de chauffage (point 2).

Modélisation numérique du memristor thermique conductif

Dans le cadre de notre analyse du MTC, nous avons résolu numériquement l'équation générale unidimensionnelle de diffusion de la chaleur sans source de chaleur interne, exprimée en termes d'enthalpie, telle que décrite dans l'Éq.2.30, par la méthode explicite des différences finies. L'Éq.2.30 peut être formulée explicitement comme le montre l'Éq.2.32. Après avoir obtenu l'enthalpie à chaque nœud pour le pas de temps suivant, nous trouvons les températures qui correspondent à ces valeurs d'enthalpie inversement. Les conductivités thermiques à chaque nœud sont alors déterminées. Nous déterminons ensuite les valeurs de température à partir des valeurs d'enthalpie actuelles en utilisant une procédure numérique complète, qui donne le même résultat que la procédure semi-analytique de Krapez, en identifiant le processus actuel (refroidissement/chauffage) du système.

En outre, Krapez a analysé un système similaire illustré à la Fig.2.4. Il a examiné une couche de 1 mm composée de VO_2 et a appliqué une condition limite sinusoïdale à la limite gauche, comme indiqué dans l'in Éq.2.38, tandis que la limite droite avait une température fixe, comme indiqué dans l'Éq.2.39 [55]. Nous avons également suivi la même procédure avec les mêmes paramètres que ceux décrits dans l'article de Krapez pour vérifier la validité de notre modèle

avant de commencer l'analyse dans le cadre de notre étude. Nous avons obtenu des résultats presque identiques pour différents paramètres, comme le montre la Fig.2.8.

Conclusion

Dans le cadre de notre étude, nous analysons les impacts de trois paramètres distincts : f, T_r et T_a pour l'analyse du MTC, comme illustré dans le Tableau 2.1. f représente la fréquence de la température sinusoïdale appliquée à la frontière, tandis que T_r correspond à une température de référence et T_a désigne l'amplitude de la composante modulée en température. Tout au long de l'étude, nous utilisons la moyenne des températures de transition de phase des processus de chauffage et de refroidissement du VO_2 pour T_r, comme indiqué dans l'Éq.2.29, sauf indication contraire. Il convient de préciser que la modification ne s'effectue que sur un seul paramètre à la fois.

En conclusion, nous avons observé que les variations non linéaires de la conductivité thermique et de la chaleur spécifique du VO_2, combinées à la zone d'hystérésis, affectent de manière significative la courbe caractéristique de Lissajous. Lorsqu'il y a un changement de phase complet grâce à l'ajustement des températures de transition T_r et T_a, nous commençons à observer une courbe caractéristique de Lissajous claire. Dans le cas contraire, la courbe caractéristique de Lissajous est déformée et devient une ligne droite s'il n'y a pas de changement de phase. Lorsque $T_r = 338.9$ K, qui correspond au milieu de la zone d'hystérésis, l'effet non linéaire devient tout à fait évident et l'effet memristor est clairement visible, car le matériau présente les deux phases et peut effectuer un cycle complet sur les courbes de chauffage et de refroidissement dans cette condition. Cependant, lorsque nous nous approchons des valeurs de T_{oh} et T_{oc}, qui représentent les températures de transition de phase critique de VO_2 pour les processus de chauffage et de refroidissement, respectivement, l'effet memristor commence à disparaître en raison d'un processus de changement de phase incomplet. En outre, lorsque la valeur de T_a est suffisamment élevée, le matériau commence à manifester une phase complète et l'effet memristor devient plus manifeste. Cependant, si la valeur de T_a continue d'augmenter, son impact finit par saturer et ne provoque aucun changement sur la courbe caractéristique de Lissajous. Nous avons également

observé que f est un autre facteur clé qui influe sur ce phénomène. Plus f est élevé, plus la courbe caractéristique de Lissajous se déforme. Par conséquent, cette étude montre que l'effet capacitif a un impact clair sur la manifestation de l'effet thermique du memristor.

Chapter 3

Conductive Thermal Diode

Contents

3.1 Introduction 132

3.2 Theoretical modeling of the linear conductive thermal diode 132

3.3 Results and discussion of the linear conductive thermal diode 135

3.4 Theoretical modeling of the conductive thermal diode under Dirichlet boundary conditions 137

3.4.1 Nondimensionalization of the transient process 140

3.4.2 Nondimensionalization of the steady-state process 142

3.4.3 Thermal rectification analysis under steady-state conditions 147

3.5 Results and discussion of the conductive thermal diode under Dirichlet boundary conditions 147

3.6 Theoretical modeling of the conductive thermal diode under dynamical boundary conditions 158

3.6.1 Models and temperature modulation of the thermal baths 158

3.7 Results and discussion of the conductive thermal diode under dynamical boundary conditions 160

3.8 Theoretical modeling of the capacitive thermal diode 163

3.8.1 Capacitive thermal diode with constant heat capacities 164

3.8.2 Capacitive thermal diode with temperature dependent heat capacity 165

3.9 Results and discussion of the capacitive thermal diode 167

3.10 Conclusion 176

3.1 Introduction

Many studies examine the thermal rectification of the thermal diodes in steady-state conditions and the interest for transient analysis is increasing as we summarized in the literature review section in Chapter 1 such as the studies [38, 39, 96, 97]. However, we have not encountered any prior work that studied conductive thermal diodes (CTD) while considering properties of VO_2 in full aspects under transient conditions, including the hysteresis zone. In addition, the capacitive effect is omitted in the literature. Therefore, in this chapter, we will study a CTD composed of VO_2 and SiO_2 with both fixed and sinusoidal boundary conditions while including the full properties of VO_2 and the capacitive effect. The thermal rectification of the CTD will be investigated in detail by changing different intrinsic and extrinsic parameters. As an introductory part, our analysis will start with a linear CTD instead of a CTD composed of VO_2 and SiO_2. Then, we will examine the thermal rectification of the CTD that is made of VO_2 and SiO_2 under fixed boundary conditions for various intrinsic and extrinsic parameters, such as different hot and cold applied boundary condition values, phase transition slope and latent heat of the PCM, ratio of the thermal conductivity of the metallic and dielectric phases of the PCM, width between the phase transition temperatures for the heating and cooling processes of the PCM, and interface thermal resistance. After that, we will continue our analysis with the same CTD by applying sinusoidal boundary conditions and including the hysteresis zone of VO_2. In this case, we will examine the thermal rectification of the CTD by changing the frequency and temperature amplitude of the applied sinusoidal boundary conditions. Finally, we will conclude this chapter with a separate case study to examine the impact of the capacitive effect in more detail.

3.2 Theoretical modeling of the linear conductive thermal diode

Although our main focus in this work is the study of the behavior of a CTD that is made of VO_2 and SiO_2, we performed an introductory part as a small case study to examine the possibility of a conductive thermal rectification behavior of a thermal diode that is made of two different solid materials with constant thermal properties. For this purpose, we examined a CTD like the one shown in Fig.3.1, but it is composed of two different solid materials 1 and 2 instead of VO_2 and SiO_2. Both solid materials have the same length l and cross section S, and they

have temperature independent thermophysical properties. We also assume a non-perfect thermal contact between the two materials, that is described by a constant interface thermal resistance.

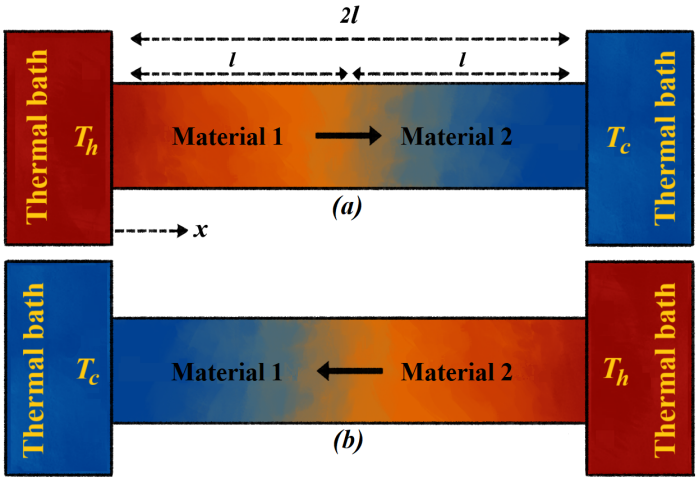

Figure 3.1: Schematic representation of the linear CTD in the forward (a) and backward (b) configurations.

The starting point of our modeling is the classical Fourier based heat diffusion equation that we shall solve in each material depending on the nature of the conditions imposed to the boundaries of the CTD. This equation is given by:

$$\frac{\partial T_i}{\partial t} - \alpha_i \frac{\partial^2 T_i}{\partial x^2} = 0 \tag{3.1}$$

where T, t and x refer to the temperature, time and spatial coordinate within each material. $\alpha_i = k_i/(\rho_i c_i)$, k_i, ρ_i and c_i are the thermal diffusivity, thermal conductivity, density and specific heat of material $i = 1$ and 2, respectively. In order to have a general approach, we adopt a nondimensional analysis by introducing the nondimensional temperature $\theta_i = T_i/T_{amb}$, time $t^* = (\overline{\alpha}t)/l^2$ and spatial coordinate $x^* = x/l$ where $\overline{\alpha} = (\alpha_1 + \alpha_2)/2$ and T_{amb} is the ambient temperature. Eq.3.1 becomes:

$$\frac{\partial^2 \theta_i}{\partial x^{*2}} - \frac{\overline{\alpha}}{\alpha_i}\frac{\partial \theta_i}{\partial t^*} = 0 \tag{3.2}$$

The nondimensional heat flux density is expressed as:

$$\phi_i^* = \frac{\phi_i}{\phi_0} = -\kappa_i \frac{\partial \theta_i}{\partial x^*} \tag{3.3}$$

where $\phi_i = -k_i \partial T_i / \partial x$ is the Fourier's law for the heat flux density, $\phi_0 = \overline{k} T_{amb}/l$, $\kappa_i = k_i/\overline{k}$ and $\overline{k} = (k_1 + k_2)/2$.

The theoretical modeling is based on the use of the thermal quadrupoles method (TQM) to solve the heat equation in each material [145]. We consider the initial temperature of the CTD to be zero. The TQM formalism is based on using Laplace's transform to solve the heat equation [145]. We note τ_{il}, τ_{ir}, φ^*_{il} and φ^*_{ir}, respectively, the Laplace transforms of the nondimensional left temperature, the nondimensional right temperature, the nondimensional left heat flux density and the nondimensional right heat flux density of the material "i" according to the direction of the x axis shown in Fig.3.1(a). Based on the TQM formalism, the vectors (temperature-heat flux density) are linked through a matrix form relation as [145]:

$$\begin{pmatrix} \tau_{il} \\ \varphi^*_{il} \end{pmatrix} = \begin{pmatrix} A^*_i = cosh(s^*_i) & B^*_i = \frac{sinh(s^*_i)}{\kappa_i s^*_i} \\ C^*_i = \kappa_i s^*_i sinh(s^*_i) & D^*_i = cosh(s^*_i) \end{pmatrix} \begin{pmatrix} \tau_{ir} \\ \varphi^*_{ir} \end{pmatrix} \tag{3.4}$$

where $s^{*2}_i = (\overline{\alpha}/\alpha_i) p^*$ and $p^* = pl^2/\overline{\alpha}$ and p represent, respectively, Laplace's number and variable. s^*_1, κ_1, s^*_2 and κ_2 can be re-expressed for layer 1 and layer 2, respectively, after substituting related variables as follows: $s^*_1 = \sqrt{[1/2 + b/2a]\, p^*}$, $s^*_2 = \sqrt{[1/2 + a/2b]\, p^*}$, $\kappa_1 = 2a/(1+a)$ and $\kappa_2 = 2/(1+a)$ where $a = k_1/k_2$ and $b = (\rho_1 c_1)/(\rho_2 c_2)$.

By exploiting the continuity of the heat flux density at the interface between the two material layers 1 and 2, we can straightforwardly obtain the relation between the vectors at the boundaries of the CTD as:

$$\begin{pmatrix} \tau_{1l} \\ \varphi^*_{1l} \end{pmatrix} = \begin{pmatrix} A^*_1 & B^*_1 \\ C^*_1 & D^*_1 \end{pmatrix} \begin{pmatrix} 1 & r^* \\ 0 & 1 \end{pmatrix} \begin{pmatrix} A^*_2 & B^*_2 \\ C^*_2 & D^*_2 \end{pmatrix} \begin{pmatrix} \tau_{2r} \\ \varphi^*_{2r} \end{pmatrix} = \begin{pmatrix} A & B \\ C & D \end{pmatrix} \begin{pmatrix} \tau_{2r} \\ \varphi^*_{2r} \end{pmatrix} \tag{3.5}$$

where r^* represents the nondimensional thermal resistance at the interface between the materials 1 and 2 that describes the discontinuity of the temperature at the interface.

In order to study the thermal rectification of the CTD, we shall assume two opposing configurations for the direction of the heat flux density; a forward configuration and a backward configuration as previously illustrated in Fig.3.1(a) and (b). Let us assume the forward configuration where the hot and cold temperature excitations are applied on the left and right boundaries,

respectively. In this case, we can rewrite Eq.3.5 as:

$$\begin{pmatrix} \tau_{Hf} \\ \varphi^*_{Hf} \end{pmatrix} = \begin{pmatrix} A & B \\ C & D \end{pmatrix} \begin{pmatrix} \tau_{Cf} \\ \varphi^*_{Cf} \end{pmatrix} \tag{3.6}$$

In the backward configuration, we have then:

$$\begin{pmatrix} \tau_{Cb} \\ \varphi^*_{Cb} \end{pmatrix} = \begin{pmatrix} A & B \\ C & D \end{pmatrix} \begin{pmatrix} \tau_{Hb} \\ \varphi^*_{Hb} \end{pmatrix} \tag{3.7}$$

From Eqs (3.6) and (3.7), we can easily get the general expression of the heat flux density at the hot and cold boundaries in both forward and backward configurations. We finally obtain the following expressions at the cold boundaries in both configurations:

$$\varphi^*_{Cf} = \frac{1}{B}\tau_{Hf} - \frac{A}{B}\tau_{Cf} \tag{3.8}$$

$$\varphi^*_{Cb} = \frac{D}{B}\tau_{Cb} - \frac{1}{B}\tau_{Hb} \tag{3.9}$$

The real time behaviors can be obtained easily using a numerical Laplace inverse transform algorithm. Also, we shall note that $\tau_{Cf} = \tau_{Cb} = \tau_C$ and $\tau_{Hf} = \tau_{Hb} = \tau_H$. Furthermore, it should be reminded here that the general information about the thermal rectification and the thermal rectification formula (Eq. 1.25) that we use in our analysis are explained in Chapter 1.

3.3 Results and discussion of the linear conductive thermal diode

We start our CTD analysis by investigating the case study of the thermal diode that is made of two different solid materials with constant thermal properties. For this purpose, we examine the thermal rectification time behavior for two different Dirichlet boundary conditions sets. The first one corresponds to fixed boundary conditions and the second one is the case where the boundary conditions are sinusoidal. In order to shed light on one of the inherent features of Fourier's heat diffusion equation in linear systems, we consider illustrative examples in which we set the nondimensional thermal resistance at the interface r^* to 1 and both a and b to 2. We only change one parameter while keeping the other two parameters the same. The parameters and the investigated values can be seen in Table 3.1. Also, the ambient temperature T_{amb} is set to 300 K. For the first case, the boundary conditions for the hot and cold sides are taken to be

352.9 K and 324.9 K, respectively. For the second case, we apply two sinusoidal temperatures at the boundaries as expressed in Eqs.(3.10) and (3.11):

$$T_L = T_h + T_a \cos(2\pi f t) \tag{3.10}$$

$$T_R = T_c + T_a \cos(2\pi f t) \tag{3.11}$$

where we set the temperatures of 352.9 K and 324.9 K for the hot side T_h and the cold side T_c, respectively. T_a and the frequency f are set to 10 K and 0.1 Hz, respectively, so that although the temperatures at both sides are sinusoidal, one side always remains hot and the other side always remains cold.

Table 3.1: Investigated parameters and cases for the linear CTD.

Case 1 - a ($b = 2$ and $r^* = 1$)			
	(i)	(ii)	(iii)
a	0.5	1	2
Case 2 - b ($a = 2$ and $r^* = 1$)			
	(i)	(ii)	(iii)
b	0.5	1	2
Case 3 - r^* ($a = 2$ and $b = 2$)			
	(i)	(ii)	(iii)
r^*	0.5	1	1.5

Henceforth after this point, the nondimensional heat flux densities will be represented as ϕ^*_+ and ϕ^*_- in the forward and backward configurations, respectively. The behaviors of the nondimensional heat flux densities ϕ^*_+ and ϕ^*_- and the thermal rectification factor R for the cases of the fixed Dirichlet boundary conditions are shown in Fig.3.2. The nondimensional heat flux density behaviors corresponding to forward and backward configurations and the thermal rectification factor behavior with respect to the dimensionless time for the parameters a, b and r^* are shown in Fig.3.2(a) and (b), (c) and (d), and (e) and (f), respectively. As our modeling is based on Fourier's law, we only account for times beyond the diffusion time in order to avoid the drawback of the parabolic nature of the heat equation. The diffusion time corresponds to the

time required for the temperature front to diffuse from the hot boundary to the cold one and can roughly be estimated as $l^2/\overline{\alpha}$. In all parameters, we actually observe a thermal rectification at the beginning of the transient process under these conditions. The values of the nondimensional heat flux densities in the forward and backward configurations increase and decrease with time, respectively, and the value of R reaches 1 in two occasions that occur when one of the two heat flux densities approaches 0. However, when ϕ_+^* and ϕ_-^* intersect, the value of R drops to 0. When the system reaches its steady-state regime, R vanishes as expected. The time behavior of R is an inherent feature of the classical Fourier's heat diffusion equation in a linear system. We can easily show that the ratio of the heat flux densities in the forward and backward configurations of the linear CTD tend exactly to the ratio of the effusivities of the two materials that make the thermal diode when time goes to zero. In fact, this dependency to the effusivities can be clearly seen by the analysis of the parameter r^*. It can be seen from Fig.3.2(f) that when time goes to zero, $R = 0.5$ and does not depend on the values of the parameter r^*.

The nondimensional heat flux densities for the sinusoidal boundary conditions cases vary throughout the entire period for all parameters as seen in Fig.3.3. The time behaviors of R show more features in these cases. They reach 1 and drop to 0 three or four times over one entire period. R drops to 0 at the dimensionless times when ϕ_+^* and ϕ_-^* have the same absolute values or intersect each other, and reaches 1 at the times when ϕ_+^* or ϕ_-^* approaches 0. Similar to the fixed Dirichlet boundary condition cases, the inherent feature is also clear for this sinusoidal boundary conditions cases. When time goes to zero, the ratio of the heat flux densities in the forward and backward configurations of the linear CTD tend exactly to the ratio of the effusivities of the two materials. Similarly, the ratios of the effusivities are the same for the cases of the parameter r^*, and R is always 0.5 regardless of the values of r^* when time goes to zero.

3.4 Theoretical modeling of the conductive thermal diode under Dirichlet boundary conditions

We consider a CTD in a plane geometry that is made of a PCM which is VO_2 and a non-PCM which is SiO_2 as illustrated in Fig.3.4. We made the same assumptions that we made for the

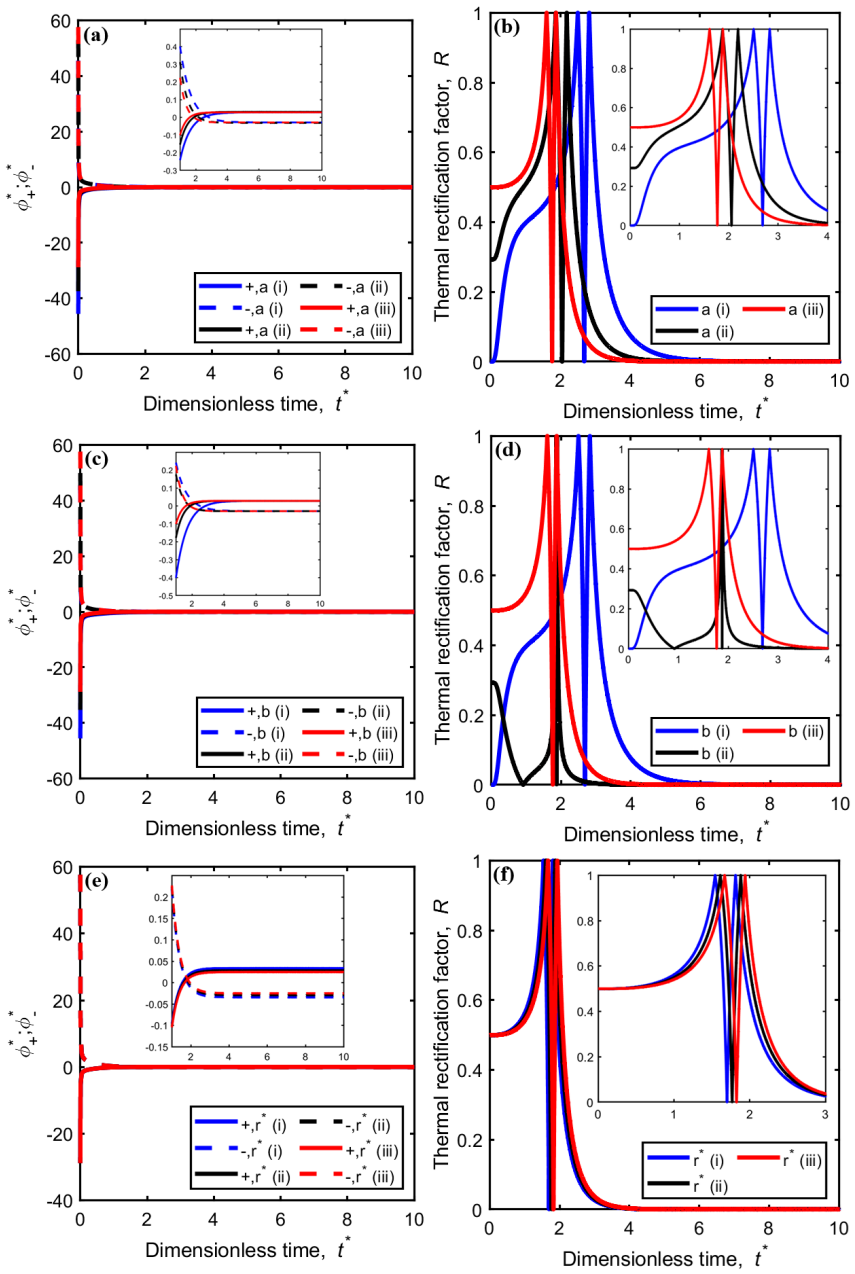

Figure 3.2: Computed dimensionless time behaviors of the nondimensional heat flux densities corresponding to the forward and backward configurations of the linear CTD and their corresponding computed dimensionless time behaviors of the thermal rectification factors for the fixed Dirichlet boundary condition for the parameters a (a)-(b), b (c)-(d) and r^* (e)-(f), respectively.

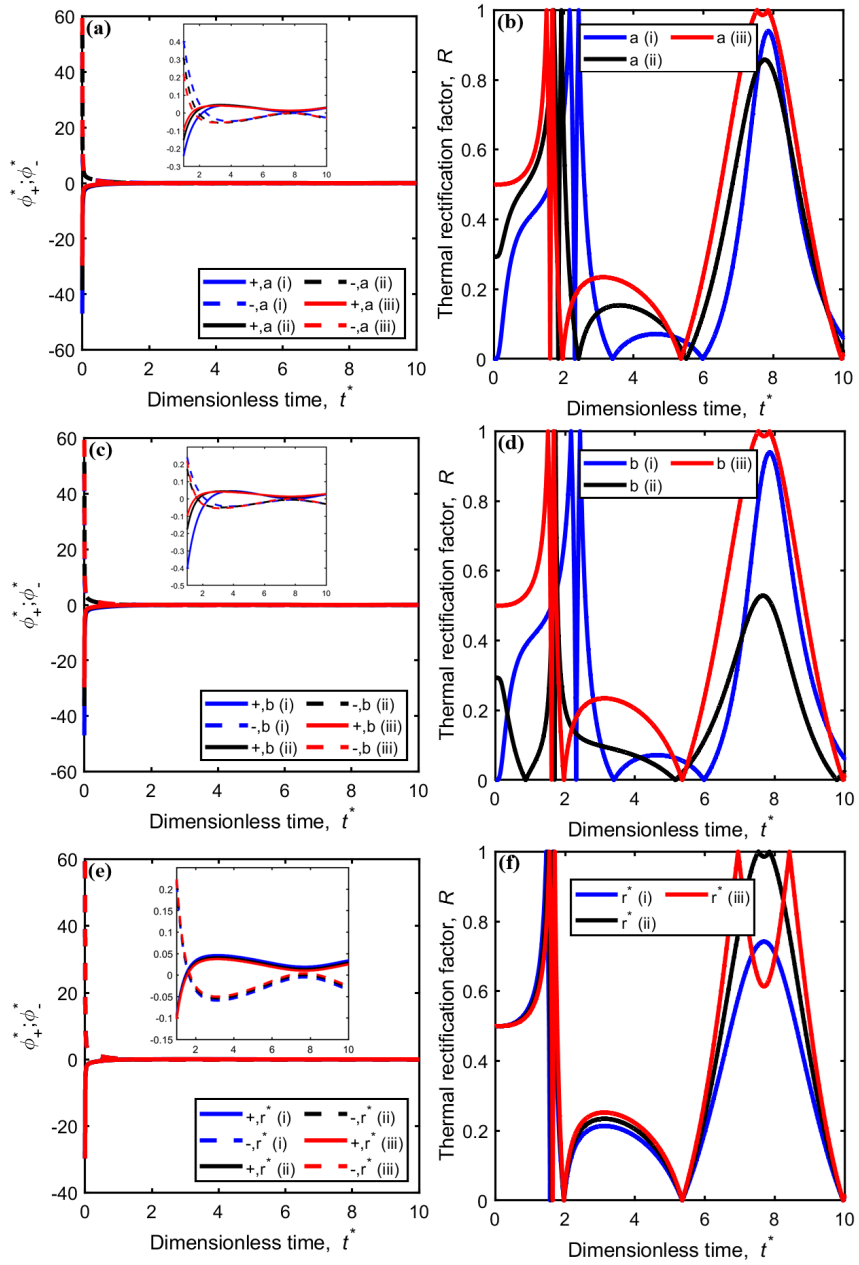

Figure 3.3: Computed dimensionless time behaviors of the nondimensional heat flux densities corresponding to the forward and backward configurations of the linear CTD and their corresponding computed dimensionless time behaviors of the thermal rectification factors for the sinusoidal Dirichlet boundary condition for the parameters a (a)-(b), b (c)-(d) and r^* (e)-(f), respectively.

linear CTD. The thermal diode to be placed between two thermal baths in a vacuum chamber so that we can neglect any heat exchange due to convection. We also assume heat exchange due to radiation to be negligible and consider conduction to be the only heat transfer mode between the two thermal baths. Therefore, there is a conductive heat exchange between the two thermal baths due to their temperature difference $T_h - T_c$. The heat flux flows from the PCM to the non-PCM in the forward configuration. Conversely, it flows in the opposite direction in the backward configuration. Heat fluxes in forward and backward configurations are driven by the thermal conductivities of the PCM and non-PCM. The total length of the model is $2l$ and both materials have equal lengths, which mean half of the total length, as shown in Fig.3.4.

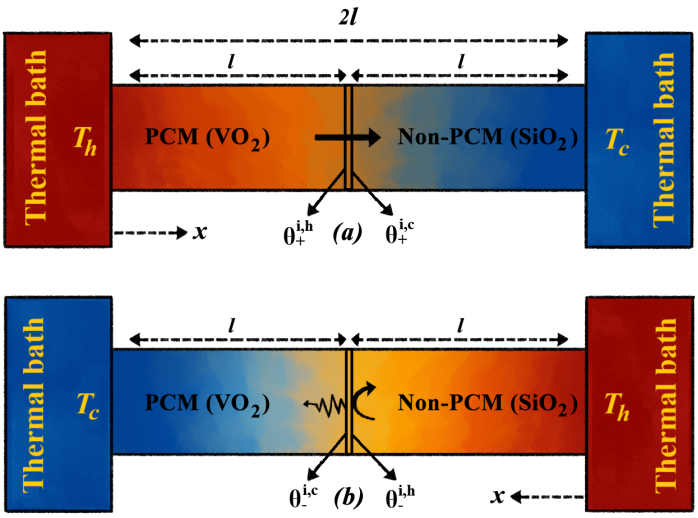

Figure 3.4: Schematic representation of the studied CTD in the forward and backward configurations [1].

3.4.1 Nondimensionalization of the transient process

The nonlinear heat diffusion equation for VO_2 is previously given in Eq.2.1 in Chapter 2 and it can be nondimensionalized easily as

$$\frac{\overline{\alpha}}{\alpha_d}\left[1+\frac{L_n}{c^D\Delta T_o}\frac{\partial v}{\partial \theta}\right]\frac{\partial \theta}{\partial t^*} = \frac{\partial}{\partial x^*}\left\{\left[1+(k_r-1)\,v(\theta)\right]\frac{\partial \theta}{\partial x^*}\right\} \tag{3.12}$$

where the dimensionless temperature is defined by $\theta = (T-T_o)/\Delta T_o$, the dimensionless length by $x^* = x/l$ and the dimensionless time by $t^* = \overline{\alpha}t/l^2$. ΔT_o is the difference between the transition

temperatures of heating and cooling processes: $\Delta T_o = T_{oh} - T_{oc}$. $\overline{\alpha}$ is the average thermal diffusivity between the one of the dielectric structure of VO_2 and SiO_2, which is $\overline{\alpha} = (\alpha_d + \alpha_s)/2$. α_d and α_s represent the thermal diffusivity of the dielectric structure of VO_2 and SiO_2, respectively. They are given by $\alpha_d = k_d/(\rho_v c^D)$ and $\alpha_s = k_s/(\rho_s c_s)$. ρ_v and ρ_s are the densities of VO_2 and SiO_2 in order. The thermal conductivity, k_s, specific heat capacity, c_s, and density, ρ_s, of SiO_2 are 1.5 W m^{-1} K^{-1}, 0.73 kJ kg^{-1} K^{-1} and 2650 kg m^{-3}, respectively. k_r=k_m/k_d and $v(\theta)$ is expressed as $v(\theta) = \left[1 + e^{-\beta \Delta T_o \theta}\right]^{-1}$.

Moreover, the heat diffusion equation in SiO_2, whose changes of the thermal conductivity and the specific heat capacity with temperature are negligible, can be nondimensionalized straightforwardly as

$$\frac{\overline{\alpha}}{\alpha_s}\frac{\partial \theta}{\partial t^*} = \frac{\partial^2 \theta}{\partial x^{*2}} \tag{3.13}$$

Eq.3.12 and Eq.3.13 are numerically solved by using implicit finite difference method and discretized in time and space for many nodes. Finally, the normalized heat flux density (ratio of the heat flux density to the quantity $\Delta T_o/l$) can be evaluated by using Eq.3.14 and Eq.3.15 for forward and backward configurations.

$$\phi_+^* = -k_s \frac{\partial \theta}{\partial x^*} \tag{3.14}$$

$$\phi_-^* = -k_d \left[1 + (k_r - 1)\, v(\theta)\right] \frac{\partial \theta}{\partial x^*} \tag{3.15}$$

where + and - signs represent forward and backward fluxes, respectively. Even though the quantities expressed in Eq.3.14 and Eq.3.15 have the dimension of a thermal conductivity, we will refer to them as nondimensional heat flux densities henceforth in this chapter.

The interface thermal resistance describing the temperature discontinuity at the interface between the two slabs of VO_2 and SiO_2 is also modeled according to the study of Yuan et al. [146]. The one-dimensional model that they developed in their study represents the interface thermal resistance with an artificial layer to analyze the heat transfer in multi layered materials including the interface thermal resistance. In our study, we create an artificial layer with a width of Δx between the two materials. Half of the length of the artificial layer is overlaid in the left

material and the other half is in the right material, which are VO_2 and SiO_2, respectively. The artificial layer has the modified thermal properties according to the features of VO_2 and SiO_2 to represent their effects at the interface of these two materials as explained in the study of Yuan et al. [146]. We define an effective thermal conductivity, k_e, that takes into account the effects of the thermal conductivities of the artificial layer, VO_2 and SiO_2 as [146]

$$\frac{1}{k_e} = \frac{1}{k_i} + \frac{1}{2k_v} + \frac{1}{2k_s} \tag{3.16}$$

k_i is the thermal conductivity of the artificial layer and can be defined as $k_i = \Delta x/r$, where r is the interface thermal resistance. Details of this model are explained in the reference [146].

3.4.2 Nondimensionalization of the steady-state process

3.4.2.1 Nondimensionalization for a case without the interface thermal resistance

The heat conduction equation is solved under steady-state conditions semi-analytically in order to validate the results of the steady-state regime that were numerically obtained during the transient regime analysis. Therefore, Eq.2.1 is nondimensionalized under steady-state conditions. Nondimensionalized Eq.2.1 can be written under steady-state conditions as follows:

$$\frac{d}{dx^*}\left[k(\theta)\frac{d\theta}{dx^*}\right] = 0 \tag{3.17}$$

where the dimensionless temperature is defined by $\theta = (T - T_o)/\Delta T_o$ and the dimensionless length by $x^* = x/l$. ΔT_o is the difference between the transition temperatures of heating and cooling processes: $\Delta T_o = T_{oh} - T_{oc}$. $k(\theta) = k_d\left[1 + (k_r - 1)\, v(\theta)\right]$, $k_r{=}k_m/k_d$ and $v(\theta)$ is expressed as $v(\theta) = \left[1 + e^{-\beta \Delta T_o \theta}\right]^{-1}$. Also, if we set $d\overline{\theta} = k(\theta)d\theta$, then Eq.3.17 can be reformulated as:

$$\frac{d^2\overline{\theta}}{dx^{*2}} = 0 \tag{3.18}$$

$\overline{\theta}(x^*) = c_1 x^* + c_2$ can be obtained from Eq.3.18. Also, if we substitute $k(\theta)$ into $d\overline{\theta} = k(\theta)d\theta$ and integrate it:

$$\overline{\theta}(\theta) = k_d\left[\theta + (k_r - 1)\int_0^{\theta} v(\theta)d\theta\right] \tag{3.19}$$

$\int_0^\theta v(\theta)d\theta$ is solved separately:

$$\int_0^\theta v(\theta)d\theta = \int_0^\theta \frac{d\theta}{1+e^{-\beta\Delta T_o\theta}} \tag{3.20}$$

we set $y = \beta\Delta T_o\theta$ and integrate Eq.3.20, we obtain:

$$\int_0^\theta v(\theta)d\theta = \theta + \frac{1}{\beta\Delta T_o} ln\left(\frac{1+e^{-\beta\Delta T_o\theta}}{2}\right) \tag{3.21}$$

then, if we substitute Eq.3.21 into Eq.3.19, we finally obtain:

$$\overline{\theta}(\theta) = k_d\left\{\frac{k_r-1}{\beta\Delta T_o} ln\left[1+e^{-\beta\Delta T_o\theta}\right] + \theta k_r + \frac{1-k_r}{\beta\Delta T_o} ln2\right\} = c_1x^* + c_2 \tag{3.22}$$

Also, the heat flux density for the forward configuration can be written as:

$$\phi_+ = -k(T)\frac{dT}{dx} = -\frac{k(T)}{l}\frac{dT}{dx^*} = -\frac{k_d\Delta T_o}{l}\left[1+(k_r-1)v(\theta)\right]\frac{d\theta}{dx^*} \tag{3.23}$$

and if we express $[k_d\Delta T_o]/l$ as ϕ_o, then, the nondimensional heat flux density for the forward configuration is

$$\phi_+^* = \frac{\phi_+}{\phi_o} = -\left[1+(k_r-1)v(\theta)\right]\frac{d\theta}{dx^*} \tag{3.24}$$

and it can be found that $d\overline{\theta}/d\theta = k(\theta)$. Moreover, the heat flux density is also:

$$\phi_+ = -\frac{\Delta T_o}{l}k(\theta)\frac{d\theta}{dx^*} = -\frac{\Delta T_o}{l}\frac{d\overline{\theta}}{dx^*} = -\frac{\Delta T_o}{l}c_1 \tag{3.25}$$

Finally, c_1 can be determined from Eq.3.25 as:

$$c_1 = -\frac{l}{\Delta T_o}\phi_+ \tag{3.26}$$

Then, after we substitute c_1 into Eq.3.22, it can be reformulated as:

$$\frac{k_r-1}{\beta\Delta T_o} ln\left[1+e^{-\beta\Delta T_o\theta}\right] + k_r\theta = -\frac{l}{k_d\Delta T_o}\phi_+x^* + \frac{c_2}{k_d} + ln2\frac{k_r-1}{\beta\Delta T_o} \tag{3.27}$$

where $l/[k_d\Delta T_o]$ is actually $1/\phi_o$ and if $\{c_2/k_d + ln2\,[(k_r-1)/(\beta\Delta T_o)]\}$ can be expressed as c^*, Eq.3.28 can be obtained finally:

$$\frac{k_r-1}{\beta\Delta T_o} ln\left[1+e^{-\beta\Delta T_o\theta}\right] + k_r\theta = -\phi_+^*x^* + c^* \tag{3.28}$$

where c^* is an integration constant. Now, if we consider the SiO_2 side and make nondimensionalization, we can obtain the following equation easily:

$$\frac{d^2\theta}{dx^{*2}} = 0 \tag{3.29}$$

and $\theta(x^*) = Ax^* + B$ can be obtained from Eq.3.29. Then, at $x^* = 1$ and $x^* = 2$, we can obtain Eq.3.30 and Eq.3.31, respectively:

$$\theta^i_+ = A + B \tag{3.30}$$

$$\theta_c = 2A + B \tag{3.31}$$

where θ^i_+ and θ_c are the nondimensional temperature at the interface and the cold nondimensional BC temperature in the forward configuration, respectively. From Eq.3.30 and Eq.3.31, $A = \theta_c - \theta^i_+$ and $B = 2\theta^i_+ - \theta_c$ can be determined , respectively. Also, at $x^* = 0$ and $x^* = 1$, Eq.3.32 and Eq.3.33 can be obtained from Eq.3.28, respectively:

$$\frac{k_r - 1}{\beta \Delta T_o} ln\left[1 + e^{-\beta \Delta T_o \theta_h}\right] + k_r \theta_h = c^* \tag{3.32}$$

$$\frac{k_r - 1}{\beta \Delta T_o} ln\left[1 + e^{-\beta \Delta T_o \theta^i_+}\right] + k_r \theta^i_+ = -\phi^*_+ + c^* \tag{3.33}$$

where θ_h is the hot nondimensional BC temperature. For simplification, we can set $\xi(\theta) = [(k_r - 1)/(\beta \Delta T_o)]\, ln\left[1 + e^{-\beta \Delta T_o \theta}\right]$. Then, the nondimensional heat flux density can be found from Eq.3.32 and Eq.3.33 as follows:

$$\phi^*_+ = \xi(\theta_h) - \xi(\theta^i_+) + k_r(\theta_h - \theta^i_+) \tag{3.34}$$

At the interface ($x^* = 1$), the heat flux density can be written as:

$$k_d \frac{\Delta T_o}{l} \left[1 + (k_r - 1)v(\theta)\right] \frac{d\theta}{dx^*} = k_s \frac{\Delta T_o}{l} \frac{d\theta}{dx^*} \tag{3.35}$$

the nondimensional heat flux density can also be written from Eq.3.35 as:

$$\phi^*_+ = \frac{k_s}{k_d}(\theta^i_+ - \theta_c) \tag{3.36}$$

Then, Eq.3.37 can be obtained from Eq.3.34 and Eq.3.36:

$$\xi(\theta^i_+) + \left[k_r + \frac{k_s}{k_d}\right] \theta^i_+ = \xi(\theta^h) + k_r \theta_h + \frac{k_s}{k_d} \theta_c \tag{3.37}$$

Eq.3.37 allows determining θ^i_+ as a function of θ_h, θ_c and the rest of the system parameters, then Eq.3.36 can be used to find the nondimensional heat flux density for the forward configuration. Then, if we consider the system for the backward configuration and follow a similar procedure, we can obtain the following Eq.3.38 and Eq.3.39 at $x^* = 0$ and $x^* = 1$, respectively:

$$\xi(\theta_c) + k_r\theta_c = c'^* \tag{3.38}$$

$$\xi(\theta^i_-) + k_r\theta^i_- = -\phi^*_- + c'^* \tag{3.39}$$

where θ^i_- is the nondimensional temperature at the interface in the backward configuration. Then, the nondimensional heat flux density for the backward configuration can be found from Eq.3.38 and Eq.3.39 as follows:

$$\phi^*_- = \xi(\theta_c) - \xi(\theta^i_-) + k_r(\theta_c - \theta^i_-) \tag{3.40}$$

Also, we can obtain the following Eq.3.41 and Eq.3.42 from Eq.3.29 at $x^* = 1$ and $x^* = 2$, respectively:

$$\theta^i_- = A' + B' \tag{3.41}$$

$$\theta_h = 2A' + B' \tag{3.42}$$

then $A' = \theta_h - \theta^i_-$ and $B' = 2\theta^i_- - \theta_h$ can be found from Eq.3.41 and Eq.3.42, respectively. Also, at $x^* = 1$, we have $-k_d\phi^*_- = k_s(\theta_h - \theta^i_-)$. Then, the nondimensional heat flux density for the backward configuration can also be found as:

$$\phi^*_- = \frac{k_s}{k_d}(\theta^i_- - \theta_h) \tag{3.43}$$

Then, Eq.3.44 can be obtained from Eq.3.40 and Eq.3.43:

$$\xi(\theta^i_-) + \left[k_r + \frac{k_s}{k_d}\right]\theta^i_- = \xi(\theta^c) + \frac{k_s}{k_d}\theta_h + k_r\theta_c \tag{3.44}$$

Eq.3.44 allows determining θ^i_- as a function of θ_h, θ_c and the rest of the system parameters, then Eq.3.43 can be used to find the nondimensional heat flux density for the backward configuration.

3.4.2.2 Nondimensionalization for a case including the interface thermal resistance

If we consider a case including the interface thermal resistance, as illustrated in Fig.3.4, and follow a similar procedure for the forward configuration. Through the interface, we can write the nondimensionalized heat flux density for the forward configuration as:

$$\phi^* = \frac{\theta_+^{i,h} - \theta_+^{i,c}}{k_d \nu} \tag{3.45}$$

where ν is defined by r/l. Therefore, we can write Eq.3.46 and Eq.3.47 by following similar procedures:

$$\xi(\theta_h) - \xi(\theta_+^{i,h}) + k_r(\theta_h - \theta_+^{i,h}) = \frac{\theta_+^{i,h} - \theta_+^{i,c}}{k_d \nu} \tag{3.46}$$

$$\frac{\theta_+^{i,h} - \theta_+^{i,c}}{k_d \nu} = \frac{k_s}{k_d}(\theta_+^{i,c} - \theta_c) \tag{3.47}$$

$\theta_+^{i,c}$ can be found from Eq.3.47 after rearranging as:

$$\theta_+^{i,c} = \frac{\theta_+^{i,h}/\nu + k_s \theta_c}{1/\nu + k_s} \tag{3.48}$$

and if we substitute Eq.3.48 into Eq.3.46, the following equation is obtained:

$$\xi(\theta_+^{i,h}) + \left[k_r + \frac{k_s}{k_d(1+\nu k_s)}\right]\theta_+^{i,h} = \xi(\theta^h) + k_r \theta_h + \frac{k_s \theta_c}{k_d(1+\nu k_s)} \tag{3.49}$$

If we consider the same system for backward configuration and follow a similar procedure, we can find Eq.3.50 and Eq.3.51:

$$\xi(\theta_c) - \xi(\theta_-^{i,c}) + k_r(\theta_c - \theta_-^{i,c}) = \frac{\theta_-^{i,c} - \theta_-^{i,h}}{k_d \nu} \tag{3.50}$$

$$\frac{\theta_-^{i,c} - \theta_-^{i,h}}{k_d \nu} = \frac{k_s}{k_d}(\theta_-^{i,h} - \theta_h) \tag{3.51}$$

$\theta_-^{i,h}$ can be found from Eq.3.51 after rearranging as:

$$\theta_-^{i,h} = \frac{\theta_-^{i,c}/\nu + k_s \theta_h}{1/\nu + k_s} \tag{3.52}$$

and if we substitute Eq.3.52 into Eq.3.50, the following equation is obtained:

$$\xi(\theta_-^{i,c}) + \left[k_r + \frac{k_s}{k_d(1+\nu k_s)}\right]\theta_-^{i,c} = \xi(\theta^c) + k_r \theta_c + \frac{k_s \theta_h}{k_d(1+\nu k_s)} \tag{3.53}$$

Eqs. 3.49 and 3.53 allow determining $\theta_+^{i,h}$ and $\theta_-^{i,c}$ as a function of θ_h, θ_c and the rest of the system parameters. Once $\theta_+^{i,h}$ and $\theta_-^{i,c}$ are determined, we can obtain straightforwardly $\theta_+^{i,c}$ and $\theta_-^{i,h}$ via Eqs.3.48 and 3.52, respectively.

3.4.3 Thermal rectification analysis under steady-state conditions

In the case of the steady-state analysis, we can easily express the thermal rectification factor by just using the nondimensional temperatures for both cases. Therefore, the thermal rectification factor that does not include the interface thermal resistance and the case including the interface thermal resistance can be found by Eqs. 3.54 and 3.55, respectively.

$$R_{ss} = \frac{\left|(\theta_h + \theta_c) - (\theta^i_+ + \theta^i_-)\right|}{max\{(\theta^i_+ - \theta_c), (\theta_h - \theta^i_-\}} \tag{3.54}$$

$$R_{ss} = \frac{\left|(\theta_h + \theta_c) - (\theta^{i,c}_+ + \theta^{i,h}_-)\right|}{max\{(\theta^{i,c}_+ - \theta_c), (\theta_h - \theta^{i,h}_-)\}} \tag{3.55}$$

3.5 Results and discussion of the conductive thermal diode under Dirichlet boundary conditions

In our analysis of the time dependent thermal rectification behavior of the suggested VO_2 based CTD under the transient Dirichlet conditions, we explore the consequences of two initial conditions: $T(t = 0) = T_c$ leading to a heating process of the full system and $T(t = 0) = T_h$ which leads to a cooling process. We investigate the impact of varying six different parameters; BC change, β, L_n, k_r, ΔT_o and r. During the study, only one parameter is changed in each analysis and the rest is kept unchanged. We firstly consider four different BC cases according to the real features of VO_2 and SiO_2. Then, we deeply analyze the remaining parameters with five different cases individually by considering the BC to be $T_h = 354$ K and $T_c = 324$ K. The cases for each parameter are shown in Table 3.2.

In the first analysis of the four different BC, we consider T_h and T_c for the heating and cooling conditions, separately, according to the real characteristic values of VO_2 and SiO_2. We fix these values with respect to T_o, which takes the value of 342.9 K for T_{oh} and the value of 334.9 K for T_{oc}, as stated before. In order to check the effect of the phase transition of VO_2 on the thermal rectification in detail, we specify the values of temperatures for the BC in various intervals surrounding the phase transition area of VO_2, which was previously shown in Figs.1.3 and 1.4. In Figs.3.5, we report the computed time behaviors of the nondimensional heat flux

Table 3.2: Investigated parameters and cases [1].

Case 1 - BC					
	(i)	(ii)	(iii)	(iv)	
Heating analysis					
T_h [K]	348	353	358	363	
T_c [K]	338	333	328	323	
Cooling analysis					
T_h [K]	340	345	350	355	
T_c [K]	330	325	320	315	
Case 2 - β					
	(i)	(ii)	(iii)	(iv)	(v)
β [K^{-1}]	0.5	1	1.6	3	5
Case 3 - L_n					
	(i)	(ii)	(iii)	(iv)	(v)
L_n [kJ kg^{-1}]	66.89 (+30%)	59.17 (+15%)	51.45	43.73 (-15%)	36.02 (-30%)
Case 4 - k_r					
	(i)	(ii)	(iii)	(iv)	(v)
k_r	1.2	1.5	1.667	3	5
Case 5 - ΔT_o					
	(i)	(ii)	(iii)	(iv)	(v)
ΔT_o [K]	2	5	8	13	17
Heating analysis					
T_{oh} [K]	336.9	339.9	342.9	347.9	351.9
Cooling analysis					
T_{oc} [K]	340.9	337.9	334.9	329.9	325.9
Case 6 - r					
	(i)	(ii)	(iii)	(iv)	(v)
r [m^2 K W^{-1}]	10^{-1}	10^{-2}	10^{-3}	10^{-4}	10^{-5}

density at the cold boundary [Figs.3.5(a) and 3.5(c)] in the forward and backward configurations and the thermal rectification factor [Figs.3.5(b) and 3.5(d)] for both the heating [Figs.3.5(a) and 3.5(b)] and cooling [Figs.3.5(c) and 3.5(d)] processes of the CTD. As our modeling is based on

Fourier's law, we only account for times beyond the diffusion time in order to avoid the drawback of the parabolic nature of the heat equation. The diffusion time corresponds to the time required for the temperature front to diffuse from the hot boundary to the cold one and can roughly be estimated as $l^2/\overline{\alpha}$. The general trend is the same for the different values of BC in each process and each configuration. In the heating process, the nondimensional heat flux density increases with time to saturate at the steady-state values for both forward and backward configurations, while there is a decreasing behavior in the cooling process. As expected the value of nondimensional heat flux density increases by increasing the temperature difference between the two boundaries. It is interesting to note that the saturation dynamics of the nondimensional heat flux density in the heating and cooling processes switches between the forward and backward configurations in each process by changing $\Delta T = T_h - T_c$. Indeed, while the nondimensional heat flux density seems to saturate faster (slower) by increasing ΔT for the forward (backward) configuration in the heating process, the opposite occurs in the cooling process. The behavior of R shows interesting nonlinear features, which are consequences of the behavior of the nondimensional heat flux densities in the forward and backward configurations for each process. In both the heating and cooling processes, R manifests a maximum R_{max}, goes to zero, then increases again to reach the steady-state value. R_{max} has a higher amplitude and occurs in early times in the cooling process in comparison to the heating process. This difference between the two processes is a direct result of the combined initial condition effect and the side nature (cold) of the CTD at which thermal rectification is considered and analyzed. The time at which R vanishes in the cooling process is almost double the one for the heating process. An indication that the dynamics of the thermal rectification lasts longer in the cooling process in comparison to the heating process. The steady-state regime values of R are therefore attained in longer periods in the cooling process. We also notice that the time at which the steady-state regime values are reached increases by decreasing ΔT. When the intervals of BCs are getting shorter and the values of their temperatures approach the critical temperature of the phase transition process of VO_2, higher R_{max} and $\widetilde{R}$ are obtained. It should be reminded here that $\widetilde{R}$ is the time-integrated thermal rectification factor which allows a better quantification of the capacitive effects. In addition to this, R in the steady-state regime is almost independent with respect to the values of ΔT.

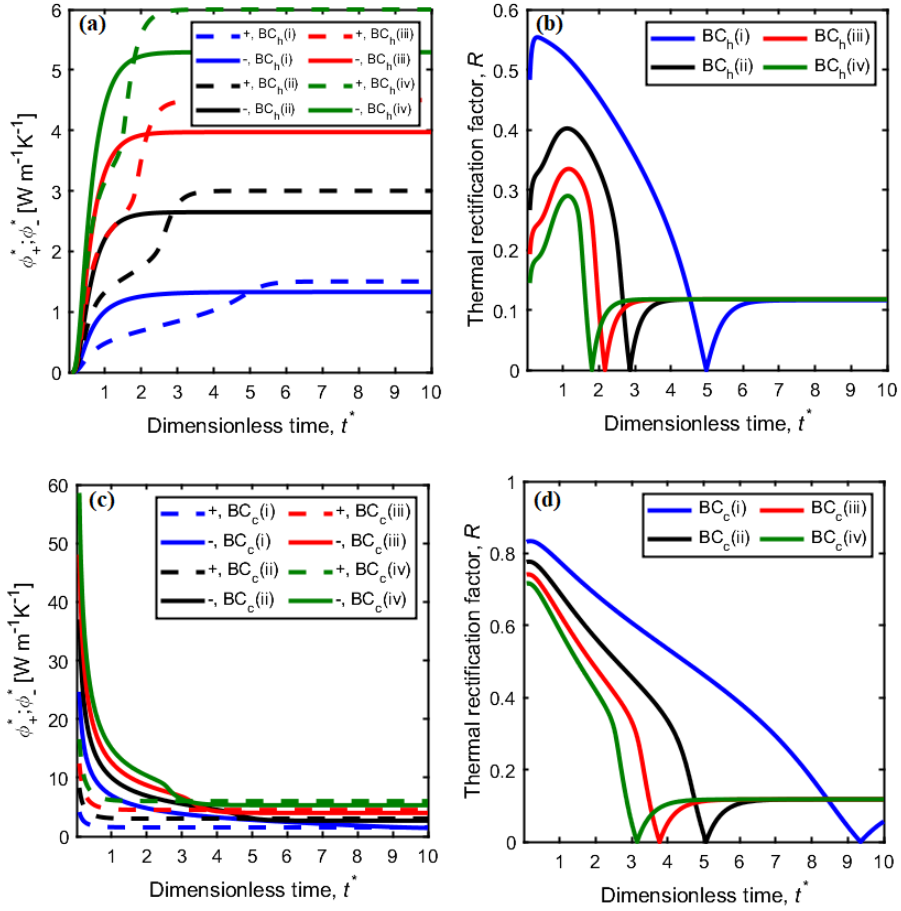

Figure 3.5: Computed time behaviors of the nondimensional heat flux density at the cold boundary and thermal rectification factor in the heating [(a) and (b)] and cooling [(c) and (d)] processes, respectively, for different values of BCs [1].

As expressed by Eqs.1.16 and 1.17, the thermal conductivity k and specific heat capacity c_p of VO_2 depend strongly on the parameter β which describes the phase transition slope in the temperature behavior of k. The variation of this parameter affects considerably the temperature profile of these two properties. Indeed, by decreasing β, the jump from the dielectric value k_d to the metallic value k_m becomes less steep and the amplitude of c_p decreases. On the other hand, sharper transition behavior occurs in k and higher c_p are observed when β increases. In Figs.3.6, we report the computed time behaviors of the nondimensional heat flux density at the cold boundary [Figs.3.6(a) and 3.6(c)] in the forward and backward configurations and the ther-

mal rectification factor [Figs.3.6(b) and 3.6(d)] for both the heating [Figs.3.6(a) and 3.6(b)] and cooling [Figs.3.6(c) and 3.6(d)] processes of the CTD for different values of β. By changing β, the main features in the time profile of ϕ_+^*, ϕ_-^* and R are almost similar to the ones shown in Figs.3.5. Although, the variation of β seems to have almost no effect on the behavior of ϕ_+^* and ϕ_-^*, the impact is more pronounced in the behavior of R. Interestingly also, it is the fact that varying β affects more R_{max} in the heating process and the time of R vanishing in the cooling process, in comparison to the opposite process, respectively. R_{max} decreases by increasing β. The effect of β becomes less pronounced in the steady-state regime. Furthermore, we notice an almost continuous decrease in $\widetilde{R}$ as β increases for the heating process, but we do not see this trend in the cooling process.

The specific heat capacity c_p has a direct effect on heat transfer under transient conditions. In the case of VO_2 and as we discussed it, the latent heat L_n plays a key role in the behavior of c_p. In Figs.3.7, we report the computed time behaviors of the nondimensional heat flux density at the cold boundary [Figs.3.7(a) and 3.7(c)] in the forward and backward configurations and the thermal rectification factor [Figs.3.7(b) and 3.7(d)] for both the heating [Figs.3.7(a) and 3.7(b)] and cooling [Figs.3.7(c) and 3.7(d)] processes of the CTD for different values of L_n. The main features in the time profile of R remain similar to the ones shown in Figs.3.5(b) and 3.5(d). While varying L_n affects more R_{max} in the heating process than in the cooling process similarly to the effect of β, it influences the time at which R vanishes in both processes. Additionally, R_{max} and $\widetilde{R}$ decrease by decreasing L_n for both processes. In the steady-state regime, the effect of L_n disappears and all the curves collapse on each other as expected. c_p has no impact on the heat transfer under steady-state conditions.

The fourth parameter we considered in our study is the ratio of the thermal conductivity of the metallic and dielectric phases of VO_2, k_r. In Figs.3.8, we report the computed time behaviors of the nondimensional heat flux density at the cold boundary [Figs.3.8(a) and 3.8(c)] in the forward and backward configurations and the thermal rectification factor [Figs.3.8(b) and 3.8(d)] for both the heating [Figs.3.8(a) and 3.8(b)] and cooling [Figs.3.8(c) and 3.8(d)] processes of the CTD for different values of k_r. While in the cooling process, the features remain similar to the

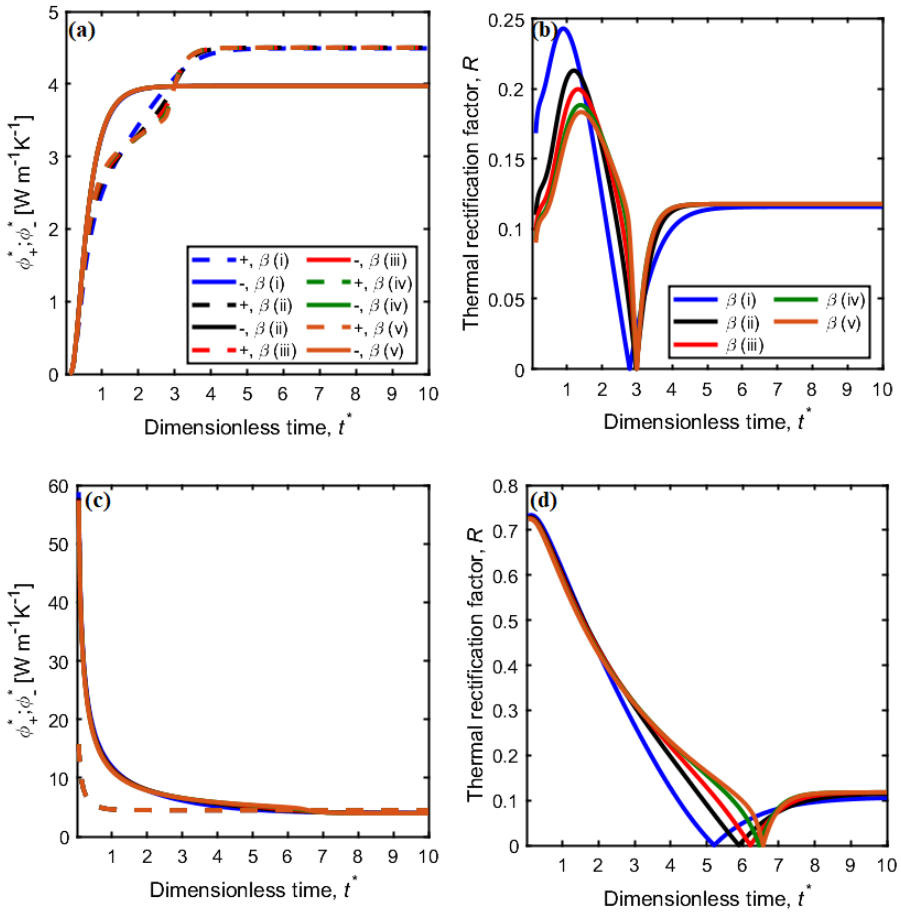

Figure 3.6: Computed time behaviors of the nondimensional heat flux density at the cold boundary and thermal rectification factor in the heating [(a) and (b)] and cooling [(c) and (d)] processes, respectively, for different values of β.

case of varying $\Delta T = T_h - T_c$, β and L_n, the time profiles of R in the heating process manifest interesting additional nonlinear features depending on the value of k_r. When k_r increases, the values of R_{max} and $\widetilde{R}$ decrease until the third case, which is the result according to the real characteristic value of VO_2. Above the third value of k_r, the behavior of R as a function of the nondimensional time changes drastically in the early moment of the transient process. Three and two peaks appear in the fourth and fifth cases, respectively, instead of just one as in the three first cases. Besides, the third peak, which is barely seen, occurs just before the value of R_{ss} in the fourth case. Thus, the value of R_{ss} is extremely close to the value of the third peak in this case

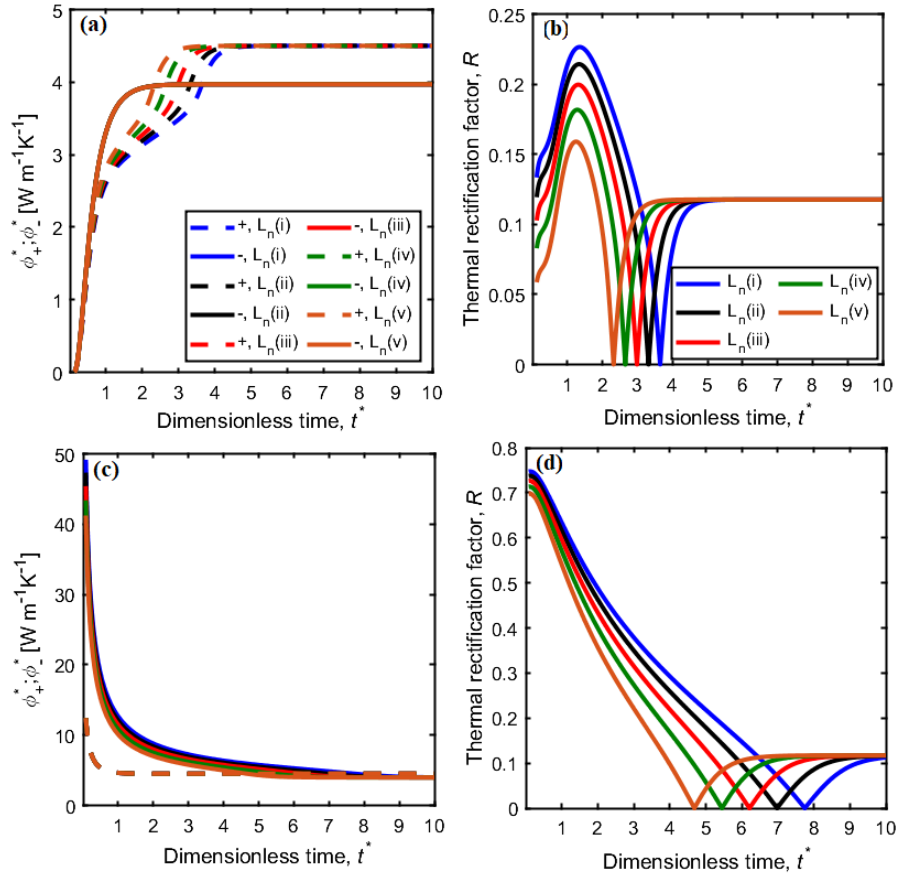

Figure 3.7: Computed time behaviors of the nondimensional heat flux density at the cold boundary and thermal rectification factor in the heating [(a) and (b)] and cooling [(c) and (d)] processes, respectively, for different values of L_n [1].

while the second peak in the fifth case gets even higher than the previous cases. Moreover, there is no systematic trend in the intersection of the nondimensional heat flux densities of the forward and backward configurations causing zero thermal rectification. It may appear more than once as in the fourth case or not at all as in the fifth case. Interestingly, the value of R_{ss} increases by increasing k_r and it is reached faster in both the heating and cooling processes. Generally, varying k_r impacts strongly the entire time profile of R spanning from the early transient regime to the steady-state regime.

There is a $\Delta T_o = T_{oh} - T_{oc} = 8$ K hysteresis effect of VO_2 between the phase transition tem-

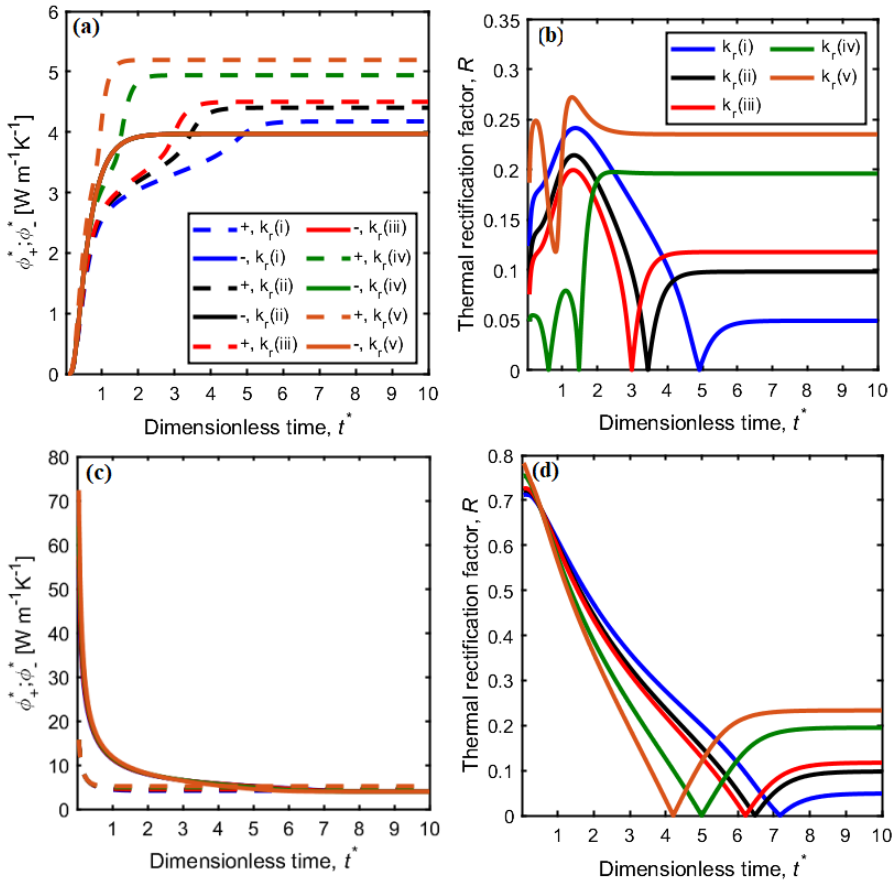

Figure 3.8: Computed time behaviors of the nondimensional heat flux density at the cold boundary and thermal rectification factor in the heating [(a) and (b)] and cooling [(c) and (d)] processes, respectively, for different values of k_r [1].

peratures for heating and cooling processes as stated before. The values of the phase transition temperatures; T_{oh}, T_{oc} and the hysteresis effect have a direct influence on the thermal rectification of the CTD as a consequence of the dependence of the thermal conductivity k and specific heat capacity c_p on these parameters as expressed by Eqs.1.16 and 1.17. We examined the influence on the thermal rectification factor by considering different values of ΔT_o. These values are obtained by varying T_{oh} and T_{oc} for the heating and cooling processes, respectively, while keeping the other temperatures fixed as shown in Table 3.2 above. In Figs.3.9, we report the computed time behaviors of the nondimensional heat flux density at the cold boundary [Figs.3.9(a) and 3.9(c)] in the forward and backward configurations and the thermal rectification factor [Figs.3.9(b) and

3.9(d)] for both the heating [Figs.3.9(a) and 3.9(b)] and cooling [Figs.3.9(c) and 3.9(d)] processes of the CTD for different values of ΔT_o. When T_{oh} and T_{oc} get closer to the BC, in other words, when ΔT_o increases, lower R and R_{max} are observed for both the heating and cooling processes of the CTD as reported in Figs.3.9(b) and 3.9(d), respectively. However, we can not identify any systematic trend for $\widetilde{R}$. Indeed, it is interesting to note that in the first four cases of the cooling process, $\widetilde{R}$ increases by increasing ΔT_o. Nevertheless, the fifth case shows a sudden decrease. This sudden decrease can also be seen in the fifth case of the heating process. Besides, in the fourth and fifth cases, the amplitude of the first peak in the thermal rectification time profile in the heating process is lower than the value at the steady-state regime. A behavior that we

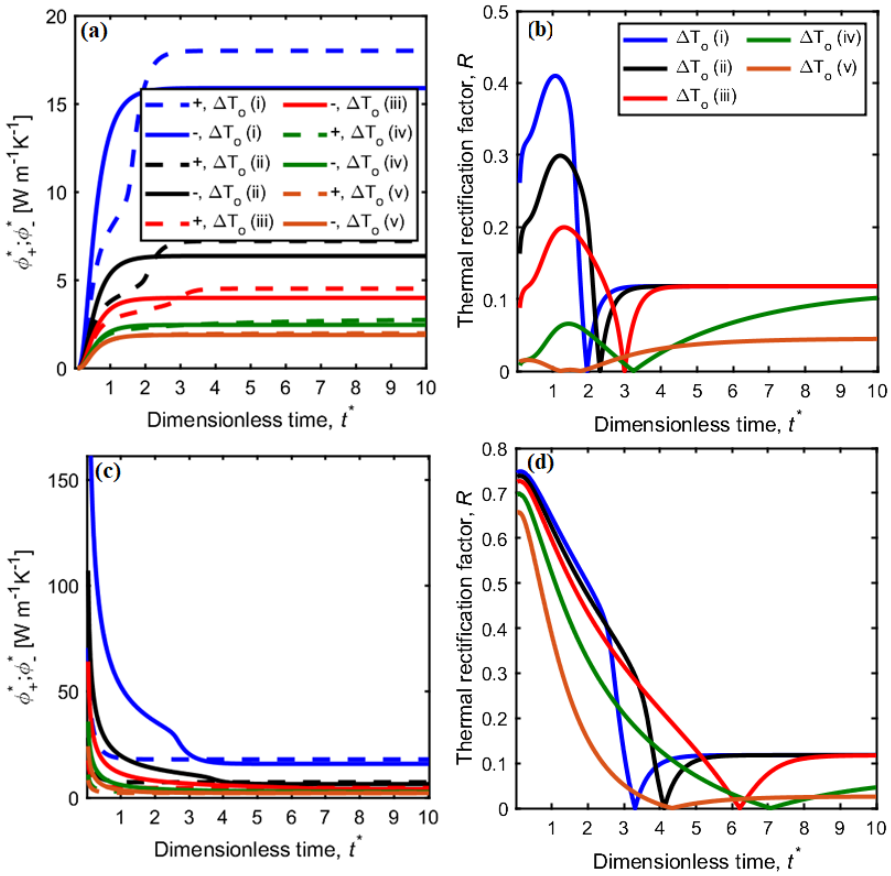

Figure 3.9: Computed time behaviors of the nondimensional heat flux density at the cold boundary and thermal rectification factor in the heating [(a) and (b)] and cooling [(c) and (d)] processes, respectively, for different values of ΔT_o [1].

encountered also while varying the ratio k_r as shown in Fig.3.8(b). Moreover, R_{ss} decreases by increasing ΔT_o for both heating and cooling processes.

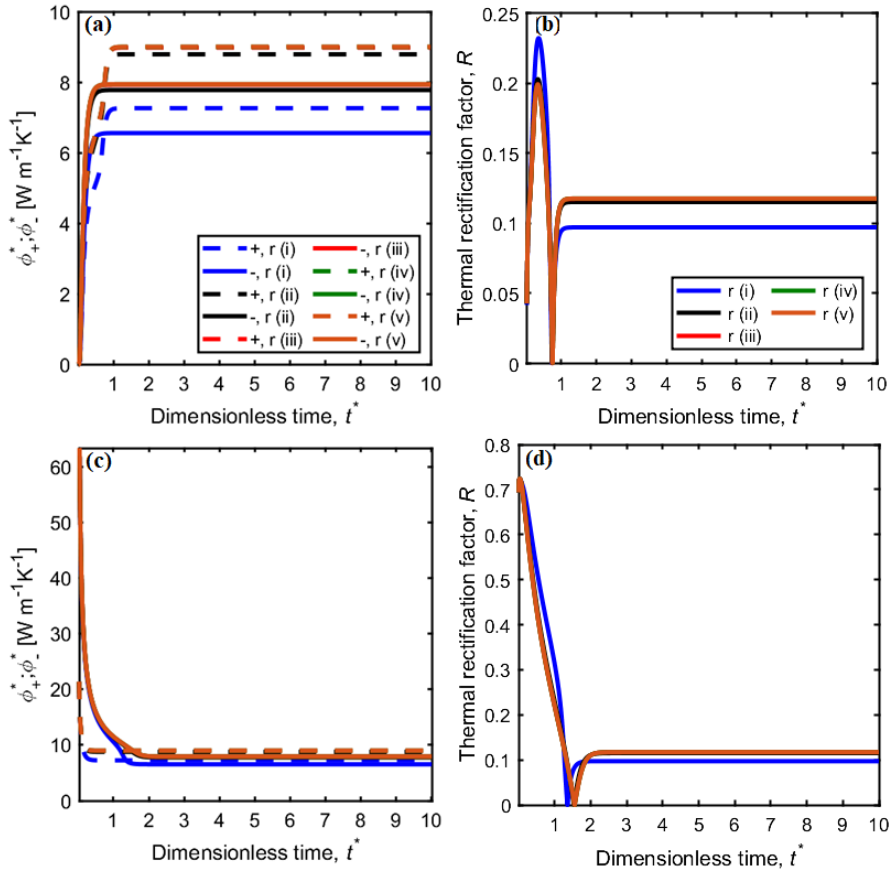

Figure 3.10: Computed time behaviors of the nondimensional heat flux density at the cold boundary and thermal rectification factor in the heating [(a) and (b)] and cooling [(c) and (d)] processes, respectively, for different values of r [1].

The analysis until this point was carried out by assuming there is no interface thermal resistance between the two slabs of VO_2 and SiO_2 composing the CTD. This constitutes the sixth and last parameter we considered in our parametric study and it is modeled by using the artificial layer approach of Yuan et al. [146] as mentioned before. In Figs.3.10, we report the computed time behaviors of the nondimensional heat flux density at the cold boundary [Figs.3.10(a) and 3.10(c)] in the forward and backward configurations and the thermal rectification factor [Figs.3.10(b) and

Table 3.3: Calculated values for the maximum thermal rectification factor, thermal rectification factor at steady-state conditions and time-integrated thermal rectification factor for all investigated cases [1].

	Heating analysis					Cooling analysis				
Case 1 - BC										
	(i)	(ii)	(iii)	(iv)		(i)	(ii)	(iii)	(iv)	
R_{max}	0.55	0.40	0.33	0.29		0.83	0.78	0.74	0.72	
R_{ss}	0.11	0.12	0.12	0.12		0.11	0.12	0.12	0.12	
$\widetilde{R}$	1.84	0.86	0.35	0.23		4.58	2.54	1.88	1.54	
Case 2 - β										
	(i)	(ii)	(iii)	(iv)	(v)	(i)	(ii)	(iii)	(iv)	(v)
R_{max}	0.24	0.21	0.20	0.19	0.18	0.73	0.73	0.73	0.73	0.73
R_{ss}	0.11	0.12	0.12	0.12	0.12	0.11	0.11	0.12	0.12	0.12
$\widetilde{R}$	0.48	0.37	0.35	0.34	0.34	2.19	2.28	2.25	2.25	2.29
Case 3 - L_n										
	(i)	(ii)	(iii)	(iv)	(v)	(i)	(ii)	(iii)	(iv)	(v)
R_{max}	0.23	0.21	0.20	0.18	0.16	0.75	0.74	0.73	0.71	0.70
R_{ss}	0.12	0.12	0.12	0.12	0.12	0.12	0.12	0.12	0.12	0.12
$\widetilde{R}$	0.47	0.41	0.35	0.29	0.24	2.78	2.51	2.25	1.98	1.71
Case 4 - k_r										
	(i)	(ii)	(iii)	(iv)	(v)	(i)	(ii)	(iii)	(iv)	(v)
R_{max}	0.24	0.21	0.20	0.05	0.25	0.71	0.72	0.73	0.75	0.78
R_{ss}	0.05	0.10	0.12	0.20	0.24	0.05	0.10	0.12	0.19	0.23
$\widetilde{R}$	0.59	0.41	0.35	0.33	0.63	2.41	2.29	2.24	2.09	1.99
Case 5 - ΔT_o										
	(i)	(ii)	(iii)	(iv)	(v)	(i)	(ii)	(iii)	(iv)	(v)
R_{max}	0.41	0.30	0.20	0.07	0.02	0.75	0.74	0.73	0.70	0.66
R_{ss}	0.12	0.12	0.12	0.11	0.04	0.12	0.12	0.12	0.08	0.03
$\widetilde{R}$	0.35	0.36	0.35	1.11	0.31	1.74	1.96	2.25	2.57	1.00
Case 6 - r										
	(i)	(ii)	(iii)	(iv)	(v)	(i)	(ii)	(iii)	(iv)	(v)
R_{max}	0.23	0.20	0.20	0.20	0.20	0.72	0.72	0.72	0.72	0.72
R_{ss}	0.10	0.11	0.12	0.12	0.12	0.09	0.11	0.12	0.12	0.12
$\widetilde{R}$	0.09	0.09	0.09	0.09	0.09	0.59	0.56	0.56	0.56	0.56

3.10(d)] for both the heating [Figs.3.10(a) and 3.10(b)] and cooling [Figs.3.10(c) and 3.10(d)] processes of the CTD for different values of r. The general trend is similar for the different values of r for heating and cooling processes as reported in Figs.3.10(b) and 3.10(d), respectively. Although this effect is not obvious in the cooling process, we get higher R_{max} and lower R_{ss} in the heating process when the value of r increases. Furthermore, especially in the cooling process, R tends to saturate at its steady-state value faster by increasing r. Nevertheless, this effect seems to be almost insignificant except between the first two cases. Similarly, it is only between these two cases, where the time-integrated thermal rectification factor $\widetilde{R}$ shows a dependence on r in the cooling process. For the rest of the cases, $\widetilde{R}$ remains almost constant as for R_{max} and R_{ss}. We summarize all the calculated values of R_{max}, R_{ss} and $\widetilde{R}$ for the different cases of each of the six parameters investigated in this study in Table 3.3.

The time dynamics of the thermal rectification has shown to be sensitive to each of the six parameters we considered in this study. It manifests a very pronounced nonlinear behavior. The degree of influence is not the same for the different parameters, but they all impact the whole time profile of the thermal rectification factor, ranging from the early transient regime to the steady-state regime. R_{max}, R_{ss} and $\widetilde{R}$ all change by varying each of the parameters. $\widetilde{R}$ which quantifies the capacitive effect of the CTD, gives a central information about the duration and magnitude of the thermal rectification dynamics span.

3.6 Theoretical modeling of the conductive thermal diode under dynamical boundary conditions

3.6.1 Models and temperature modulation of the thermal baths

We now consider the same CTD in a plane geometry under dynamical boundary conditions as seen in Fig.3.11(a) and (b) for the forward and backward configurations, respectively. In the first forward configuration of the CTD, the temperature of the left thermal bath is higher than the one of the right thermal bath. Therefore, the CTD allows the flow of heat. On the contrary, the temperatures of the thermal baths are exchanged in the second backward configuration and the heat flux strongly decreases in this reverse situation when compared to the first one. The total

length of the CTD is 2 mm. Also, both materials composing the CTD have equal lengths, which mean half of the total length. We again assume both systems to be placed between two thermal baths in a vacuum chamber so that we can neglect any heat exchange due to convection. We also assume heat exchange due to radiation to be negligible and consider conduction to be the only heat transfer mode between the two thermal baths.

In our model, we apply two sinusoidal temperatures at its boundaries, which are expressed in Eqs.3.56 and 3.57 for the left and right sides, respectively:

$$T_L = T_h + T_a \cos(2\pi f t) \tag{3.56}$$

$$T_R = T_c + T_a \cos(2\pi f t) \tag{3.57}$$

where $T_h = 352.9$ K, which is 10 K more than T_{oh} and $T_c = 324.9$ K, which is 10 K less than T_{oc}. As a reminder, T_{oh} and T_{oc} represent the values of the phase critical transition temperature of VO_2 for the heating and cooling processes, respectively [35]. We consider the variation of T_a so that one side of the CTD is always at the highest temperature and the other side is at the lowest temperature. The left side, which is the side of VO_2, is always hotter than the right boundary during the forward configuration as illustrated in Fig.3.11(a). On the contrary, the

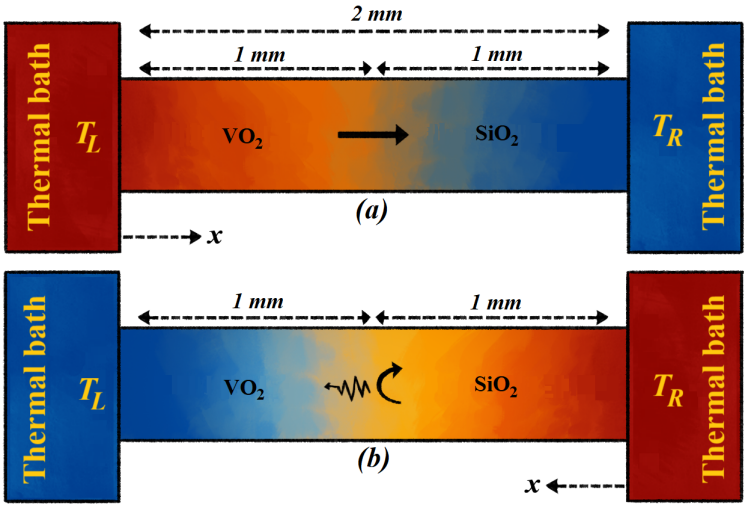

Figure 3.11: Schematic representation of the studied CTD during the forward (a) and backward (b) configurations [52].

right side, which is the side of SiO_2, is always hotter than the left boundary during the backward configuration as shown in Fig.3.11(b).

3.7 Results and discussion of the conductive thermal diode under dynamical boundary conditions

The computed time behavior of the heat flux densities at the cold boundary according to frequencies of 10^{-4} Hz, 10^{-3} Hz, 10^{-2} Hz and 10^{-1} Hz while applying the values of T_a that were defined as case 1 in Table 3.4 are reported in Fig.3.12(a), (b), (c) and (d), respectively. We observe that both frequency and T_a affect the heat flux density and thermal rectification factor R, the results of which are shown in Figs.3.13. Although the variation of the heat flux density is small enough to be considered constant at low frequencies such as 10^{-4} Hz and 10^{-3} Hz as seen in Fig.3.12(a) and (b), respectively, there is still a variation as a result of the phase change process of the material. We observe that the material starts the phase change process at case 1 (iv) during the forward configuration as previously shown in Fig.3.11(a) and at case 1 (iii) during the backward configuration as shown in Fig.3.11(b) even if these are not a full phase change cycles. The cooling stops before completing the cooling branch and it starts to heat up until the fully metallic phase is reached during the forward configuration. On contrary, the heating stops before completing the heating branch and it starts to cool down until the fully dielectric phase is attained during the backward configuration. The nonlinear variations of the thermal conductivity of VO_2 as a function of temperature combined with the hysteresis effect are responsible for the peculiar behavior of the heat flux density even at low frequencies as observed in Fig.3.12(a) and (b). When T_a and frequency are increased, the impact of the phase change process becomes more pronounced as seen in Fig.3.12(c) and (d).

The computed time behaviors over one cycle of the thermal rectification R according to frequencies of 10^{-4} Hz, 10^{-3} Hz, 10^{-2} Hz and 10^{-1} Hz while applying the values of T_a that were defined as case 1 in Table 3.4 are reported in Fig.3.13(a), (b), (c) and (d), respectively. The behavior of R shows interesting nonlinear and peculiar features, which are consequences of the behavior of the heat flux densities in the forward and backward configurations of the CTD

Table 3.4: Investigated parameters and cases for the conductive and capacitive thermal diodes [52].

Case 1 - Conductive thermal diode				
	(i)	(ii)	(iii)	(iv)
T_a [K]	3	6	9	12
Case 2 - Capacitive thermal diode (I)				
	(i)	(ii)	(iii)	(iv)
ξ	0.2	0.5	2	5
Case 3 - Capacitive thermal diode (I)				
	(i)	(ii)	(iii)	(iv)
T_a [K]	6	8	10	12
Case 4 - Capacitive thermal diode (I)				
	(i)	(ii)	(iii)	(iv)
w^*	0.5	1	2	4
Case 5 - Capacitive thermal diode (I)				
	(i)	(ii)	(iii)	(iv)
$\overline{\Delta T}$ [K]	12	16	20	24
Case 6 - Capacitive thermal diode (II)				
	(i)	(ii)	(iii)	(iv)
r_r	0.5	1	1.5	2
Case 7 - Capacitive thermal diode (II)				
	(i)	(ii)	(iii)	(iv)
ξ	0.2	0.5	2	5
Case 8 - Capacitive thermal diode (II)				
	(i)	(ii)	(iii)	(iv)
T_a [K]	22	24	26	28
Case 9 - Capacitive thermal diode (II)				
	(i)	(ii)	(iii)	(iv)
w^*	0.5	1	2	4
Case 10 - Capacitive thermal diode (II)				
	(i)	(ii)	(iii)	(iv)
$\overline{\Delta T}$ [K]	32	36	40	44

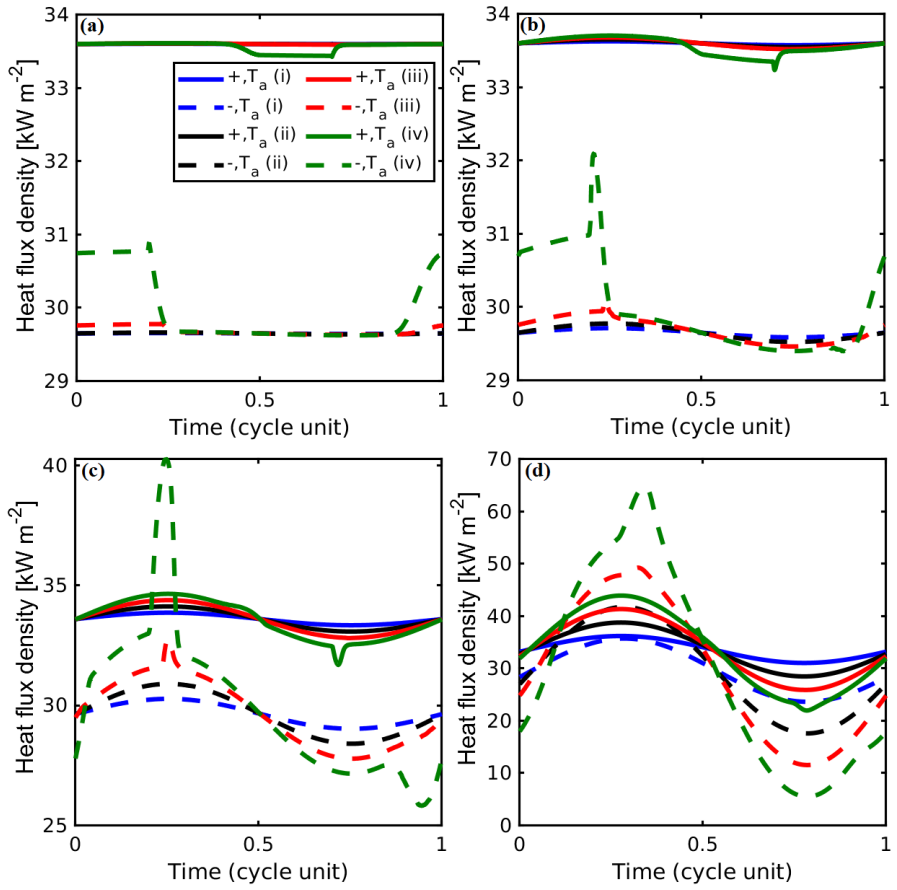

Figure 3.12: Computed time behaviors of the heat flux density at the cold boundary corresponding to the forward and backward configurations of the CTD for different values of T_a when f is set to 10^{-4} Hz (a), 10^{-3} Hz (b), 10^{-2} Hz (c) and 10^{-1} Hz (d) [52].

depending on the nature of the process undergone by VO_2; heating or cooling. Furthermore, one can see that R is almost constant with small values during the low frequencies such as 10^{-4} Hz and 10^{-3} Hz due to the small variation of the heat flux densities. If we observe deeply the results of the frequency of 10^{-3} Hz, one can see that a change in the behavior of R becomes obvious at case 1 (iii) and case 1 (iv). It should be remembered that these were the cases where the phase change process goes on. On the other hand, when the frequency of the modulated boundary temperature increases, R tends to oscillate more and its maximum becomes even higher. Generally, the nonlinearities become exacerbated. R drops down to zero when the heat flux densities intersect between the two configurations. These two effects become more

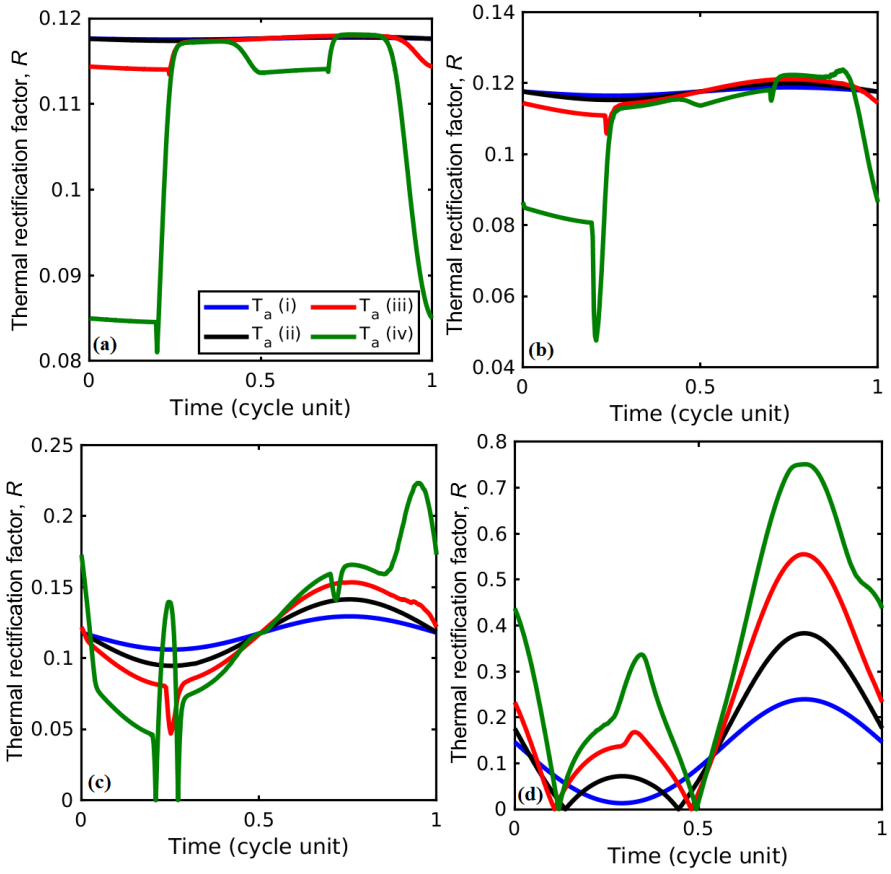

Figure 3.13: Computed time behaviors of R for different values of T_a when f is set to 10^{-4} (a), 10^{-3} (b), 10^{-2} (c) and 10^{-1} (d) [52].

pronounced by increasing T_a as one can see in Fig.3.13(c) and (d).

3.8 Theoretical modeling of the capacitive thermal diode

In order to emphasize the impact of the capacitive effect on the behavior of a CTD under dynamical boundary conditions, we consider a simple configuration of the thermal diode in which the two layers are sufficiently thin so that we can neglect in each the temperature spatial variation. Both layers will have uniform temperatures that only depend on time (frequency). We assume one of the layers to have a temperature dependent heat capacity (this could be a PCM) whereas the other layer has a constant heat capacity. We name this type of the thermal diode,

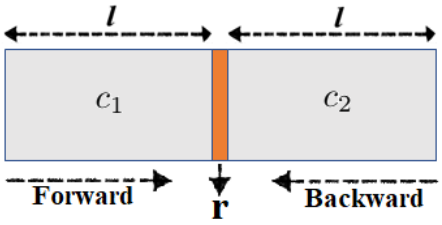

Figure 3.14: Schematic representation of the capacitive thermal diode [52].

capacitive thermal diode. Fig.3.14 shows a schematic representation of this type of thermal diode.

3.8.1 Capacitive thermal diode with constant heat capacities

First, let us start the analysis of the capacitive thermal diode by assuming both layers to have constant heat capacities. We set the specific heat of the first layer as c_1 and the one of the second layer as c_2. The interface thermal resistance between the two layers is included and it is represented as r. In the forward configuration, the first layer at the left is set at T_h and the second layer at the right is set at T_c. We interchange the temperatures of the two layers in the backward configuration. Based on the energy conservation law, we can easily express the heat flux densities in the backward and forward configurations of this capacitive thermal diode as given by Eq.3.58 and Eq.3.59, respectively.

$$q_-(t) = \frac{T_h - T_c}{r} - c_1\rho_1 l\frac{dT_c}{dt} \tag{3.58}$$

$$q_+(t) = \frac{T_h - T_c}{r} - c_2\rho_2 l\frac{dT_c}{dt} \tag{3.59}$$

where l represents the length of the layers. Let us now multiply both sides of Eq.3.58 and Eq.3.59 by r. We get:

$$q_-^{*,I}(t) = T_h - T_c - rc_1\rho_1 l\frac{dT_c}{dt} \tag{3.60}$$

$$q_+^{*,I}(t) = T_h - T_c - rc_2\rho_2 l\frac{dT_c}{dt} \tag{3.61}$$

where $q_-^{*,I}(t)$ and $q_+^{*,I}(t)$ symbolize the heat flux densities multiplied by r, which are $rq_-(t)$ and $rq_+(t)$, respectively. Furthermore, we assume $T_h(t)$ to be constant and $T_c(t)$ to be sinusoidal.

They are expressed as $T_h(t) = \overline{T}_h$ and $T_c(t) = \overline{T}_c + T_a cos(wt)$. Then, $q_-^{*,I}(t)$ and $q_+^{*,I}(t)$ can be written as

$$q_-^{*,I}(t) = \overline{T}_h - \overline{T}_c - T_a \cos(wt) + rc_1\rho_1 lwT_a \sin(wt) \quad (3.62)$$

$$q_+^{*,I}(t) = \overline{T}_h - \overline{T}_c - T_a \cos(wt) + rc_2\rho_2 lwT_a \sin(wt) \quad (3.63)$$

We set: $\theta_a = T_a/\overline{\Delta T}$ where $\overline{\Delta T} = \overline{T}_h - \overline{T}_c$, $w^* = \zeta_1 w$, $t^* = t/\zeta_1$, $\xi = \zeta_2/\zeta_1$, $\zeta_1 = rc_1\rho_1 l$ and $\zeta_2 = rc_2\rho_2 l$ into Eq.3.62 and Eq.3.63. We can express the nondimensionalized heat flux densities $\phi_-^{*,I}(t^*)$ and $\phi_+^{*,I}(t^*)$ as:

$$\phi_-^{*,I}(t^*) = \frac{q_-^{*,I}(t)}{\overline{\Delta T}} = 1 - \theta_a \left[\cos(w^*t^*) - w^* \sin(w^*t^*)\right] \quad (3.64)$$

$$\phi_+^{*,I}(t^*) = \frac{q_+^{*,I}(t)}{\overline{\Delta T}} = 1 - \theta_a \left[\cos(w^*t^*) - \xi w^* \sin(w^*t^*)\right] \quad (3.65)$$

3.8.2 Capacitive thermal diode with temperature dependent heat capacity

We now make the analysis for the case of the capacitive thermal diode, where one layer (first layer) has a temperature dependent heat capacity and the other layer (second layer) has a constant heat capacity by following the same steps as above. The first layer is assumed to be a PCM. The expressions of $q_-(t)$ and $q_+(t)$ remain the same in the time domain, whether c_1 and c_2 are constant or temperature-dependent (including even a potential temperature dependency of r). Therefore, we generally have for the case of a capacitive thermal diode with a temperature dependent heat capacity:

$$q_-^{*,II}(t) = \overline{T}_h - \overline{T}_c - T_a \cos(wt) + r(T_m)c_1(T_c)\rho_1 lwT_a \sin(wt) \quad (3.66)$$

$$q_+^{*,II}(t) = \overline{T}_h - \overline{T}_c - T_a \cos(wt) + r(T_m)c_2\rho_2 lwT_a \sin(wt) \quad (3.67)$$

where $q_-^{*,II}(t)$ and $q_+^{*,II}(t)$ symbolize the heat flux densities multiplied by $r(T_m)$, which are $r(T_m)q_-(t)$ and $r(T_m)q_+(t)$, respectively. We can assume $r(T_m)$ to have the same formal expression as the one of the thermal conductivity given in Eq.1.16 in Chapter 1 [5] and write it down as $r(T_m) = r_d + (r_m - r_d)v(T_m)$ where $T_m = (T_h + T_c)/2$. Furthermore, similarly, the expression of the specific heat of VO_2 is described in Eq.1.17 in Chapter 1 and can be written here as [5]:

$$c(T) = c^D(T) + L_n \frac{dv(T)}{dT} \quad (3.68)$$

where c^D represents the specific heat predicted by Debye's model which we assume to be constant. Therefore, $c_1(T_c)$ can be written as $c_1(T_c) = c_1^D + L_n \frac{dv(T_c)}{dT_c}$. If the heating and cooling processes do not stop on the heating and cooling curves and make a full cycle each of them, we can generally write the expression of the function $v(T)$ to take into account the effect of the thermal hysteresis of the PCM when the boundary temperature is modulated in time (periodic) as:

$$\frac{1}{v(T)} = 1 + e^{-\beta[T + T_a\cos(wt) - T_{oh}H(-\sin(wt)) - T_{oc}H(\sin(wt))]} \tag{3.69}$$

Here also, we can adopt a nondimensional analysis by setting: $\zeta_1 = r_d c_1^D \rho_1 l$, $\zeta_2 = r_d c_2 \rho_2 l$, $r_r = r_m/r_d$, $\theta_a = T_a/\overline{\Delta T}$ where $\overline{\Delta T} = \overline{T_h} - \overline{T_c}$, $\overline{L} = L_n/(c_1^D \overline{\Delta T})$, $\theta_{oh} = T_{oh}/\overline{\Delta T}$, $\theta_{oc} = T_{oc}/\overline{\Delta T}$, $\theta_h = \overline{T_h}/\overline{\Delta T}$, $\theta_c = \overline{T_c}/\overline{\Delta T}$, $\theta_m = \overline{T_m}/\overline{\Delta T}$ where $\overline{T_m} = (\overline{T_h} + \overline{T_c})/2$, $B = \beta\overline{\Delta T}$, $t^* = t/\zeta_1$, $w^* = \zeta_1 w$ and $\xi = \zeta_2/\zeta_1$ into Eq.3.66, Eq.3.67 and Eq.3.69. The nondimensionalized $\phi_-^{*,II}(t)$, $\phi_+^{*,II}(t)$ and $1/v(T)$, for the considered configuration where the first layer has a temperature dependent heat capacity (PCM), can be expressed as follows:

$$\phi_-^{*,II}(t^*) = 1 - \theta_a \left\{\cos(w^*t^*) - [1 + (r_r - 1)\overline{v}(\theta_m)][1 + \overline{L}B\overline{v}(\theta_c)(1 - \overline{v}(\theta_c))]w^*\sin(w^*t^*)\right\} \tag{3.70}$$

$$\phi_+^{*,II}(t^*) = 1 - \theta_a \left\{\cos(w^*t^*) - [1 + (r_r - 1)\overline{v}(\theta_m)]\xi w^*\sin(w^*t^*)\right\} \tag{3.71}$$

Also, $\overline{v}(\theta_c)$ and $\overline{v}(\theta_m)$ can be written as

$$\frac{1}{\overline{v}(\theta_c)} = 1 + e^{-B[\theta_c + \theta_a\cos(w^*t^*) - \theta_{oh}H(-\sin(w^*t^*)) - \theta_{oc}H(\sin(w^*t^*))]} \tag{3.72}$$

$$\frac{1}{\overline{v}(\theta_m)} = 1 + e^{-B[\theta_m + (\theta_a/2)\cos(w^*t^*) - \theta_{oh}H(-\sin(w^*t^*)) - \theta_{oc}H(\sin(w^*t^*))]} \tag{3.73}$$

It should be noted here that when the direction of $\phi_+^{*,I}$ (or $\phi_+^{*,II}$) or $\phi_-^{*,I}$ (or $\phi_-^{*,II}$) changes, the sign of them also changes as will be seen in the result section of the capacitive thermal diode analysis. We therefore cannot apply the thermal rectification formula (Eq. 1.25) that we expressed in Chapter 1, because then both heat fluxes flow in the same direction; the system behaves like a perfect thermal diode so that $R = 1$. However, if both $\phi_+^{*,I}$ (or $\phi_+^{*,II}$) and $\phi_-^{*,I}$ (or $\phi_-^{*,II}$) change their directions, the given equation (Eq. 1.25) of the thermal rectification factor applies.

3.9 Results and discussion of the capacitive thermal diode

The concept of the capacitive thermal diode is a simple configuration that allows to analyze the behavior of the CTD under transient conditions by omitting the heat diffusion process and putting light on only the capacitive process in each of the two terminals or sides of the thermal device. We assume both sides to have constant heat capacities (case I) or one side has a temperature-dependent heat capacity (case II) and we investigate the effect of the capacity in detail by changing various parameters. In the first analysis, we consider the two layers of the capacitive thermal diode to have constant heat capacities. We choose four different values of ξ which are defined as case 2 in Table 3.4 while w^* and T_a are taken as 1 and 8 K, respectively. $\overline{T}_h$ is also taken as 354.9 K which is 12 K more than T_{oh} and $\overline{T}_c$ is taken as 338.9 K which is the average of T_{oh} and T_{oc}. The system can make full heating and cooling processes with these conditions. We report the results of $\phi_+^{*,I}$ and $\phi_-^{*,I}$ in Fig.3.15(a) and the results of the thermal rectification factor R in Fig.3.16(a) according to these four different values of ξ. The heat capacity times the density $c_1\rho_1$ of the first layer is higher than the second layer $c_2\rho_2$ during the first two values of ξ, which are 0.2 and 0.5 and we observe that the oscillation amplitude of $\phi_+^{*,I}$ is always lower than the oscillation amplitude of $\phi_-^{*,I}$. However, when ξ increases to 2 and 5, which means that $c_2\rho_2$ is now higher than the first layer $c_1\rho_1$, the oscillation amplitude of $\phi_+^{*,I}$ increases and becomes higher than the oscillation amplitude of $\phi_-^{*,I}$. Also, when ξ increases, the peak points of $\phi_+^{*,I}$ shift to the left due to the capacity effect. The latter effect is described by the second term in the right hand side of Eq.3.58 and Eq.3.59, and becomes more important than the Fourier effect, which is described by the first term in the right hand side of these equations. Indeed, this situation causes $\phi_+^{*,I}$ to become negative over a certain time interval while $\phi_-^{*,I}$ is always positive as it does not depend on ξ as seen in Fig.3.15(a). When we look at the behavior of R with these conditions as shown in Fig.3.16(a), it can be seen that R firstly decreases as ξ increases. $\phi_+^{*,I}$ and $\phi_-^{*,I}$ have the same amplitude when ξ equals 1 and this causes zero R. Then, when ξ gets higher than 1, R starts to increase. In addition, during the time interval when $\phi_+^{*,I}$ becomes negative, the system manifests the behavior of a perfect thermal diode and the time interval corresponding to this behavior increases by increasing ξ.

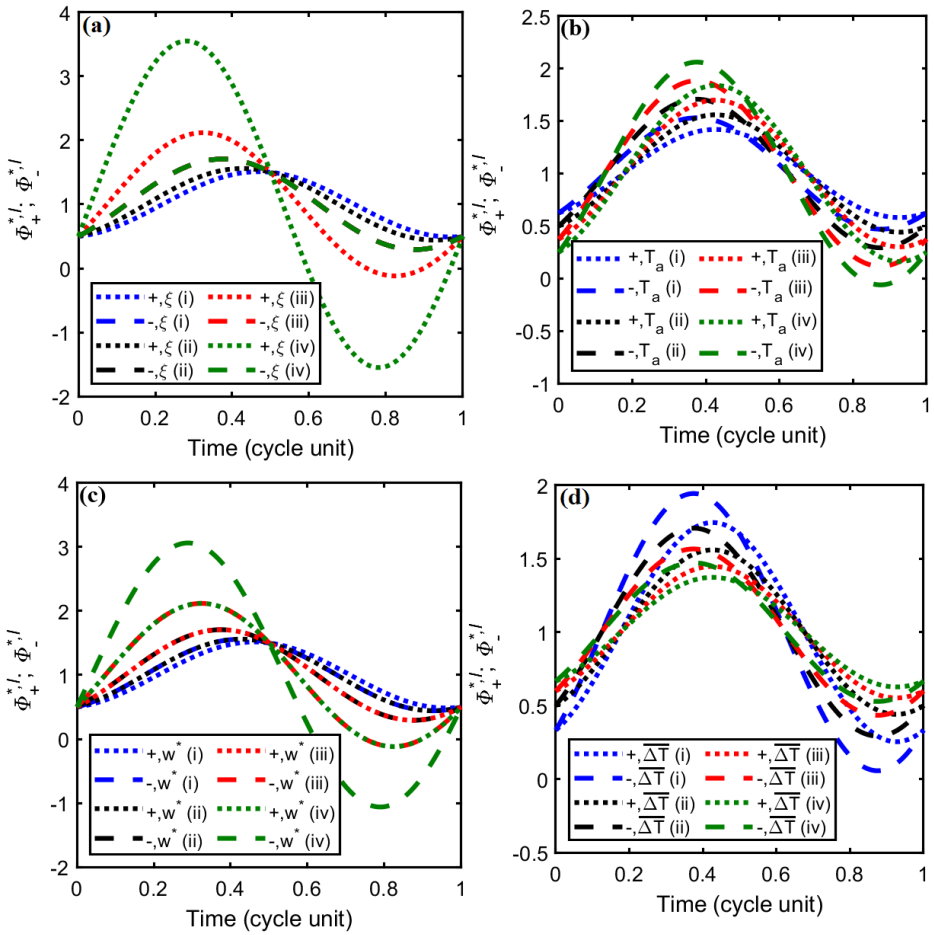

Figure 3.15: Computed time behaviors of $\phi_+^{*,I}$ and $\phi_-^{*,I}$ corresponding to the configuration of the capacitive thermal diode with constant heat capacities for the two layers for various investigated parameters: ξ (a), T_a (b), w^* (c) and $\overline{\Delta T}$ (d) [52].

The modulated temperature amplitude T_a is also examined with various values as defined as case 3 in Table 3.4. The values are carefully set to allow the system to make the heating and cooling processes completely and considering that the sum of the mean temperature $\overline{T}_c$ and the temperature amplitude T_a at the cold side remains always lower than the temperature at the hot side $\overline{T}_h$. While examining various values of T_a, the other parameters are taken identical as before and ξ is set to the value of 0.5. This means $c_1\rho_1$ is twice higher than $c_2\rho_2$. As seen in Fig.3.15(b), the oscillation amplitudes of $\phi_+^{*,I}$ and $\phi_-^{*,I}$ increase when the value of T_a gets higher. However, T_a does not seem to affect the optimal time at which $\phi_+^{*,I}$ and $\phi_-^{*,I}$ reach their

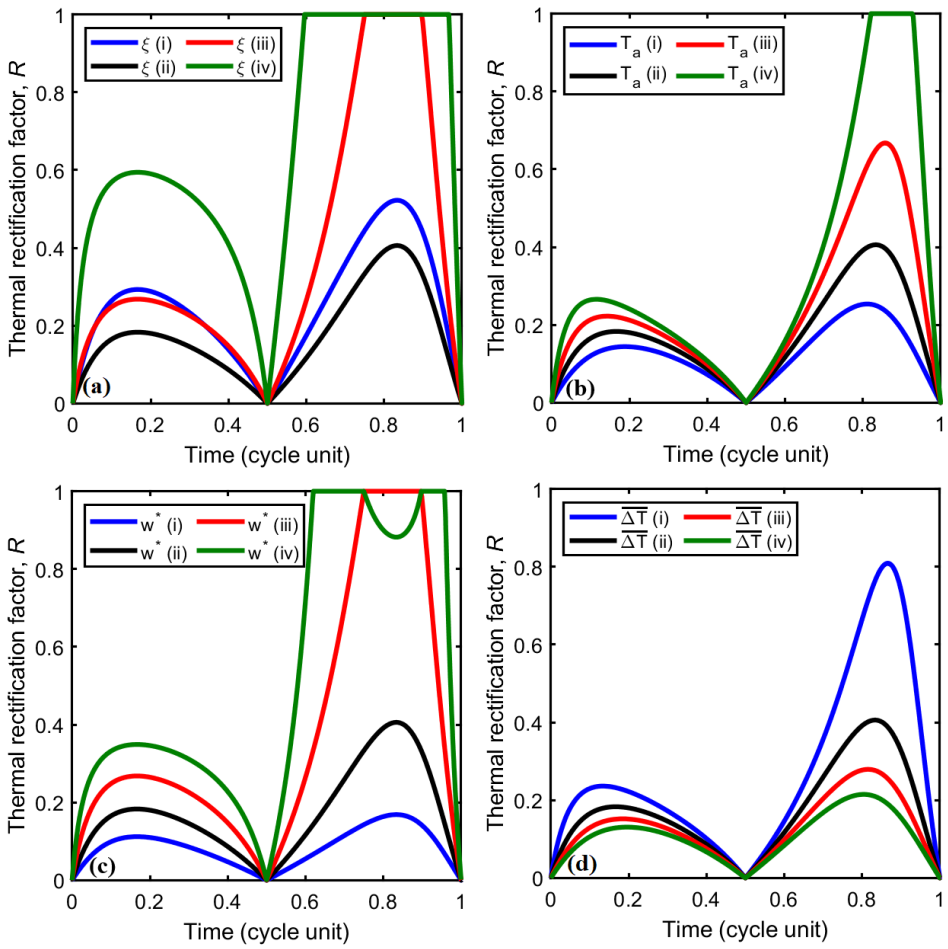

Figure 3.16: Computed time behaviors of R corresponding to the configuration of the capacitive thermal diode with constant heat capacities for the two layers for various investigated parameters: ξ (a), T_a (b), w^* (c) and $\overline{\Delta T}$ (d) [52].

extrema: maximum and minimum. When we examine R as shown in Fig.3.16(b), it generally increases when T_a increases until the time where R goes to zero. After that time, the increase of R continues as T_a increases, but the system also starts to manifest the behavior of a perfect thermal diode as seen in case 3 (iv).

We now investigate the dependence of our system on the parameter w^* and the examined values are defined as case 4 in Table 3.4. The other parameters are taken as before and ξ is again equal to 0.5. We almost see a similar behavior to the one observed regarding the analysis of ξ as

shown in Fig.3.15(c), both $\phi_+^{*,I}$ and $\phi_-^{*,I}$ rise up and shift left as w^* increases. Due to the higher $c_1\rho_1$, the oscillation amplitude of $\phi_-^{*,I}$ is always higher than the oscillation amplitude of $\phi_+^{*,I}$ as previously seen during the analysis of ξ. Additionally, we made the analysis according to $\xi = 2$ with the same investigated parameters of w^* and observed an opposite behavior to the latter one. Indeed, the oscillation amplitude of $\phi_+^{*,I}$ is always higher than the oscillation amplitude of $\phi_-^{*,I}$ with this condition. When we look at R as reported in Fig.3.16(c), we see that the effect is more pronounced generally when w^* increases. At $w^* = 2$, R goes to 1 during a certain time interval, which means the perfect thermal diode is again obtained. Nevertheless, as w^* continues to increase such as $w^* = 4$, both $\phi_+^{*,I}$ and $\phi_-^{*,I}$ switch to negative values for a time interval and consequently, R decreases over these intervals and the perfect thermal diode effect disappears.

The last parameter we examine in our study of the behavior of the capacitive thermal diode with constant heat capacities is $\overline{\Delta T}$ which is $\overline{\Delta T} = \overline{T}_h - \overline{T}_c$. The investigated values are defined as case 5 in Table 3.4. The other parameters are taken the same as before except $\overline{T}_h$. $\overline{T}_h$ is arranged according to $\overline{\Delta T}$ while $\overline{T}_c$ is always 338.9 K for all cases. We find that $\overline{\Delta T}$ affects the behavior of $\phi_+^{*,I}$ and $\phi_-^{*,I}$ in a similar way to the parameter T_a as shown in Fig.3.15(d). The only difference is that the oscillation amplitudes of $\phi_+^{*,I}$ and $\phi_-^{*,I}$ decrease as $\overline{\Delta T}$ increases; recall that they were increasing as T_a increases. Furthermore, the optimal time corresponding to the peak values of $\phi_+^{*,I}$ and $\phi_-^{*,I}$ does not seem to vary according to $\overline{\Delta T}$ as previously observed during the investigation of parameter T_a. The values of R get higher by decreasing the values of $\overline{\Delta T}$ as reported in Fig.3.16(d), but there is no perfect thermal diode behavior, because $\phi_-^{*,I}$ does not switch to negative values.

The analysis until this point was carried out by assuming that the heat capacities of both layers are constant. Now, let us consider that the first layer is made of a PCM with a temperature-dependent heat capacity. We start to see significant nonlinear effects on both $\phi_+^{*,II}$ and $\phi_-^{*,II}$ due to the phase transition as seen in Fig.3.17. For the temperature-dependent heat capacity analysis, we revisited the previous four parameters that we examined during the constant heat capacity analysis: ξ, w^*, T_a and $\overline{\Delta T}$, but we also examined one additional parameter, r_r. As stated before, it is the ratio of r_m to r_d. Therefore, we examined a total of five different param-

eters as seen in Table 3.4 and changed only one parameter while keeping the others the same. Unless otherwise stated, the parameters are set as described in this paragraph throughout the temperature-dependent heat capacity analysis. $\overline{T}_h$ is set to 354.9 K again, but it should be noted that the values of $\overline{T_c}$ and T_a should be carefully adjusted considering the interface temperature $\overline{T_m} = (\overline{T_h} + \overline{T_c})/2$ and the cold temperature $\overline{T_c}$, because the system at both locations has to perform complete heating and cooling processes. In fact, this can be clearly seen in Eq.3.72 and Eq.3.73. Therefore, $\overline{T}_c$ and T_a are set to 322.9 K and 28 K, respectively, respect this condition. Also, ξ is set according to the real characteristic values of VO_2 and SiO_2. This means that the first and second layers are composed of VO_2 and SiO_2, respectively. Therefore, $\xi = \zeta_2/\zeta_1$ where $\zeta_1 = r_d c_1^D \rho_1 l$ and $\zeta_2 = r_d c_2 \rho_2 l$. As previously stated, c_1^D and ρ_1 are 0.71 kJ kg^{-1} K^{-1} and 4670 kg m^{-3} for the first VO_2 layer, and c_2 and ρ_2 are 0.73 kJ kg^{-1} K^{-1} and 2650 kg m^{-3} for the second SiO_2 layer, respectively. Thus, $\xi = 0.59$ throughout the study. In addition, r_r is set to 0.5.

We start our examination with the parameter r_r by examining 4 different cases, defined as case 6 in Table 3.4. The temperature-dependent interface thermal resistance causes nonlinear variations on $\phi_+^{*,II}$ and $\phi_-^{*,II}$ as it changes with respect to the mean temperature. If we first examine $\phi_+^{*,II}$ as separately shown inside of Fig.3.17(a). The nonlinearity here only occurs due to the temperature-dependent interface thermal resistance. In one cycle, we observe both the heating and cooling phase transitions so that $\overline{v}(\theta_m)$ fully varies. Firstly, the mean temperature moves from hot temperature to cold temperature by following the cooling curve in the time interval between 0.24 and 0.35. Secondly, it heats up completely by following the heating curve in the time interval between 0.75 and 0.86. In fact, these are the time intervals where we observe the effect of the temperature-dependent interface thermal resistance on $\phi_+^{*,II}$ and $\phi_-^{*,II}$. The impact of case 6 (i) on $\phi_+^{*,II}$ and $\phi_-^{*,II}$ is different than case 6 (iii) and (iv), because $r_r = 0.5$ in case 6 (i), which means that r_m is twice lower than r_d. Oppositely, r_m is higher than r_d in case 6 (iii) and (iv). However, when $r_r = 1$ in case 6 (ii), r_m and r_d are the same and the interface thermal resistance does not vary with temperature. This situation can be seen from Eq.3.70 and Eq.3.71. When $r_r = 1$, the term including $\overline{v}(\theta_m)$ in the equations vanishes and Eq.3.71 for the forward configuration actually turns into Eq.3.65, because the second SiO_2 layer has a constant heat capacity. For the backward configuration, the effect of the temperature-dependent

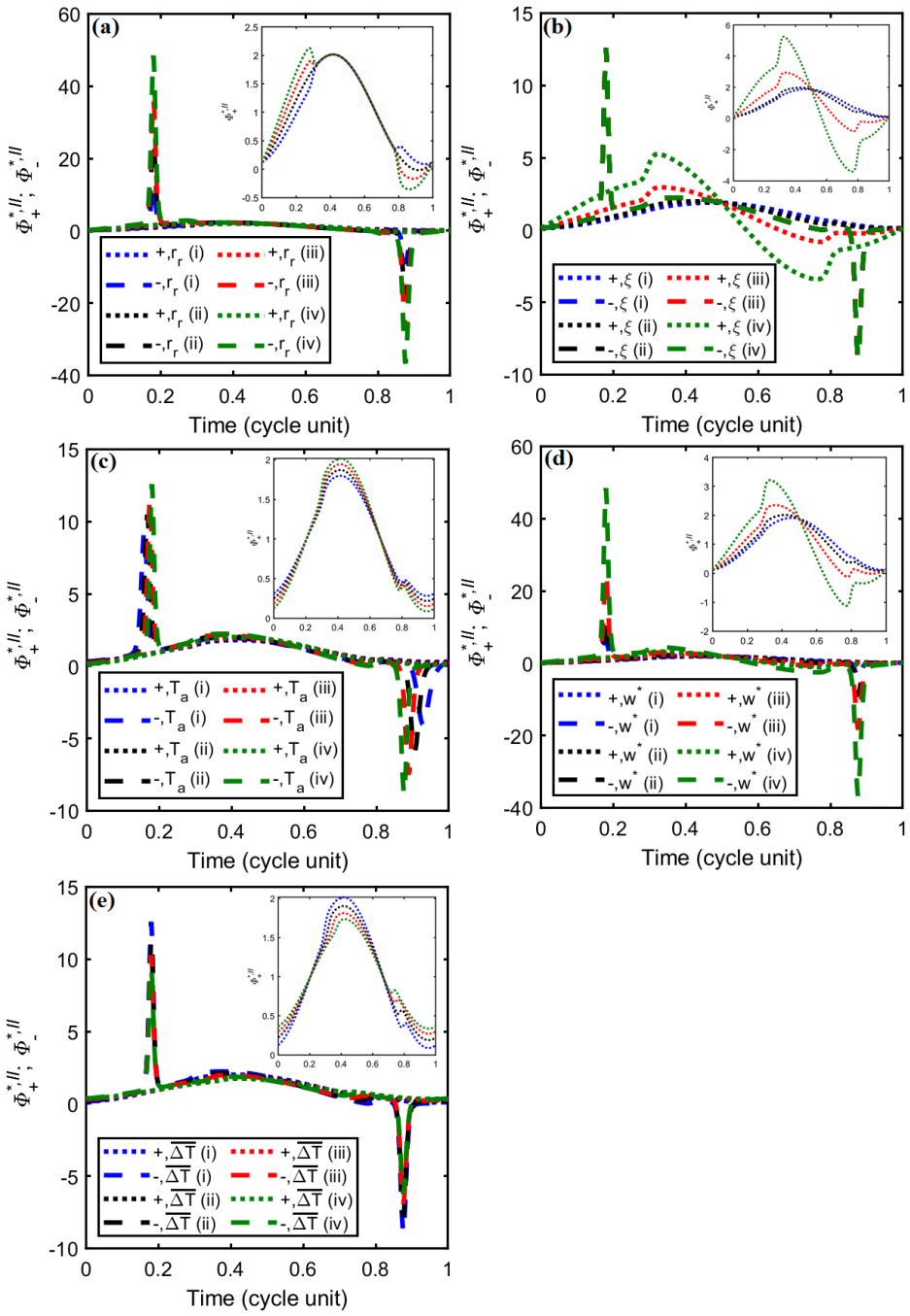

Figure 3.17: Computed time behaviors of $\phi_+^{*,II}$ and $\phi_-^{*,II}$ when the left layer has a temperature-dependent heat capacity for various investigated parameters: r_r (a), ξ (b), T_a (c), w^* (d) and $\overline{\Delta T}$ (e). The insets show the computed time behavior of $\phi_+^{*,II}$ separately [52].

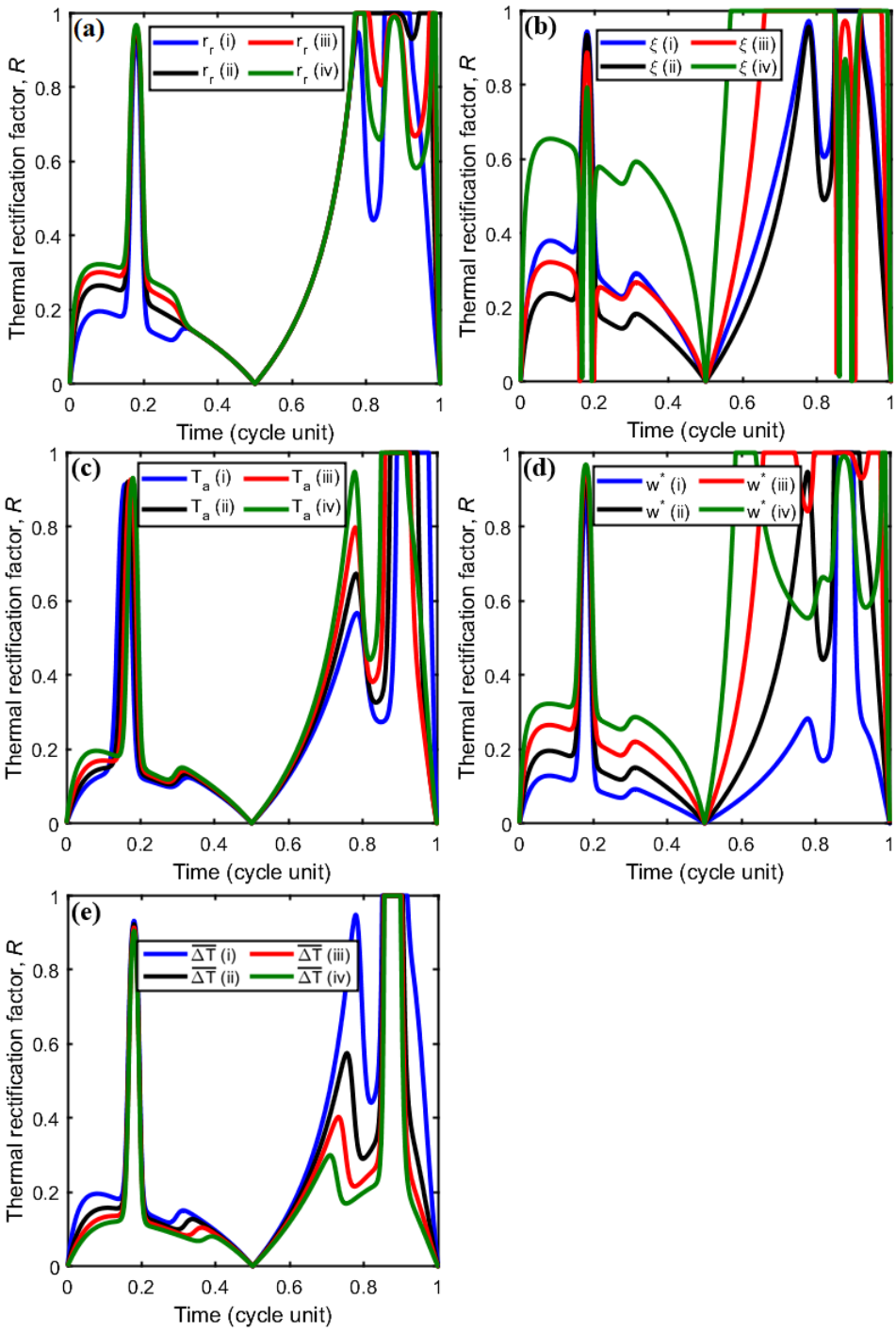

Figure 3.18: Computed time behaviors of R when the left layer has a temperature-dependent heat capacity for various investigated parameters: r_r (a), ξ (b), T_a (c), w^* (d) and $\overline{\Delta T}$ (e) [52].

heat capacity of the VO_2 layer can be seen on $\phi_-^{*,II}$ in Fig.3.17(a). The phase change of VO_2 occurs in two different time intervals and $\overline{v}(\theta_c)$ fully varies. Firstly, it cools down in the time interval between 0.15 and 0.21 and follows the cooling curve fully. Then, it heats up and follows the heating curve in the time interval between 0.85 and 0.92. Furthermore, the variations on $\phi_+^{*,II}$ and $\phi_-^{*,II}$ become more pronounced and the peak area increases as r_r increases. When we examine the results of R, we see a trend while both $\phi_+^{*,II}$ and $\phi_-^{*,II}$ have positive values. The maximum value of R gets higher as r_r increases as seen in Fig.3.18(a), but there is no specific behavior afterwards. The perfect thermal diode behavior is reached over few intervals of time.

We examine the parameter ξ as the second parameter instead of setting its value to 0.59 and its value is defined as case 7 in Table 3.4. We first examine $\phi_+^{*,II}$, shown as a small figure inside of Fig.3.17(b). Although there is a nonlinear behavior due to the temperature-dependent interface thermal resistance as we observed in the analysis of the parameter r_r, the peaks of $\phi_+^{*,II}$ are shifting to the left and the oscillation amplitude increases as ξ increases. We also observed this similar behavior in the constant heat capacity analysis. On the other hand, when we examine $\phi_-^{*,II}$, we see again the nonlinear behavior due to the temperature-dependent interface thermal resistance, but the majority of the variations on $\phi_-^{*,II}$ is due to the temperature-dependent heat capacity. The latent heat has a great impact on $\phi_-^{*,II}$ over the same two time intervals as in the analysis of the parameter r_r. Similar to the constant heat capacity analysis, the change of the parameter ξ does not affect the behavior of $\phi_-^{*,II}$. When we examine the behavior of R in Fig.3.18(b), some of the behaviors are similar to the constant heat capacity analysis. However, we see the significant impact of the temperature-dependent heat capacity on the general behavior of R. R firstly decreases as ξ increases as we see in case 7 (i) and (ii), then it starts to increase during a certain time interval, which is indeed the time until the middle of the time cycle where $\phi_+^{*,II}$ and $\phi_-^{*,II}$ intersect. When $\phi_+^{*,II}$ becomes negative, the system manifest the behavior of the perfect thermal diode and the time interval corresponding to this behavior increases by increasing ξ. However, R decreases and the perfect thermal diode effect vanishes over the time intervals when both $\phi_+^{*,I}$ and $\phi_-^{*,I}$ switch to negative values.

Considering the modulated temperature amplitude T_a, defined as case 8 in Table 3.4, it

should be noted that T_a affects both the cold temperature and the mean temperature at the interface as mentioned before. This situation differs the temperature-dependent heat capacity analysis from the constant heat capacity analysis. Therefore, we set T_a by considering that it can provide complete cycles of $\overline{v}(\theta)$ according to the variation of cold and mean temperatures, as previously explained and shown in Eq.3.72 and Eq.3.73, respectively. This changes the time intervals where we see the phase transition cycles for the interface thermal resistance and the heat capacity of VO_2. In other words, when T_a changes, the time intervals at which we see the variations of $\overline{v}(\theta_m)$ and $\overline{v}(\theta_c)$ shift slightly as seen in Fig.3.17(c). Apart from this shift, the oscillation amplitude of $\phi_+^{*,II}$ and $\phi_-^{*,II}$ increases as T_a increases, as we observed in the constant heat capacity analysis. When we examine R, we see that R increases as T_a increases as seen in Fig.3.18(c). After the middle of the cycle, we observe the perfect thermal diode behaviors again. In fact, these time intervals for the perfect thermal diodes generally occur at the time intervals where we see the peaks on $\phi_-^{*,II}$ due to the heat capacity variation of VO_2.

The parameter w^*, defined as case 9 in Table 3.4, is investigated through 4 different values. Although the temperature-dependent interface thermal resistance has an effect on $\phi_+^{*,II}$ and $\phi_-^{*,II}$ as reported in Fig.3.17(d), the oscillation amplitude of $\phi_-^{*,II}$ is always slightly higher than the oscillation amplitude of $\phi_+^{*,II}$ over the time interval where there is no phase transition of VO_2. In other words, over the time interval where there is no effect of the temperature-dependent heat capacity, because ξ is lower than 1. In addition, the oscillation amplitudes of both $\phi_+^{*,II}$ and $\phi_-^{*,II}$, and the absolute values of the peaks on $\phi_-^{*,II}$ increase as w^* increases. When we examine the behavior of R as shown in Fig.3.18(d), we see that R increases as w^* increases until the middle of the time cycle where $\phi_+^{*,II}$ and $\phi_-^{*,II}$ intersect. However, the time intervals where the perfect thermal diode behavior is observed decrease, because both $\phi_+^{*,II}$ and $\phi_-^{*,II}$ become negative at longer time periods due to the effect of latent heat when they are compared to the constant heat capacity analysis.

The consideration we made for the analysis of parameter T_a should also be taken into account for the analysis of the last parameter $\overline{\Delta T}$, because all investigated cases for $\overline{\Delta T}$ must provide complete phase transition cycles with respect to the variation of the cold and mean temperatures.

The investigated values are defined as case 10 in Table 3.4. As we previously stated, $\overline{\Delta T} = \overline{T}_h - \overline{T}_c$ and $\overline{T}_h$ is set according to $\overline{\Delta T}$ while $\overline{T}_c$ is always 322.9 K for all cases. We see the complete variations of $\overline{v}(\theta_m)$ and $\overline{v}(\theta_c)$ in all investigated cases with these configurations of $\overline{\Delta T}$ and $\overline{T}_c$. In fact, the variation of $\overline{v}(\theta_c)$ always occurs at the same time intervals for all cases as expected, because $\overline{T}_c$ is always the same. Therefore, the peaks of $\phi_-^{*,II}$ always occur at the same time as seen in Fig.3.17(e). On the other hand, the temperature at the interface $\overline{T_m} = (\overline{T_h} + \overline{T_c})/2$ also depends on $\overline{T_h}$. Therefore, the time intervals where we see the interface thermal resistance or $\overline{v}(\theta_m)$ variations slightly change in the examined cases. Moreover, we observe that the oscillation amplitude of $\phi_+^{*,II}$ and $\phi_-^{*,II}$ and the absolute values at the peaks on $\phi_-^{*,II}$ decrease as $\overline{\Delta T}$ increases. Also, when we examine R as reported in Fig.3.18(e), we see that R decreases by increasing $\overline{\Delta T}$. After the middle of the cycle, we observe the perfect thermal diode behaviors at the time intervals where there are peaks on $\phi_-^{*,II}$.

3.10 Conclusion

We started this chapter with an introductory analysis of a linear CTD. The CTD is composed of two different solid materials with constant thermal properties instead of VO_2 and SiO_2. We analyzed it with two different configurations. The first one is when both boundary conditions are fixed and the second one is when one side is fixed and the other side has sinusoidal boundary conditions. The analysis of the first configuration showed that the thermal rectification vanishes when the system reaches its steady-state regime in a linear system. Moreover, this analysis showed that when time goes to zero, the ratio of the heat flux densities in the forward and backward configurations of the linear CTD tend exactly to the ratio of the effusivities of the two materials.

Later, we have theoretically analyzed the thermal rectification factor of a CTD composed of VO_2 and SiO_2 considering the Dirichlet boundary conditions under transient conditions. The heat flux density behavior at the cold side of the thermal diode and its consequence on the thermal rectification factor of the thermal diode have been investigated deeply by considering various intrinsic and extrinsic parameters: the hot T_h and cold T_c applied boundary condition

values, the phase transition slope β and the latent heat L_n of the PCM, the ratio of the thermal conductivity of the metallic and dielectric phases k_r of the PCM, the width between the phase transition temperatures for the heating and cooling processes ΔT_o of the PCM, and the interface thermal resistance r. It has been shown that the thermal conductivity and the specific heat capacity have a major impact on the nonlinear time behavior of the thermal rectification under transient conditions. Furthermore, we obtained higher thermal rectification under transient conditions than steady-state conditions for almost all investigated parameter values. There is an effect of the interface thermal resistance on the thermal rectification for both steady-state and transient conditions, but this effect seems to be generally small in comparison with the other intrinsic parameters we analyzed.

We then performed a detailed analysis for the CTD by applying dynamical boundary conditions while considering the full properties of VO_2 and including the hysteresis zone. Similarly, the CTD is made of VO_2 and SiO_2. We extended the analysis by examining the role of the capacitive effect on the thermal rectification by changing the frequency f and the temperature amplitude T_a of the applied sinusoidal boundary conditions. We observed that the nonlinear variations of the thermal conductivity of VO_2, combined with the hysteresis zone, significantly affect the thermal rectification. As a consequence of the phase transition, we see peculiar behaviors on the heat flux density even at low frequencies for the CTD. We observed that the frequency of the applied boundary sinusoidal temperature is another key factor that affects the thermal rectification. The thermal rectification oscillates more and its maximum value becomes higher when the frequency increases.

Lastly, the capacitive effect is generally omitted in the literature as mentioned before. Therefore, we actually addressed this in a separate case study to reveal its effect on the thermal rectification in depth. As seen from the analysis of the temperature-dependent heat capacity case, we observed more pronounced variations in the thermal rectification as a result of the nonlinear behavior of this property for VO_2.

Considering the reasonable outcomes of these theoretical studies, further research should be

conducted on this type of thermal diodes especially under different transient boundary conditions in order to demonstrate the full benefits of the transient analysis for a better control of practical thermal management systems. Especially in the analysis of the dynamical conditions, the hysteresis zone should be included to better understand the behaviors of the thermal diodes and to reveal their further potential in order to integrate them into daily use.

Résumé du Chapitre 3

De nombreuses études examinent la rectification thermique des diodes thermiques conductives (DTC) dans des conditions stationnaires, et l'intérêt pour l'analyse transitoire ne cesse de croître. Cependant, nous n'avons pas rencontré de travaux antérieurs qui aient étudié la DTC en tenant compte de l'ensemble des propriétés du VO_2 dans des conditions transitoires, y compris dans la zone d'hystérésis. Par conséquent, dans le Chapitre 3, nous étudions une DTC composée de VO_2 et de SiO_2, avec des conditions aux limites fixes et sinusoïdales, y compris les propriétés complètes du VO_2 et l'effet capacitif. Nous avons étudié en détail la rectification thermique de la DTC en modifiant différents paramètres intrinsèques et extrinsèques.

Ce chapitre se compose de 4 parties. Dans l'introduction, nous commençons par analyser une DTC linéaire au lieu d'une DTC composée de VO_2 et SiO_2. Nous examinons ensuite le facteur de rectification thermique R de la DTC composée de VO_2 et SiO_2 dans des conditions aux limites fixes pour divers paramètres intrinsèques et extrinsèques. Nous poursuivons ensuite notre analyse avec la même DTC en appliquant des conditions aux limites sinusoïdales et en incluant la zone d'hystérésis du VO_2. Enfin, nous concluons ce chapitre par une étude de cas distincte dans laquelle nous examinons l'impact de l'effet capacitif sur le comportement d'une DTC dans des conditions limites dynamiques. Dans l'ensemble des analyses présentées dans ce chapitre, une seule variable est modifiée, tandis que les autres demeurent constantes. Il convient également de noter que nous utilisons la formule de R (Éq. 1.25) présentée au Chapitre 1.

Modélisation théorique de la diode thermique conductive linéaire

Nous avons réalisé une étude de cas introductive afin d'examiner la possibilité d'un comportement de rectification thermique pour une DTC constituée de deux matériaux solides différents aux propriétés thermiques constantes, comme le montre la Fig.3.1. Nous supposons également que le contact thermique entre les deux matériaux n'est pas parfait. Le point de départ de notre modélisation est l'équation classique de diffusion de la chaleur basée sur le modèle de Fourier (Éq.3.1), que nous résolvons dans chaque matériau en fonction des conditions aux limites im-

posées de la DTC. Nous adoptons une analyse nondimensionnelle et obtenons l'Éq.3.2. Ensuite, nous utilisons la méthode des quadripôles thermiques (MQT) pour résoudre l'équation de la chaleur dans chaque matériau [145]. Enfin, nous obtenons les comportements en temps réel à l'aide d'un algorithme numérique de la transformée inverse de Laplace.

Conclusion pour l'analyse de la diode thermique conductive linéaire

Nous examinons le comportement temporel de la rectification thermique pour deux ensembles différents de conditions limites de Dirichlet et nous l'étudions avec 3 paramètres différents, selon les valeurs indiquées dans le Tableau 3.1. Le premier correspond à des conditions aux limites fixes et le second au cas où les conditions aux limites sont sinusoïdales. Dans tous les paramètres, nous observons effectivement un R plus élevé au début du processus transitoire dans ces conditions pour les conditions aux limites fixes. Ensuite, R s'annule lorsque le système atteint son régime permanent, comme prévu. Pour les conditions limites sinusoïdales, le comportement temporel de R présente davantage de caractéristiques, atteignant 1 et tombant à 0 trois ou quatre fois chacun sur une période entière. De plus, ce comportement temporel est une caractéristique inhérente à l'équation de Fourier classique de diffusion de la chaleur dans un système linéaire. Nous pouvons facilement montrer que le rapport des densités de flux de chaleur dans les configurations directe et inverse de la DTC linéaire tend exactement vers le rapport des effusivités thermiques des deux matériaux qui composent la diode thermique lorsque le temps tend vers zéro.

Modélisation théorique de la diode thermique conductive dans des conditions limites de Dirichlet

Nous poursuivons notre analyse sur la DTC composé de VO_2 et SiO_2 dans des conditions limites de Dirichlet, comme illustré sur la Fig.3.4. Dans cette analyse, nous pouvons utiliser directement l'Éq.1.16 pour la conductivité thermique et l'Éq.1.17 pour la capacité thermique spécifique, car nous fixons les valeurs des conditions aux limites de manière à toujours provoquer un processus de transition de phase complet sur la courbe de chauffage et de refroidissement.

Nous avons nondimensionné l'équation non linéaire de diffusion de la chaleur (Éq.2.1) pour le VO_2 et elle peut être écrite comme dans l'Éq.3.12. De plus, l'équation de diffusion de la chaleur dans le SiO_2 peut être non dimensionnée directement comme dans l'Éq.3.13. Ensuite, les équations Éq.3.12 et Éq. 3.13 sont résolues numériquement à l'aide de la méthode implicite des différences finies. Enfin, la densité de flux thermique normalisée peut être évaluée à l'aide des Éq.3.14 et Éq.3.15 pour les configurations directe et inverse. En outre, nous résolvons l'équation de conduction thermique (Éq.2.1) en régime permanent de manière semi-analytique afin de valider les résultats obtenus numériquement au cours de l'analyse du régime transitoire. Enfin, R en régime permanent peut être trouvé à l'aide des équations Éq.3.48, Éq.3.49, Éq.3.52 et Éq.3.53.

Conclusion pour l'analyse de la diode thermique conductive dans des conditions limites de Dirichlet

Nous avons étudié l'impact de la variation de 6 paramètres différents, comme indiqué dans le Tableau 3.2. En somme, nous avons observé que la dynamique temporelle de R était sensible à chacun des 6 paramètres pris en compte dans cette étude. Elle manifeste un comportement non linéaire très marqué. Le degré d'influence de chaque paramètre n'est pas le même, mais ils ont tous un impact sur l'ensemble du profil temporel de R, depuis le régime transitoire précoce jusqu'au régime permanent. $\widetilde{R}$ quantifie l'effet capacitif de la DTC et fournit des informations essentielles sur la durée et l'ampleur de la dynamique de la rectification thermique.

Modélisation théorique de la diode thermique conductive dans des conditions limites dynamiques

Nous considérons la DTC avec une longueur de 2 mm dans une géométrie plane, sous des conditions limites dynamiques, comme on le voit dans les Fig.3.11(a) et (b) pour les configurations directe et inverse, respectivement. Dans notre modèle, nous appliquons deux températures sinusoïdales à ses frontières, comme indiqué dans les Éq.3.56 et Éq.3.57. Nous considérons toujours la variation de l'amplitude de température T_a de sorte qu'un côté de la diode thermique soit toujours à la température la plus élevée et l'autre côté à la température la plus basse.

Conclusion pour l'analyse de diode thermique conductive dans des conditions limites dynamiques

Nous examinons le comportement de la rectification thermique en fonction de 4 fréquences différentes, tout en appliquant les valeurs de T_a qui ont été définies comme cas 1 dans le Tableau 3.4. En somme, nous observons que la fréquence f et T_a affectent la densité du flux thermique et R comme indiqué dans les Fig.3.12 et Fig.3.13, respectivement. Bien que la variation de la densité du flux thermique soit suffisamment faible pour être considérée comme constante à faible f, il existe toujours une variation résultant du processus de changement de phase du matériau. Les variations non linéaires de la conductivité thermique de VO_2 en fonction de la température, combinées à l'effet d'hystérésis, sont responsables du comportement particulier de la densité du flux de chaleur, même à faible f. Par conséquent, le comportement de R présente également des caractéristiques non linéaires et particulières intéressantes. Lorsque T_a et f augmentent, l'impact du processus de changement de phase devient plus prononcé et R a tendance à osciller davantage et son maximum devient encore plus élevé.

Modélisation théorique de la diode thermique capacitive

Afin de souligner l'impact de l'effet capacitif sur le comportement d'une DTC dans des conditions limites dynamiques, nous considérons une configuration simple de la diode thermique dans laquelle les deux couches sont suffisamment fines pour que nous puissions négliger la variation spatiale de la température dans chacune d'elles. Les deux couches ont des températures uniformes qui ne dépendent que du temps (fréquence). Nous supposons que l'une des couches a une capacité thermique dépendant de la température (il pourrait s'agir d'un MCP) tandis que l'autre couche a une capacité thermique constante. Ce type de diode thermique est appelé diode thermique capacitive. La Fig.3.14 montre une représentation schématique de ce type de diode thermique.

Nous commençons d'abord l'analyse de la diode thermique capacitive en supposant que les deux couches ont une capacité thermique constante. Sur la base de la loi de conservation de l'énergie, nous pouvons facilement exprimer les densités de flux de chaleur dans les configurations directe et inverse de cette diode thermique capacitive comme indiqué par Éq.3.58 and

Éq.3.59, respectivement. Après un peu d'algèbre et de nondimensionnalisation, nous pouvons exprimer les densités de flux de chaleur nondimensionnées pour les 2 configurations; directe et inverse comme dans les Éq.3.64 et Éq.3.65, respectivement.

Ensuite, nous effectuons l'analyse pour le cas de la diode thermique capacitive, dans laquelle une première couche a une capacité thermique dépendante de la température (MCP) et une deuxième couche a une capacité thermique constante. De même, après un peu d'algèbre et de nondimensionnalisation, nous pouvons exprimer les densités de flux de chaleur nondimensionnées pour les 2 configurations; directe et inverse comme dans les Éq.3.70 et Éq.3.71, respectivement.

Conclusion pour l'analyse de la diode thermique capacitive

Les paramètres étudiés pour la diode thermique capacitive sont répertoriés dans le Tableau 3.4. Les cas 2, 3, 4 et 5 présentent les paramètres et leurs valeurs pour la diode thermique capacitive dont les deux couches ont des capacités thermiques constantes, tandis que les cas 6, 7, 8, 9 et 10 présentent les paramètres et leurs valeurs pour la diode thermique capacitive dont une couche a une capacité thermique dépendant de la température. Dans les deux configurations, nous constatons clairement l'effet capacitif sur le redressement thermique. Cependant, nous observons une variation plus prononcée de la rectification thermique dans l'analyse du cas de la capacité thermique dépendant de la température, en raison du comportement non linéaire de VO_2.

Chapter 4

Conductive Thermal Transistor

Contents

4.1 Introduction 185
4.2 Conductive thermal transistor with a phase change material base . . . 187
4.3 Results and discussion of the conductive thermal transistor with a phase change material base 192
4.4 Conductive thermal transistor made of different phase change materials 206
4.5 Results and discussion of the conductive thermal transistor made of different phase change materials 209
4.6 Conclusion 219

4.1 Introduction

In this chapter, we examine the conductive thermal transistor (CTT) in detail. There are many studies that examine the thermal transistor concept as summarized in the literature review section of Chapter 1, but the majority of it is related to the radiative regime of heat transfer; either the near-field or the far-field as well as in the quantum framework except one or two studies. Indeed, to the best of our knowledge, except the pioneer work of Li et al. [116] and the recent work of Wu et al. [118], no other macroscopic concept of a thermal transistor in the conductive regime of heat transfer has been presented. This constitutes the novelty of our study, in which we theoretically analyze the behavior of a PCM based CTT which has an analogy with an electronic bipolar transistor. The classical thermal transistor functions such as amplification and switching are deeply investigated.

We conduct the study by examining two different CTT concepts. The first one is a CTT with a PCM base and the second one is a CTT made of different PCMs, which are illustrated in Fig.4.1 and Fig.4.2, respectively. The collector and emitter elements of both devices can be made of metals, semi-metals or highly doped semi-conductors. In the first concept, the base can be made of an insulating-metal PCM, which is VO_2 in our case as mentioned before. In this concept, the base element is considered so thin so that it behaves as an interface thermal resistance between the collector and the emitter that is characterized with a thermal resistance or conductance that only depends on its temperature T. We can neglect the influence of T_C and T_E. On the other hand, in the second concept, the base element can also be made of similar materials used for the collector and emitter elements, while the interfaces collector-base and base-emitter are made of an insulating-metal PCM. We shall show that both concepts manifest well the NDTR or the transistor effect. Also, we assume the collector, the emitter and the base to be characterized with a spatially uniform temperature each; T_C, T_E and T, respectively. Our analysis considers the steady-state regime of operation of the thermal transistor, throughout which we always assume

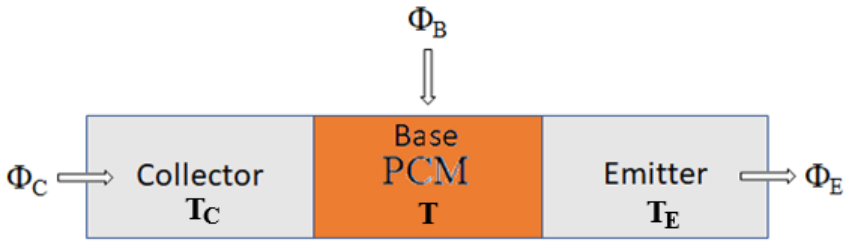

Figure 4.1: Schematic representation of the CTT with a PCM base [56].

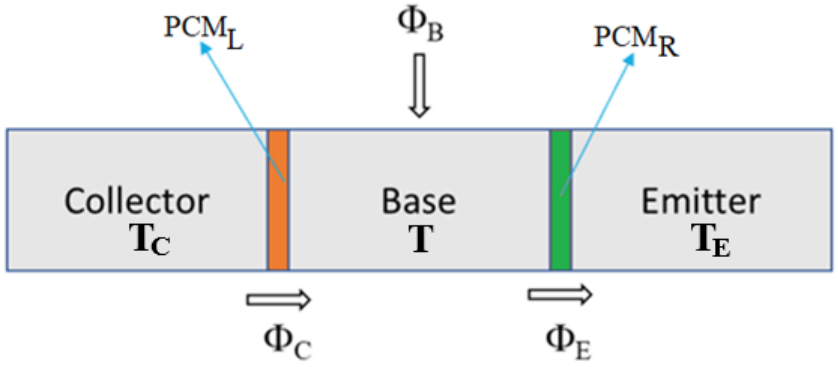

Figure 4.2: Schematic representation of the CTT with different PCMs.

$T_C > T > T_E$.

4.2 Conductive thermal transistor with a phase change material base

Firstly, we will start by examining the CTT with a PCM base as illustrated in Fig.4.1. The heat flux densities ϕ_E and ϕ_C can be written as:

$$\phi_E = G(T)\,[T - T_E] \tag{4.1}$$

$$\phi_C = G(T)\,[T_C - T] \tag{4.2}$$

the input heat flux density of the VO_2 base, ϕ_B, is obtained according to the heat flux conservation condition in the steady-state regime as:

$$\phi_B = \phi_E - \phi_C \tag{4.3}$$

We assume the thermal conductance of the VO_2 base $G(T)$ to have a similar temperature behavior to the one that governs the thermal conductivity of VO_2 in the heating and cooling regimes. Therefore, we can express $G(T)$ as [5, 35]:

$$G(T) = G_D + (G_M - G_D)v(T) \tag{4.4}$$

where G_D and G_M are the thermal conductances in the dielectric and metallic phases, respectively. As mentioned before, $v(T)$ represents the volume fraction of the metallic domains and it is expressed as $v(T) = \left[1 + e^{-\beta(T-T_o)}\right]^{-1}$. In addition, β is the phase transition slope and its value is 1.6 K^{-1} [35], and T_o is the critical phase transition temperature of VO_2 which is around 340 K [63].

At thermal equilibrium, $\phi_B = 0$, therefore $\phi_C = \phi_E$. The equilibrium temperature is obtained straightforwardly from Eqs (4.1) and (4.2) as:

$$T_{eq} = \frac{T_E + T_C}{2} \tag{4.5}$$

T_{eq} can be arranged according to the temperatures of the collector T_C and emitter T_E. We set T_C and T_E to 380 K and 300 K, respectively, in this study unless otherwise stated. Thus,

$T_{eq} = 340$ K which is the same temperature as the transition temperature T_o of VO_2. Thanks to this arrangement, we can induce a phase transition from insulator-to-metallic and vice versa by a small increase or decrease of the base temperature T by changing the input heat flux density ϕ_B.

The amplification factor Γ of the CTT can be defined with respect to the emitter and the collector as follows [116]:

$$\Gamma_{E,C} = \left|\frac{\partial\phi_{E,C}}{\partial\phi_B}\right| = \left|\frac{\partial\phi_{E,C}/\partial T}{\partial\phi_B/\partial T}\right| \tag{4.6}$$

In order to have an amplification, $\Gamma_{E,C}$ needs to be higher than 1 and the NDTR regime has to be met [116]. This regime requires that one of the two thermal resistances $-(\partial\phi_C/\partial T)^{-1}$ or $(\partial\phi_E/\partial T)^{-1}$ to be negative. The treatment of the amplification factors Γ_E and Γ_C are very similar. Indeed, the two are related based on Eq.4.3. Therefore, we detail the theoretical part only for the case of Γ_E. We can write Γ_E as:

$$\Gamma_E = \left|\frac{\partial\phi_E}{\partial\phi_B}\right| = \left|\frac{R_C}{R_C + R_E}\right| \tag{4.7}$$

where R_C and R_E are the differential thermal resistances. They can be expressed as $R_C = -(\partial\phi_C/\partial T)^{-1}$ and $R_E = (\partial\phi_E/\partial T)^{-1}$, respectively. In order to have Γ_E greater than 1, it is clear to see from Eq.4.7 that R_C or R_E has to be negative. On the other hand, Γ_E cannot be greater than 1 in the cases where R_C and R_E are both positive, which means that no amplification is achieved. As we shall see later on, the condition of the NDTR regime will indeed occur with some circumstances during the phase transition of the VO_2 base. Besides, this NDTR regime will be explained in more detail in the results and discussion section based on one case we examine.

We can easily show that Γ_E is given by:

$$\Gamma_E^{-1} = \left|\frac{\partial(\phi_E - \phi_C)}{\partial\phi_E}\right| = 2\left|\frac{G'(T)\,[T - T_{eq}] + G(T)}{G'(T)\,[T - T_E] + G(T)}\right| \tag{4.8}$$

$G'(T)$ is almost 0 when the base temperature T is set outside of the transition zone. Therefore, $\Gamma_E = 0.5$ and, in fact, $R_C = R_E$ as seen from Eq.4.7 and Eq.4.8. This is also true for Γ_C. Now, if we examine the transition zone for the amplification, Eq.4.8 can be expressed after substituting

$G(T)$ and $G'(T)$ as follows:

$$\Gamma_E^{-1} = \left|\frac{\partial(\phi_E - \phi_C)}{\partial\phi_E}\right| = 2\left|\frac{\beta\left[1-v(T)\right]\left[T-T_{eq}\right] + \frac{1}{g-1}v^{-1}(T) + 1}{\beta\left[1-v(T)\right]\left[T-T_E\right] + \frac{1}{g-1}v^{-1}(T) + 1}\right| \tag{4.9}$$

where $g = G_M/G_D > 1$. Then, Γ_E can be rewritten as:

$$\Gamma_E = \frac{1}{2}\left|\frac{\beta\left[1-v(T)\right]\left[T-T_E\right] + Av^{-1}(T) + 1}{\beta\left[1-v(T)\right]\left[T-T_{eq}\right] + Av^{-1}(T) + 1}\right| \tag{4.10}$$

where $A = 1/(g-1)$. If we set $\beta\left[1-v(T)\right] = \chi(T)$ and $Av^{-1}(T) + 1 = Y(T)$, Eq.4.10 can be modified as:

$$\Gamma_E = \frac{1}{2}\left|\frac{\chi(T)\left[T-T_E\right] + Y(T)}{\chi(T)\left[T-T_{eq}\right] + Y(T)}\right| \tag{4.11}$$

if we take the derivative of Eq.4.11 with respect to temperature, the following equation is obtained:

$$\frac{d\Gamma_E}{dT} = \pm\frac{\left[Y\chi' - \chi(\chi + Y')\right]\left[T_{eq} - T_E\right]}{2\left\{\chi\left[T-T_{eq}\right] + Y\right\}^2} \tag{4.12}$$

the derivatives of $\chi(T)$ and $Y(T)$ are:

$$\frac{d\chi}{dT} = \chi' = -\beta^2 v[1-v(T)] \tag{4.13}$$

$$\frac{dY}{dT} = Y' = -\frac{\beta A[1-v(T)]}{v(T)} \tag{4.14}$$

We substitute Eq.4.13 and Eq.4.14 into Eq.4.12. The following numerator part of Eq.4.12 has to be 0 to determine the temperature at which Γ_E reaches its maximum (T_{max}):

$$-v(T_{max})\left[1 + \frac{A}{v(T_{max})}\right] - \left[1 - v(T_{max})\right]\left[1 - \frac{A}{v(T_{max})}\right] = 0 \tag{4.15}$$

where $v(T_{max})$ has to be between 0 and 1 ($0 < v(T_{max}) < 1$). Then, $v(T_{max})$ can be written from Eq.4.15 as:

$$v(T_{max}) = \frac{1}{1 + e^{-\beta(T_{max} - T_o)}} = \frac{A}{2A+1} \tag{4.16}$$

then, T_{max} can be analytically expressed as:

$$T_{max} = T_o + \frac{1}{\beta} ln\left(\frac{A}{A+1}\right) \tag{4.17}$$

and if we substitute A into Eq.4.17, the final analytical equation for T_{max} can be written as:

$$T_{max} = T_o - \frac{1}{\beta} ln(g) \tag{4.18}$$

It is analytically seen from Eq.4.18 that T_{max} is always less than T_o ($T_{max} < T_o$) in any circumstances. Therefore, the base temperature T has to be set just before the transition temperature T_o to have the maximum amplification factor. The expression of Γ_E^{max} is obtained straightforwardly by replacing T_{max} into Eq.4.10 as:

$$\Gamma_E^{max} = \frac{1}{2} \left| \frac{\beta \left[1 - \frac{1}{1+g}\right] [T_{max} - T_E] + \frac{g+1}{g-1} + 1}{\beta \left[1 - \frac{1}{1+g}\right] [T_{max} - T_{eq}] + \frac{g+1}{g-1} + 1} \right| \tag{4.19}$$

then, after rearranging the terms in Eq.4.19, the final analytical expression to determine Γ_E^{max} can expressed as:

$$\Gamma_E^{max} = \frac{1}{2} \left| 1 + \frac{\beta [T_C - T_E]}{\beta \left[2T_o - T_E - T_C\right] - 2ln(g) + 4 \left[\frac{g+1}{g-1}\right]} \right| \tag{4.20}$$

We can easily show that the expression of Γ_C is given by:

$$\Gamma_C = \frac{1}{2} \left| \frac{\beta \left[1 - v(T)\right] [T_C - T] - Av^{-1}(T) - 1}{\beta \left[1 - v(T)\right] [T - T_{eq}] + Av^{-1}(T) + 1} \right| \tag{4.21}$$

This expression manifests a maximum at the same temperature T_{max} as Γ_E (Eq.4.18) and this maximum has the following analytical expression:

$$\Gamma_C^{max} = \frac{1}{2} \left| \frac{\beta [T_C - T_E]}{\beta \left[2T_o - T_E - T_C\right] - 2ln(g) + 4 \left[\frac{g+1}{g-1}\right]} - 1 \right| \tag{4.22}$$

We shall note that based on the definition of Γ_E and Γ_C and by using the heat flux conservation equation as given by Eq.4.3, we can show that $\Gamma_C < \Gamma_E + 1$ which implies that $\Gamma_C^{max} < \Gamma_E^{max} + 1$. An equality that is confirmed by Eqs. (4.20) and (4.22).

In order to have a nondimensionalized analysis of the changes of the heat flux density profiles with respect to the parameter g throughout the study, we divide Eq.4.1, Eq.4.2 and Eq.4.3 by

$G_D T_{amb}$ where T_{amb} is the ambient temperature that we take to be 300 K:

$$\phi_E^* = \frac{\{1 + [g-1]\, v(T)\}\, [T - T_E]}{T_{amb}} \tag{4.23}$$

$$\phi_C^* = \frac{\{1 + [g-1]\, v(T)\}\, [T_C - T]}{T_{amb}} \tag{4.24}$$

$$\phi_B^* = \frac{\{1 + [g-1]\, v(T)\}\, [2T - T_C - T_E]}{T_{amb}} \tag{4.25}$$

where ϕ_E^*, ϕ_C^* and ϕ_B^* are the nondimensionalized heat flux densities given by $\phi_E/G_D T_{amb}$, $\phi_C/G_D T_{amb}$ and $\phi_B/G_D T_{amb}$, respectively.

We will see in the following that the two CTT core functions (amplification or switch) occur in different heat flux density ϕ_B^* regimes. Therefore, it is crucial to examine the behaviors of the heat flux density profiles to understand these two functions. Furthermore, all equations for the studied CTT with a PCM base in Fig.4.1 are also valid for the concept of a CTT that is shown in Fig.4.3, whose collector-base and base-emitter interfaces are made of the same PCM and whose base element can be made of metals, semi-metals or highly doped semi-conductors. In fact, both give exactly the same results under the assumption that the interface thermal resistance depends only on the base temperature T. Therefore, we explain the results of the investigated parameters only with respect to the CTT concept shown in Fig.4.1, but they can also be applied to the configuration shown in Fig.4.3. Moreover, the concept explained here and the analytical expressions are generally applicable to all solid oxides that show similar crystalline transition structures such as VO_2 that we consider in our study.

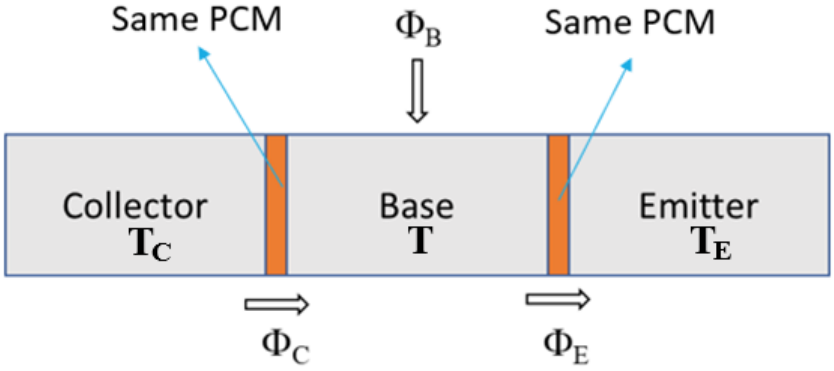

Figure 4.3: Schematic representation of a CTT made of the same PCMs.

4.3 Results and discussion of the conductive thermal transistor with a phase change material base

We investigate 5 different parameters; g, T_E, T_C, T_o and β for the CTT analysis in this study. During the study, only one parameter is changed in each analysis while the others are kept unchanged. Unless otherwise stated, all parameters are set with the values mentioned in this paragraph throughout the study. The temperatures of the collector T_C and the emitter T_E are set to be 380 K and 300 K, respectively. As mentioned before, we assume that the thermal conductance profile follows the same temperature behavior as the thermal conductivity profile of VO_2. The thermal conductivities of VO_2 in the dielectric and metallic phases are 3.6 $Wm^{-1}K^{-1}$ and 6 $Wm^{-1}K^{-1}$, respectively [7]. Therefore, we set g to 1.67, which is the ratio of the thermal conductivity in the metallic phase over the thermal conductivity in the dielectric phase of VO_2. We set the phase transition temperature of VO_2 to 340 K and the value of β to 1.6 K^{-1}. [35, 63]. Although the values of the parameters are investigated in a wider range, the results of some specific cases that are shown in Table 4.1 are individually represented in more detail in order to explain the behaviors and help the visualization of their changes.

The ratio of the thermal conductances g, which is case 1 in Table 4.1, is analyzed as the first parameter. The computed behaviors of the nondimensional heat flux densities from the collector to the base ϕ_C^*, to the base ϕ_B^* and from the base to the emitter ϕ_E^* with respect to the base temperature T are shown in Fig.4.4(a) for 4 different values of g. The amplification factors, Γ_C and Γ_E, are reported in Fig.4.4(b). It is clearly seen in these figures how increasing g affects the T profile of the different heat flux densities and consequently Γ_E and Γ_C. When there is a slight increase in ϕ_B^* around the transition temperature T_o, there is a pronounced increase in both ϕ_C^* and ϕ_E^*. By increasing g, both Γ_E and Γ_C increase and the position of their maxima move far away to the left of T_o as predicted by Eqs. (4.18), (4.20) and (4.22). In order to show exactly how Γ_E^{max}, Γ_C^{max} and T_{max} change by increasing g, we report the computed behaviors of these quantities as functions of g varying from 1.5 up to 10 in Fig.4.5. It is interesting to notice that both Γ_E^{max} and Γ_C^{max} get steeper as g increases.

Table 4.1: Investigated parameters and cases for the CTT with a PCM base [56].

Case 1 - g				
	(i)	(ii)	(iii)	(iv)
g	1.67	2	4	6
Case 2 - T_E				
	(i)	(ii)	(iii)	(iv)
T_E [K]	280	290	310	320
Case 3 - T_C				
	(i)	(ii)	(iii)	(iv)
T_C [K]	360	370	390	400
Case 4 - T_o				
	(i)	(ii)	(iii)	(iv)
T_o [K]	330	335	340	345
Case 5 - β				
	(i)	(ii)	(iii)	(iv)
β [K^{-1}]	0.5	1	1.6	3

The nondimensional heat flux densities ϕ_C^*, ϕ_B^* and ϕ_E^*, and the amplification factor Γ_E of case 1 (i) are shown in Fig.4.6(a) and (b), respectively. We emphasize this case separately in order to explain the NDTR phenomenon that induces the amplification. As mentioned before, the NDTR regime requires that one of the two thermal resistances $-(\partial\phi_C/\partial T)^{-1}$ or $(\partial\phi_E/\partial T)^{-1}$ to be negative. Fig.4.6(a) shows that $\partial\phi_C^*/\partial T$ and $\partial\phi_E^*/\partial T$ have negative and positive values outside of the transition region, respectively, and this makes the amplification factor $\Gamma_E = 0.5$ as seen in Fig.4.6(b). However, $\partial\phi_C^*/\partial T$ starts to be positive at $T = 337.7$ K so that both $\partial\phi_C^*/\partial T$ and $\partial\phi_E^*/\partial T$ have positive values until $T = 342$ K. Therefore, the condition of the NDTR regime to have an amplification is satisfied in the region between these temperatures and this causes an amplification with Γ_E higher than 1 as seen in Fig.4.6(b).

As a second parameter, we examined the emitter temperature T_E by examining 4 different values as shown in case 2 of Table 4.1. As seen in Fig.4.7(a), although ϕ_C^* profile remains the

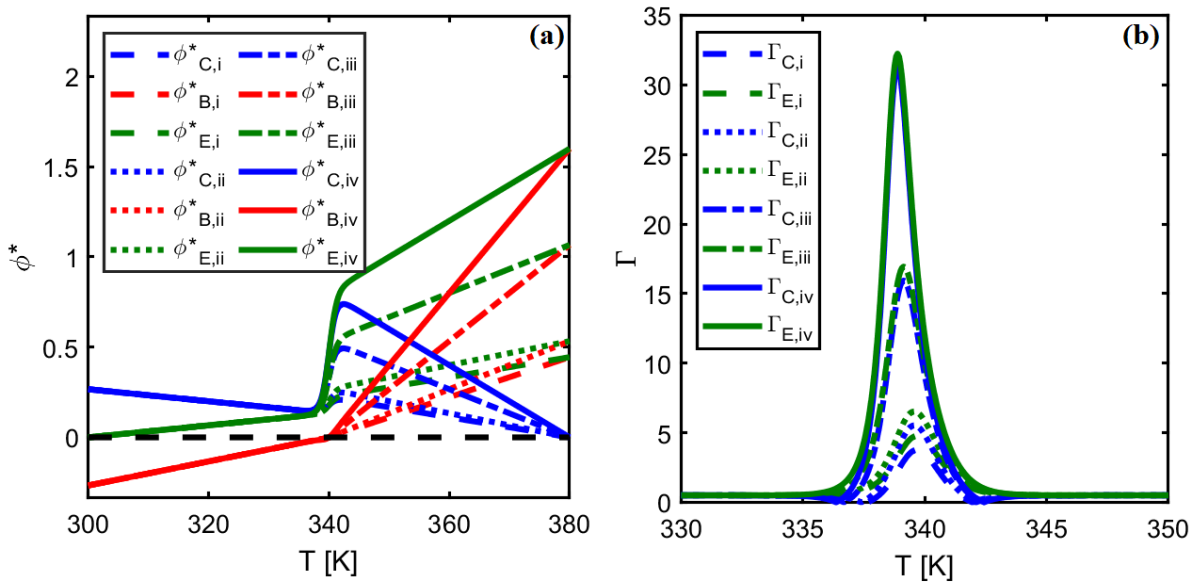

Figure 4.4: The computed behaviors of the nondimensional heat flux density profiles ϕ^*_C, ϕ^*_B and ϕ^*_E (a), and the amplification factors Γ_C and Γ_E (b) as functions of the base temperature T for different values of g [56].

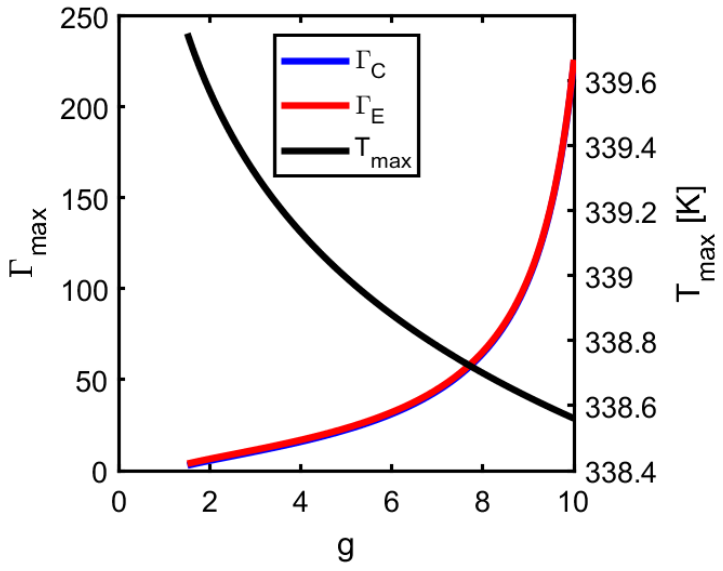

Figure 4.5: The computed behaviors of the maximum amplification factors Γ^{max}_C and Γ^{max}_E, and the optimal base temperature T_{max} as functions of g [56].

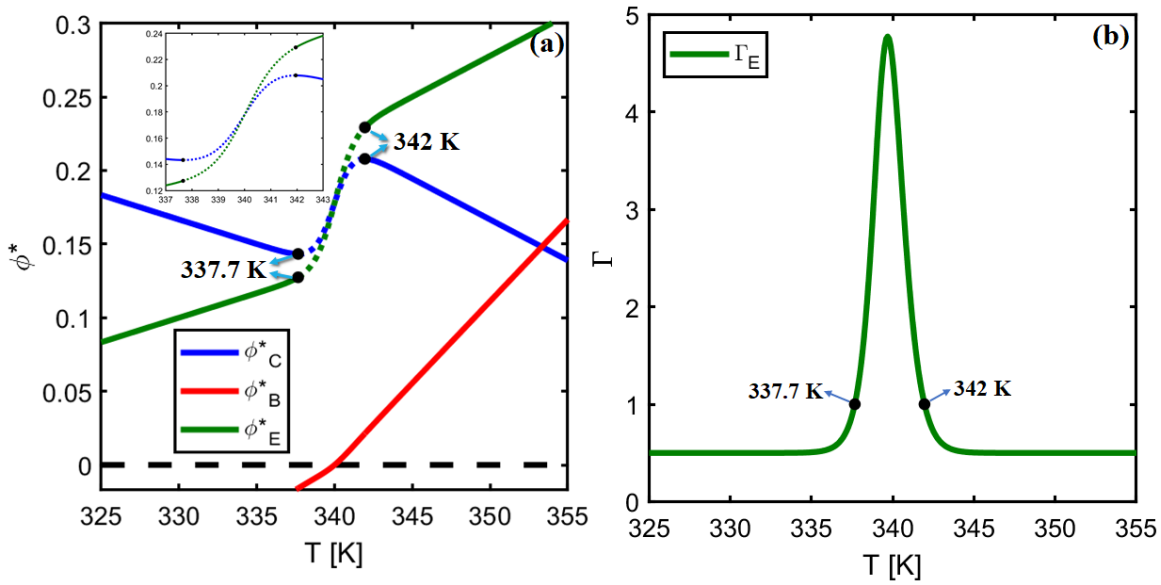

Figure 4.6: The computed behaviors of the nondimensional heat flux density profiles ϕ^*_C, ϕ^*_B and ϕ^*_E (a), and the amplification factor Γ_E (b) as functions of the base temperature T for case 1 (i). The region shown by the dotted lines is the region we see the NDTR regime and the amplification. A zoom of this region is reported in the inset of (a) [56].

same, ϕ^*_E and ϕ^*_B profiles tend to move downwards when T_E increases. We observe two different behaviors of ϕ^*_B profiles in this case. As mentioned earlier, it can be clearly seen here that when one function or mode of the thermal transistor (amplification or switch) works, the other does not and we see the amplification function of the transistor in case 2 (i) and (ii) and the switch function in case 2 (iii) and (iv). Γ^{max}_C and Γ^{max}_E increase when T_E increases as seen in Fig.4.7(b) and this is shown with a wider range of T_E in Fig.4.8(a). Additionally, Γ^{max}_C and Γ^{max}_E show an almost vertical increase just before the CTT mode transition to a switch and even reach very high values, almost 100, because ϕ^*_B makes an almost horizontal line just before the temperature range corresponding to the switch function. This means that the value of $\partial\phi^*_B/\partial T$ approaches 0, but its sign still does not change. In fact, this situation can be seen by monitoring the change of ϕ^*_B profiles with respect to the investigated cases from Fig.4.7(a). We also see this behavior in the analysis of the other parameters T_C and T_o, which are examined later. Moreover, the variation of T_E does not affect T_{max} and it remains constant when T_E increases as can be seen in both Fig.4.7(b) and Fig.4.8(a). It should be noted that this is already expressed in Eq.4.18.

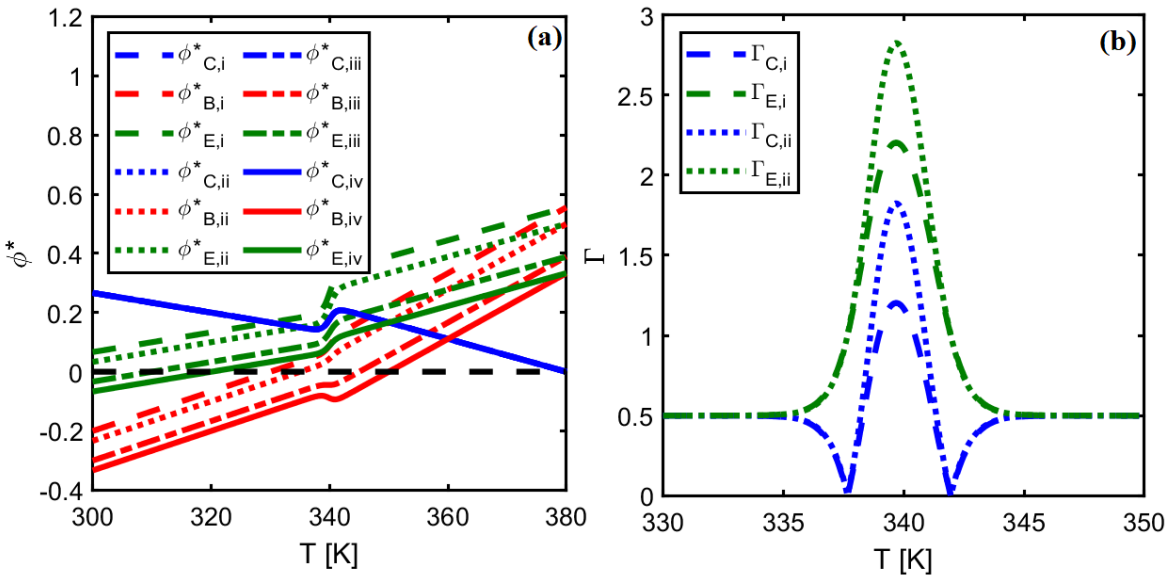

Figure 4.7: The computed behaviors of the nondimensional heat flux density profiles ϕ^*_C, ϕ^*_B and ϕ^*_E (a), and the amplification factors Γ_C and Γ_E (b) as functions of the base temperature T for different values of T_E [56].

In order to understand the behavior of the switch function of the proposed CTT, we will move forward to Fig.4.9, which is a zoomed version of case 2 (iv) on ϕ^*_B, before examining the other figures in Fig.4.8. There are two local extrema; $T_{cri.,up}$ and $T_{cri.,down}$. At these critical temperatures, Γ_C and Γ_E reach infinite values, leading to a bistability shape or regime of the VO_2 base and allowing the CTT to be used as a thermal switch. These critical temperatures are obtained numerically and the region between $T_{cri.,up}$ and $T_{cri.,down}$, shown by the dotted line in the figure, corresponds to another manifestation of the NDTR regime, which means that the derivative of ϕ^*_B with respect to the base temperature T is negative in this region. For instance, when ϕ^*_B increases from -0.107, i.e., if there is heating, the system reaches the first local extrema $T_{cri.,up}$ and the input heat flux density for this temperature is denoted as $\phi^*_{Bcri.,up}$ in the figure. The same input ϕ^*_B is obtained again when T continues to increase and this is the post-critical temperature $T_{post-cri.,up}$. Oppositely, when ϕ^*_B decreases from -0.067, i.e., if there is cooling, the other local extrema $T_{cri.,down}$ can be reached with an input heat flux density $\phi^*_{Bcri.,down}$ that is again obtained at the post-critical temperature $T_{post-cri.,down}$.

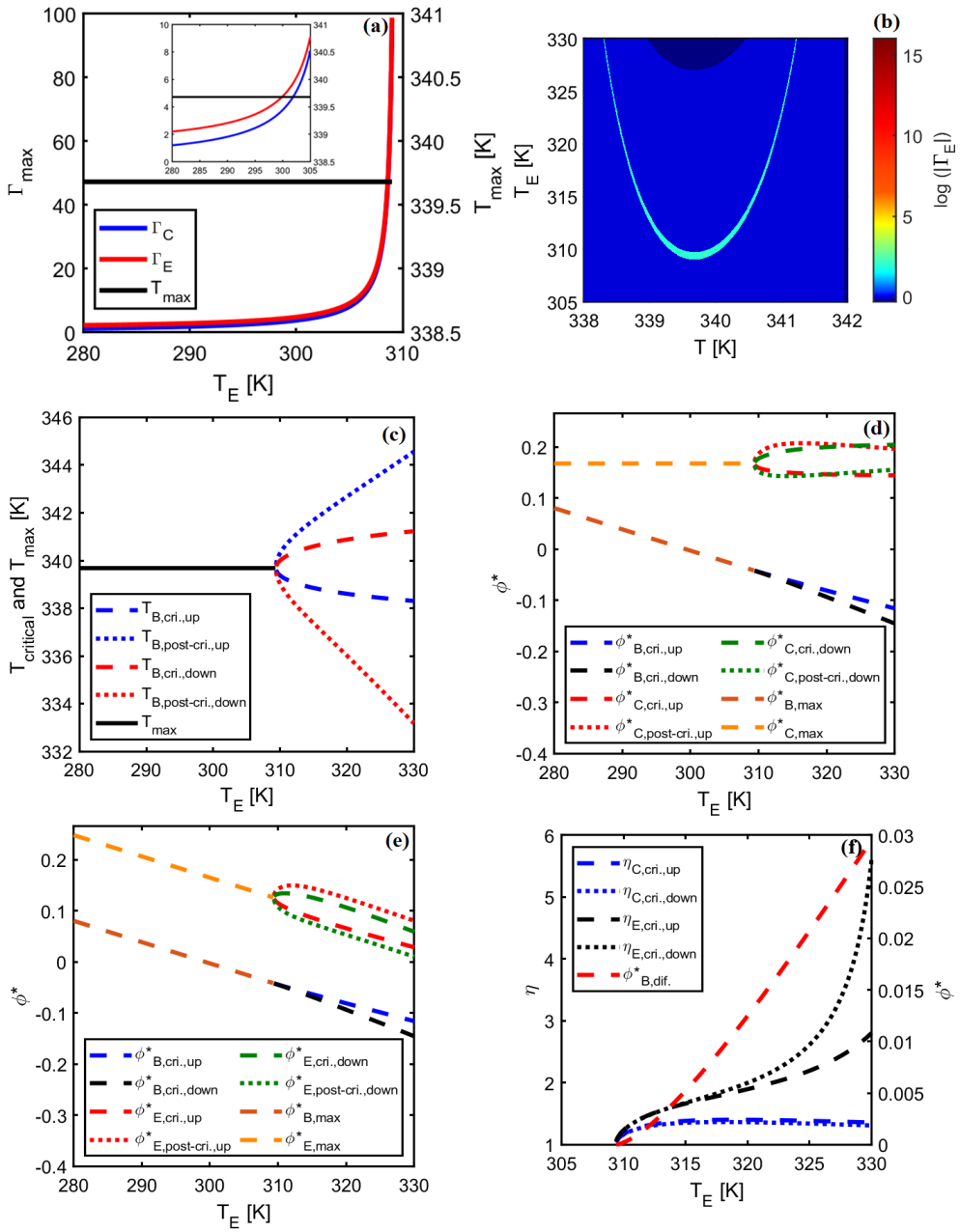

Figure 4.8: The computed behaviors of the maximum amplification factors Γ_C^{max} and Γ_E^{max}, and the optimal base temperature T_{max} (a), the infinity profile caused by the two local extrema that induce the bistability regime (b), T_{max}, the critical and the post-critical base temperatures (c), the nondimensional heat flux densities for the critical and the post-critical base temperatures from collector-to-base (d) and from base-to-emitter (e), the switching input amplitude and the switching ratios (f) as functions of T_E [56].

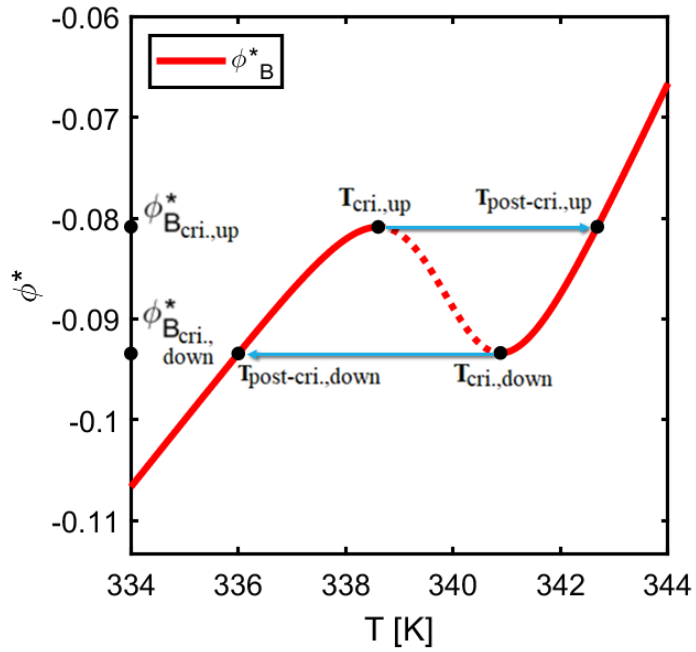

Figure 4.9: The zoomed version of case 2 (iv) on ϕ^*_B, which shows the critical temperatures and their corresponding input nondimensional heat flux densities. The region shown by the dotted lines between $T_{cri.,up}$ and $T_{cri.,down}$ is the region where the NDTR regime occurs [56].

The bistability regime is shown in more detail according to T_E ranging from 305 K to 330 K and T from 338 K to 342 K in Fig.4.8(b). If we continue to increase T_E from around 309 K, it can be seen that there are two infinite local values and the switch function of the transistor begins to emerge. The first one denotes $T_{cri.,up}$ for the heating process and the second one is $T_{cri.,down}$ for the cooling process. Moreover, the interval between these two critical temperatures increases as T_E increases, which can be seen clearly in Fig.4.8(c) including $T_{post-cri.,up}$ and $T_{post-cri.,down}$. Furthermore, $T_{cri.,up}$ and $T_{post-cri.,up}$ have an even more pronounced divergence, moving further apart as T_E increases. The same trend is also seen between $T_{cri.,down}$ and $T_{post-cri.,down}$. The trend of the nondimensional heat flux density profiles that we see in Fig.4.7(a) is also seen with a wider range of T_E in Fig.4.8(d) and (e). We consider the maximum values of ϕ^*_C, ϕ^*_E and ϕ^*_B over the T interval [338 K - 342 K]. $\phi^*_{C,max}$ remains constant, but $\phi^*_{B,max}$ and $\phi^*_{E,max}$ decrease as T_E increases. $\phi^*_{B,max}$ has even negative values for T_E larger than 299 K. At the beginning of

the switch function, the differences between $\phi^*_{C,cri.,up}$ and $\phi^*_{C,post-cri.,up}$, and between $\phi^*_{C,cri.,down}$ and $\phi^*_{C,post-cri.,down}$ first increase. Then, both of them decrease slightly as seen in Fig.4.8(d). The same behavior is also observed for the differences between $\phi^*_{E,cri.,up}$ and $\phi^*_{E,post-cri.,up}$, and between $\phi^*_{E,cri.,down}$ and $\phi^*_{E,post-cri.,down}$ as reported in Fig.4.8(e).

During the heating process, when ϕ^*_B becomes larger than $\phi^*_{B,cri.,up}$, ϕ^*_C increases abruptly from $\phi^*_{C,cri.,up}$ to $\phi^*_{C,post-cri.,up}$ and ϕ^*_E from $\phi^*_{E,cri.,up}$ to $\phi^*_{E,post-cri.,up}$. Oppositely, during the cooling process, when ϕ^*_B decreases abruptly to $\phi^*_{B,cri.,down}$, ϕ^*_C falls from $\phi^*_{C,cri.,down}$ to $\phi^*_{C,post-cri.,down}$ and ϕ^*_E from $\phi^*_{E,cri.,down}$ to $\phi^*_{E,post-cri.,down}$. The switching input amplitude $\phi^*_{B,dif.} = \phi^*_{B,cri.,up} - \phi^*_{B,cri.,down}$ increases almost linearly from around 309 K to 330 K as shown in Fig.4.8(f). Moreover, we define the switching ratios that represent the switching efficiencies as $\eta_{C,cri.,up} = \phi^*_{C,post-cri.,up}/\phi^*_{C,cri.,up}$ and $\eta_{E,cri.,up} = \phi^*_{E,post-cri.,up}/\phi^*_{E,cri.,up}$ for the heating process and similarly $\eta_{C,cri.,down} = \phi^*_{C,cri.,down}/\phi^*_{C,post-cri.,down}$ and $\eta_{E,cri.,down} = \phi^*_{E,cri.,down}/\phi^*_{E,post-cri.,down}$ for the cooling process. After the quick first increase, the switching ratios $\eta_{C,cri.,up}$ and $\eta_{C,cri.,down}$ remain almost constants. On the other hand, the behaviors of $\eta_{E,cri.,up}$ and $\eta_{E,cri.,down}$ are completely different. They both increase as functions of T_E with a faster increase for $\eta_{E,cri.,down}$ especially after $T_E = 325$ K, because $\phi^*_{E,post-cri.,down}$ approaches almost 0 as seen in Fig.4.8(e).

For the third parameter, we studied the collector temperature T_C with the values shown as case 3 of Table 4.1 and over a wider range in detail. We will also detail this parameter, but before we do it, it is worth mentioning that we found that varying T_C has an extremely similar impact to the one of varying T_E on almost all the different behaviors shown above in Figs 4.7, 4.8 and 4.9. However, we observed a difference in the behaviors of the switching ratios. If we start to detail the parameter T_C, ϕ^*_E profile remains the same when T_C increases as seen in Fig.4.10(a), but ϕ^*_C and ϕ^*_B profiles are in tendency to move upward and downward, respectively. As we observed earlier during the analysis of the parameter T_E, we again see two different behaviors of ϕ^*_B profiles: the CTT performs the amplification function in case 3 (i) and (ii), while it performs the switch function in case 3 (iii) and (iv). Similarly, Γ^{max}_C and Γ^{max}_E increase when T_C increases as seen in Fig.4.10(b) and with a wider range of T_C in Fig.4.11(a). Before the CTT mode transi-

tion to the switch function, Γ_C^{max} and Γ_E^{max} show an almost vertical increase and reach very high values, almost 120, due to the fact that $\partial\phi_B^*/\partial T$ is very close to 0 as observed in the study of the parameter T_E. In addition, similarly, the change of T_C does not affect T_{max} which remains constant when T_C increases as can be seen in both Fig.4.10(b) and Fig.4.11(a).

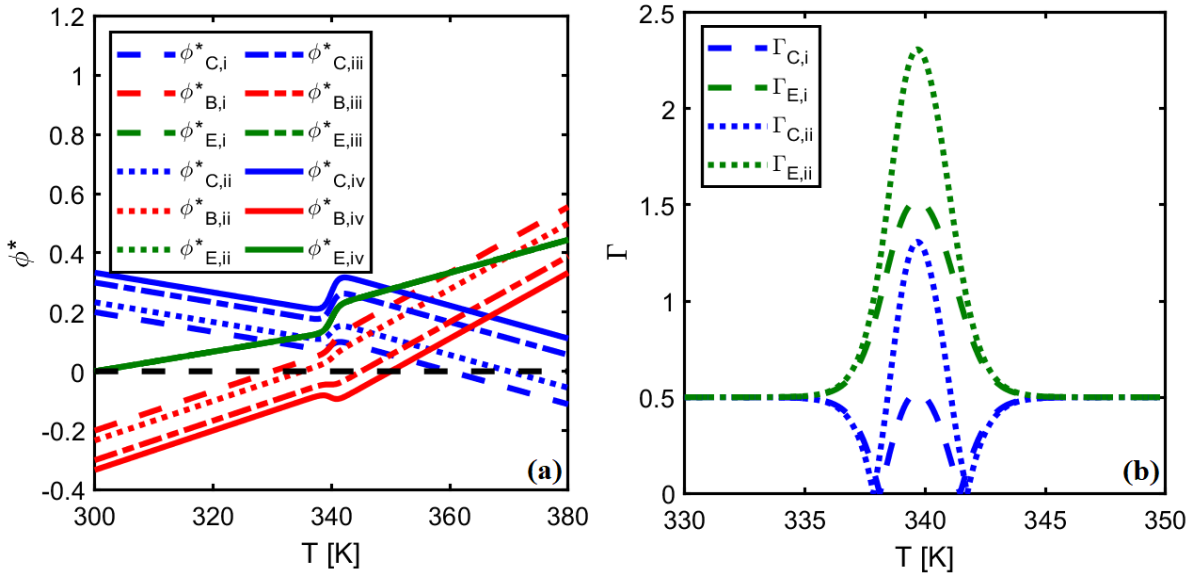

Figure 4.10: The computed behaviors of the nondimensional heat flux density profiles ϕ_C^*, ϕ_B^* and ϕ_E^* (a), and the amplification factors Γ_C and Γ_E (b) as functions of the base temperature T for different values of T_C.

The bistability regime is shown in more detail according to T_C ranging from 385 K to 400 K and T from 338 K to 342 K in Fig.4.11(b). After T_C around 389 K, the switch function of the CTT starts to emerge. As previously seen for the parameter T_E, the difference between $T_{cri.,up}$ and $T_{cri.,down}$ is increasing as T_C increases, which can be clearly seen in Fig.4.11(c). Similar to the case of T_E, this increase is valid for the differences between $T_{post-cri.,up}$ and $T_{post-cri.,down}$, between $T_{cri.,up}$ and $T_{post-cri.,up}$, and between $T_{cri.,down}$ and $T_{post-cri.,down}$. Furthermore, when we examine the nondimensional heat flux density profiles and the maximum values of ϕ_C^*, ϕ_E^* and ϕ_B^* over the T interval [338 K - 342 K], we see that $\phi_{B,max}^*$ and $\phi_{C,max}^*$ diverge from each other as T_C increases. Similarly, this is also observed for $\phi_{B,max}^*$ and $\phi_{E,max}^*$. These can be seen in Fig.4.11(d) and Fig.4.11(e), respectively. Moreover, while $\phi_{E,max}^*$ remains the same, $\phi_{B,max}^*$

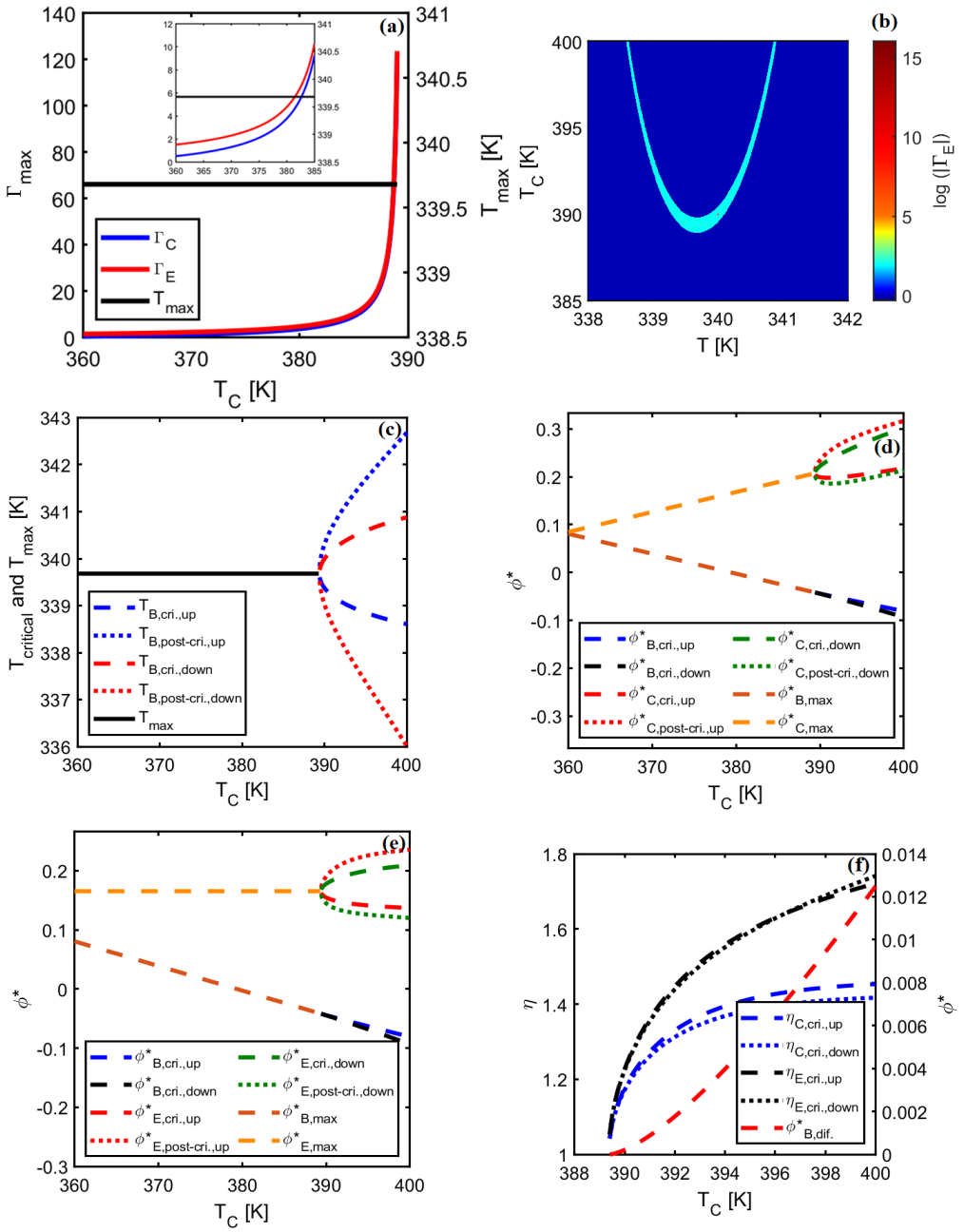

Figure 4.11: The computed behaviors of the maximum amplification factors Γ_C^{max} and Γ_E^{max}, and the optimal base temperature T_{max} (a), the infinity profile caused by the two local extrema that induce the bistability regime (b), T_{max}, the critical and the post-critical base temperatures (c), the nondimensional heat flux densities for the critical and the post-critical base temperatures from collector-to-base (d) and from base-to-emitter (e), the switching input amplitude and the switching ratios (f) as functions of T_C [56].

and $\phi^*_{C,max}$ decreases and increases, respectively, as T_C increases. Indeed, $\phi^*_{B,max}$ changes its sign and has negative values when T_C is around 379 K as previously observed in the analysis of the parameter T_E. Actually, these can also be seen from the nondimensional heat flux density profiles in Fig.4.10(a). Furthermore, the switching input amplitude $\phi^*_{B,dif.}$, which shows a similar behavior to the one we observed for the parameter T_E, increases as T_C increases, but all the switching ratios $\eta_{C,cri.,up}$ and $\eta_{E,cri.,up}$ for the heating process, and $\eta_{C,cri.,down}$ and $\eta_{E,cri.,down}$ for the cooling process increase faster at the beginning of the switch effect, but tend to slow down when T_C continues to increase as seen in Fig.4.11(f).

The fourth parameter we investigated in this study is the transition temperature T_o of the PCM. We can obtain both the amplification and switch functions of the CTT by adjusting it accordingly as for the parameters T_E and T_C. However, we see the bistability regime in the cases of lower values of T_o such as case 4 (i) and (ii) of Table 4.1 and this is actually the difference between the parameter T_o and the parameters T_E and T_C. When $T_o = 330$ K or $T_o = 335$ K, the CTT can be used as a switch as seen in Fig.4.12(a), and when $T_o = 340$ K or $T_o = 345$ K, the CTT operates in the amplification mode as clearly seen in Fig.4.12(b). The amplification Γ^{max}_C and Γ^{max}_E decrease as T_o increases. Also, it should be noted that T_o affects T_{max} which lies always to the left of T_o, as shown analytically in Eq.4.18 earlier. This change can be seen with a wider range of T_o in Fig.4.13(a). T_{max} increases linearly with increasing T_o, but the amplification decreases and we see a sudden fall at the beginning followed by a slower one. The bistability is shown in more detail according to T_o ranging from 300 K to 340 K and T from 300 K to 340 K in Fig.4.13(b). However, when we look deeper into the behavior of the two local extrema in Fig.4.13(b); the first and second lines denote $T_{cri.,up}$ and $T_{cri.,down}$, respectively, we see that the behavior is different from the behaviors we have seen in the analysis of the parameters T_E and T_C. They lie from left-down corner to right-up corner. We can see the switch function up to the maximum value of T_o around 335 K. Hence, this behavior that we did not see during the analysis of T_E and T_C has to be taken into account carefully, and T and T_o should adjust accordingly to have the switch function or the amplification function. If we examine Fig.4.13(c), we see that the differences between $T_{cri.,up}$ and $T_{cri.,down}$, between $T_{cri.,up}$ and $T_{post-cri.,up}$, and between $T_{cri.,down}$ and $T_{post-cri.,down}$, respectively, decrease as T_o increases. The amplification

mode starts when T_o becomes higher than 335 K.

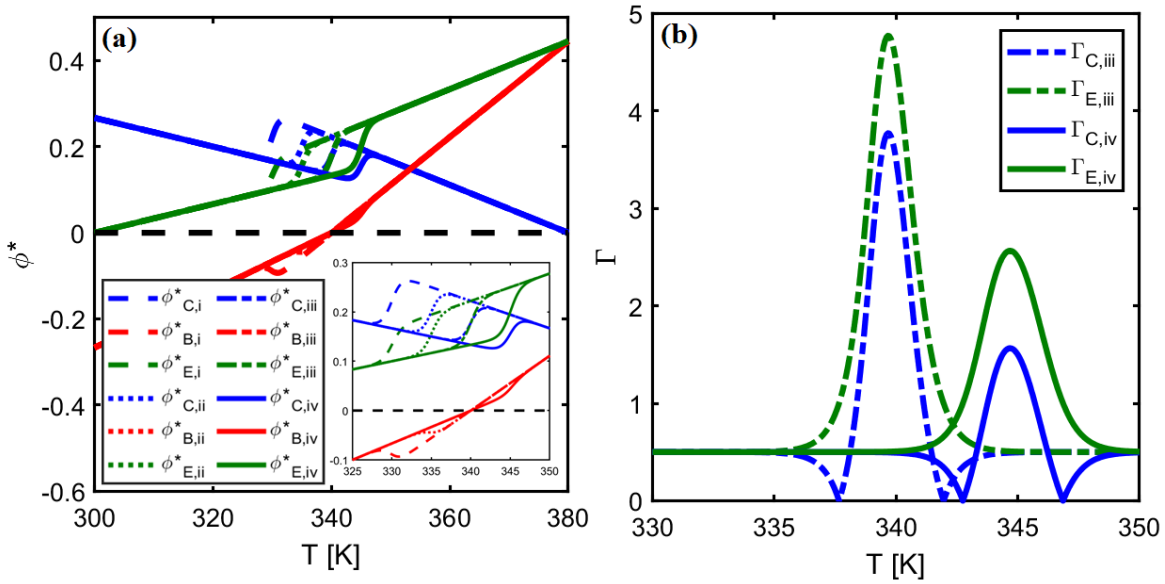

Figure 4.12: The computed behaviors of the nondimensional heat flux density profiles ϕ^*_C, ϕ^*_B and ϕ^*_E (a), and the amplification factors Γ_C and Γ_E (b) as functions of the base temperature T for different values of T_o [56].

The input nondimensional heat flux densities $\phi^*_{B,cri.,up}$ and $\phi^*_{B,cri.,down}$ increase, but the difference between them decreases slightly when T_o increases as seen in Fig.4.13(d) and (e). Furthermore, the differences between $\phi^*_{C,cri.,up}$ and $\phi^*_{C,post-cri.,up}$ during the heating process and between $\phi^*_{C,cri.,down}$ and $\phi^*_{C,post-cri.,down}$ during the cooling process decrease slightly when T_o increases at low temperatures. The same behavior is seen for the base-to-emitter nondimensional heat flux density regarding the behavior of the difference between $\phi^*_{E,cri.,up}$ and $\phi^*_{E,post-cri.,up}$ for the heating process and between $\phi^*_{E,cri.,down}$ and $\phi^*_{E,post-cri.,down}$ for the cooling process as reported in Fig.4.13(e). During the analysis of the parameters T_E and T_C, $\phi^*_{C,max}$ and $\phi^*_{E,max}$ were constant with respect to the increase of T_E and T_C, respectively. However, we observe that $\phi^*_{B,max}$ and $\phi^*_{E,max}$ increase with respect to the increase of T_o, while $\phi^*_{C,max}$ decreases as seen in Fig.4.13(d) and (e). This behavior can be seen from the nondimensional heat flux density profiles of case (iii) and case (iv) shown in Fig.4.12(a). Moreover, the switching input amplitude $\phi^*_{B,dif.}$ decreases as T_o increases as seen in Fig.4.13(f). The switching ratios $\eta_{C,cri.,up}$, $\eta_{C,cri.,down}$,

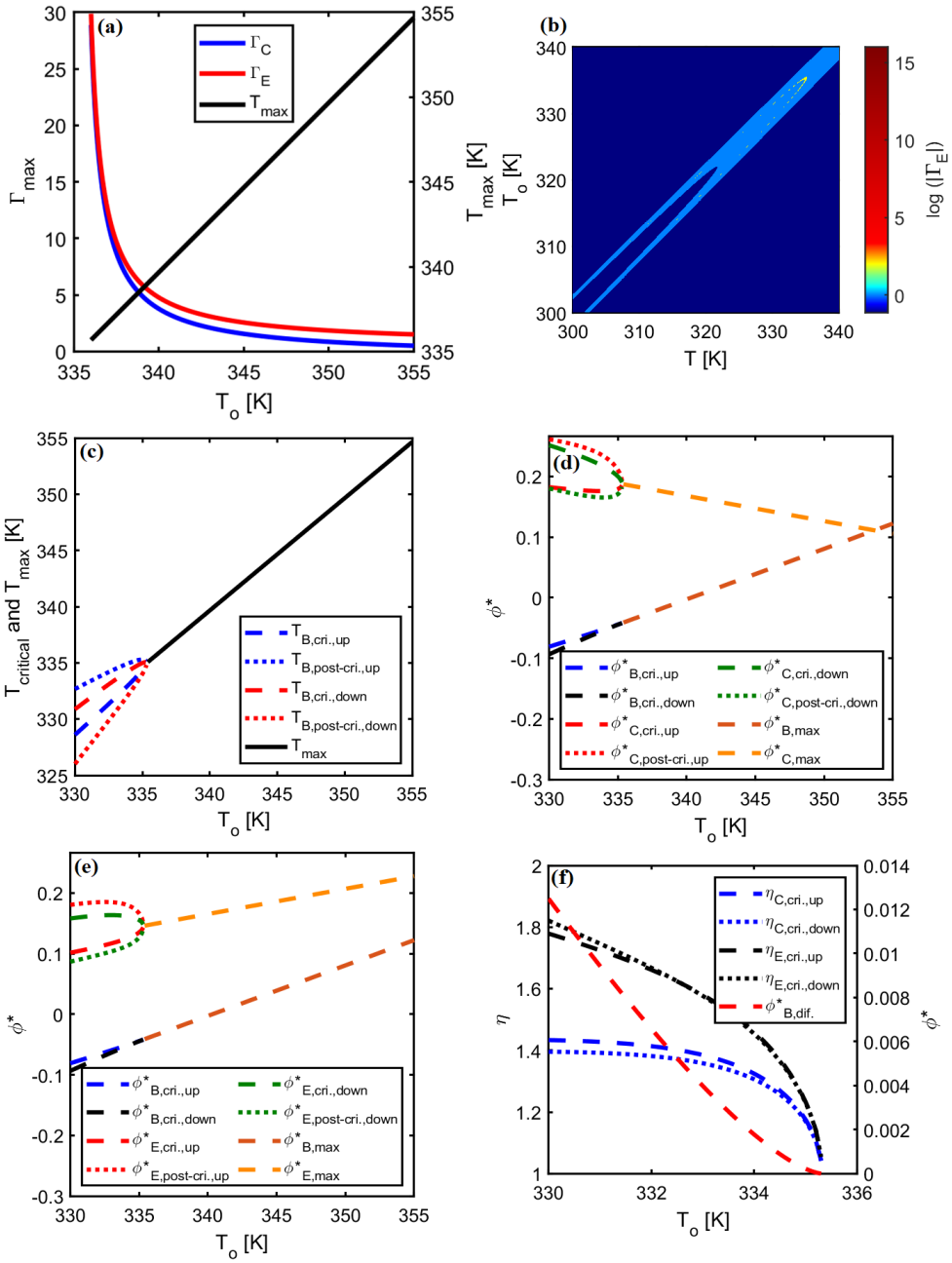

Figure 4.13: The computed behaviors of the maximum amplification factors Γ_C^{max} and Γ_E^{max}, and the optimal base temperature T_{max} (a), the infinity profile caused by the two local extrema that induce the bistability regime (b), T_{max}, the critical and the post-critical base temperatures (c), the nondimensional heat flux densities for the critical and the post-critical base temperatures from collector-to-base (d) and from base-to-emitter (e), the switching input amplitude and the switching ratios (f) as functions of T_o [56].

$\eta_{E,cri.,up}$ and $\eta_{E,cri.,down}$ manifest similar behaviors as they all decrease when T_o increases, but the decrease gets faster when T_o approaches its maximum value for the thermal switch mode. In addition, the switching ratios $\eta_{E,cri.,up}$ and $\eta_{E,cri.,down}$ are always higher than $\eta_{C,cri.,up}$ and $\eta_{C,cri.,down}$. The same feature as for the case of changing T_E and T_C.

The nondimensional heat flux density profiles ϕ_C^*, ϕ_B^* and ϕ_E^* and the amplification factors Γ_C and Γ_E for case 5 in Table 4.1, related to the last parameter β we examined in this study, are shown in Fig.4.14(a) and (b), respectively. When β increases, we observe a steeper increase in ϕ_C^* and ϕ_E^* around the phase transition temperature T_o, which leads to an increase in Γ_C^{max} and Γ_E^{max}. In fact, the change of β affects the operational range of the amplification mode of the CTT. Although the increase of β leads to an increase in Γ_C^{max} and Γ_E^{max}, the operational range for the amplification decreases as seen in Fig.4.14(b). The increase of β can be observed over a wider range up to $\beta = 5\ \mathrm{K}^{-1}$ in Fig.4.15, where Γ_C^{max} and Γ_E^{max} increase linearly with increasing it. Furthermore, β affects T_{max} as previously expressed in Eq.4.18. Especially at lower values of β, there is a sudden increase of T_{max}, which tends to slow down or to saturate as the value of β

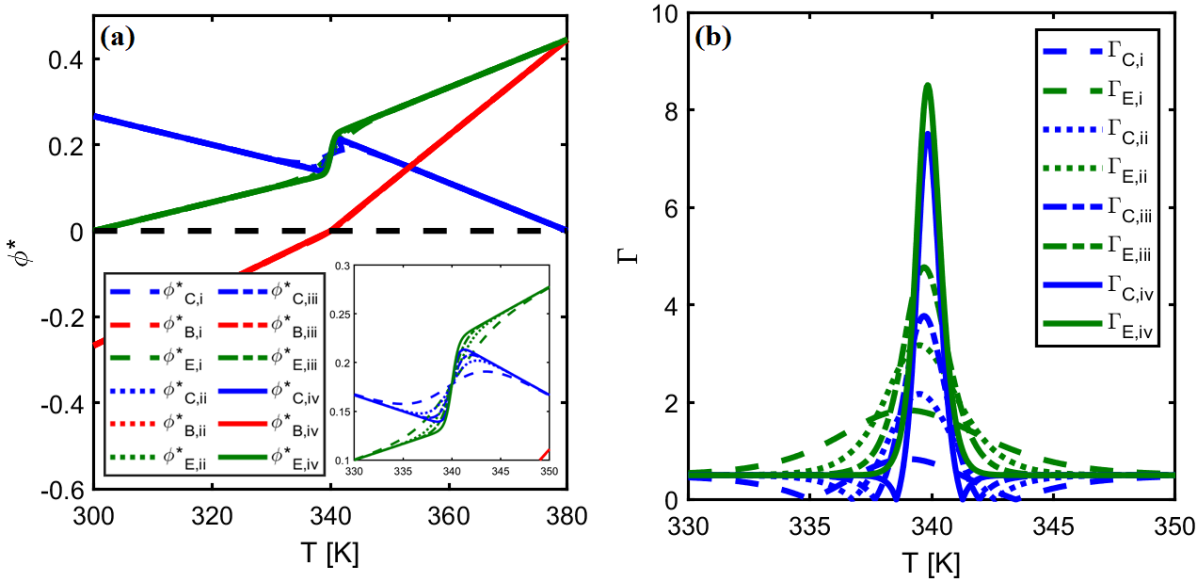

Figure 4.14: The computed behaviors of the nondimensional heat flux density profiles ϕ_C^*, ϕ_B^* and ϕ_E^* (a), and the amplification factors Γ_C and Γ_E (b) as functions of the base temperature T for different values of β [56].

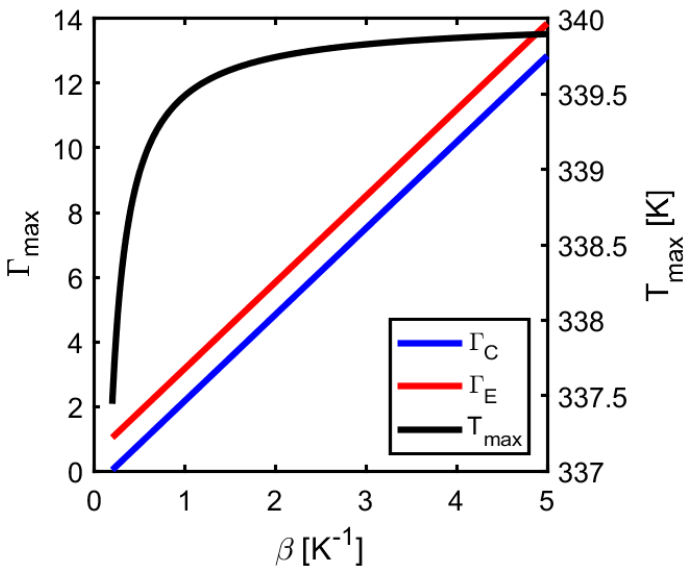

Figure 4.15: The computed behaviors of the maximum amplification factors Γ_C^{max} and Γ_E^{max}, and the optimal base temperature T_{max} as functions of β [56].

continues to increase. T_{max} converges to a nearly constant value just before T_o.

4.4 Conductive thermal transistor made of different phase change materials

For the second CTT concept, we studied a CTT made of different PCMs as shown in Fig.4.2. As mentioned before, the collector, base and emitter elements can be made of metals, semi-metals or highly doped semi-conductors, while the interfaces collector-base and base-emitter are made of insulating-metal PCMs. Similar to the first CTT concept, the collector, the emitter and the base are assumed to be characterized with a spatially uniform temperature each; T_C, T_E and T, respectively. Also, the interface thermal resistances depend only on the base temperature T. Our analysis considers the steady-state regime of operation of the thermal transistor, throughout which we always assume $T_C > T > T_E$. Considering the complexity of the analytical expression, we preferred a full numerical approach for this case. It is still possible to study theoretically the behavior of the heat flux densities and the amplification factors by changing some parameters to see if the functions (modes) of the CTT are possible. The heat flux densities ϕ_E, ϕ_C and ϕ_B of

this CTT concept can be written as:

$$\phi_E = G_R(T)\,[T - T_E] \tag{4.26}$$

$$\phi_C = G_L(T)\,[T_C - T] \tag{4.27}$$

$$\phi_B = \phi_E - \phi_C \tag{4.28}$$

We assume again the same thermal conductance behavior assumption that we did for the CTT with a PCM base analysis. $G_L(T) = G_D^L + [G_M^L - G_D^L]v_L(T)$ and $G_R(T) = G_D^R + [G_M^R - G_D^R]v_R(T)$ where L and R symbolize the left and right PCMs, respectively. Γ_E can be written for this case by using Eq.4.6 as:

$$\Gamma_E = \left| \frac{G'_R(T)[T - T_E] + G_R(T)}{G'_R(T)[T - T_E] + G_R(T) + G'_L(T)[T - T_C] + G_L(T)} \right| \tag{4.29}$$

Γ_E can be rewritten after substituting $G_L(T), G'_L(T), G_R(T)$ and $G'_R(T)$ into Eq.4.29:

$$\Gamma_E = \left| \frac{G_\Delta^R\{\beta_R v_R(1 - v_R)[T - T_E] + v_R\} + G_D^R}{G_\Delta^R\{\beta_R v_R(1 - v_R)[T - T_E] + v_R\} + G_D^R + G_\Delta^L\{\beta_L v_L(1 - v_L)[T - T_C] + v_L\} + G_D^L} \right| \tag{4.30}$$

We set $g_R = G_M^R/G_D^R$ (the ratio of the thermal conductances of the metallic phase to dielectric phase of the right PCM) and $[G_M - G_D] = G_\Delta$, then:

$$\Gamma_E = \left| \frac{[g_R - 1]\{\beta_R v_R(1 - v_R)[T - T_E] + v_R\} + 1}{[g_R - 1]\{\beta_R v_R(1 - v_R)[T - T_E] + v_R\} + 1 + \frac{G_\Delta^L\{\beta_L v_L(1 - v_L)[T - T_C] + v_L\} + G_D^L}{G_D^R}} \right| \tag{4.31}$$

then if we set $g_L = G_M^L/G_D^L$ (the ratio of the thermal conductances of the metallic phase to dielectric phase of the left PCM) and $g_D = G_D^L/G_D^R$ (the ratio of the two PCM thermal conductances in the dielectric phase), the following Eq.4.32 can be obtained for Γ_E:

$$\Gamma_E = \left| \frac{[g_R - 1]\{\beta_R v_R(1 - v_R)[T - T_E] + v_R\} + 1}{[g_R - 1]\{\beta_R v_R(1 - v_R)[T - T_E] + v_R\} + 1 + g_D([g_L - 1]\{\beta_L v_L(1 - v_L)[T - T_C] + v_L\} + 1)} \right| \tag{4.32}$$

therefore, it is possible to calculate Γ_E using Eq.4.32 with three different parameters: g_R, g_L and g_D.

Moreover, if we follow the same steps for Γ_C. It can be written by using Eq.4.6 as:

$$\Gamma_C = \left| \frac{G'_L(T)[T_C - T] - G_L(T)}{G'_R(T)[T - T_E] + G_R(T) + G'_L(T)[T - T_C] + G_L(T)} \right| \tag{4.33}$$

Then, Γ_C can be rewritten after substituting $G_L(T), G'_L(T), G_R(T)$ and $G'_R(T)$ into Eq.4.33:

$$\Gamma_C = \left| \frac{G^L_\Delta\{\beta_L v_L(1-v_L)[T_C - T] - v_L\} - G^L_D}{G^R_\Delta\{\beta_R v_R(1-v_R)[T-T_E] + v_R\} + G^R_D + G^L_\Delta\{\beta_L v_L(1-v_L)[T-T_C] + v_L\} + G^L_D} \right| \quad (4.34)$$

then:

$$\Gamma_C = \left| \frac{\frac{G^L_\Delta\{\beta_L v_L(1-v_L)[T_C-T]-v_L\}-G^L_D}{G^R_D}}{[g_R-1]\{\beta_R v_R(1-v_R)[T-T_E]+v_R\} + 1 + \frac{G^L_\Delta\{\beta_L v_L(1-v_L)[T-T_C]+v_L\}+G^L_D}{G^R_D}} \right| \quad (4.35)$$

Hence, the following Eq.4.36 can be obtained for Γ_C:

$$\Gamma_C = \left| \frac{g_D([g_L-1]\{\beta_L v_L(1-v_L)[T_C-T]-v_L\}-1)}{[g_R-1]\{\beta_R v_R(1-v_R)[T-T_E]+v_R\}+1+g_D([g_L-1]\{\beta_L v_L(1-v_L)[T-T_C]+v_L\}+1)} \right| \quad (4.36)$$

We can also examine the heat flux density profiles for this concept with the same principle that we applied to the first concept of a CTT with a PCM base. Therefore, if we substitute $G_R(T)$ and $G_L(T)$ into Eq.4.26 and Eq.4.27, respectively:

$$\phi_E = \{G^R_D + [G^R_M - G^R_D]v_R\}[T - T_E] \quad (4.37)$$

$$\phi_C = \{G^L_D + [G^L_M - G^L_D]v_L\}[T_C - T] \quad (4.38)$$

and divide Eq.4.37 and Eq.4.38 by $G^R_D T_{amb}$, we will obtain:

$$\phi^*_E = \frac{\{G^R_D + [G^R_M - G^R_D]v_R\}[T - T_E]}{G^R_D T_{amb}} \quad (4.39)$$

$$\phi^*_C = \frac{\{G^L_D + [G^L_M - G^L_D]v_L\}[T_C - T]}{G^R_D T_{amb}} \quad (4.40)$$

where ϕ^*_E and ϕ^*_C are the nondimensionalized heat flux densities given by $\phi_E/G^R_D T_{amb}$ and $\phi_C/G^R_D T_{amb}$, respectively. Finally, Eq.4.41 and Eq.4.42 can be obtained for ϕ^*_E and ϕ^*_C, respectively:

$$\phi^*_E = \frac{\{1 + [g_R - 1]v_R(T)\}[T - T_E]}{T_{amb}} \quad (4.41)$$

$$\phi^*_C = \frac{g_D\{1 + [g_L - 1]v_L(T)\}[T_C - T]}{T_{amb}} \quad (4.42)$$

In addition, ϕ^*_B can be expressed in Eq.4.43 as:

$$\phi^*_B = \frac{\{1 + [g_R - 1]v_R(T)\}[T - T_E] - g_D\{1 + [g_L - 1]v_L(T)\}[T_C - T]}{T_{amb}} \quad (4.43)$$

After this simplification, we can examine the nondimensional heat flux density profiles and the amplification factors for a CTT made of different PCMs based on using three grouped parameters g_L, g_R and g_D.

4.5 Results and discussion of the conductive thermal transistor made of different phase change materials

We investigate 6 different parameters as shown in Table 4.2; g_L, g_D, T_o^L, T_o^R, β_L and β_R for the analysis of the CTT made of different PCMs. Only one parameter is changed in each analysis while the others are kept unchanged. Unless otherwise stated, all parameters are set with the values mentioned in this paragraph throughout the study. The temperatures of the collector T_C and the emitter T_E are set to be 380 K and 300 K, respectively. We can show the amplification and the switch functions of the CTT with different hypothetical g_L, g_R and g_D values. Thus, we examine three different cases (case 1, case 2 and case 3 in Table 4.2) to show these functions. In addition, although we examine completely hypothetical g_L, g_R and g_D values in this CTT configuration, we again set the values of VO_2 for the phase transition temperature and the slope which are 340 K and 1.6 K^{-1}, respectively [35, 63].

We start our analysis by examining the ratio of the thermal conductances of the left PCM g_L, and the ratio of thermal conductances of the left PCM to right PCM in the dielectric phases g_D. The ratio of the thermal conductances of the right PCM, g_R, always remains constant and is taken as 5. The examined g_L values with three different g_D values can be seen in Table 4.2 as case 1, case 2 and case 3 for $g_D = 0.5$, $g_D = 1$ and $g_D = 2$, respectively. When $g_D = 0.5$, the thermal conductance of the right PCM in the dielectric phase is twice higher than the left one. Oppositely, when $g_D = 2$, the thermal conductance of the left PCM in the dielectric phase is twice higher than the right one. When $g_D = 1$, the thermal conductances of both left and right PCMs in the dielectric phase are the same. The computed behaviors of the nondimensional heat flux densities from the collector to the base ϕ_C^*, to the base ϕ_B^* and from the base to the emitter ϕ_E^* with respect to the base temperature T are shown in Fig.4.16(a), (c) and (e) for 3 different values of g_L as case 1, case 2 and case 3, respectively. Similarly, the amplification factors, Γ_C and Γ_E, for case 1, case 2 and case 3 are reported in Fig.4.16(b), (d) and (f), respectively. As can be seen from the various configurations that are examined in case 1, case 2 and case 3, the amplification and switch functions of the CTT are possible with different PCMs, but the choices of g_L for the amplification mode are limited.

Table 4.2: Investigated parameters and cases for the CTT made of different PCMs.

Case 1 - g_L ($g_D = 0.5$ and $g_R = 5$)			
	(i)	(ii)	(iii)
g_L	4	8	12
Case 2 - g_L ($g_D = 1$ and $g_R = 5$)			
	(i)	(ii)	(iii)
g_L	2	4	6
Case 3 - g_L ($g_D = 2$ and $g_R = 5$)			
	(i)	(ii)	(iii)
g_L	2	4	6
Case 4 - T_o^L or T_o^R ($g_D = 1$, $g_L = 5$ and $g_R = 5$))			
	(i)	(ii)	(iii)
T_o^L or T_o^R [K]	335	340	345
Case 5 - β_L or β_R ($g_D = 1$, $g_L = 5$ and $g_R = 5$)			
	(i)	(ii)	(iii)
β_L or β_R [K^{-1}]	1	1.6	3
Case 6 - T_o^L [T_o^R] ($g_D = 1$, $g_L = 5$ and $g_R = 5$)			
	(i)	(ii)	(iii)
T_o^L [T_o^R] [K]	356 [316]	361 [321]	366 [326]

The amplification mode can be obtained with higher values of g_L if g_D is lower than 1, such as in case 1, as can be seen in Fig.4.16(a) and (b). When $g_L = 4$ and $g_L = 8$ in case 1, the CTT performs the amplification function, but if g_D increases, this mode can be obtained with lower values of g_L, as seen in case 2 and case 3, respectively. In fact, the amplification function is obtained when $g_L = 2$ and $g_L = 4$ in case 2, but it can only be obtained when $g_L = 2$ in case 3. This behavior can be seen with a wider range of g_L for $g_D = 0.5$, $g_D = 1$ and $g_D = 2$ in Fig.4.17(a), (c) and (e), respectively. It can be seen that the CTT performs the switch function of the transistor with higher values of g_L when g_D decreases. Moreover, the difference between the two local extrema; $T_{cri.,up}$ and $T_{cri.,down}$, which lead to a bistability shape or regime and allow the thermal transistor to be used as a thermal switch, gets higher when g_D increases.

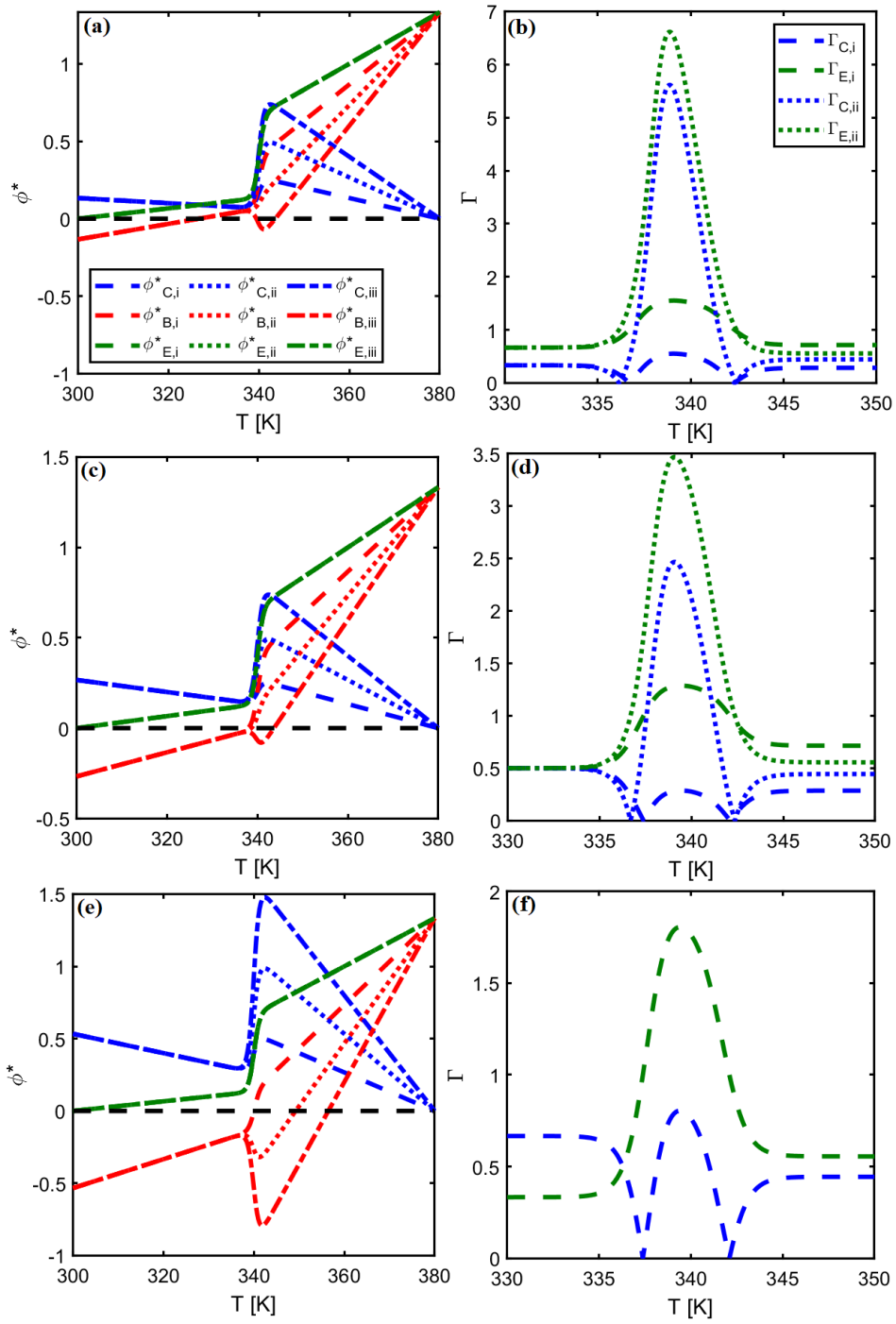

Figure 4.16: The computed behaviors of the nondimensional heat flux density profiles ϕ^*_C, ϕ^*_B and ϕ^*_E for case 1 (a), case 2 (c) and case 3 (e), respectively, and their corresponding amplification factors Γ_C and Γ_E (b), (d) and (f) in the same order as functions of the base temperature T for different values of g_L.

Apart from these, the nondimensional heat flux density ϕ_C^*, ϕ_B^* and ϕ_E^* profiles, and the amplification factors Γ_C and Γ_E show similar behaviors in case 1, case 2 and case 3 as seen in Fig.4.16. The profile of ϕ_E^* remains the same, but the profiles of ϕ_C^* and ϕ_B^* move upward and downward, respectively, and Γ_C and Γ_E increase when g_L increases. We can also see that ϕ_B^* manifests the NDTR, which means that the derivative of ϕ_B^* with respect to the base temperature T is negative as explained before. Γ_E^{max}, Γ_C^{max} and T_{max} variations by increasing g_L with a wider range can be seen for case 1, case 2 and case 3 in Fig.4.17(b), (d) and (f), respectively. In fact, the changes of Γ_E^{max}, Γ_C^{max} and T_{max} are similar to the g analysis in the first concept of a CTT with a PCM base. Both Γ_E^{max} and Γ_C^{max} get steeper, and T_{max} decreases as g_L increases.

We investigated the case where $g_R = 5$ and $g_D = 2$ in more detail to explain the bistability regime of the CTT made of different PCMs. The bistability regime is shown with respect to g_L ranging from 1 to 20 and T from 335 K to 345 K in Fig.4.17(e). The behavior of the bistability regime is quite similar to the T_E and T_C analysis of the CTT with a PCM base as previously shown in Fig.4.8(b) and Fig.4.11(b), respectively. In addition, $T_{cri.,up}$ and $T_{cri.,down}$ also show a similar behavior as seen in Fig.4.18(a), the interval between them increases as g_L increases. Furthermore, the intervals between $T_{cri.,up}$ and $T_{post-cri.,up}$, and between $T_{cri.,down}$ and $T_{post-cri.,down}$ have even more pronounced divergences. They move further apart as g_L increases. When we consider the maximum values of ϕ_C^*, ϕ_E^* and ϕ_B^* over the T interval [338 K - 342 K], we see that $\phi_{C,max}^*$ increases slightly, but $\phi_{B,max}^*$ and $\phi_{E,max}^*$ decrease as g_L increases. Furthermore, $\phi_{B,max}^*$ has also negative values for this analysis as we saw before during the analysis of the CTT with a PCM base. At the beginning of the switch function, the differences between $\phi_{C,cri.,up}^*$ and $\phi_{C,post-cri.,up}^*$, and between $\phi_{C,cri.,down}^*$ and $\phi_{C,post-cri.,down}^*$ first increase. Then, the increase is smaller for both of them as seen in Fig.4.18(b). The same behavior is also observed for the differences between $\phi_{E,cri.,up}^*$ and $\phi_{E,post-cri.,up}^*$, and between $\phi_{E,cri.,down}^*$ and $\phi_{E,post-cri.,down}^*$ as reported in Fig.4.18(c). In addition, we exactly see the same behavior for the switching input amplitude and the switching ratios that we saw during the T_E analysis of the CTT with a PCM base as previously shown in Fig.4.8(f). $\phi_{B,dif.}^*$ increases almost linearly from around 3.15 to 4.5 as seen in Fig.4.18(d). The switching ratios $\eta_{C,cri.,up}$, $\eta_{C,cri.,down}$ and $\eta_{E,cri.,up}$ remain almost constant after a quick first increase. However, the behavior of $\eta_{E,cri.,down}$ is totally different. We

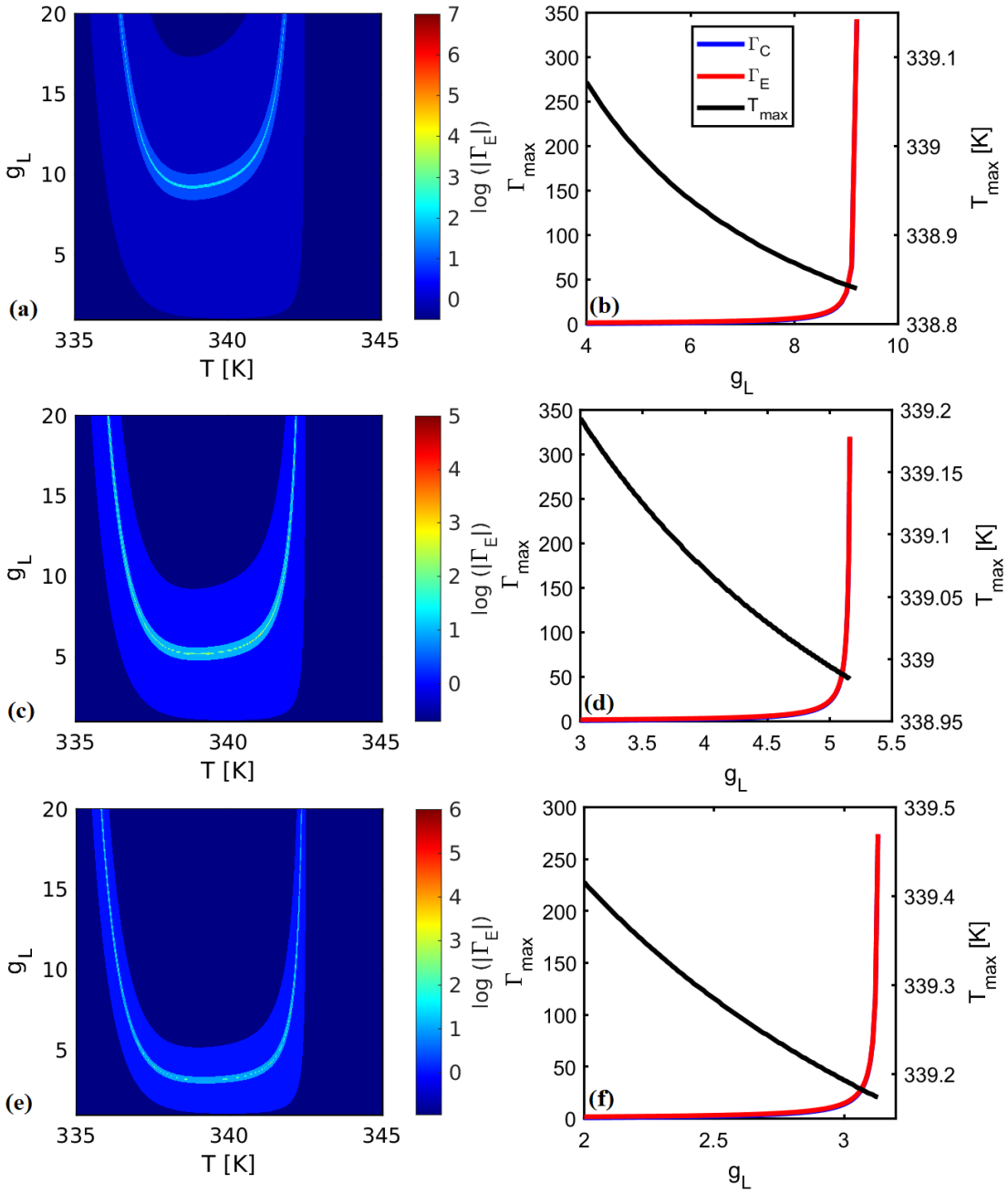

Figure 4.17: The infinity profile caused by the two local extrema that induce the bistability regime when $g_R = 5$, and $g_D = 0.5$ (a), $g_D = 1$ (c) and $g_D = 2$ (e), respectively, and the computed behaviors of the maximum amplification factors Γ_C^{max} and Γ_E^{max}, and the optimal base temperature T_{max} (b), (d) and (f) in the same order as functions of g_L.

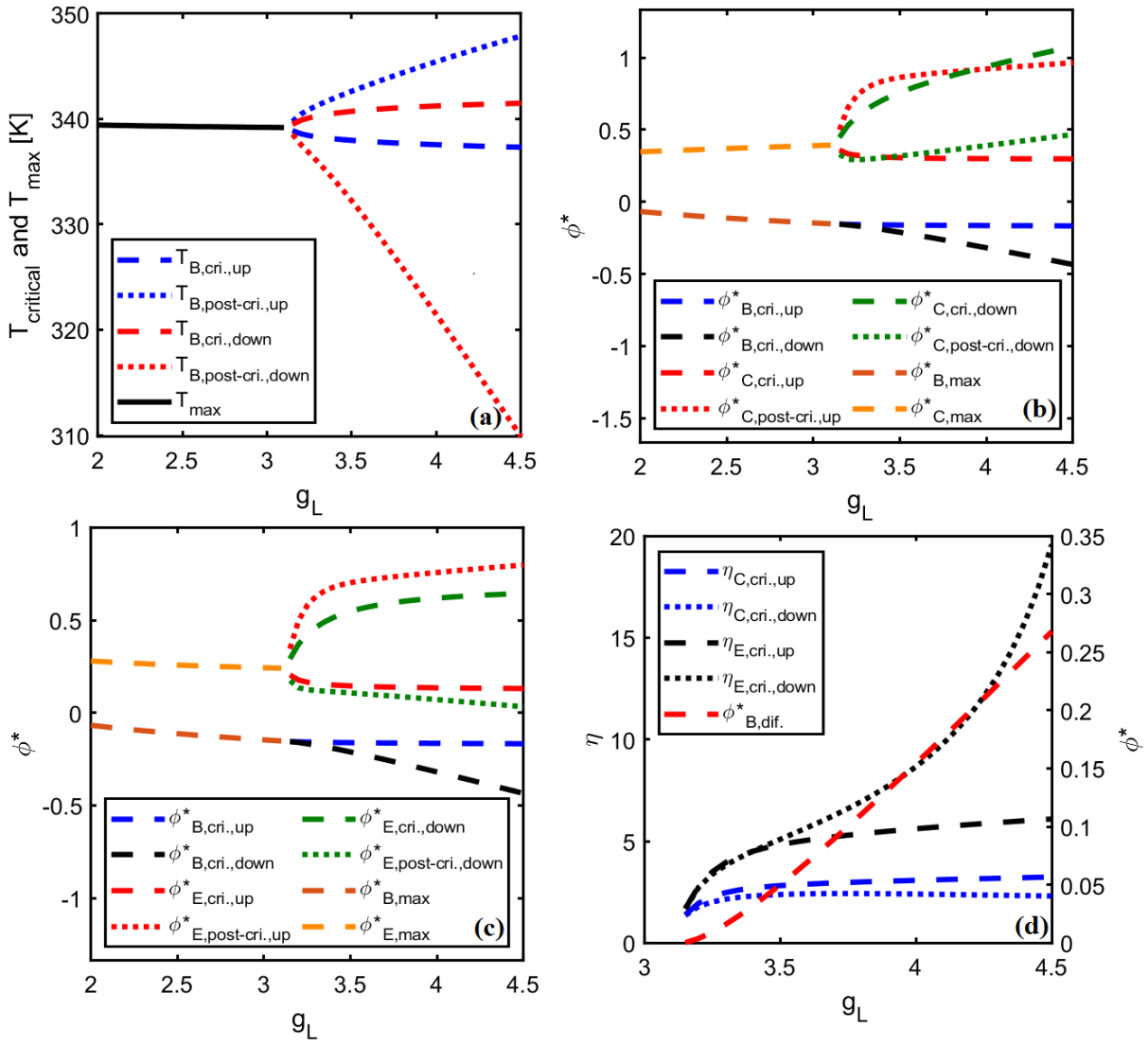

Figure 4.18: The computed behaviors of T_{max}, the critical and the post-critical base temperatures (a), the nondimensional heat flux densities for the critical and the post-critical base temperatures from collector-to-base (b) and from base-to-emitter (c), the switching input amplitude and the switching ratios (d) when $g_R = 5$ and $g_D = 2$ as functions of g_L.

observe a sudden increase for $\eta_{E,cri.,down}$ at the beginning of the increase of g_L, but this increase becomes faster especially after $g_L = 4.1$, because $\phi^*_{E,post-cri.,down}$ approaches almost 0 as seen in Fig.4.18(c).

In order to understand the effect of the parameters T_o^L, T_o^R, β_L and β_R, we fixed the values of g_L, g_R and g_D as 5, 5 and 1, respectively. This means that the left and right PCMs have the same features except for the parameter under study at a time. Therefore, we only changed one parameter in each analysis that is shown in Table 4.2 as case 4 and case 5, while the others are kept unchanged. The computed behaviors of the nondimensional heat flux densities ϕ^*_C, ϕ^*_B and ϕ^*_E are shown in Fig.4.19(a) when T_o^R is fixed at 340 K, but T_o^L is 335 K, 340 K and 345 K as reported in case 4 (i), (ii) and (iii), respectively. Oppositely, ϕ^*_C, ϕ^*_B and ϕ^*_E can be seen in Fig.4.19(b) when T_o^L is fixed to 340 K, but T_o^R is 335 K, 340 K and 345 K. It can be seen from both figures that the CTT can only be achieved when the transition temperatures of the PCMs are the same. When T_o^L or T_o^R are 335 K or 345 K as in case 4 (i) or (iii), the computed ϕ^*_B shows peculiar behaviors as seen in Fig.4.19(a) and (b). The amplification factors Γ_C and Γ_E for case 4 are reported in Fig.4.20, and the amplification is only achieved in case 4 (ii). Moreover, we also examined β_L and β_R by following the same principle. The computed ϕ^*_C, ϕ^*_B and ϕ^*_E are shown in Fig.4.19(c) when β_R is fixed to 1.6 K^{-1}, but β_L is 1 K^{-1}, 1.6 K^{-1} and 3 K^{-1} as reported in case 5 (i), (ii) and (iii), respectively. Oppositely, the computed behaviors of ϕ^*_C, ϕ^*_B and ϕ^*_E can be seen in Fig.4.19(d) when β_L is fixed to 1.6 K^{-1}, but β_R is 1 K^{-1}, 1.6 K^{-1} and 3 K^{-1}. Similar to the transition temperature, the CTT can only be achieved when β_L and β_R are the same, and the computed ϕ^*_B shows peculiar behaviors when they are different as in case 5 (i) and (iii). The amplification is also achieved only in case 5 (ii) and it is in fact identical to case 4 (ii) that is shown in Fig.4.20. In fact, it should be noticed here that the CTT with these two cases (case 4 (ii) and case 5 (ii)) becomes the CTT configuration in Fig.4.3.

We also examined the CTT shown in Fig.4.2 by taking the temperatures of the left and right PCMs as the average temperatures of the collector T_C and base T temperatures, and the base T and emitter T_E temperatures instead of just the base temperature. In this analysis, T_C and T_E are also set to 380 K and 300 K, respectively, and the other assumptions that were mentioned

in the first paragraph are also applied to this configuration. The values of g_L, g_R and g_D are again set to 5, 5 and 1, respectively. However, it should be noted that the volume fractions of the metallic domains of the left and the right PCMs for this analysis can be determined by $v_L(\frac{T+T_C}{2})$ and $v_R(\frac{T+T_E}{2})$, respectively. The computed behaviors of the nondimensional heat flux densities ϕ_C^*, ϕ_B^* and ϕ_E^* and the amplification factors Γ_C and Γ_E are reported in Fig.4.21(a) and (b), respectively, when T_o^L (T_o^R) is 356 K (316 K), 361 K (321 K) and 366 K (326 K) as shown in case 6 (i), (ii) and (iii) in Table 4.2, respectively. When T_o^L and T_o^R are 356 K and 316 K, respectively, i.e., case 6 (i), the CTT performs the switch function as seen in the figure. However, when T_o^L and T_o^R are 361 K and 321 K, respectively, i.e., case 6 (ii), the amplification functions appears, and the most pronounced amplification is achieved in case 6 (ii). It should be noted that the base temperature T is around 340 K. Therefore, the left and right temperatures of the PCMs are around 360 K and 320 K, respectively. When T_o^L and T_o^R continue to increase, the amplification factors Γ_C and Γ_E decrease, then the amplification function disappears after a certain point, as seen in case 6 (iii).

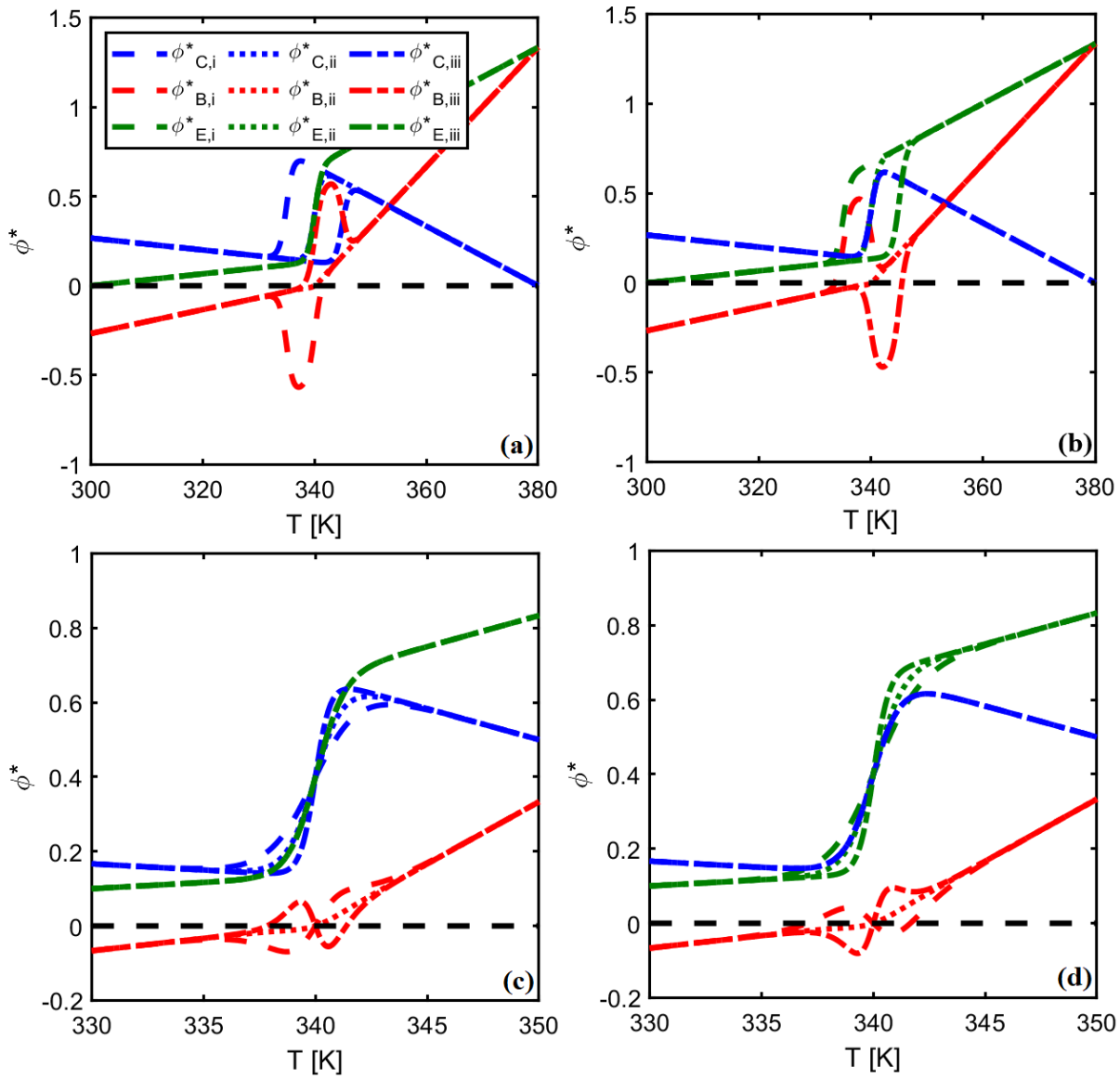

Figure 4.19: The computed behaviors of the nondimensional heat flux density profiles ϕ^*_C, ϕ^*_B and ϕ^*_E as functions of the base temperature T for different values of T^L_o (a), T^R_o (b), β_L (c) and β_R (d).

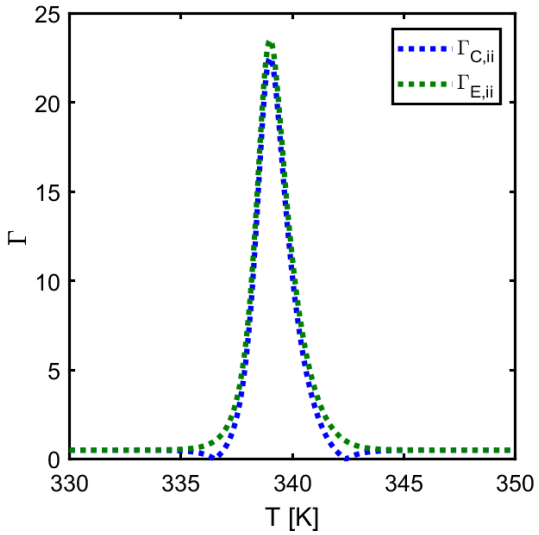

Figure 4.20: The amplification factors Γ_C and Γ_E as functions of the base temperature T for case 4 and case 5.

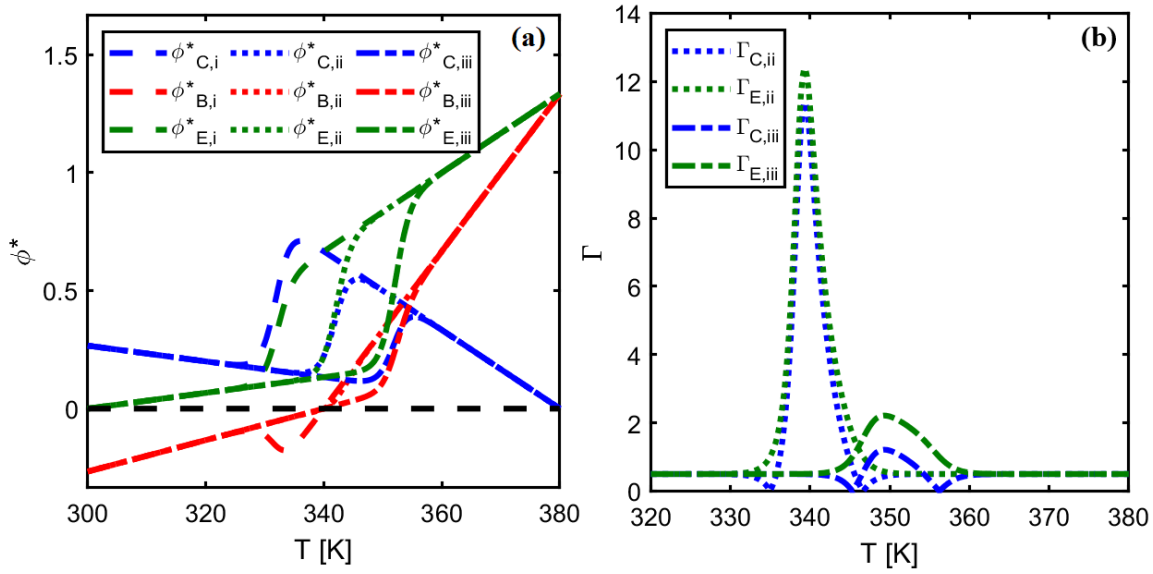

Figure 4.21: The computed behaviors of the nondimensional heat flux density profiles ϕ_C^*, ϕ_B^* and ϕ_E^* (a), and the amplification factors Γ_C and Γ_E (b) as functions of the base temperature T for different values of T_o^L (T_o^R) when the temperatures of the left and right PCMs are taken to be the average temperatures of the collector T_C and base T temperatures, and the base T and emitter T_E temperatures, respectively.

4.6 Conclusion

We examined two different conductive thermal transistor (CTT) concepts and showed that the CTT can be achieved by utilizing an oxide PCM that exhibits insulator-to-metallic transition. In the first concept, which is the CTT with a PCM base, all of the 5 examined parameters (the thermal conductance ratio g, the emitter temperature T_E, the collector temperature T_C, the phase transition temperature T_o of the PCM and the phase transition slope β of the PCM) affect the two operation modes, amplification and switching, of the CTT. While the amplification mostly depends on the ratio of the thermal conductances g between the insulating and metallic states and the stiffness of the phase transition β, the bistability regime that allows the thermal switching (temperature jump) is observed according to the temperatures of the collector T_c, the emitter T_E and the phase transition T_o of the PCM. Therefore, the device can also be used as a switch depending on the temperatures of these elements, and the operating range of the amplification mode of the CTT can be modified to some extent by the stiffness of the phase transition. In addition, the base temperature resulting in the highest amplification factor is always obtained when it is lower than and close to the phase transition temperature. Moreover, the parametric study we performed suggests no maximum limit for the collector temperature T_C as long as the inequality $T_C > T > T_E$ is respected and the phase transition temperature T_o of the material used is within the interval $[T_C, T_E]$. It should also be emphasized here that the CTT with a PCM base and a CTT whose collector-base and base-emitter interfaces are made of the same PCM give the same results under the assumption that the interface thermal resistance depends only on the base temperature.

In the first concept, we observed a different behavior in the analysis of the phase transition parameter T_o than in the analysis of the collector T_C and emitter T_E temperatures although the CTT can operate in both amplification and switch modes depending on these temperatures. In a condition where the other parameters are fixed, the CTT first operates in the amplification mode when the collector or emitter temperatures are relatively low. It then starts operating in the switch mode if the collector or emitter temperatures increase. On the other hand, the phase transition temperature parameter shows the opposite behavior, the CTT shows the switch

mode at relatively lower temperatures, but it operates in the amplification mode at higher temperatures. Despite this difference, in all three parameters, the amplification factor reaches the highest value before the CTT mode transitions to the switch mode. However, the switching efficiencies decrease to the lowest values before the CTT mode transitions to the amplification mode. Furthermore, the switching efficiencies for the collector-to-base are always less than the ones for the base-to-emitter.

In the second concept, which is the CTT made of different PCMs, we examined 6 different parameters: the ratio of the thermal conductances of the left PCM g_L, the ratio of thermal conductances of the left PCM to right PCM in the dielectric phases g_D, the phase transition temperature of the left PCM T_o^L, the phase transition temperature of the right PCM T_o^R, the phase transition slope of the left PCM β_L and the phase transition slope of the right PCM β_R. We observed that the two operation modes of the CTT are again possible, but the parameter configurations are quite limited for this concept. The ratios of the thermal conductances between the insulating and metallic states of the left g_L and right g_R PCMs separately, and the ratios of the thermal conductances in the dielectric state of the left PCM to right one g_D can be different to achieve the CTT. However, the phase transition temperatures (T_o^L and T_o^R) and stiffness (β_L and β_R) of both PCMs have to be the same. In addition, we considered a separate case with a CTT where the temperatures of the left and right PCMs are the average temperatures of the collector and base temperatures, and the base and emitter temperatures, respectively, instead of the base temperature. In this case, we observed that the CTT can perform the amplification and switch functions depending on the transition temperatures of the left T_o^L and right T_o^R PCMs, but they have to be set carefully considering the collector and the emitter temperatures.

The analytical expressions that are derived for the first concept are generally applicable for a CTT similar to the one that is investigated as long as the phase transition behavior of the base element exhibits similar phase transition characteristics with VO_2. Considering the reasonable outcomes of this theoretical study, further researches should be conducted under transient conditions by taking into account the hysteresis region during the phase transition of the oxide PCM. Moreover, we considered the base element to be so thin so that it behaves as

an interface thermal resistance and depends only on the base temperature. However, it should be better to solve the heat diffusion equation in the PCM without this assumption, where the temperature would not be constant everywhere, for more realistic situations. Besides, the studied CTT in the first concept, as a macroscopic concept, can be very promising as it constitutes a simple alternative that can be experimentally proven. It has also the advantage to be generalized for other solid-oxide phase change materials whose transition can be described similarly with VO_2.

Résumé du Chapitre 4

Dans le Chapitre 4, nous examinons en détail le transistor thermique conductif (TTC). À notre connaissance, à l'exception du travail de pionnier Li et al. [116] et du travail récent de Wu et al. [118], aucun autre concept macroscopique de transistor thermique dans le régime de transfert de chaleur par conduction n'a été présenté. Ceci constitue la nouveauté de notre étude, dans laquelle nous analysons théoriquement le comportement d'un TTC basé sur un matériau à changement de phase (MCP) présentant une analogie avec un transistor bipolaire électronique. Les fonctions classiques du transistor, telles que l'amplification et la commutation, font l'objet d'une étude approfondie.

Nous menons l'étude en examinant deux concepts différents du TTC. Le premier est un TTC avec la base composée d'un MCP, et le second est un TTC composé de différents MCP, illustrés respectivement dans les Fig.4.1 et Fig.4.2. Les éléments collecteur et émetteur des deux dispositifs peuvent être constitués de métaux, de semi-métaux ou de semi-conducteurs fortement dopés. Dans le premier concept, la base peut être constituée d'un MCP présentant une transition métal-isolant (TMI), le VO_2 dans notre cas, comme mentionné précédemment. Dans ce concept, l'élément de base est considéré si mince qu'il se comporte comme une résistance thermique d'interface entre le collecteur et l'émetteur, dont la conductance ou la résistance thermique ne dépend que de sa température T. Nous supposons que le collecteur, l'émetteur et la base ont une température uniforme dans l'espace, notée T_C, T_E et T, respectivement, et on peut négliger l'influence de T_C et T_E. D'autre part, dans le second concept, l'élément de base peut également être constitué de matériaux similaires à ceux utilisés pour les éléments du collecteur et de l'émetteur, tandis que les interfaces collecteur-base et base-émetteur sont constituées d'un MCP présentant une TMI. Nous montrons que les deux concepts manifestent bien la régime de la résistance thermique différentielle négative (RTDN) ou l'effet transistor. Notre analyse porte sur le régime permanent de fonctionnement du transistor thermique, pour lequel nous supposons toujours $T_C > T > T_E$.

Transistor thermique conductif à base de matériau à changement de phase

Nous commençons par examiner le TTC avec une base constituée par un MCP présentant une TMI, comme illustré sur la Fig.4.1. Les densités de flux thermique ϕ_E, ϕ_C et ϕ_B peuvent être écrites comme dans les Éq.4.1, Éq.4.2 et Éq.4.3, respectivement. En outre, nous supposons que la conductance thermique de la base $G(T)$ a un comportement thermique similaire à celui qui régit la conductivité thermique de VO_2 dans les régimes de chauffage et de refroidissement. Par conséquent, nous pouvons exprimer la conductance thermique $G(T)$ comme dans l'Éq.4.4 [5, 35]. La température d'équilibre T_{eq} peut être obtenue directement à partir des Éq.4.1 et Éq.4.2, comme indiqué dans l'Éq.4.5. T_{eq} peut être arrangée en fonction des températures du collecteur T_C et de l'émetteur T_E. Dans cette étude, nous avons fixé les températures du collecteur T_C et de l'émetteur T_E à 380 K et 300 K, respectivement, sauf indication contraire. Ainsi, T_{eq} est de 340 K, la même température que la température de transition T_o du VO_2. Grâce à cette disposition, nous pouvons induire une transition de phase de l'isolant au métal et vice versa en modifiant légèrement la température de base T tout en conservant la densité du flux thermique d'entrée ϕ_B.

Le facteur d'amplification Γ du TTC peut être défini par rapport à l'émetteur et au collecteur, comme dans l'Éq.4.6 [116]. Pour qu'il y ait amplification, les facteurs d'amplification $\Gamma_{E,C}$ doivent être supérieurs à 1 et le régime RTDN doit être respecté. Ce régime exige que l'une des deux résistances thermiques $-(\partial\phi_C/\partial T)^{-1}$ ou $(\partial\phi_E/\partial T)^{-1}$ soit négative. Le traitement des facteurs d'amplification Γ_E et Γ_C est très similaire. En effet, d'après l'Éq.4.3, ils sont liés. Après quelques opérations algébriques, nous pouvons écrire analytiquement l'équation finale pour T_{max}, c'est-à-dire la température à laquelle Γ_E atteint son maximum, comme dans l'Éq.4.18. L'Éq.4.18 montre analytiquement que T_{max} est toujours inférieur à T_o ($T_{max} < T_o$), quelles que soient les circonstances. Par conséquent, la température de base T doit être fixée juste avant la température de transition T_o pour obtenir le facteur d'amplification maximal. L'expression analytique finale permettant de déterminer Γ_E^{max} peut également être exprimée comme dans l'Éq.4.20. L'expression analytique de Γ_C^{max} présente un maximum à la même température T_{max} que Γ_E (Éq.4.18). Il peut donc être exprimé comme dans l'Éq.4.22.

Il est à noter que nous avons également examiné un TTC illustré à la Fig.4.3, dont les interfaces collecteur-base et base-émetteur sont constituées du même MCP, et dont l'élément de base peut être constitué de métaux, de semi-métaux ou de semi-conducteurs fortement dopés. En effet, les deux TTC représentés dans les Fig.4.1 et Fig.4.3 donnent exactement les mêmes résultats en supposant que la résistance thermique de l'interface ne dépend que de la température de base T.

Transistor thermique conductif composé de différents matériaux à changement de phase

Pour le deuxième concept de TTC, nous avons étudié le TTC composé de différents MCP, comme le montre la Fig.4.2. Compte tenu de la complexité de l'expression analytique, nous avons préféré une approche entièrement numérique. Toutefois, il est toujours possible d'étudier théoriquement le comportement des densités de flux de chaleur et des facteurs d'amplification en modifiant certains paramètres afin de vérifier si les fonctions (modes) du TTC sont réalisables. Les densités de flux thermique ϕ_E, ϕ_C et ϕ_B de ce concept peuvent être écrites comme dans les Éq.4.26, Éq.4.27 and Éq.4.28, respectivement. Après quelques opérations algébriques, il est possible de calculer Γ_E et Γ_C à l'aide des équations Éq.4.32 and Éq.4.36, à l'aide de trois paramètres groupés : g_R (le rapport des conductances thermiques de la phase métallique à la phase diélectrique du MCP droit), g_L (le rapport des conductances thermiques de la phase métallique à la phase diélectrique du MCP gauche) et g_D (le rapport des conductances thermiques des deux phases diélectriques des deux MCP).

Conclusion

Dans le premier concept, l'ensemble des 5 paramètres indiqués dans le Tableau 4.1 sont examinés pour les deux modes de fonctionnement du TTC : l'amplification et la commutation. L'amplification dépend principalement du rapport des conductances thermiques entre les états isolant et métallique, ainsi que de la rigidité de la transition de phase du MCP. Le régime de

bistabilité qui permet la commutation thermique (saut de température) est observé en fonction des températures du collecteur, de l'émetteur et de la transition de phase du MCP. Par conséquent, le dispositif peut également être utilisé comme commutateur selon les températures de ces éléments, et la plage de fonctionnement du mode d'amplification du TTC peut être modifiée dans une certaine mesure par la rigidité de la transition de phase. En outre, la température de base entraînant le facteur d'amplification le plus élevé est toujours obtenue lorsqu'elle est inférieure à la température de transition de phase et proche de celle-ci.

Dans le deuxième concept, nous avons examiné le TTC avec 6 cas différents pour les deux modes de fonctionnement, comme indiqué dans le Tableau 4.2. Nous avons observé que les deux modes de fonctionnement du TTC, l'amplification et la commutation, sont possibles, mais que les configurations de paramètres de ce concept sont assez limitées. Les rapports des conductances thermiques entre les états isolant et métallique des MCP gauche et droit séparément, ainsi que les rapports des conductances thermiques dans l'état diélectrique du MCP gauche par rapport au MCP droit peuvent être différents pour réaliser le TTC. Toutefois, les températures de transition de phase et la rigidité des deux MCP doivent être identiques. En outre, nous avons considéré un cas particulier où les températures des MCP de gauche et de droite sont les températures moyennes des températures du collecteur et de la base, et de la base et de l'émetteur, respectivement, au lieu de la température de la base. Dans ce cas, nous avons observé que le TTC peut assurer les fonctions d'amplification et de commutation en fonction des températures de transition des MCP gauche et droit, mais qu'il faut régler ces températures avec soin en tenant compte des températures du collecteur et de l'émetteur.

General Conclusion

In this thesis, we conducted a theoretical study of three main thermal components of thermotronics: the thermal diode, the thermal memristor and the thermal transistor. We investigated these components in the conductive regime of heat transfer. One of the alternatives for conceiving these thermal components is vanadium dioxide (VO_2). Therefore, all three components are composed of VO_2 in our analysis and we investigated them with various intrinsic and extrinsic parameters.

In our analysis of the conductive thermal diode (CTD), we found that the thermal conductivity and the specific heat have a major impact on the nonlinear time behavior of the thermal rectification under transient conditions. Furthermore, we obtained higher thermal rectification under transient conditions than steady-state conditions for almost all parameter values. The interface thermal resistance also affects the thermal rectification, although this effect generally seems to be minor in comparison with the other intrinsic parameters of the CTD. As a consequence of the phase transition of VO_2, we see peculiar behaviors on the heat flux density even at low frequencies for the CTD. We also found that the thermal rectification oscillates more and its maximum value becomes higher when the frequency of the applied temperature boundary conditions increases.

In our analysis of the conductive thermal memristor (CTM), we found that the nonlinear variations of the thermal conductivity and specific heat of VO_2, combined with the hysteresis zone, significantly affect the Lissajous characteristic curve. The capacitive effect has a clear impact on the thermal memristor effect manifestation. The temperature amplitude of the applied boundary conditions affects the Lissajous characteristic curve until a certain value, after which its effect becomes insignificant. This temperature amplitude value corresponds to the smallest one leading to a complete phase transition cycles. We also observed that the Lissajous characteristic curve of the CTM deteriorates as the frequency of the applied boundary conditions increases.

We examined two different concepts for the conductive thermal transistor (CTT). The first

one is a CTT with a PCM base and the second one is a CTT made of different PCMs. We found that the ratio of the thermal conductances between the states of the PCM and the stiffness of the phase transition greatly affect the amplification. In addition, the CTT can be used as a switch according to the phase transition temperature of the PCM and the temperatures of the three elements of the transistor: the collector, the base and the emitter. Furthermore, we demonstrated that the base temperature that induces the highest amplification factor is always less than the phase transition temperature, but lies in its vicinity. In the second concept, we found that the two operation modes (amplification and switch) of the CTT are possible. However, the parameter configurations are quite limited for this concept. The ratios of the thermal conductances between the insulating and metallic states of the left and right PCMs separately, and the ratios of the thermal conductances in the dielectric state of the left PCM to right one can be different to achieve the CTT, but the phase transition temperatures and stiffness of both PCMs must be the same.

Consequently, more studies should be conducted under transient and dynamical boundary conditions by including the hysteresis zone to enhance our understanding of the behaviors of CTD and CTM. This also can benefit to reveal their further potential in order to integrate them into daily use like their electronic analogous: the electronic diode and the electronic memristor. Further studies can help to demonstrate the full benefits of the transient analysis for a better control of practical thermal management systems. We conducted the CTT analysis under steady-state conditions, but further researches should similarly be conducted under transient conditions by taking into account the hysteresis region during the phase transition of the oxide PCM. A full understanding of the CTT concept could bring us closer to an advanced thermal computing scheme.

Conclusion Générale

Dans cette thèse, nous avons mené une étude théorique de trois composants thermiques principaux de la thermotronique : la diode thermique, le memristor thermique et le transistor thermique. Nous avons étudiés ces composants dans le régime conductif du transfert de chaleur. L'une des alternatives pour concevoir ces composants thermiques est le dioxyde de vanadium (VO_2). Dans notre analyse, les trois composants sont donc composés de VO_2 et nous les avons étudiés avec différents paramètres intrinsèques et extrinsèques.

Dans notre analyse de la diode thermique conductive (DTC), nous avons constaté que la conductivité thermique et la chaleur spécifique ont un impact majeur sur le comportement temporel non linéaire de la rectification thermique dans des conditions transitoires. En outre, nous avons observé que la rectification thermique était plus élevée en conditions transitoires qu'en conditions stationnaires pour presque toutes les valeurs des paramètres. La résistance thermique de l'interface affecte également la rectification thermique, bien que cet effet semble généralement mineur par rapport aux autres paramètres intrinsèques de la DTC. En raison de la transition de phase du VO_2, nous observons des comportements particuliers concernant la densité du flux de chaleur, même à basse fréquence pour la DTC. Nous avons également constaté que la rectification thermique oscille davantage et que sa valeur maximale devient plus élevée lorsque la fréquence de la température des conditions limites appliquées augmente.

Dans notre analyse du memristor thermique conductif (MTC), nous avons constaté que les variations non linéaires de la conductivité thermique et de la chaleur spécifique de VO_2, combinées à la zone d'hystérésis, affectent de manière significative la courbe caractéristique de Lissajous. L'effet capacitif a un impact clair sur la manifestation de l'effet memristor thermique. L'amplitude de température des conditions limites appliquées affecte la courbe caractéristique de Lissajous jusqu'à une certaine valeur, après quoi son effet devient insignifiant. Cette valeur d'amplitude de température correspond à la plus petite valeur conduisant à un cycle complet de transition de phase. Nous avons également observé que la courbe caractéristique de Lissajous du

MTC se détériore à mesure que la fréquence de la température des conditions limites appliquées augmente.

Nous avons examiné deux concepts différents pour le transistor thermique conductif (TTC). Le premier est un TTC avec une la base constituée de MCP, et le second est un TTC composé de différents MCP. Nous avons constaté que le rapport des conductances thermiques entre les états du MCP et la rigidité de la transition de phase a une grande influence sur l'amplification. En outre, le TTC peut être utilisé comme commutateur en fonction de la température de transition de phase du MCP et des températures des trois éléments du transistor : le collecteur, la base et l'émetteur. Nous avons également démontré que la température de la base qui induit le facteur d'amplification le plus élevé est toujours inférieure à la température de transition de phase, mais se situe à proximité de celle-ci. Concernant le deuxième concept, nous avons constaté que le TTC peut exécuter deux modes de fonctionnement différents : l'amplification et la commutation. Cependant, les configurations de paramètres pour ce concept sont assez limitées. Les rapports des conductances thermiques entre les états isolant et métallique des MCP gauche et droit séparément, et les rapports des conductances thermiques dans l'état diélectrique du MCP gauche par rapport au MCP droit peuvent être différents pour réaliser le TTC, mais les températures de transition de phase et la rigidité des deux MCP doivent être les mêmes.

Par conséquent, d'autres études devraient être menées dans des conditions transitoires et dynamiques en incluant la zone d'hystérésis afin d'améliorer notre compréhension des comportements des DTC et des MTC. Cela peut également servir à révéler leur potentiel supplémentaire pour les intégrer à l'utilisation quotidienne comme leurs analogues électroniques : la diode électronique et le memristor électronique. D'autres études pourraient permettre de démontrer tous les avantages de l'analyse transitoire pour un meilleur contrôle des systèmes pratiques de gestion thermique. Si nous avons effectué l'analyse TTC dans des conditions du régime permanent (stationnaire), d'autres recherches devraient également être menées dans des conditions transitoires en tenant compte de la région d'hystérésis pendant la transition de phase matériau oxyde à changement de phase. Une compréhension complète du concept du TTC pourrait nous rapprocher d'un schéma informatique avancé pour le calcul thermique.

Bibliography

[1] C. Haratoka, K. Joulain, and Y. Ezzahri, "Thermal rectification of a vanadium dioxide based conductive thermal diode under transient dirichlet conditions," *International Journal of Heat and Mass Transfer*, vol. 214, p. 124452, 2023. (Cited on pages xi, xviii, xxiii, 15, 16, 50, 51, 86, 140, 148, 150, 153, 154, 155, 156 and 157.)

[2] Z. Yang, C. Ko, and S. Ramanathan, "Oxide electronics utilizing ultrafast metal-insulator transitions," *Annual Review of Materials Research*, vol. 41, no. Volume 41, 2011, pp. 337–367, 2011. (Cited on pages xi, 17, 18, 22 and 83.)

[3] D. Wegkamp and J. Stähler, "Ultrafast dynamics during the photoinduced phase transition in vo2," *Progress in Surface Science*, vol. 90, no. 4, pp. 464–502, 2015. (Cited on pages xi, 19 and 20.)

[4] J. M. Atkin, S. Berweger, E. K. Chavez, M. B. Raschke, J. Cao, W. Fan, and J. Wu, "Strain and temperature dependence of the insulating phases of vo_2 near the metal-insulator transition," *Phys. Rev. B*, vol. 85, p. 020101, Jan 2012. (Cited on pages xi, 19, 20, 21 and 22.)

[5] J. Ordonez-Miranda, Y. Ezzahri, K. Joulain, J. Drevillon, and J. J. Alvarado-Gil, "Modeling of the electrical conductivity, thermal conductivity, and specific heat capacity of vo_2," *Phys. Rev. B*, vol. 98, p. 075144, Aug 2018. (Cited on pages xi, 15, 16, 22, 23, 84, 165, 187 and 224.)

[6] M. M. Qazilbash, M. Brehm, G. O. Andreev, A. Frenzel, P.-C. Ho, B.-G. Chae, B.-J. Kim, S. J. Yun, H.-T. Kim, A. V. Balatsky, O. G. Shpyrko, M. B. Maple, F. Keilmann, and D. N. Basov, "Infrared spectroscopy and nano-imaging of the insulator-to-metal transition in vanadium dioxide," *Phys. Rev. B*, vol. 79, p. 075107, Feb 2009. (Cited on pages xi, 22 and 23.)

[7] D.-W. Oh, C. Ko, S. Ramanathan, and D. G. Cahill, "Thermal conductivity and dynamic heat capacity across the metal-insulator transition in thin film vo2," *Applied Physics Letters*, vol. 96, no. 15, p. 151906, 2010. (Cited on pages xi, 14, 22, 23, 83 and 192.)

[8] D. W. Hahn and M. N. Özisik, *Heat conduction*. John Wiley & Sons, 2012. (Cited on pages xi, 12, 13, 24 and 25.)

[9] N. Li, J. Ren, L. Wang, G. Zhang, P. Hänggi, and B. Li, "Colloquium: Phononics: Manipulating heat flow with electronic analogs and beyond," *Rev. Mod. Phys.*, vol. 84, pp. 1045–1066, Jul 2012. (Cited on pages xi, xii, xiii, 25, 26, 27, 29, 32, 33, 56, 58, 81, 84, 85 and 87.)

[10] B. Li, L. Wang, and G. Casati, "Thermal diode: Rectification of heat flux," *Phys. Rev. Lett.*, vol. 93, p. 184301, Oct 2004. (Cited on pages xii, 28, 29, 30 and 37.)

[11] C. W. Chang, D. Okawa, A. Majumdar, and A. Zettl, "Solid-state thermal rectifier," *Science*, vol. 314, no. 5802, pp. 1121–1124, 2006. (Cited on pages xii, 30 and 31.)

[12] N. Yang, N. Li, L. Wang, and B. Li, "Thermal rectification and negative differential thermal resistance in lattices with mass gradient," *Phys. Rev. B*, vol. 76, p. 020301, Jul 2007. (Cited on pages xii, 31 and 32.)

[13] G. Wu and B. Li, "Thermal rectification in carbon nanotube intramolecular junctions: Molecular dynamics calculations," *Phys. Rev. B*, vol. 76, p. 085424, Aug 2007. (Cited on pages xii, 32, 33 and 35.)

[14] N. Yang, G. Zhang, and B. Li, "Carbon nanocone: A promising thermal rectifier," *Applied Physics Letters*, vol. 93, p. 243111, 12 2008. (Cited on pages xii, 32 and 33.)

[15] N. Yang, G. Zhang, and B. Li, "Thermal rectification in asymmetric graphene ribbons," *Applied Physics Letters*, vol. 95, p. 033107, 07 2009. (Cited on pages xii and 33.)

[16] J. W. Jiang, J. S. Wang, and B. Li, "Topology-induced thermal rectification in carbon nanodevice," *Europhysics Letters*, vol. 89, p. 46005, mar 2010. (Cited on pages xii, 33 and 34.)

[17] H. Zhao, X. Yang, C. Wang, R. Lu, T. Zhang, H. Chen, and X. Zheng, "Progress in thermal rectification due to heat conduction in micro/nano solids," *Materials Today Physics*, vol. 30, p. 100941, 2023. (Cited on pages xii, 34 and 35.)

[18] W.-R. Zhong, W.-H. Huang, X.-R. Deng, and B.-Q. Ai, "Thermal rectification in thickness-asymmetric graphene nanoribbons," *Applied Physics Letters*, vol. 99, p. 193104, 11 2011. (Cited on pages xii, 34 and 35.)

[19] M. M. Rojo, Z. Li, C. Sievers, A. C. Bornstein, E. Yalon, S. Deshmukh, S. Vaziri, M.-H. Bae, F. Xiong, D. Donadio, and E. Pop, "Thermal transport across graphene step junctions," *2D Materials*, vol. 6, p. 011005, nov 2018. (Cited on pages xii, 34 and 35.)

[20] S. Ju and X. Liang, "Thermal rectification and phonon scattering in asymmetric silicon nanoribbons," *Journal of Applied Physics*, vol. 112, p. 024307, 07 2012. (Cited on pages xii, 34 and 35.)

[21] Y. Wang, A. Vallabhaneni, J. Hu, B. Qiu, Y. P. Chen, and X. Ruan, "Phonon lateral confinement enables thermal rectification in asymmetric single-material nanostructures," *Nano Letters*, vol. 14, no. 2, pp. 592–596, 2014. PMID: 24393070. (Cited on pages xii and 35.)

[22] G. Lei, H. Cheng, H. Liu, and W. Rao, "Thermal rectification in asymmetric graphyne nanoribbons: A nonequilibrium molecular dynamics study," *Materials Letters*, vol. 189, pp. 101–103, 2017. (Cited on pages xii, 35 and 36.)

[23] H. Ma and Z. Tian, "Significantly high thermal rectification in an asymmetric polymer molecule driven by diffusive versus ballistic transport," *Nano Letters*, vol. 18, no. 1, pp. 43–48, 2018. PMID: 29215898. (Cited on pages xii, 35 and 36.)

[24] W. Li, Y.-H. Feng, J.-J. Tang, and X.-X. Zhang, "Thermal conductivity and thermal rectification of carbon nanotube y junctions," *Acta Phys. Sin.*, 2013. (Cited on pages xii, 35 and 36.)

[25] A. Aiyiti, Z. Zhang, B. Chen, S. Hu, J. Chen, X. Xu, and B. Li, "Thermal rectification in y-junction carbon nanotube bundle," *Carbon*, vol. 140, pp. 673–679, 2018. (Cited on pages xii, 35, 36 and 37.)

[26] Z. Zhang, Y. Chen, Y. Xie, and S. Zhang, "Transition of thermal rectification in silicon nanocones," *Applied Thermal Engineering*, vol. 102, pp. 1075–1080, 2016. (Cited on pages xii, 35 and 37.)

[27] N. A. Roberts and D. G. Walker, "Computational study of thermal rectification from nanostructured interfaces," *Journal of Heat Transfer*, vol. 133, p. 092401, 07 2011. (Cited on pages xii, 37 and 38.)

[28] H.-Y. Cao, H. Xiang, and X.-G. Gong, "Unexpected large thermal rectification in asymmetric grain boundary of graphene," *Solid State Communications*, vol. 152, no. 19, pp. 1807–1810, 2012. (Cited on pages xii, 37, 38 and 39.)

[29] B. Liu, J. A. Baimova, C. D. Reddy, S. V. Dmitriev, W. K. Law, X. Q. Feng, and K. Zhou, "Interface thermal conductance and rectification in hybrid graphene/silicene monolayer," *Carbon*, vol. 79, pp. 236–244, 2014. (Cited on pages xii, 38 and 39.)

[30] S. Li, Z.-X. Guo, and J. Ding, "Interface thermal transport of graphene-based intralayer heterostructures," *Physica B: Condensed Matter*, vol. 561, pp. 164–169, 2019. (Cited on pages xii, 38 and 40.)

[31] X.-K. Chen, Z.-X. Xie, Y. Zhang, Y.-X. Deng, T.-H. Zou, J. Liu, and K.-Q. Chen, "Highly efficient thermal rectification in carbon/boron nitride heteronanotubes," *Carbon*, vol. 148, pp. 532–539, 2019. (Cited on pages xii, 38 and 40.)

[32] W. Kobayashi, Y. Teraoka, and I. Terasaki, "An oxide thermal rectifier," *Applied Physics Letters*, vol. 95, p. 171905, 10 2009. (Cited on pages xiii, 41 and 42.)

[33] D. Sawaki, W. Kobayashi, Y. Moritomo, and I. Terasaki, "Thermal rectification in bulk materials with asymmetric shape," *Applied Physics Letters*, vol. 98, p. 081915, 02 2011. (Cited on pages xiii, 41, 42, 43 and 46.)

[34] W. Kobayashi, D. Sawaki, T. Omura, T. Katsufuji, Y. Moritomo, and I. Terasaki, "Thermal rectification in the vicinity of a structural phase transition," *Applied Physics Express*, vol. 5, p. 027302, jan 2012. (Cited on pages xiii, 43 and 44.)

[35] J. Ordonez-Miranda, J. M. Hill, K. Joulain, Y. Ezzahri, and J. Drevillon, "Conductive thermal diode based on the thermal hysteresis of vo2 and nitinol," *Journal of Applied Physics*, vol. 123, no. 8, p. 085102, 2018. (Cited on pages xiii, 14, 22, 46, 47, 83, 84, 98, 159, 187, 192, 209 and 224.)

[36] S. O. Kasali, J. Ordonez-Miranda, and K. Joulain, "Conductive thermal diode based on two phase-change materials," *International Journal of Thermal Sciences*, vol. 153, p. 106393, 2020. (Cited on pages xiii and 47.)

[37] S. O. Kasali, J. Ordonez-Miranda, K. Alaili, and K. Joulain, "Spherical and cylindrical conductive thermal diodes based on two phase-change materials," *Zeitschrift für Naturforschung A*, vol. 77, no. 2, pp. 181–190, 2022. (Cited on pages xiii, 47 and 48.)

[38] F. A. Herrera, T. Luo, and D. B. Go, "Thermal Rectification Under Transient Conditions: The Role of Thermal Capacitance and Thermal Conductivity," *Journal of Heat Transfer*, vol. 139, 05 2017. 091301. (Cited on pages xiii, 48, 49, 50, 55, 85, 86 and 132.)

[39] L. L. Zurdo, L. G. Chej, A. G. Monastra, and M. F. Carusela, "Thermal diode assisted by geometry under cycling temperature," *International Journal of Heat and Mass Transfer*, vol. 222, p. 125110, 2024. (Cited on pages xiii, 51, 52, 86 and 132.)

[40] L. Wang and B. Li, "Thermal logic gates: Computation with phonons," *Phys. Rev. Lett.*, vol. 99, p. 177208, Oct 2007. (Cited on pages xiii, 56, 58, 59, 60, 61, 77, 81 and 87.)

[41] P. Ben-Abdallah and S.-A. Biehs, "Near-field thermal transistor," *Phys. Rev. Lett.*, vol. 112, p. 044301, Jan 2014. (Cited on pages xiv, 60, 61 and 62.)

[42] K. Joulain, Y. Ezzahri, J. Drevillon, and P. Ben-Abdallah, "Modulation and amplification of radiative far field heat transfer: Towards a simple radiative thermal transistor," *Applied Physics Letters*, vol. 106, p. 133505, 04 2015. (Cited on pages xiv, 62, 63 and 64.)

[43] H. Prod'homme, J. Ordonez-Miranda, Y. Ezzahri, J. Drevillon, and K. Joulain, "Optimized thermal amplification in a radiative transistor," *Journal of Applied Physics*, vol. 119, p. 194502, 05 2016. (Cited on pages xiv, 63, 64, 65 and 66.)

[44] Y. Li, Y. Dang, S. Zhang, X. Li, Y. Jin, P. Ben-Abdallah, J. Xu, and Y. Ma, "Radiative thermal transistor," *Phys. Rev. Appl.*, vol. 20, p. 024061, Aug 2023. (Cited on pages xiv, 65, 66 and 67.)

[45] D. B. Strukov, G. S. Snider, D. R. Stewart, and R. S. Williams, "The missing memristor found," *nature*, vol. 453, no. 7191, pp. 80–83, 2008. (Cited on pages xiv, 68, 69, 70 and 88.)

[46] D. R. Stewart, D. A. A. Ohlberg, P. A. Beck, Y. Chen, R. S. Williams, J. O. Jeppesen, K. A. Nielsen, and J. F. Stoddart, "Molecule-independent electrical switching in pt/organic monolayer/ti devices," *Nano Letters*, vol. 4, no. 1, pp. 133–136, 2004. (Cited on pages xiv, 69 and 70.)

[47] P. Ben-Abdallah, "Thermal memristor and neuromorphic networks for manipulating heat flow," *AIP Advances*, vol. 7, p. 065002, 06 2017. (Cited on pages xiv, xv, 70, 71, 80, 81, 88, 91 and 125.)

[48] F. Yang, M. P. Gordon, and J. J. Urban, "Theoretical framework of the thermal memristor via a solid-state phase change material," *Journal of Applied Physics*, vol. 125, p. 025109, 01 2019. (Cited on pages xiv, 71, 72, 88, 91 and 125.)

[49] J. Ordonez-Miranda, Y. Ezzahri, J. A. Tiburcio-Moreno, K. Joulain, and J. Drevillon, "Radiative thermal memristor," *Phys. Rev. Lett.*, vol. 123, p. 025901, Jul 2019. (Cited on pages xv, 70, 73 and 88.)

[50] M. Wong, C. Tso, T. Ho, and H. Lee, "A review of state of the art thermal diodes and their potential applications," *International Journal of Heat and Mass Transfer*, vol. 164, p. 120607, 2021. (Cited on pages xv, 26, 27, 34, 37, 55, 74, 75, 76, 77, 78 and 79.)

[51] A. Hamed, M. Elzouka, and S. Ndao, "Thermal calculator," *International Journal of Heat and Mass Transfer*, vol. 134, pp. 359–365, 2019. (Cited on pages xv, 56, 78, 79 and 81.)

[52] C. Haratoka, K. Joulain, and Y. Ezzahri, "Conductive thermal diode based on vanadium dioxide under dynamical boundary conditions," *International Journal of Heat and Mass Transfer*, vol. 255, p. 127702, 2026. (Cited on pages xv, xix, xxiii, 51, 99, 159, 161, 162, 163, 164, 168, 169, 172 and 173.)

[53] J.-G. Ramírez, A. Sharoni, Y. Dubi, M. E. Gómez, and I. K. Schuller, "First-order reversal curve measurements of the metal-insulator transition in vo_2: Signatures of persistent metallic domains," *Phys. Rev. B*, vol. 79, p. 235110, Jun 2009. (Cited on pages xv, 99, 100 and 126.)

[54] M. Gurvitch, S. Luryi, A. Polyakov, and A. Shabalov, "Nonhysteretic behavior inside the hysteresis loop of VO2 and its possible application in infrared imaging," *Journal of Applied Physics*, vol. 106, p. 104504, 11 2009. (Cited on pages xvi, 100, 101 and 126.)

[55] J.-C. Krapez, "Influence of thermal hysteresis on the heat shuttling effect: The case of VO2," *Journal of Applied Physics*, vol. 133, p. 195102, 05 2023. (Cited on pages xvi, 92, 101, 103, 104, 105, 126 and 127.)

[56] C. Haratoka, K. Joulain, and Y. Ezzahri, "Concept of a simple conductive thermal transistor based on an oxide phase change material," *International Journal of Heat and Mass Transfer*, vol. 256, p. 128085, 2026. (Cited on pages xix, xx, xxi, xxiii, 59, 60, 186, 193, 194, 195, 196, 197, 198, 201, 203, 204, 205 and 206.)

[57] Y. Çengel and A. Ghajar, *Heat and Mass Transfer: Fundamentals & Applications*. McGraw Hill Education, 2015. (Cited on pages 10, 11, 13, 14 and 15.)

[58] N. W. Ashcroft and N. D. Mermin, *Solid state physics*. New York, NY: Holt, Rinehart and Winston, 1976. (Cited on page 10.)

[59] S. Kakac, Y. Yener, and C. Naveira-Cotta, *Heat Conduction, Fifth Edition (5th ed.)*. CRC Press, 2018. (Cited on page 11.)

[60] S. Raoux, "Phase change materials," *Annual Review of Materials Research*, vol. 39, no. 1, pp. 25–48, 2009. (Cited on pages 14 and 40.)

[61] C. N. Berglund and H. J. Guggenheim, "Electronic properties of vo_2 near the semiconductor-metal transition," *Phys. Rev.*, vol. 185, pp. 1022–1033, Sep 1969. (Cited on pages 16, 84 and 102.)

[62] P. L. Kapitza, "Heat transfer and superfluidity of helium ii," *Phys. Rev.*, vol. 60, pp. 354–355, Aug 1941. (Cited on page 16.)

[63] F. J. Morin, "Oxides which show a metal-to-insulator transition at the neel temperature," *Phys. Rev. Lett.*, vol. 3, pp. 34–36, Jul 1959. (Cited on pages 17, 83, 187, 192 and 209.)

[64] Z. Shao, X. Cao, H. Luo, and P. Jin, "Recent progress in the phase-transition mechanism and modulation of vanadium dioxide materials," *NPG Asia Materials*, vol. 10, no. 7, pp. 581–605, 2018. (Cited on pages 17, 18, 19 and 83.)

[65] N. F. MOTT, "Metal-insulator transition," *Rev. Mod. Phys.*, vol. 40, pp. 677–683, Oct 1968. (Cited on pages 18 and 83.)

[66] R. E. Peierls, *Quantum theory of solids*. Clarendon Press, 1996. (Cited on pages 18 and 83.)

[67] M. S. Grinolds, V. A. Lobastov, J. Weissenrieder, and A. H. Zewail, "Four-dimensional ultrafast electron microscopy of phase transitions," *Proceedings of the National Academy of Sciences*, vol. 103, no. 49, pp. 18427–18431, 2006. (Cited on page 19.)

[68] J. B. Goodenough, "The two components of the crystallographic transition in vo2," *Journal of Solid State Chemistry*, vol. 3, no. 4, pp. 490–500, 1971. (Cited on page 19.)

[69] C. Swaminathan and V. R. Voller, "On the enthalpy method," *International Journal of Numerical Methods for Heat & Fluid Flow*, vol. 3, no. 3, pp. 233–244, 1993. (Cited on pages 24 and 84.)

[70] N. Eyres, D. R. Hartree, J. Ingham, R. Sarjant, and J. Wagstaff, "The calculation of variable heat flow in solids," *Philosophical Transactions of the Royal Society of London. Series A, Mathematical and Physical Sciences*, vol. 240, no. 813, pp. 1–57, 1946. (Cited on pages 24 and 84.)

[71] N. Shamsundar and E. Sparrow, "Analysis of multidimensional conduction phase change via the enthalpy model," *Journal of Heat Transfer*, vol. 97, pp. 333–340, Aug. 1975. (Cited on page 24.)

[72] J. Bardeen and W. H. Brattain, "The transistor, a semi-conductor triode," *Phys. Rev.*, vol. 74, pp. 230–231, Jul 1948. (Cited on pages 26, 56, 85, 86 and 87.)

[73] N. Roberts and D. Walker, "A review of thermal rectification observations and models in solid materials," *International Journal of Thermal Sciences*, vol. 50, no. 5, pp. 648–662, 2011. (Cited on pages 26, 27, 81 and 85.)

[74] G. Wehmeyer, T. Yabuki, C. Monachon, J. Wu, and C. Dames, "Thermal diodes, regulators, and switches: Physical mechanisms and potential applications," *Applied Physics Reviews*, vol. 4, no. 4, p. 041304, 2017. (Cited on pages 26 and 27.)

[75] C. Starr, "The copper oxide rectifier," *Physics*, vol. 7, no. 1, pp. 15–19, 1936. (Cited on pages 26 and 85.)

[76] Y. Li, W. Li, T. Han, X. Zheng, J. Li, B. Li, S. Fan, and C.-W. Qiu, "Transforming heat transfer with thermal metamaterials and devices," *Nature Reviews Materials*, vol. 6, no. 6, pp. 488–507, 2021. (Cited on pages 27 and 81.)

[77] M. Terraneo, M. Peyrard, and G. Casati, "Controlling the energy flow in nonlinear lattices: A model for a thermal rectifier," *Phys. Rev. Lett.*, vol. 88, p. 094302, Feb 2002. (Cited on pages 27 and 28.)

[78] L. Wang and B. Li, "Phononics gets hot," *Physics World*, vol. 21, p. 27, mar 2008. (Cited on pages 27 and 30.)

[79] B. Li, J. Lan, and L. Wang, "Interface thermal resistance between dissimilar anharmonic lattices," *Phys. Rev. Lett.*, vol. 95, p. 104302, Sep 2005. (Cited on pages 28 and 29.)

[80] J. Hone, M. Whitney, C. Piskoti, and A. Zettl, "Thermal conductivity of single-walled carbon nanotubes," *Phys. Rev. B*, vol. 59, pp. R2514–R2516, Jan 1999. (Cited on page 30.)

[81] C. W. Chang, W. Q. Han, and A. Zettl, "Erratum: "thermal conductivity of b–c–n and bn nanotubes" [j. vac. sci. technol. b 23, 1883 (2005)]," *Journal of Vacuum Science & Technology B: Microelectronics and Nanometer Structures Processing, Measurement, and Phenomena*, vol. 27, pp. 199–199, 02 2009. (Cited on page 30.)

[82] J. Hu, X. Ruan, and Y. P. Chen, "Thermal conductivity and thermal rectification in graphene nanoribbons: A molecular dynamics study," *Nano Letters*, vol. 9, no. 7, pp. 2730–2735, 2009. PMID: 19499898. (Cited on page 34.)

[83] M. Peyrard, "The design of a thermal rectifier," *Europhysics Letters*, vol. 76, p. 49, aug 2006. (Cited on page 41.)

[84] C. Dames, "Solid-state thermal rectification with existing bulk materials," *Journal of Heat Transfer*, vol. 131, p. 061301, 03 2009. (Cited on page 41.)

[85] E. Pallecchi, Z. Chen, G. E. Fernandes, Y. Wan, J. H. Kim, and J. Xu, "A thermal diode and novel implementation in a phase-change material," *Mater. Horiz.*, vol. 2, pp. 125–129, 2015. (Cited on pages 44 and 45.)

[86] T. Zhang and T. Luo, "Giant thermal rectification from polyethylene nanofiber thermal diodes," *Small*, vol. 11, no. 36, pp. 4657–4665, 2015. (Cited on pages 44 and 45.)

[87] R. Chen, Y. Cui, H. Tian, R. Yao, Z. Liu, Y. Shu, C. Li, Y. Yang, T. Ren, G. Zhang, *et al.*, "Controllable thermal rectification realized in binary phase change composites," *Scientific reports*, vol. 5, no. 1, p. 8884, 2015. (Cited on page 45.)

[88] A. L. Cottrill and M. S. Strano, "Analysis of thermal diodes enabled by junctions of phase change materials," *Advanced Energy Materials*, vol. 5, no. 23, p. 1500921, 2015. (Cited on page 45.)

[89] K. Garcia-Garcia and J. Alvarez-Quintana, "Thermal rectification assisted by lattice transitions," *International Journal of Thermal Sciences*, vol. 81, pp. 76–83, 2014. (Cited on page 45.)

[90] A. L. Cottrill, S. Wang, A. T. Liu, W.-J. Wang, and M. S. Strano, "Dual phase change thermal diodes for enhanced rectification ratios: Theory and experiment," *Advanced Energy Materials*, vol. 8, no. 11, p. 1702692, 2018. (Cited on page 45.)

[91] Y. Yang, H. Chen, H. Wang, N. Li, and L. Zhang, "Optimal thermal rectification of heterojunctions under fourier law," *Phys. Rev. E*, vol. 98, p. 042131, Oct 2018. (Cited on pages 45 and 46.)

[92] T. Takeuchi, H. Goto, R.-s. Nakayama, Y.-i. Terazawa, K. Ogawa, A. Yamamoto, T. Itoh, and M. Mikami, "Improvement in rectification ratio of an al-based bulk thermal rectifier working at high temperatures," *Journal of Applied Physics*, vol. 111, p. 093517, 05 2012. (Cited on page 46.)

[93] R.-s. Nakayama and T. Takeuchi, "Thermal rectification in bulk material through unusual behavior of electron thermal conductivity of al-cu-fe icosahedral quasicrystal," *Journal of Electronic Materials*, vol. 44, pp. 356–361, 2015. (Cited on page 46.)

[94] H. Wang, S. Hu, K. Takahashi, X. Zhang, H. Takamatsu, and J. Chen, "Experimental study of thermal rectification in suspended monolayer graphene," *Nature communications*, vol. 8, no. 1, p. 15843, 2017. (Cited on page 46.)

[95] H. Kang, F. Yang, and J. J. Urban, "Thermal rectification via heterojunctions of solid-state phase-change materials," *Phys. Rev. Applied*, vol. 10, p. 024034, Aug 2018. (Cited on pages 46 and 47.)

[96] K. Klinar, M. Muñoz Rojo, Z. Kutnjak, and A. Kitanovski, "Toward a solid-state thermal diode for room-temperature magnetocaloric energy conversion," *Journal of Applied Physics*, vol. 127, no. 23, p. 234101, 2020. (Cited on pages 49, 86 and 132.)

[97] T. J. Shimokusu, Q. Zhu, N. Rivera, and G. Wehmeyer, "Time-periodic thermal rectification in heterojunction thermal diodes," *International Journal of Heat and Mass Transfer*, vol. 182, p. 122035, 2022. (Cited on pages 49, 50, 86 and 132.)

[98] C. R. Otey, W. T. Lau, and S. Fan, "Thermal rectification through vacuum," *Phys. Rev. Lett.*, vol. 104, p. 154301, Apr 2010. (Cited on pages 51 and 52.)

[99] S. Basu and M. Francoeur, "Near-field radiative transfer based thermal rectification using doped silicon," *Applied Physics Letters*, vol. 98, p. 113106, 03 2011. (Cited on pages 51 and 52.)

[100] L. P. Wang and Z. M. Z. and, "Thermal rectification enabled by near-field radiative heat transfer between intrinsic silicon and a dissimilar material," *Nanoscale and Microscale Thermophysical Engineering*, vol. 17, no. 4, pp. 337–348, 2013. (Cited on page 52.)

[101] P. J. van Zwol, K. Joulain, P. Ben Abdallah, J. J. Greffet, and J. Chevrier, "Fast nanoscale heat-flux modulation with phase-change materials," *Phys. Rev. B*, vol. 83, p. 201404, May 2011. (Cited on page 52.)

[102] P. J. van Zwol, K. Joulain, P. Ben-Abdallah, and J. Chevrier, "Phonon polaritons enhance near-field thermal transfer across the phase transition of vo_2," *Phys. Rev. B*, vol. 84, p. 161413, Oct 2011. (Cited on page 52.)

[103] P. J. van Zwol, L. Ranno, and J. Chevrier, "Emissivity measurements with an atomic force microscope," *Journal of Applied Physics*, vol. 111, p. 063110, 03 2012. (Cited on page 52.)

[104] P. J. van Zwol, L. Ranno, and J. Chevrier, "Tuning near field radiative heat flux through surface excitations with a metal insulator transition," *Phys. Rev. Lett.*, vol. 108, p. 234301, Jun 2012. (Cited on page 52.)

[105] P. Ben-Abdallah and S.-A. Biehs, "Phase-change radiative thermal diode," *Applied Physics Letters*, vol. 103, p. 191907, 11 2013. (Cited on pages 52 and 53.)

[106] Y. Yang, S. Basu, and L. Wang, "Radiation-based near-field thermal rectification with phase transition materials," *Applied Physics Letters*, vol. 103, p. 163101, 10 2013. (Cited on page 53.)

[107] E. Nefzaoui, K. Joulain, J. Drevillon, and Y. Ezzahri, "Radiative thermal rectification using superconducting materials," *Applied Physics Letters*, vol. 104, p. 103905, 03 2014. (Cited on page 53.)

[108] E. Nefzaoui, J. Drevillon, Y. Ezzahri, and K. Joulain, "Simple far-field radiative thermal rectifier using fabry–perot cavities based infrared selective emitters," *Appl. Opt.*, vol. 53, pp. 3479–3485, Jun 2014. (Cited on page 53.)

[109] K. Ito, K. Nishikawa, H. Iizuka, and H. Toshiyoshi, "Experimental investigation of radiative thermal rectifier using vanadium dioxide," *Applied Physics Letters*, vol. 105, p. 253503, 12 2014. (Cited on page 53.)

[110] A. Fiorino, D. Thompson, L. Zhu, R. Mittapally, S.-A. Biehs, O. Bezencenet, N. El-Bondry, S. Bansropun, P. Ben-Abdallah, E. Meyhofer, and P. Reddy, "A thermal diode based on nanoscale thermal radiation," *ACS Nano*, vol. 12, no. 6, pp. 5774–5779, 2018. PMID: 29790344. (Cited on pages 53 and 54.)

[111] I. Forero-Sandoval, J. Chan-Espinoza, J. Ordonez-Miranda, J. Alvarado-Gil, F. Dumas-Bouchiat, C. Champeaux, K. Joulain, Y. Ezzahri, J. Drevillon, C. Gomez-Heredia, and J. Ramirez-Rincon, "Vo2 substrate effect on the thermal rectification of a far-field radiative diode," *Phys. Rev. Appl.*, vol. 14, p. 034023, Sep 2020. (Cited on page 54.)

[112] A. Ghanekar, J. Ji, and Y. Zheng, "High-rectification near-field thermal diode using phase change periodic nanostructure," *Applied Physics Letters*, vol. 109, p. 123106, 09 2016. (Cited on page 54.)

[113] A. Ghanekar, Y. Tian, M. Ricci, S. Zhang, O. Gregory, and Y. Zheng, "Near-field thermal rectification devices using phase change periodic nanostructure," *Opt. Express*, vol. 26, pp. A209–A218, Jan 2018. (Cited on page 54.)

[114] L. Wang and B. Li, "Thermal memory: A storage of phononic information," *Phys. Rev. Lett.*, vol. 101, p. 267203, Dec 2008. (Cited on pages 56, 81 and 87.)

[115] W. Shockley, "A unipolar "field-effect" transistor," *Proceedings of the IRE*, vol. 40, no. 11, pp. 1365–1376, 1952. (Cited on pages 56 and 87.)

[116] B. Li, L. Wang, and G. Casati, "Negative differential thermal resistance and thermal transistor," *Applied Physics Letters*, vol. 88, p. 143501, 04 2006. (Cited on pages 57, 82, 87, 89, 185, 188, 223 and 224.)

[117] L. Esaki, "New phenomenon in narrow germanium $p - n$ junctions," *Phys. Rev.*, vol. 109, pp. 603–604, Jan 1958. (Cited on page 57.)

[118] T. Wu, Y. Yang, T. Wang, X. Li, and L. Zhang, "Optimizing the performance of the thermal transistor based on negative differential thermal resistance," *Applied Physics Letters*, vol. 124, p. 112201, 03 2024. (Cited on pages 59, 82, 87, 89, 185 and 223.)

[119] L. Castelli, Q. Zhu, T. J. Shimokusu, and G. Wehmeyer, "A three-terminal magnetic thermal transistor," *Nature Communications*, vol. 14, no. 1, p. 393, 2023. (Cited on pages 66, 67 and 78.)

[120] I. Alonzo-Zapata, C. Champeaux, F. Enguehard, J. Ordonez-Miranda, and F. Dumas-Bouchiat, "Emissivity measurements of vanadium dioxide thin films through the thermal wave resonant cavity and its applications in radiative thermal diode and transistor simulations," *International Journal of Heat and Mass Transfer*, vol. 224, p. 125298, 2024. (Cited on page 68.)

[121] L. Chua, "Memristor-the missing circuit element," *IEEE Transactions on Circuit Theory*, vol. 18, no. 5, pp. 507–519, 1971. (Cited on pages 68 and 88.)

[122] L. Chua, "Resistance switching memories are memristors," *Handbook of memristor networks*, pp. 197–230, 2019. (Cited on page 68.)

[123] K. Wang, M. Wang, B. Sun, C. Yang, Z. Cao, T. Wu, K. Gao, H. Ma, W. Yan, H. Wang, L. Fu, X. Li, and J. Shao, "An innovative biomimetic technology: Memristors mimic human sensation," *Nano Energy*, vol. 136, p. 110698, 2025. (Cited on pages 70 and 80.)

[124] Z. Z. S. K. Y. J. X. W. Yongyue Xiao, Bei Jiang and C. Ye, "A review of memristor: material and structure design, device performance, applications and prospects," *Science and Technology of Advanced Materials*, vol. 24, no. 1, p. 2162323, 2023. PMID: 36872944. (Cited on pages 70 and 80.)

[125] M. Westwood, *Thermal Rectification to Increase Power and Efficiency of Solar-Thermal Electricity Generation*. Master of science report, University of California at Berkeley, 2015. (Cited on pages 73 and 74.)

[126] X. Zhao, *Thermal Diode Bridge Applied to Solar Energy Harvesting.* Master of science report, University of California at Berkeley, 2015. (Cited on pages 73 and 74.)

[127] A. Pugsley, A. Zacharopoulos, J. Deb Mondol, and M. Smyth, "Theoretical and experimental analysis of a horizontal planar liquid-vapour thermal diode (plvtd)," *International Journal of Heat and Mass Transfer*, vol. 144, p. 118660, 2019. (Cited on page 74.)

[128] H. Zhao, Y. Wu, H. Sun, B. Lin, M. Zhong, G. Jiang, and S. Wu, "A novel building envelope combined with jumping-droplet thermal diode: From theory to practice," *Renewable Energy*, vol. 218, p. 119278, 2023. (Cited on page 74.)

[129] Y. Wu, Y. Gao, C. Wang, Q. Chen, and T. Ming, "The energy saving performance of the thermal diode composite wall in different climate regions," *Renewable Energy*, vol. 219, p. 119360, 2023. (Cited on page 74.)

[130] L. Castelli, M. V. Kumar, and G. Wehmeyer, "Multi-season passive variable insulation for buildings using magnetic thermal diodes," *Cell Reports Physical Science*, vol. 5, no. 11, p. 102283, 2024. (Cited on pages 75 and 76.)

[131] A. Kitanovski, U. Plaznik, U. Tomc, and A. Poredoš, "Present and future caloric refrigeration and heat-pump technologies," *International Journal of Refrigeration*, vol. 57, pp. 288–298, 2015. (Cited on page 76.)

[132] K. Klinar and A. Kitanovski, "Thermal control elements for caloric energy conversion," *Renewable and Sustainable Energy Reviews*, vol. 118, p. 109571, 2020. (Cited on page 76.)

[133] P. Ben-Abdallah and S.-A. Biehs, "Towards boolean operations with thermal photons," *Phys. Rev. B*, vol. 94, p. 241401, Dec 2016. (Cited on page 78.)

[134] A. Hamed and S. Ndao, "Nanothermomechanical and and or logic gates," *Scientific Reports*, vol. 10, no. 1, p. 2437, 2020. (Cited on page 78.)

[135] A. L. Moore and L. Shi, "Emerging challenges and materials for thermal management of electronics," *Materials Today*, vol. 17, no. 4, pp. 163–174, 2014. (Cited on pages 79 and 81.)

[136] Y. V. Pershin, S. La Fontaine, and M. Di Ventra, "Memristive model of amoeba learning," *Phys. Rev. E*, vol. 80, p. 021926, Aug 2009. (Cited on page 80.)

[137] Y. V. Pershin and M. Di Ventra, "Spin memristive systems: Spin memory effects in semiconductor spintronics," *Phys. Rev. B*, vol. 78, p. 113309, Sep 2008. (Cited on page 80.)

[138] W. Huh, D. Lee, and C.-H. Lee, "Memristors based on 2d materials as an artificial synapse for neuromorphic electronics," *Advanced Materials*, vol. 32, no. 51, p. 2002092, 2020. (Cited on page 80.)

[139] M. Browne, B. Norton, and S. McCormack, "Phase change materials for photovoltaic thermal management," *Renewable and Sustainable Energy Reviews*, vol. 47, pp. 762–782, 2015. (Cited on page 81.)

[140] Z. Rao and S. Wang, "A review of power battery thermal energy management," *Renewable and Sustainable Energy Reviews*, vol. 15, no. 9, pp. 4554–4571, 2011. (Cited on page 81.)

[141] A. Pasupathy, R. Velraj, and R. Seeniraj, "Phase change material-based building architecture for thermal management in residential and commercial establishments," *Renewable and Sustainable Energy Reviews*, vol. 12, no. 1, pp. 39–64, 2008. (Cited on page 81.)

[142] G. Andersson, C. Parck, U. Ulfvarson, E. Stenhagen, and B. Thorell, "Studies on vanadium oxides. ii. the crystal structure of vanadium dioxide.," *Acta Chemica Scandinavica*, vol. 10, pp. 623–628, 1956. (Cited on page 83.)

[143] C. Leroux, G. Nihoul, and G. Van Tendeloo, "From $vo_2(b)$ to $vo_2(r)$: theoretical structures of vo_2 polymorphs and in situ electron microscopy," *Phys. Rev. B*, vol. 57, pp. 5111–5121, Mar 1998. (Cited on pages 84 and 102.)

[144] M. N. Özişik, H. R. Orlande, M. J. Colaço, and R. M. Cotta, *Finite difference methods in heat transfer*. CRC press, 2017. (Cited on pages 92, 93, 103 and 125.)

[145] D. Maillet, S. André, J. C. Batsale, A. Degiovanni, and C. Moyne, "Thermal quadrupoles: solving the heat equation through integral transforms," *(Wiley)*, 2000. (Cited on pages 134 and 180.)

[146] W. bin Yuan, N. Yu, L. yuan Li, and Y. Fang, "Heat transfer analysis in multi-layered materials with interfacial thermal resistance," *Composite Structures*, vol. 293, p. 115728, 2022. (Cited on pages 141, 142 and 156.)